Characterisation of Powders Using Microwave Cavity Perturbation

by Jerome Alexander Cuenca

A thesis submitted to Cardiff University

for the degree of Doctor of Philosophy

2015

Declaration

This work has not previously been accepted in substance for any degree and is not concurrently submitted in candidature for any degree.

Signed: ..... Date: .....

Statement 1

This thesis is being submitted in partial fulfilment of the requirements for the degree of PhD.

Signed: ..... Date: .....

Statement 2

This thesis is the result of my own independent work/investigation, except where otherwise stated. Other sources are acknowledged by explicit references. The views expressed are my own.

Signed: ..... Date: .....

Statement 3

I confirm that the electronic copy is identical to the bound copy of the thesis.

Signed: ..... Date: .....

Statement 4

I hereby give consent for my thesis, if accepted, to be available for photocopying and for inter-library loan, and for the title and summary to be made available to outside organisations.

Signed: ..... Date: .....

Abstract

The contribution in this thesis is a novel application of microwave cavity perturbation in the characterisation of the fundamental properties of powders.

This thesis shows that microwave cavity perturbation is very good at characterising the magnetite to maghemite phase change through dielectric and magnetic measurements. This is very important in material science since conventional techniques, though powerful and are able to verify the change, use complex methods. Quantifying different forms of magnetite and maghemite is important for magnetic drug delivery and EMI absorbers.

This thesis shows that microwave cavity perturbation can be used to measure the impurities of nanodiamonds through simple dielectric measurements. This is important because other methods again may involve complex systems, while microwave cavity perturbation can provide a fast, sensitive figure of merit. Nanodiamonds are used in drug delivery and bio-labelling which requires accurate surface characterisation.

This thesis shows that microwave cavity perturbation can measure in-situ temperature dependent and photocatalytic responses in materials such as titania using a novel correction procedure. Microwave cavity perturbation has not been used with this correction procedure before which simplifies the system when monitoring systematic errors. This work is important as it shows how simple microwave cavity perturbation systems can provide insight to thermally activated processes and verification of some photocatalytic mechanisms in powders for use in pigmentation and light induced drug delivery.

Acknowledgements

I would like to express my sincerest gratitude and thanks to my supervisor, *Prof. Adrian Porch* who has guided me and given me the opportunity to research microwaves and fascinating materials with such a fantastic group at Cardiff University.

My thanks extend to *Reinhold Rüger*, *Sylke Klein*, *Björn Kleist*, *Johann Bauer* and my fellow colleagues in the functional pigments group at Merck KGaA, who have always provided guidance and meaningful insight to my research. It has been a great pleasure.

My thanks go to *Prof. Oliver Williams* and his team at the Cardiff School of Physics and Astronomy who have encouraged collaboration and have allowed my research to flourish, *Dr. Paul Williams* at the Cardiff Wolfson Centre for Magnetics who trained me during my magnetics research and *Prof. Stuart Taylor* and all at the Cardiff Catalysis Institute who welcomed and guided me from a material science perspective. This work would not have been possible without the help and patience from my fellow colleagues in the Centre of High Frequency Engineering with special thanks to *Jon Hartley*, *Heungjae Choi* and *Nicholas Clark* who helped make this subject engaging and created an animated working environment.

I would also like to thank my parents *Rosita* and *Vivencio* who have wholeheartedly supported my career decisions throughout my life.

Last but not least, this work would not have been possible without the love and patience from my partner *Marié Nevin*, who I depended upon for support during the most challenging part of my career. She has always provided balanced insight and pulled me back to reality to ensure my completion of this degree. まりえの献身的な応援のおかげで、この論文を完成することができました。

The following experimental work was not conducted by the author:

- Raw XRD scans in Chapter 5 were done by *Keith Bugler* from the Cardiff Catalysis Institute. Insight to the results was provided while the analysis in this thesis was written by the author.
- Raw XPS scans given in Chapter 5 were done by *David Morgan* from the Cardiff Catalysis Institute. Insight to the results was provided while the analysis in this thesis was written by the author.
- Raw XRD scans given in Chapter 6 were done by *Tom Davies* from the Cardiff Catalysis Institute. Insight to the results was provided while the analysis in this thesis was written by the author.
- Raw FESEM scans given in Chapter 6 were done by *Soumen Mandal* from the Cardiff School of Physics and Astronomy. Insight to the results was provided while the analysis in this thesis was written by the author.

Publications

Journals and Conferences:

J. A. Cuenca, K. Bugler, S. Taylor, D. Morgan, P. Williams, J. Bauer, and A. Porch, "*Study of the magnetite to maghemite transition using microwave permittivity and permeability measurements*," J. Condens. Matter Phys., *Accepted Dec. 2015.*

J. A. Cuenca, E. Thomas, S. Mandal, O. Williams, and A. Porch, "*Investigating the broadband microwave absorption of nanodiamond impurities*," IEEE Trans. Microw. Theory Tech., vol. 63, pp. 4110-4118, Dec. 2015.

J. A. Cuenca, E. Thomas, S. Mandal, O. Williams, and A. Porch, "*Microwave determination of sp^2 carbon fraction in nanodiamond powders*," Carbon J., vol. 81, pp. 174-178, Jan. 2015.

J. A. Cuenca, E. Thomas, S. Mandal, O. Williams, and A. Porch, "*Broadband microwave measurements of nanodiamond*," in Microwave Conference (APMC), 2014, pp. 441-443.

J. A. Cuenca, S. Klein, R. Rüger, and A. Porch, "*Microwave complex permeability of magnetite using non-demagnetising and demagnetising cavity modes*," in Microwave Conference (EuMC), 2014 44th European, 2014, pp. 128-131.

J. A. Cuenca, H. Choi, J. Hartley, and A. Porch, "*Microwave detection of photodielectric effects in antimony tin oxide*," in International Symposium on Information Technology Convergence (ISITC), 2014.

Co-Author:

A. Imtiaz, Z. A. Mokhti, J. Cuenca, and J. Lees, "*An integrated inverse-F power amplifier design approach for heating applications in a microwave resonant cavity*," in Microwave Conference (APMC), 2014 Asia-Pacific, 2014, pp. 756-758.

H. Choi, J. Cuenca, G. Attard, and A. Porch, "*A Novel Concentration Detection Method of Hydrogen Peroxide Using Microwave Cavity Perturbation Technique*," in Microwave Conference (EuMC), 2014 44th European, 2014, no. 1, pp. 632-635.

H. Choi, J. A. Cuenca, J. Hartley, and A. Porch, "*Observation of change in microwave properties during solid to liquid phase transformation of gallium*," in International Symposium on Information Technology Convergence (ISITC), 2014.

J. Hartley, H. Choi, J. A. Cuenca, and A. Porch, "*Assessment of machine oil quality by microwave cavity perturbation method*," in International Symposium on Information Technology Convergence (ISITC), 2014.

Contents

List of Figures

List of Tables

Abbreviations

AMTMP	**A**dvanced **M**ethod of **T**ransient **M**icrowave **P**hoto-conductivity
CVD	**C**hemical **V**apour **D**eposition
DC	**D**irect **C**urrent
EMI	**E**lectro-**M**agnetic **I**nterference
EPR	**E**lectron **P**aramagnetic **R**esonance
ESR	**E**lectron **S**pin **R**esonance
FESEM	**F**ield **E**mission **S**canning **E**lectron **M**icroscopy
FTIR	**F**ourier **T**ransform **I**nfra-**R**ed
IR	**I**nfra-**R**ed
LDS	**L**aser **D**irect **S**tructuring
HPHT	**H**igh **P**ressure **H**igh **T**emperature
HRTEM	**H**igh **R**esolution **T**ransmission **E**lectron **M**icroscopy
JPL	**J**onscher **P**ower **L**aw
MBCP	**M**icrowave **B**roadband **C**oaxial **P**robe
MCP	**M**icrowave **C**avity **P**erturbation
MRI	**M**agnetic **R**esonance **I**maging
NMR	**N**uclear **M**agnetic **R**esonance
ROS	**R**eactive **O**xygen **S**pecies
RDX	**R**esearch **D**epartment e**X**plosive
SLPL	**S**uper **L**inear **P**ower **L**aw
SQUID	**S**uper-conducting **QU**antum **I**nterference **D**evice
TMP	**T**ransient **M**icrowave **P**hoto-conductivity
TNT	**T**ri**N**itro**T**oluene
UV-VIS	**U**ltra **V**iolet **- VIS**ible
UDD	**U**ltra **D**ispersed **D**iamond
VSM	**V**ibrating **S**ample **M**agnetometry
VNA	**V**ector **N**etwork **A**nalyser
XANES	**X**-Ray **A**bsorption **N**ear **E**dge **S**pectroscopy
XPS	**X**-Ray **P**hotoelectron **S**pectroscopy
XRD	**X**-**R**ay **D**iffraction

Physical Constants

Bohr Magneton	μ_B	=	9.274×10^{-24} J T^{-1}
Boltzmann Constant	k_B	=	1.381×10^{-23} J K^{-1}
Electron Charge	e	=	1.602×10^{-19} C
Electron Mass	m_e	=	9.109×10^{-31} kg
Speed of Light	c	=	2.998×10^{8} m s^{-1}
Permeability of Free Space	μ_0	=	1.257×10^{-6} H m^{-1}
Permittivity of Free Space	ε_0	=	8.854×10^{-12} F m^{-1}
Planck Constant	$\hbar$	=	1.054×10^{-34} J s

CHAPTER 1

Literature Survey: Applications of Powders

Functional powders are a new and emerging technology, but the big questions are:

What are the features that need to be characterised?
Can these features be measured easily using microwaves?

This thesis attempts to answer these questions for a selection of new and promising nanoparticle technologies which are prominent in biomedical applications and including:

- Magnetic nanoparticles (Fe_3O_4 and γ-Fe_2O_3)
- Nanoscale diamonds (nanodiamonds)
- Photo-catalytic titania (TiO_2)

In this section, some key applications are outlined where microwave spectroscopy can be used to measure certain useful properties. Next, fundamental material mechanisms which microwaves measure are presented, and the information that can be gained from such measurements. Finally, some microwave measurement techniques are outlined, and the use of MCP is justified for a simple quality control system for material scientists.

1.1 Magnetite and Maghemite Nanoparticles

Magnetic nanoparticles (Fe_3O_4 and γ-Fe_2O_3) have a lot of flexibility in biomedicine applications, including magnetic resonance imaging[1–3], targeted drug delivery[4] and magnetic hyperthermia[5]. They are also one of the few materials which remain magnetic at microwave frequencies, making them valuable for high speed systems[6] and EMI absorbers[7]. Magnetism arises in materials with unpaired electron spins such that there is a net magnetic moment. Normally, it is separated into multiple domains, but if it can be made on the nanoscale, a single domain particle can be made where the thermal energy of the particle is large enough to overcome any magnetic moment alignment (no remanence). This feature is known as super-paramagnetism. At room temperature there is no observable magnetic moment, however, upon the application of a field, a large magnetic moment develops. This large controllable magnetic moment in a small volume is what makes these particles useful for the above applications[8].

In the next sections a few applications have been outlined where Fe_3O_4 and γ-Fe_2O_3 are used, and the features which make them useful. Close attention should be paid to the ***highlighted*** text which is the feature that could potentially be measured using microwave measurements.

1.1.1 EMI in Electronic Devices

The rapid growth and use of electronics increases concerns of EMI especially in medical applications. EMI is when wanted and unwanted radiation from electronic devices affects the performance of the device of interest. This occurs when the required current in a circuit is altered through an incoming electromagnetic wave, giving the possibility of incorrect or invalid data[9]. This issue becomes increasingly important when such devices determine the mortality of a patient; in one case a phone call from a mobile phone has caused an epinephrine pump to malfunction and deliver a toxic dose of 999 mL per hour instead of 30 mL per hour[10]. In other cases, it is believed that powered wheelchairs have been steered off course due to EMI[11]. While it is now common knowledge to switch off mobile phones in hospitals and other sensitive areas, EMI still exists from the communications devices

that emergency services use, with one case showing that these caused disruptions in 41% of medical devices within 1 metre[12].

The way to address this problem is to encase sensitive circuits in materials which absorbs EMI and converts it into heat. There are a number of companies developing absorbing materials for minimising EMI in medical electronics. These are simple layers of material which attenuate any incoming interference before it reaches the device. Some companies are utilising technologies to integrate EMI absorbers around a circuit through a technique known as Laser Direct Structuring (LDS). LDS uses laser marking to build circuit tracks directly onto plastics. Merck KGaA is developing pigments for lasering while Molex have developed the MediSpec^{TM} range to build circuits for medical devices directly into materials. Combining these technologies and using EMI materials, the potential for miniaturised and shielded medical electronics is realised.

Microwave magnetic materials have important applications in EMI, where attenuation of waves around a device is achieved using both heavily absorbing dielectric and magnetic materials[13]. Magnetic nanoparticles show promise as effective absorbers due to an increase in surface dampening effects with smaller sizes[14]. One of the simplest materials used as a microwave absorber is Fe_3O_4 due to the ease of its synthesis and abundance in nature[7, 15–18]. Other more complex materials have been explored including hexaferrites[19–21], carbonyl-iron powders[22, 23], NiCo[24], MnZn ferrites[25] and MnO_2[26], while patterning of these materials has also been investigated[27–29]. The key component of all of absorbing technology is in their ***dielectric permittivity and magnetic permeability in the frequency band***, which determines the attenuation of any EM waves.

1.1.2 Magnetic Hyperthermia

Materials with magnetism at microwave frequencies have been estimated to heat extremely well in a microwave magnetic field[30]. Therefore, they have very important applications in microwave hyperthermia for the treatment of cancer tumours[31–33]. Hyperthermia is defined as a state where the temperature of the body is much higher than normal. In biomedical applications, RF or microwave hyperthermia involves exposing a cancer tumour to radiation to induce heating resulting in apoptosis (cell death). The amazing

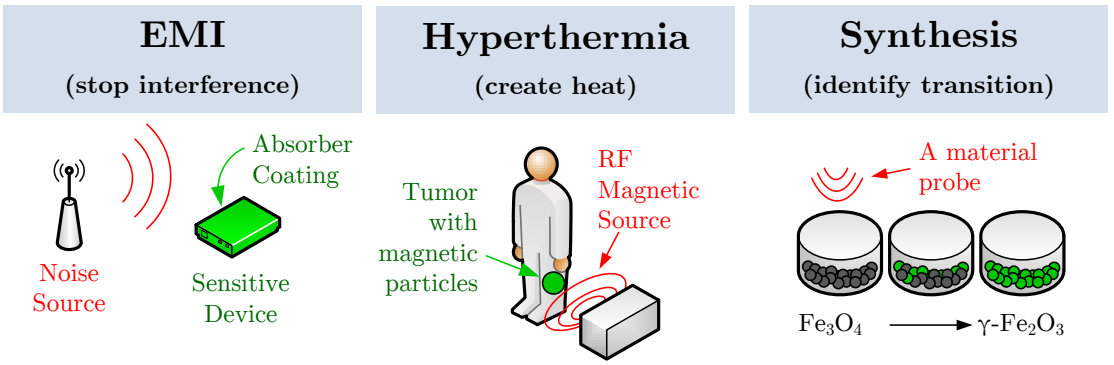

FIGURE 1.1: Simplified view of microwave applications for Fe_3O_4 and γ-Fe_2O_3. Microwave absorption is required to screen interference or create heat. Quantifying γ-Fe_2O_3 from Fe_3O_4 is currently difficult with conventional probe methods.

find which makes this possible was the discovery that cancer cells are more sensitive to temperature and it is known that heating a tumour to 42-45 °C is sufficient to induce apoptosis[34]. However, given that the rest of the body has a finite dielectric constant and loss, non-cancerous tissue is equally susceptible to the microwave radiation, causing the destruction of healthy tissues as well as tumours. The lack of selectivity is an issue in the administration of efficient heating of unwanted tumours. This is where magnetic nanoparticles come in, as the energy dissipation in these particles is a mixture of both dielectric and magnetic losses. As well as injecting the nanoparticles into the tumour site (or in intravenously to reach the tumour site[35]) for heating, selectivity can be achieved by using an RF or a microwave magnetic field where magnetite was one of the first to be recognised as having this potential[36, 37]. The theory behind this is that the magnetic permeability and losses of biological tissue is almost negligible when compared to those in a magnetic particle, hence the particle will absorb most of the energy and convert it into heat. With this approach, the key property that must be measured in the magnetic nanoparticles is the ***magnetic permeability in the frequency band***. This property also changes with temperature as the particle is heated which again must be characterised, and so the ***magnetic permeability as a function of temperature*** is just as important.

Optimum administration frequencies are still currently under research with solutions ranging from the MHz range [35, 38] all the way up to the GHz range by making use of ferromagnetic resonance[39, 40], where 2.45 GHz is coined as an acceptable ISM standard frequency. However, frequencies up to 10 GHz have shown promise in minimising the volumetric heating in surrounding healthy tissues by focusing microwaves into certain

spaces using the interference of multiple antennas[41]. In fact, in these studies magnetic nanoparticles are not even considered as part of the energy loss mechanism which will further improve heating at the site at lower power levels. This technique can also be combined with targeted drug delivery applications, where conjugating molecules which target tumours in the lymph nodes onto the magnetic nanoparticles will allow very targeted hyperthermia treatment. Different iron oxides (Fe_3O_4 and γ-Fe_2O_3) are used in this application with γ-Fe_2O_3 showing better absorption rates[42] of which identification of these oxides becomes paramount for optimising materials. This material characterisation issue is identified in the next section.

1.1.3 MRI Contrast Agents and Drug Delivery

Magnetic nanoparticles can also be used for drug delivery, where the therapeutic agent is attached to the nanoparticle and directed to the desired site with the application of an external magnetic field[4]. Their small size and large surface area allow these particles to be loaded with a large capacity of drugs which have been shown to allow a sustained release[43]. The nanoparticles can also be used for diagnostic applications as in magnetic resonance imaging (MRI) where these particles are coated in biocompatible materials and injected into specific sites to increase the contrast of the obtained images [1–3]. Some of the key features required for these nanoparticles to be useful include the nanoscale size, super-paramagnetic nature, the chemical stability, high saturation magnetisation and of course biocompatibility.

Super-paramagnetism is extremely important for the activation of the particles towards the site only when there is an applied magnetic field. If the particles were permanent magnets, agglomerations could form inside the blood vessel causing obstructions or embolisms[44, 45]. Super-paramagnetism also sets the requirement of size (shown to be less than 100 nm[46]), since larger particles are generally removed from the bloodstream quickly by the immune system[47] and also have multiple domains (thus domains align anti-parallel reducing the net magnetic moment of the particle).

Chemical stability is also important and is the main reason why Nickel and other transition metals in their pure form are not used because they oxidise very easily. Even the medically acceptable Fe_3O_4 undergoes oxidation over time. To stop this from happening,

the particles are normally coated with a shell material such as dextran and polyethylene glycol[35, 36, 45, 48] which stabilises the surfaces of the particles for drug attachment. The addition of these materials on the surfaces, however, inherently affects the magnetic properties.

Biocompatibility is the property which trumps them all, where Fe_3O_4 and γ-Fe_2O_3 have been identified as acceptable candidates by the Food and Drug Administration (FDA) and the European Medicines Agency[4, 42, 49] and even then, some potential toxicity exists as they can generate reactive oxygen species (ROS) when cells interact with the bare nanoparticles, resulting in apoptosis[50, 51]. Nevertheless, these particles are still readily synthesised with promising results. Though, the one key difference between Fe_3O_4 and γ-Fe_2O_3 (which consequently may be the reason why higher oxidative DNA damage was reported by Karlsson et al.) is that γ-Fe_2O_3 is thermally stable from room temperature to 350 °C whereas Fe_3O_4 is not and can continuously oxidise[52–55]. Hence in considering this, Fe_3O_4 is normally oxidised to produce γ-Fe_2O_3 and therefore ***determination of the oxidised Fe_3O_4 to γ-Fe_2O_3*** is important for particle synthesis in biomedicine[56]. Interestingly another difference between these materials is in their conductivity which may be used as a measurand to identify the phase change, thus microwave dielectric and conductivity measurements may be of use in this application.

1.2 Nanodiamond

Diamond is not only a much sought after stone for jewellery but an extremely useful material due to its chemical structure and stability for scientific and industrial applications. Pure diamond is made up of a repeating tetrahedral sp^3 hybridised carbon lattice, which forms a face-centred cubic unit cell (lattice parameter of 3.57Å). In its pure form it has a wide band gap of ($\approx$ 5eV) which results in no free electrons and thus high electrical resistivity. In 1963, particles with diameters in the range of 2-8nm were discovered through detonation of trinitrotoluene (TNT) or cyclotrimethylene trinitramine (RDX) in a closed chamber. This type of nanodiamond is known as ultra-dispersed diamond (UDD). This discovery meant that the hard structure, chemical inertness, electrically insulating and thermally conductive properties of nanodiamond could potentially be realised on the nanoscale, gaining great interest in biolabelling[57, 58], ammonia absorption[59] and protein adsorption for drug delivery[60, 61]. Since then, other methods to synthesise nanodiamonds have been researched including milling of larger high pressure, high temperature synthesised (HPHT) diamonds and chemical vapour deposition (CVD) techniques[62].

1.2.1 Drug Delivery

Studies have shown that administration of chemotherapy agents with nanodiamond drug platforms has the potential to increase tumour deterioration[60, 61, 63]. The efficacy of these particles for the applications mentioned is linked to the surface termination as this determines agglomerate formation and hence the effective surface area to adsorb drugs onto. Different synthesis methods yield different surface impurities. For HPHT nanodiamonds, impurities are introduced when a larger diamond is milled, leaving trace amounts of the milling media on the surfaces of the particles. The fracturing of the crystal also causes reconstruction of the un-terminated diamond to sp^2 carbon[64]. For biomedical applications particle sizes of less than 100 nm are generally required, where UDD is the most commercially available product. Nanodiamond produced in this way have coatings of various functional groups including amorphous (or disordered) carbon, sp^2 hybridised carbon (or graphitic carbon) and other metals dependent upon the material that the closed detonation chamber is made of. Vigorous hydrofluoric and nitric acid treatments are capable of removing many of these impurities[65] but may also introduce different functional

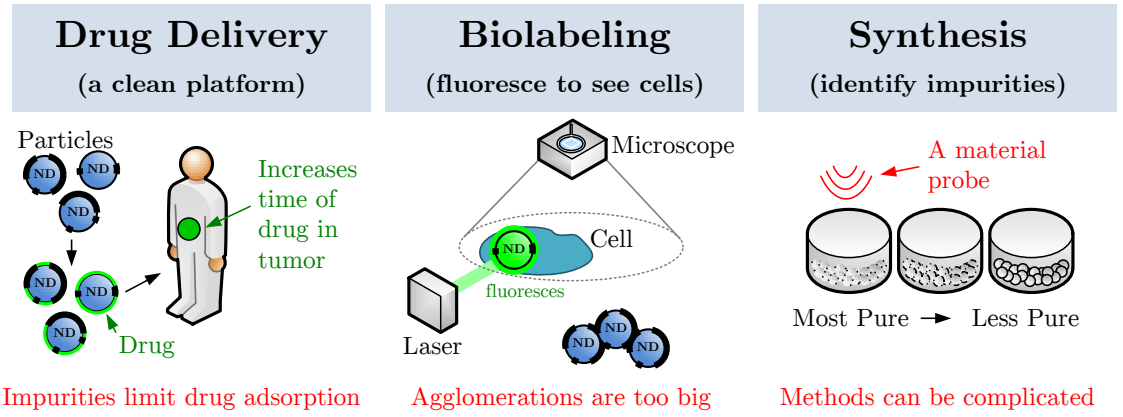

FIGURE 1.2: Simplified view of nanodiamond applications. Nanodiamond surface impurities cause agglomeration which limits drug adsorption and also makes particles too big for individual cell imaging. Quantifying impurities can be difficult with conventional probe methods.

groups[66]. The surface functional groups are useful as they encase the incredibly stable particles and allow for different chemical attachment, Fast and easy examination of the ***surface purity of nanodiamonds*** becomes paramount for large scale production. Non-diamond carbon is incidentally a very good microwave absorber while diamond is an insulator thus differences in electrical properties may allow quantification of surface purity.

1.2.2 BIOLABELLING

As well as platforms for chemotherapeutic agents, nanodiamonds can instead be conjugated with proteins which target specific antibodies. This is useful because nanodiamonds can be made to fluoresce and thus be used to track cells[67]. Some of the main advantages of using nanodiamonds over other technologies (for example quantum dots and nanogold) include their chemically stability (hence not prone to photo bleaching) and their non-cytotoxicity[68]. To make fluorescent nanodiamonds, defects such as nitrogen are introduced into the carbon structure through high energy electron or proton bombardment such that vacancies are created within the lattice. This is known as a nitrogen vacancy centre (NV^-) which allows the diamond to fluoresce at approximately 575 nm[69]. For performance, as well as determination of high concentrations of NV^- centres, surface termination plays a large role as non-diamond carbon such as sp^2 and amorphous carbon can quench the optical properties of the NV^- centres. Thus the ***surface purity of the fluorescent nanodiamonds*** is an important feature to measure for biolabelling. It follows

that non-diamond carbon is a very good microwave absorber while diamond is an insulator, thus differences in electrical properties may allow quantification of surface purity.

1.3 Titania

Titania (TiO_2) is known for its remarkable optical properties with its strikingly white colour. Due to the abundance of titanium rich ores in all parts of the world, it is commonly used as a pigment in paints, food colourings and textiles[70]. TiO_2 exists in three main forms; anatase, rutile and brookite, all with different crystallographic structures used for different applications. The most common forms are rutile and anatase. In rutile the Ti^{4+} cations are arranged octahedrally and the O^{2-} anions arranged in a trigonal planar fashion forming a slightly distorted hexagonal closed-packed structure. Anatase atoms have the same coordination, however, it is in a more distorted cubic closed pack structure. This difference in structure gives rise to varying levels of photo-reactivity where anatase is more photo-reactive than rutile[71]. The solid white colour is due to a large band gap (E_g) of approximately 3 to 3.2 eV, and is therefore semiconducting in nature, with excess conduction electrons provided by the p orbital O electrons resulting in n-type behaviour. TiO_2 is also a very effective photo-catalyst, capable of the adsorption and subsequent decomposition of various volatile species in the atmosphere such as pollutants and bacteria[72, 73]. This is achieved by the absorption of photons (where $E_{\text{photon}} > E_g$) and the creation of excitons with subsequent diffusion of electrons and holes to the surface allows the charge carriers to interact with the atmosphere which creates hydroxyl radicals and ROS. Anatase has been shown to be a better photo-catalyst compared to rutile[71].

1.3.1 Pigmentation

As stated, TiO_2 is a brilliantly white pigment for coatings. One example is in white paints for interiors and exteriors of buildings. The white aesthetic reflects light in spaces, providing suitable ambient lighting conditions. However, as stated previously, TiO_2 is a photo-catalyst in that the absorption of light creates excess electron-hole pairs which generates hydroxyl radicals and reactive oxygen species (ROS) on the surface of the material. Though this process cleanses the atmosphere by allowing the generated reactive species

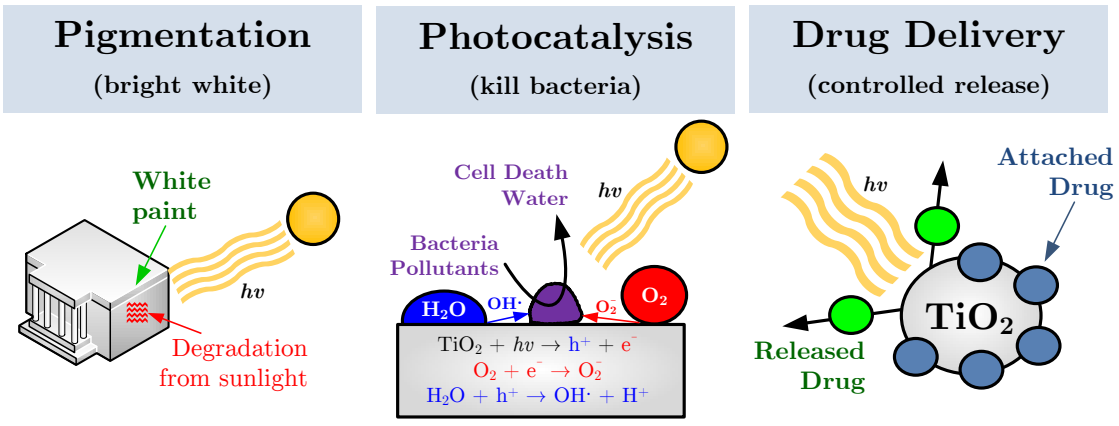

FIGURE 1.3: Simplified view of TiO_2 applications. Photo-reactivity degrades TiO_2 based pigments[74]. On certain surfaces, photo-reactivity can be used to clean the atmosphere[73]. The photo-reactivity can also be a release mechanism for targeted drug delivery[75–77].

to decompose bacteria and pollutants, it is actually detrimental to the overall lacquer matrix within which the TiO_2 particles are hosted. This results in 'chalking', where the photo-degradation of the host matrix occurs and the coating starts to crack and crumble off of the painted surface[74]. This is an unwanted effect and, therefore, requires routine maintenance (re-painting the surfaces). Because of this, certain grades of TiO_2 particles are used which suppress this photocatalytic activity. In this case, rutile is used since it is less photo-reactive than the anatase polymorph[71]. Coating the nanoparticles in silica (SiO_2) and alumina (Al_2O_3) is another option to separate the surfaces of the TiO_2 from the lacquer[74]. Hence, in the development of 'chalk-resistant' grade TiO_2 pigments, the determination of ***photo-reactivity under UV and visible light irradiation*** is required to evaluate their performance.

1.3.2 Light Controlled Drug Delivery

An interesting new approach to controlled drug delivery has emerged where chemotherapeutic agents can be bound to a nanoparticle and released on command upon light irradiation[75–77]. The principle of this system works by binding the drug to a particle and sealing it with an organic shell with high biocompatibility (such as polyethylenimine)[75]. Additionally, other proteins may be attached to the shell to target specific antigens. The nanoparticles are administered at the tumour site and upon UV irradiation, assuming the particles are not too deep into the tissue, the organic shell is degraded due to the

photocatalytic processes in TiO_2 and the drug is released. Now, this particular method triumphs over other externally controlled delivery mechanisms such as temperature; coherent photonic irradiation (at the tumour site) is not a natural phenomenon and mitigates the risk of accidental dosage whilst also allowing time for any targeting mechanisms to reach the antigen. The efficacy of this process depends on the response to light of the initial photocatalytic grade TiO_2 particles and hence determination of ***photo-reactivity under UV and visible light irradiation*** is required to evaluate performance.

1.4 Summary of Potentially Measurable Properties

Now, let us summarise the key features highlighted and how these can potentially be addressed through different microwave measurement systems:

Magnetic permittivity and permeability in the frequency band:
Microwave permittivity and permeability measurements are required and can be measured using a simple non-contact multi-mode MCP system (Chapter 3).

Magnetic permeability as a function of temperature:
Temperature dependent microwave magnetic permeability measurements are required. An extension to the MCP technique has been applied to measure this using an oven and procedures to calibrate temperature related systematic errors (Chapter 4).

Determination of the oxidised magnetic precursor:
A difference in a measurand between the precursor and the end product is required for characterisation. Using the previously designed non-contact systems, microwave permittivity and permeability are evaluated as potential measurands on the premise that the precursor is conducting while the end product is an insulator (Chapter 5).

Surface purity of nanodiamonds:
A difference in a measurand between pure and impure samples is required to quantify purity. Using the previously designed systems, microwave permittivity is evaluated as a potential measurand on the premise that pure diamond is an insulator and the impurities absorb may potentially microwaves (Chapter 6).

Photo-reactivity under UV and visible light irradiation:
A measurement of reactivity with response to light is required. Using a modified MCP system similar to the previous ones, microwave permittivity is evaluated as a way to infer photocatalytic activity on the premise that photo-reactivity may be linked to the photo-dielectric properties of the material (Chapter 7).

1.5 Introduction to Dielectric and Magnetic Spectroscopy

Emphasis has been given on using MCP, but what is MCP? And what does it measure? MCP is a form of dielectric and magnetic spectroscopy whereby electromagnetic polarisation is measured as function of frequency and mechanisms are identified based on the obtained spectra. In the case of MCP, the spectrum is obtained at microwave frequencies. When an electromagnetic field (DC or AC) is applied across a material, the polarisable constituents attempt to align themselves in the direction of the field. Alignment is not instantaneous and energy is lost (dielectric loss or magnetic loss), as functions of the effective mass and mobility of the polarisation mechanism; polar molecules for example will take a longer time to align with an applied field than electrons since they have a larger mass which results in a relaxation phenomenon at lower frequencies. These features become more prominent if the applied field is oscillating, where frequency dependence of polarisation mechanisms can be modelled as harmonic-oscillators. Thus, a material's ability to store and dissipate electromagnetic energy can be defined through the complex quantities of dielectric permittivity and magnetic permeability relative to free space denoted as:

$$\varepsilon = \varepsilon_0 \varepsilon_r = (\varepsilon_{r,1} - j\varepsilon_{r,2})\,\varepsilon_0 \tag{1.1a}$$

$$\mu = \mu_0 \mu_r = (\mu_{r,1} - j\mu_{r,2})\,\mu_0 \tag{1.1b}$$

where $j = \sqrt{-1}$, $\varepsilon_{r,1}$ is the relative dielectric constant, $\varepsilon_{r,2}$ is the relative dielectric loss, $\mu_{r,1}$ is the relative magnetic permeability, $\mu_{r,2}$ is the relative magnetic loss and ε_0 and μ_0 are the free space permittivity and permeability respectively. In this section, the different contributions to polarisation are outlined, how they can be observed through measurement of the frequency dependent polarisation and also determine the mechanisms which can be observed at microwave frequencies in Fe_3O_4, nanodiamond and TiO_2.

1.6 Dielectric Polarisation

Dielectric polarisation is a combination of numerous mechanisms including free electrons moving through the material, the displacement of ionic particles, dipole rotation, atomic displacement and distortions in electron positions around their nuclei. An estimation of these contributions as a function of frequency is shown in Fig. 1.4. Normally, the contribution to ε_r is separated into conductivity mechanisms ($\sigma_{\text{eff}}(\omega)$) and other polarisation related mechanisms ($\varepsilon_{r,1}(\omega)$ and $\varepsilon_{r,2}(\omega)$) using a relation from a combination of Maxwell's equations:

$$\nabla \times \bar{H} = j\omega\varepsilon_0\bar{E}\left[\varepsilon_{r,1}(\omega) - j\left(\varepsilon_{r,2}(\omega) + \frac{\sigma_{\text{eff}}(\omega)}{\omega\varepsilon_0}\right)\right] \equiv j\omega\varepsilon_0\varepsilon_r\bar{E} \tag{1.2}$$

where $\bar{E}$ and $\bar{H}$ are the vectors of the electromagnetic field and ω is the angular frequency. This form shows that if conduction losses dominate, then the imaginary term will have a dependence on $1/\omega$.

Relaxation is normally modelled using the Debye model. This model is for polarisation processes which do not happen instantaneously and take a finite time to occur. The delay is modelled using a time dependent system which relaxes to equilibrium exponentially ($y(t) = e^{-t\omega_{\text{r}}}$). The equivalent Fourier transform ($\frac{1}{\omega_{\text{r}}+j\omega}$) results in the complex Debye equations for a dielectric[78]:

$$\varepsilon_{r,\text{Debye}}(\omega) = \varepsilon_\infty + \frac{\varepsilon_s - \varepsilon_\infty}{1 + \left(j\frac{\omega}{\omega_{\text{r}}}\right)} \tag{1.3}$$

where ω_{r} is the relaxation frequency of the Debye mechanism and ε_∞ and ε_s are the high and low frequency permittivities respectively. This type of behaviour results in a decrease in the real part and a peak in the imaginary part at the relaxation frequency of the complex function. If the process has a restoring force, then the Lorentz resonator model is used[79], where:

$$\varepsilon_{\text{Lorentz}}(\omega) = \varepsilon_\infty + \varepsilon_s\frac{\omega_p^2}{\omega_r^2 - \omega^2 + j\gamma\omega_r\omega} \tag{1.4}$$

where ω_{r} is now the resonance frequency, γ is the dampening coefficient and ω_p is known as the plasma frequency which is a function of the number of charges (n), the charge (q)

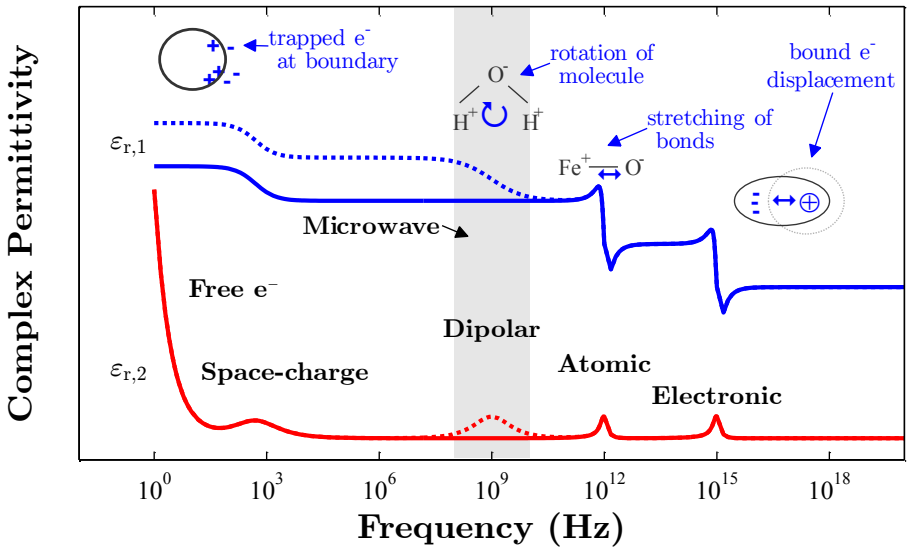

FIGURE 1.4: Estimated frequency dependent complex permittivity[79–82]. Static conductivity follows a $1/\omega$ dependence[83]. Space charge and dipoles are described using relaxation[82]. Atomic and electronic polarisation are described by resonance[82]. The dotted line is for polar species. The microwave region (shaded) is influenced by decay from conduction and steady state atomic and electronic polarisation.

and effective mass (m_{eff}) of the polarisation mechanism. This function also has a decrease in the real part and loss peak at the resonance frequency of the complex function, however, the difference between this and the Debye model is that the observed real part can be *less than 1* at frequencies higher than ω_r. Examples of relaxation and resonance are shown in Fig. 1.4 and Fig. 1.5 which are described in the following section.

1.6.1 Drude Conductivity Relaxation

Conductivity arises from the movement of charged particles (electrons or ions). In a solid material, free electrons (ones that do not participate in bonding) can contribute to this. In insulators and dielectrics there are not many free electrons and thus any observable conductivity is due to conducting impurities. In metals and semiconductors, large concentrations of charge carriers contribute to conductivity. It is normally described using the Drude model, which assumes a gas of charged particles which scatter in a classic 'pinball' fashion. Upon application of a DC E-field, the electrons collide with one another with a net drift opposite to the direction of the field. This flow of electrons creates a DC

current with density $\bar{J}$ related to the applied electric field strength $\bar{E}$ through Ohm's law:

$$\bar{J} = \frac{ne^2\tau}{m_{\text{eff}}}\bar{E} = \sigma_{\text{dc}}\bar{E} \tag{1.5}$$

where n is the density of electrons, e is the electron charge, τ is the time between collisions, m_{eff} is the effective electron mass and σ_{dc} is the static DC conductivity. The electrostatic repulsion between other electrons and other ions in the lattice is accounted for in m_{eff} which is larger than the mass of an electron owing to the increase in impedance that an otherwise free space electron would experience[84].

If charge conduction takes some finite time to accelerate due to surrounding obstacles, then instead of modelling an instantaneous response, a finite decay time τ gives an effective AC conductivity:

$$\sigma_{\text{ac}}(\omega) = \frac{ne^2\tau}{m_{\text{eff}}}\frac{1}{1-j\omega\tau} = \frac{\sigma_{\text{dc}}}{1-j\omega\tau} \tag{1.6}$$

This is known as the Drude AC model and is a relaxation phenomenon. Incorporating 1.6 into 1.2 yields:

$$\varepsilon_{r,\text{Drude}} = \varepsilon_{r,1} - \frac{\sigma_{\text{dc}}\tau}{\varepsilon_0(1+\omega^2\tau^2)} - j\left(\varepsilon_{r,2} + \frac{\sigma_{\text{dc}}}{\varepsilon_0\omega(1+\omega^2\tau^2)}\right) \tag{1.7}$$

Hence, any signs of conductivity can appear as a decrease in the real part and an increase in the imaginary part at $\omega \approx 1/\tau$. If τ is very small such that the free electrons are almost constantly bombarding with their surroundings (the DC case), then contributions to the real part can be neglected while the effects will still show in the imaginary part with a $1/\omega$ dependence[83, 85]. There is, however, some misinterpretation of this equation, in that studies often directly convert ε_2 to conductivity, which is not necessarily static electron conductivity but a polarisation related loss[86]. Nevertheless, we can generally identify the effects of static electron conductivity through this $1/\omega$ dependence in the loss.

In metals, on application of an AC E-Field, the large density of free electrons is high enough to screen the field in the material, hence no energy is stored and the permittivity is large and imaginary. The conductivity of the material and the frequency determine how much E-Field gets screened. The depth to which the field penetrates to $1/e \approx 37\%$ of its

surface value is known as the skin depth:

$$\delta_s = \sqrt{\frac{2}{\omega \mu_0 \mu_r \sigma_{\mathrm{dc}}}} \tag{1.8}$$

When working at frequencies approaching 10^{10} Hz, then metallic materials such as aluminium ($\sigma_{\mathrm{dc}} = 3.5 \times 10^7$ S/m) screen the field to approximately 840 nm. This equation is significant as it can identifies a limit on the depth to which microwaves can probe in conducting materials. The materials measured in this thesis are, however, semi-metallic at best with graphite being the most conducting over the others, (graphite $\sigma_{\mathrm{dc}} \approx 10^5$ S/m[87]) yielding a skin depth of at least $\delta_s \approx 16\mu$m at 10 GHz which is equivalent to the particle size. Hence measurements of this material may decrease with frequency.

1.6.2 Space Charge Relaxation

Space-charge or interfacial polarisation is also a phenomenon related to static electron conduction but results from collections of these charges getting trapped at *boundaries* in multi-phase materials[82, 88, 89]. If the mixture consists of a semi-metal and dielectric inclusions, then on the application of an E-field, the collections of free electrons move but are impeded by grain boundaries between the different phases. Charges therefore get trapped at interfaces. In their trapped state, they contribute to polarisation through their displacement. One could argue that this also happens in a conducting material at the extremities but the difference is that this build-up of charge increases the polarisation inside the dielectric inclusions, causing the overall observed complex permittivity to increase. As frequency increases, this effect decreases depending upon the effective mass of the impeded electrons.

This feature is mainly prominent in mixed phase materials as opposed to solid blocks of metal and semiconductors. It can occur when fabricating a capacitor around the material using metal electrodes[90] and the measured value is not intrinsic due to the space charge at the interfaces. This effect is a qualitative feature and has no accepted analytical model since the mechanics of this phenomena are still unknown, however, it is can be modelled as a process with a very low Debye relaxation frequency as shown in Fig. 1.4 and its identification at microwave frequencies is achieved through decreases in *both* real and imaginary parts with frequency[88].

1.6.3 Dipolar Relaxation

Some materials contain molecules with permanent dipole moments such as water or hydrogen peroxide. When these molecules are subject to an alternating field, the electro-negative oxygen and electro-positive hydrogen atoms align with the field accordingly, hence all the molecules polarise the material and energy is lost in the rotation process of the whole polar molecule. This type of polarisation is the reason why water heats so well under microwave irradiation. The mechanism is normally represented using the Debye model at microwave frequencies as shown in Fig. 1.4 but will not be present in non-polar powders since individual molecules cannot be rotated in a solid repeating lattice.

1.6.4 Atomic and Electronic Resonance

At THz frequencies, relaxations of atomic and electronic polarisation occur due to the shift from positive charges in the nuclei and distortions of electron clouds. These effects will contribute to the polarisation of the material as shown in Fig. 1.4 but these are fast processes with the overshoot modelled by the restoring force from the nucleus of the atom or the bond stretching of the atoms. This process has a resonant frequency which is greater than microwave frequencies, however, the real part still contributes to the polarisation while the imaginary part may show a slight increase with frequency. Ions, in particular, having a certain charge will move with the field due to classical laws of electrostatics. Ions can contribute to polarisation in two ways: liquid ionic conductivity, ionic displacement and solid state ionic hopping. In liquid ionic conductivity, ions are free charge carrier molecules and contribute to the dielectric response as a charge conduction process explained previously with relaxations at low frequencies. In the case of crystalline solids, ions are restricted to physical displacements about their position in the lattice; salt (NaCl) for example has a closed pack cube of alternating Na and Cl atoms which simply move towards one another with an applied E-field.

1.6.5 Ionic Hopping Conductivity (Arrhenius and Jonscher Power Law)

Solid state ionic hopping is where ions migrate through the lattice through a transfer of electrons. Mixed-valence metal oxides such as Fe_3O_4 can show this type of behaviour.

If two cations with a difference in oxidation state (Fe^{2+} and Fe^{3+} for example) are close to one another such that their d orbitals overlap then electrons localised to one cation can effectively jump to the other via the overlap. This results in a small redox reaction (Fe^{2+} and Fe^{3+} become Fe^{3+} and Fe^{2+} respectively). In a repeating lattice, the Fe^{2+} atom seemingly migrates resulting in ionic conduction. The hopping conduction depends upon the overlap and whether the electron receives enough energy to 'hop' to the next site. This is normally modelled by a thermally activated process through an Arrhenius equation[91]:

$$\sigma_{\text{ion}}(T) = \frac{\psi_{\text{ion}}}{T}\exp\left(-\frac{E_c}{k_B T}\right) \tag{1.9}$$

where E_c is the energy required for the electron to hop to the next ion, k_B is Boltzmann's constant, T is the temperature and ψ_{ion} is a pre-exponential constant for the ionic conductivity. E_c can be inferred by measuring conductivity as a function of temperature. As a function of frequency, however, electron transport through exchange interactions have both a DC and AC contribution. Hopping conductivity is modelled using the empirical Jonscher Power Law model, with separate AC and DC components[92]:

$$\sigma_{\text{Jonscher}}(\omega) = \sigma_{\text{ion,dc}} + \underbrace{\psi_{\text{ion,ac}}\omega^k}_{\sigma_{\text{ion,ac}}(\omega)} \tag{1.10}$$

where k is the exponent (normally less than or equal to 1) and $\psi_{\text{ion,ac}}$ is a pre-exponential constant. Substituting 1.10 into 1.2 yields the losses as a function of ion hopping:

$$\varepsilon_{2,\text{ion}}(\omega) = \varepsilon_{r,2} + \frac{\sigma_{\text{ion,dc}}}{\omega\varepsilon_0} + \frac{\psi_{\text{ion,ac}}\omega^{k-1}}{\varepsilon_0} \tag{1.11}$$

Therefore, assuming that $\sigma_{\text{ion,dc}}$ is small and $\varepsilon_{r,2}$ has minimal frequency dependence, then extraction of k can be determined, though there is no real acceptable explanation as to why hopping is modelled in this way. One explanation is that at lower frequencies only long range conductivity is active while at higher frequencies (past a critical frequency dependent upon the effective speed of the migrating ions) more conduction paths become available and hence the conductivity increases[93].

1.7 Magnetic Polarisation

1.7.1 Magnetic Polarisation Mechanisms

The magnetic moment of a material mainly arises from atoms with unpaired electron spins. The more atoms with unpaired electron spins, the more magnetic the material is, assuming they are all aligned parallel (ferromagnetism). If equal numbers of unpaired spins are aligned anti-parallel, the net magnetic moment (anti-ferromagnetism), though some materials have unbalanced spins (ferrimagnetism) resulting in a net magnetic moment. In some cases, spins are randomly oriented but when a field is applied, they align parallel (paramagnetic). Materials without unpaired electron spins can still react to a magnetic field through their nuclear spin moment which, in contrast to electron spins, tend to oppose the applied field (diamagnetism).

Hence the fundamental contribution to magnetism (and thus permeability) is due to the number of electron spins aligned parallel and anti-parallel. Some of the frequency dependent magnetic polarisation mechanisms which arise from this are Brownian relaxation, Néel relaxation, domain wall resonance and ferromagnetic resonance. There are also hysteresis losses which occur when the magnetic moments are driven into saturation and reversed, as well as eddy current losses which become dominant when the skin depth of the material is less than the particle size. For the former this generally only occurs for high fields[94] and is not witnessed for small super-paramagnetic particles since the coercivity and remanence approaches zero, and the hysteresis loop has a very small area[34]. For eddy current losses, however, this is more problematic for materials with high metallic conductivity as opposed to oxides which have much lower conductivities.

1.7.2 Hysteresis and Eddy Current Relaxation

When a material with conduction electrons is subject to a time varying magnetic field, eddy currents are generated. The electrons attempt to cancel out the field inside the material in a similar fashion to the dielectric equivalent of electron conduction loss. This again is present at low frequencies through a Drude or Debye model[95].

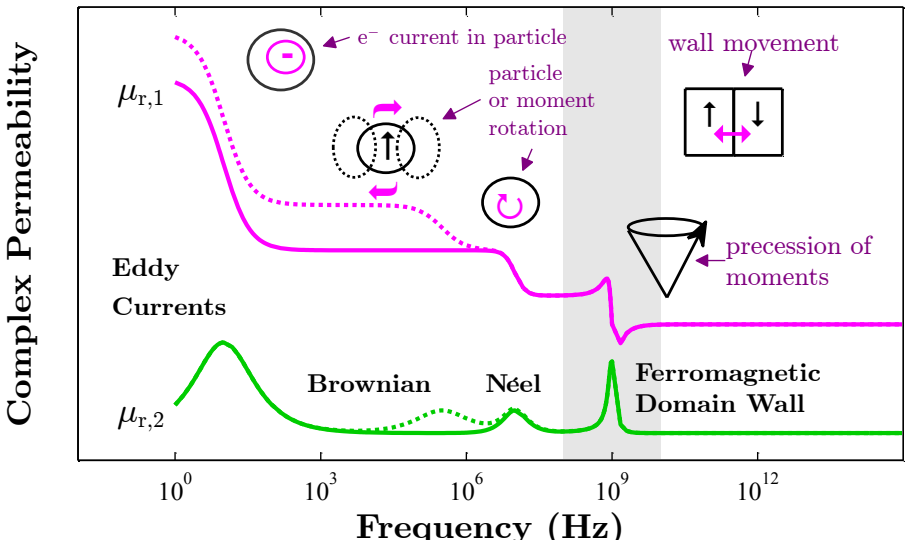

FIGURE 1.5: Estimated frequency dependent complex permeability[80]. Conductivity and hysteresis loss occurs at low frequencies. Brownian and Néel relaxation may occur at MHz frequencies[36] (where the dotted line is for materials in solution). At microwave frequencies, natural and ferromagnetic resonance occurs[96].

1.7.3 Brownian Relaxation

When magnetic particles are suspended in a fluid medium with finite viscosity, relaxation occurs which is related to the physical rotation of the particle[34]. This is the equivalent of dipolar molecule relaxation of water except the molecules are particles and hence their relaxation occurs at lower frequencies. This results in a Debye type relaxation of the particle at kHz to MHz frequencies and only occurs with suspensions such as ferrofluids and are not measured in this work.

1.7.4 Néel Relaxation

At high MHz frequencies, relaxation occurs due to the magnetic moments related to the electron spins. The Néel relaxation mechanism is associated with the finite time required to reverse the net magnetic moments (or spins) within a particle without physically rotating it. In Néel relaxation, when particles experience an applied AC H-field the internal unpaired spins attempt to align with it in a characteristic Debye manner. The relaxation time is a function of the material's anisotropy, volume and temperature modelled by a

thermally activated process through an Arrhenius equation[97]:

$$\tau_{\text{Néel}} = \tau_0 \exp\left(\frac{KV}{k_B T}\right) \tag{1.12}$$

where τ_0 is the time constant, K is the anisotropy constant and V is the particle volume. K is simply a figure of merit for directivity of the magnetic moment in a material, where some directions are easier to magnetise than others (known as the 'easy axis'). This value varies with different materials. This equation shows that the Néel relaxation frequency is a function of both temperature and frequency. This relaxation is, however, *only* present for super-paramagnetic particles, with the multi-domain equivalent being domain wall resonance.

1.7.5 Domain Wall Resonance

A bulk collection of magnetic moments aligned in the same way is known as a domain. However, a large solid block of magnetic material generally does not exist in one domain. This is because, in this case, the flux lines emanating from the material to join north and south poles result in a large magnetostatic energy[98]. A more energetically favourable state is to divide the large domain into smaller ones, resulting in much shorter flux lines and thus lower magnetostatic energy. The formation of domains with different alignments creates boundaries or domain walls between them. Applying a magnetic field across the material moves these domain walls by giving the spins at the boundary enough energy to change direction. Similarly, this process may also be thermally activated through an Arrhenius equation:

$$\tau_{\text{dom}} = \tau_0 \exp\left(\frac{\Delta E_{\text{dom}}}{k_B T}\right) \tag{1.13}$$

where ΔE_{dom} is equal to the activation energy. A domain wall can be modelled as a quasi-particle with some effective mass and with a restoring force, hence it can be modelled using a Lorentzian resonance with 1.4. When the domain wall movement can keep up with the AC field, the net magnetic polarisation will increase. At very high frequencies, wall movements may be frozen out though at microwave frequencies, it has been shown that domain wall resonance can occur. This effect is mainly for bulk materials. For powders with small particle sizes (roughly less than 100 nm), it is more energetically favourable for

the particle to have a single domain[46] (hence super-paramagnetic) and thus these effects should not be noticed. The magnetic powders used in this thesis have a maximum size of 300 nm and thus resonance may be due to domain walls.

Distinguishing between Néel and domain wall resonance can therefore not be achieved with magnetic spectroscopy and can only really be achieved by determining whether the material is super-paramagnetic or not through coercivity and remanence measurements.

1.7.6 Ferromagnetic Resonance

Ferromagnetic resonance happens when precession occurs of an electron spin. This precession can be excited when an AC field is applied normal to the easy axis. Ferromagnetic resonance can occur by applying an external DC and AC magnetic field but it can also be present due to a consequence of the remanent magnetism from unpaired spins in a ferromagnetic or a ferrimagnetic material. The latter case is known as natural resonance since the precession occurs without an applied field which is the type of resonance dealt with in microwave permeability measurements[80]. The natural resonance frequency can be calculated for a material with spherical particles through the Kittel formula[96]:

$$f_r = \gamma H_{\text{eff}} \tag{1.14}$$

where $\gamma = 2\mu_B/\hbar$ is the gyromagnetic ratio and H_{eff} is the effective applied field; whether it is an external DC magnet or the anisotropy field caused by neighbouring magnetic moments. In this thesis, external DC magnets are not used and hence any resonance is due to the anisotropy field which is an intrinsic property of the material.

1.8 What is measured at microwave frequencies?

At microwave frequencies, in non-polar materials all of the dielectric processes occur apart from dipolar polarisation. Magnetic properties will mainly be dominated by domain wall, natural and ferromagnetic resonances. Referring to Fig. 1.4, for an insulating dielectric, the main contribution to the real part of the dielectric function is from atomic and electronic displacement in the lattice with no expected relaxation. For the imaginary part of the complex function, small contributions from atomic polarisation loss (increasing loss with frequency towards the relaxation peaks at THz) may be measurable. For a material with some conductivity, the real part may show a decay with frequency (space charge conduction effects) and the imaginary part may show a decreasing loss with frequency due to a $1/\omega$ dependence. This allows some identification of the mechanisms involved in the polarisation at microwave frequencies. For a magnetic material, natural ferromagnetic resonance can be identified through loss peaks, but more prominently through decreases in the real part of the permeability below 1.

For Fe_3O_4 and γ-Fe_2O_3, the main dielectric processes that can be measured are the atomic and electronic polarisation in the real part whereas the imaginary part will be a contribution from both ionic conductivity and some polarisation losses from the ions. The magnetic processes will be dominated by domain wall and natural ferromagnetic resonance mechanisms.

For nanodiamond, the main dielectric processes that can be measured are the atomic and electronic polarisation in the real part whereas the imaginary part will be a contribution from the polarisation losses from the atoms. However, with increasing concentration of non-diamond carbon impurities, the imaginary part is expected to increase greatly due to conduction losses and increasing polarisation losses from the non-crystalline materials with frequency.

For TiO_2, the main dielectric processes that can be measured are the atomic and electronic polarisation in the real part whereas the imaginary part will be a contribution from the polarisation losses from the atoms. Upon irradiation with light, however, the excitation is expected to generate excess charge carriers and excitons, resulting in increases in electron conductivity and polarisation mechanisms respectively.

1.9 Microwave Techniques

In this section, the methods of measuring these dielectric and magnetic mechanisms at microwave frequencies are outlined and a justification of the use of MCP is presented. Measurement of these properties at microwave frequencies has existed for a very long time, dating as far back as the 1940's with numerous methods that are generally grouped into resonant and non-resonant techniques.

1.9.1 Resonant Techniques

Resonant techniques (as primarily used in this thesis) involve altering the frequency dependent characteristics of a microwave resonator and attributing these changes to properties of the material. This is achieved by reflecting EM waves within a structure and attempting to measure the phase velocity and decay through shifts in wavelength (hence frequency) and the power at resonance. Examples of structures used include cavity, dielectric and microstrip type ring resonators.

Cavity Resonator

Hollow cavity resonators (box, cylindrical and spherical) create electromagnetic standing waves within their space which a sample can perturb. The change in frequency when this occurs can be related to the electric or magnetic properties of the material, depending on whether the perturbation is in an E or H field. The advantages of this resonator type are that separation of fields is very easy, as the standing waves are based on simple geometries. Cavities can also have very high sensitivities due to high Q factors owing to the high density of electromagnetic energy stored in the space. This is largely due to the high reflectivity of the metal walls and minimal surface current losses[99, 100]. This does, however, depend upon the surface roughness of the cavity and how well it is machined (since reflections depend upon the surface currents along the walls and discontinuities disrupt this process). The main disadvantages of this technique are that the structures can be large when measuring materials at around 2 - 5 GHz. Also this technique fails when examination of small individual particles is required. This is because the sample to cavity filling ratio can be very small, resulting in small perturbations in the E-field and therefore

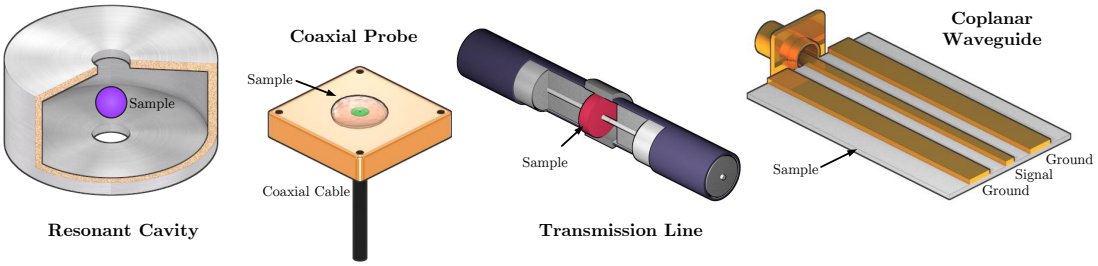

FIGURE 1.6: Examples of different microwave structures to measure permittivity and permeability. The resonant cavity is the only method which can have no sample contact and has high sensitivity but only provides a measurement at the resonant frequencies of the structure. The coaxial probe, transmission line and coplanar waveguide are capable of providing measurements over a frequency spectrum but has a much lower sensitivity.

low sensitivity. Maintaining the measurement frequencies to low GHz values is almost impossible when the structures need to be made smaller. Some of the earliest studies using resonators involve the dielectric and magnetic properties of gases including nitrogen, oxygen and carbon dioxide [99], humidity in industrial gases[101] and carbon dioxide, nitrogen and helium laser gases[102]. In all of these cases, the gases are injected into the cavity atmosphere, either directly or into a tube which sits in the cavity and the frequency response is measured using microwave sources and detectors. These studies demonstrated that water based samples give large dielectric responses in the microwave region making these methods sensitive for looking at gaseous and liquid phases. Solid materials have also been studied including dielectric plates [103–105], thin films[106], rods and ferrites[100].

Dielectric Resonator

Dielectric resonators have the same principle except that either the sample is fabricated into a geometry that resonates (such as a cylinder[107]) or the evanescent fields of a low loss dielectric material are perturbed[107–109]. In the former, this involves meticulous fabrication procedures though in the case of the latter, the system can be reused. The advantage of using dielectric resonators for permittivity measurements is that they generally have high Q factors. They also address the size issue in that the free space wavelength is altered inside the dielectric such that much smaller geometries can be achieved without increasing the measurement frequency too much. Practically, however, the system is heavily dependent upon the quality of the dielectric in that they must be low loss, crystalline and have an isotropic dielectric property. As well as this, to make use of the high density of fields, they must be modified with sample slots and holes which may complicate the

fabrication process. Split posts offer an elegant solution to simplifying the fabrication, however, positioning must be exact to retain repeatability.

Microstrip and Ring Resonator

Microstrip ring and split ring resonators are simple loops of wire or transmission lines which may feature breaks in the loop. They can be easily fabricated using planar circuit milling machines or out of rigid wire. The high density electric and magnetic fields alternate around the loop, making exclusive magnetic and dielectric perturbation possible at point locations in small structures. This is particularly advantageous in examining materials in micro-fluidic systems[110]. They can be made as open structures to allow sensitive probing of much larger areas including biological tissue[111] or gasses[112]. The disadvantages of these structures, however, are that the Q factor is generally far less than those that can be achieved with more 'rugged' systems such as the cavity.

Advantages and Disadvantages

The problem which is common to all resonant measurements is the measurements are all conducted at *one* resonant frequency of the structure. The dielectric properties of water containing samples have a large dependence on frequency, generally modelled using the Debye model explained previously, which may be troublesome with a resonator. This is due to the sparse measurement points in the frequency domain. Also though their sensitivity may be high, large permittivity materials are actually harder to measure since the principle of operation involves dampening a resonator, and lossy materials may destroy the initial resonance.

1.9.2 Non-Resonant Techniques

The conventional solution to looking at the frequency dependence of a material is to use transmission/reflection methods. The principle of operation for these techniques are that a wave is sent into a structure and the amplitude and phase of the transmitted and reflected waves are related to the material. These methods involve building the sample into a transmission line or reflection structure by either placing the sample inside a high density field,

terminating a line with the sample or building a microwave structure out of the sample.

Waveguide

The microwave properties of powders are generally investigated using waveguide approaches with main emphasis on determining the powders' microwave absorbing capability for EMI[20,113,114]. This involves placing a plate of material at the anti-node of a waveguide mode and performing a power transmission and reflection measurement of the waveguide system. Fe_3O_4 which is used mainly in later chapters for example has been measured using the waveguide approach from 2-18 GHz to obtain both the dielectric and magnetic properties[113]. There are, however, larger sample requirements (typical measurements at 2.5 GHz require a sample cross section of 86×43 mm and a thickness of much less than 1/4 of the wavelength) which may be troublesome for scarce powders. Also broadband measurements are only achieved through piecewise measurements from separate waveguide systems, with a single system providing a typical range of 2 to 3 GHz. With this approach it is also hard to determine how accurate the measurements actually are, as those in the literature are seemingly taken once with no evidence of any error bars. It does, however, provide an excellent spread over the range as well as extraction of both permittivity and permeability in a 2 port measurement.

Coaxial and Coplanar Methods

The requirement for a large sample in waveguide approaches is eliminated in the coaxial probe and coplanar approaches[115]. This is a simple transmission line which is either terminated into the sample or the sample is integrated into the line. In this approach, the sample requirements are much smaller, since coaxial lines can accommodate microwaves for a smaller inner and outer diameter of cable; typically terminated 3.5 mm coaxial cables or air spaced APC-7 connectors (7 mm diameter from centre to the outer conductor) can be used for reflection and transmission measurements with similar scales also achieved with coplanar waveguides. Although large frequency ranges can be achieved from 10 MHz to 10 GHz, these measurements require intimate sample contact and are thus used for liquids[116–118]. Consistent powder packing is a challenge when high precision is required, not to mention sample preparation and mounting onto the system.

1.9.3 Decision on Microwave Technique

In this thesis, emphasis on using hollow cavities for measurements of the dielectric and magnetic properties of powders is presented. The reason that this method has been chosen is due to:

- Simplicity of fabrication
- Ease of use
- High sensitivity
- High stability

which is important for a bench-top quality control system. Also, sample preparation is simple for this approach; for a cavity resonator one can simply fill a low loss tube with the powder and place it inside the cavity. High sensitivity is paramount in this research since it is a proof of concept, to 'see if microwaves can measure the useful properties' and if measurable differences are not possible through these measurements, they will not be in others. Though planar structures are effective as point probes in the material, the sensitivity may not be high enough. This thesis will also try and make the most of the cavity by evaluating its potential as a partial broadband tool for powders by utilising a myriad of different cavity modes explained later. Although dielectric powders generally have little frequency dependence, the ferromagnetic resonance phenomenon in Fe_3O_4 can potentially be measurable if the measurement frequencies lie either side of the resonance.

1.10 Conclusions

In summary, a literature survey of different powders is given and certain challenges have been highlighted which need to be addressed. A brief proposal on how these properties can be measured using microwaves has been presented. Following this, some of the fundamental dielectric and magnetic mechanisms of materials have been described and those that will be measured at microwave frequencies. Finally, some microwave techniques are also outlined and MCP has been justified as the chosen method.

CHAPTER 2

Theory:
Microwave Cavity Perturbation

The General Problem - Understanding

Now that microwaves have been evaluated as a potentially useful tool, one needs to understand the microwave cavity perturbation (MCP) method. Though vigorous analysis on these techniques is given in some parts of the literature, the underlying physics is often missed.

The Approach

In this chapter, an attempt to explain the fundamentals of the MCP technique for a wide audience is given. It has been written for the benefit of researchers and students who are unfamiliar with these techniques and wish to understand the basis of the systems used in this work.

Key Findings

MCP involves measuring the resonant characteristics of a hollow metal space with and without a sample inside. The changes in the frequency response yields information about the material. The resonant frequency of the cavity is determined by the geometry. Materials placed parallel to their field yield the highest sensitivity.

2.1 Principle of MCP

The microwave cavity perturbation method is a simple characterisation procedure based upon placing a sample into a space with a resonant electromagnetic standing wave. This can be achieved with a hollow metal cavity as shown in Fig. 2.1, where the hollow geometry can be rectangular, cylindrical or spherical. The analysis behind this is achieved with the cavity perturbation equation (derived from Maxwell's equations) which states that when the fields of a resonating system are perturbed by a material, the complex resonant frequency is changed depending on the complex permittivity and permeability of the material[119–123]:

$$\frac{\Delta\omega}{\omega_0} \approx \frac{\int_{V_{\text{samp}}} \varepsilon_0(\varepsilon_r - 1)\bar{E}_{\text{samp}} \cdot \bar{E}^*_{\text{cav}} + \mu_0(\mu_r - 1)\bar{H}_{\text{samp}} \cdot \bar{H}^*_{\text{cav}} dV}{\int_{V_{\text{cav}}} \varepsilon_0 \bar{E}_{\text{cav}} \cdot \bar{E}^*_{\text{cav}} + \mu_0 \bar{H}_{\text{cav}} \cdot \bar{H}^*_{\text{cav}} dV} \tag{2.1}$$

where $\bar{E}_{\text{samp}}$ and $\bar{H}_{\text{samp}}$ are the electric and magnetic fields at the sample location, $\bar{E}_{\text{cav}}$ and $\bar{H}_{\text{cav}}$ are the unperturbed fields and ε_r and μ_r are the complex relative permittivity and permeability respectively. The notion of complex frequency is derived later on but essentially is made up of a real part (the resonant frequency) and an imaginary part (related to the bandwidth or quality factor).

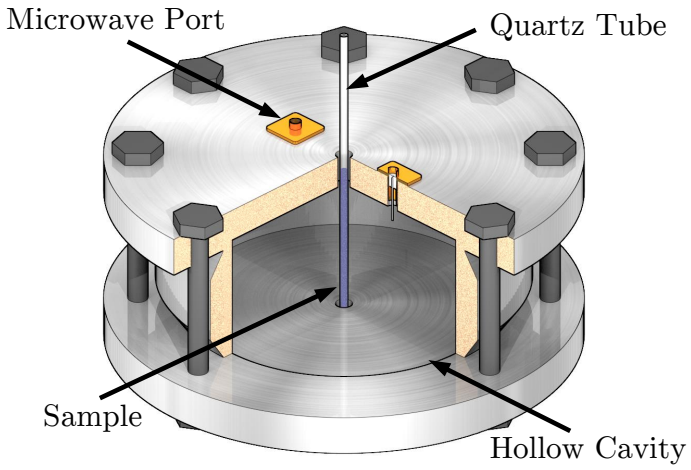

Figure 2.1: Cut view of a simple cavity perturbation set-up. Sample is placed inside the hollow space while complex frequency is measured using the microwave ports.

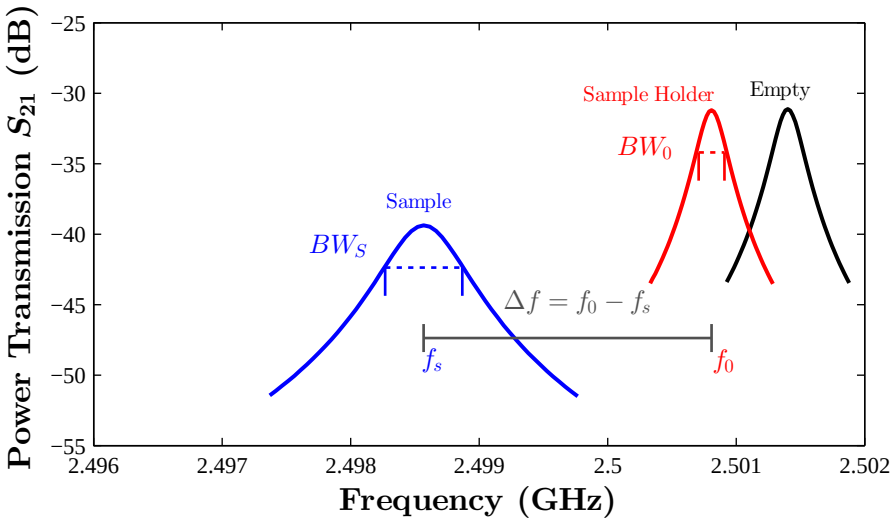

FIGURE 2.2: Example of the traces obtained in an MCP measurement. When a material is placed inside the resonator, the resonant frequency and bandwidth of the space change according to the properties of the sample.

2.1.1 SIMPLIFIED MCP EQUATION

In its current state, 2.1 is generally unusable since the field quantities are unknown and immeasurable. A simpler and more practical version can be derived by making assumptions on the perturbation condition.

The first simplification is that when we are measuring permittivity or permeability, the vast majority of the sample is placed into either an electric (E) or magnetic (H) field maximum of the standing wave. This zeroes one of the terms in the numerator (for the purposes of this derivation, permittivity will be used and H_{samp} is zero). Also, the denominator is 4 times the time average stored electrical or magnetic energy in the cavity which can be expressed in terms of just the E field (since $\varepsilon_0 \bar{E}^2_{\text{cav}} = \mu_0 \bar{H}^2_{\text{cav}}$).

The second assumption is that the sample perturbation does not vastly affect the field distribution inside of the cavity. This allows some cancellations in the integrals to remove the field components from the equation. Field distribution alterations happen when the sample produces a dipole moment or if the sample is a bulk conductor and is placed parallel to an E-field (for example placing a perfect metal rod parallel to an E-field distorts the field distribution by forcing the field to zero inside it). If the condition can be met where $\bar{E}_{\text{samp}} \approx \bar{E}_{\text{cav}}$ then parts of the integrals can be simplified. This is met when the sample is placed in the cavity with a minimal depolarisation field, achieved by placing any sample

edges parallel to the excitation field. A practical example would be to place a rod of material along an E-Field as opposed to perpendicular to it. If we can make meet these conditions, the resultant equations thus become:

$$\varepsilon_{r,1} \approx -2\ \Re\left(\frac{\Delta\omega}{\omega_0}\right)\frac{V_{\text{cav}}}{V_{\text{samp}}}G_{nmp} + 1 \tag{2.2a}$$

$$\varepsilon_{r,2} \approx 2\ \Im\left(\frac{\Delta\omega}{\omega_0}\right)\frac{V_{\text{cav}}}{V_{\text{samp}}}G_{nmp} \tag{2.2b}$$

where V_{cav} and V_{samp} are the cavity and sample volumes respectively and G_{nmp} is the mode dependent field scaling constant. The G_{nmp} value represents how much of the cavity volume is filled with EM fields and also how much of this is exposed to the sample. Notice that in this form, one simply needs to calculate or measure the sample volume, cavity volume, mode dependent field scaling constant and the complex resonant frequency all of which are discussed in later sections.

The key advantage of this form is that energy storage mechanisms (dielectric constant or magnetic permeability) are measured through the real part (frequency) and any energy loss mechanisms (dielectric or magnetic loss) are measured through the imaginary part (bandwidth or quality factor).

2.1.2 Depolarising and Demagnetising MCP Equation

Materials can still be measured if field distortions caused by a sample dipole moment occur but this cannot be achieved through 2.2a and 2.2b. This is because the field inside the sample ($\bar{E}_{\text{samp}}$ or $\bar{H}_{\text{samp}}$) is dependent upon the sample geometry as charges gather at the edges to try and cancel out the applied field. An example of this is shown in Fig. 2.3. Minimising the surface areas normal to the field, minimises this depolarisation effect.

Ideally, the applied high density field in the cavity needs to penetrate the sample as much as possible but is sometimes unavoidable. For the context of Chapter 3, demagnetisation will be considered. Here, an equation is presented which takes into account the demagnetising factor (N) caused by the geometry of the sample, allowing N to be interchanged if the geometry of the sample changes.

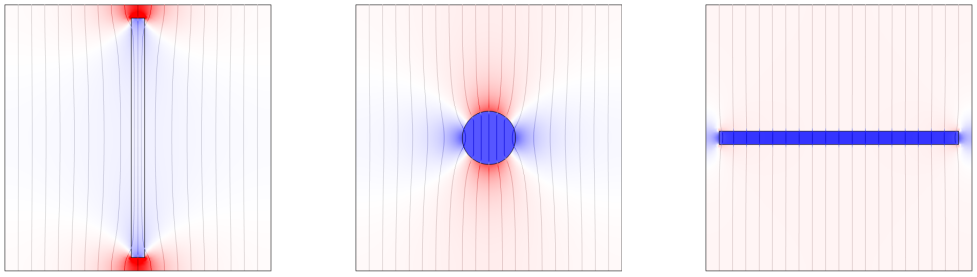

(a) $N_z \approx 0$ (b) $N_z = 1/2$ (c) $N_z \approx 1$

FIGURE 2.3: Examples of induced demagnetisation in an applied field using COMSOL. (a) has a sample of equal height to the cavity, placed parallel along the field. (b) shows a cylindrical sample with a perpendicular field. (c) has a flat sample with perpendicular field. Blue regions show a reduction in the applied field while red regions shown an increase. Notice that when $N_z = 1$, the applied field is reduced dramatically, making the measurement less sensitive to the bulk of the sample.

The demagnetising field is caused by the dipoles aligning themselves accordingly with the applied field resulting in charge build-up on the interfaces. Thus, the following constitutive field relation:

$$\bar{H}_{\text{samp}} = \bar{H}_{\text{cav}} - N\bar{M} \tag{2.3}$$

must apply[124], where N is the demagnetisation factor and $\bar{H}_{\text{cav}}$ and M are the applied and induced magnetisation fields, respectively. Assuming the applied field is in one direction (arbitrarily as $\hat{a}_z$), and assuming an isotropic material:

$$\bar{M} = \frac{(\mu_r - 1)}{1 + N_z(\mu_r - 1)} \bar{H}_{\text{cav}} \tag{2.4}$$

where N_z is the demagnetisation in the $\hat{a}_z$ direction. The N_z factors have been calculated for a sphere ($N_z = 1/3$), a cylinder in the radial direction ($N_z = 1/2$) and normal to a flat sample ($N_z = 1$)[79, 125]. The effective field is reduced in any case where N_z is non-zero, see Fig. 2.3. Parallel orientation allows most of the field into the sample while a flat interface effectively screens most of the field thus reducing sensitivity. For only a H-field perturbation, substituting 2.4 into 2.3 and then into 2.1 yields:

$$-\frac{\Delta\omega}{\omega} \approx \frac{(\mu_r - 1)}{1 + N_z(\mu_r - 1)} \frac{\int_{V_{\text{samp}}} \bar{H}_{\text{cav}}^2 dV}{\int_{V_{\text{cav}}} \bar{H}_{\text{cav}}^2 dV} \tag{2.5}$$

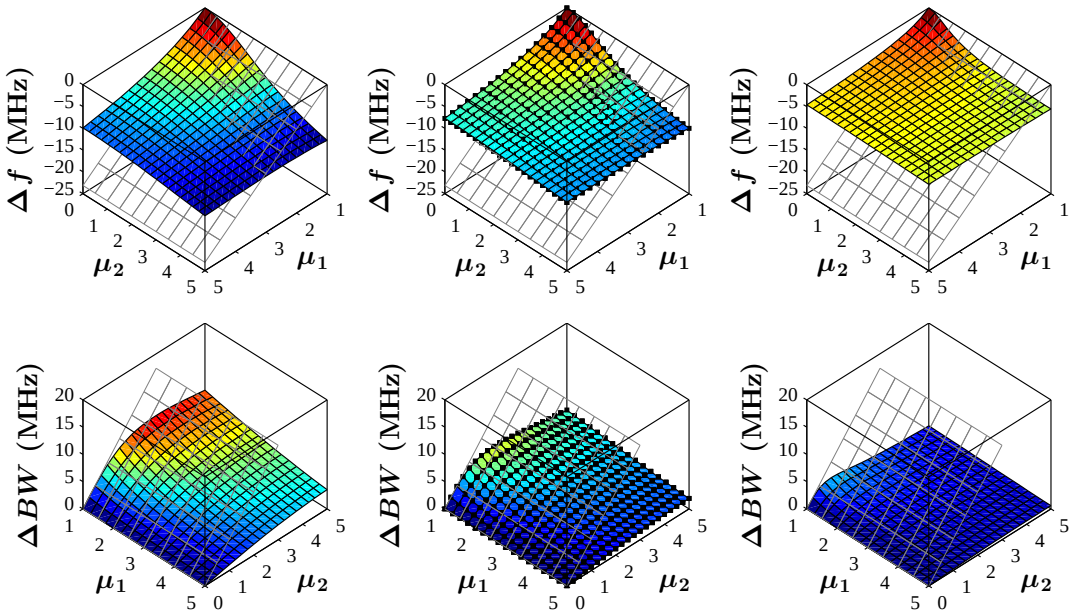

(a) $N_z = 1/3$ (b) $N_z = 1/2$ (c) $N_z = 1$

FIGURE 2.4: Example of the change in complex resonance of a demagnetising cylindrical sample (radius = 2 mm, height = 40 mm) in the cylindrical TM_{110} cavity mode (radius = 47.5 mm, height = 40 mm, $G_{nmp} = 0.399$, $f = 3.787$ GHz). Dots show COMSOL simulation while the grid shows the shift for $N_z = 0$.

Rearranging to a similar format as 2.2a and 2.2b gives:

$$\gamma \approx \frac{(\mu_r - 1)}{1 + N_z(\mu_r - 1)} \approx -2\,\frac{\Delta\omega}{\omega}\frac{V_{\text{cav}}}{V_{\text{samp}}}G_{nmp} \tag{2.6}$$

where γ is the scaled complex frequency shift. Solving for real and imaginary yields:

$$\mu_1 \approx \frac{\gamma_r - N_z(\gamma_r^2 + \gamma_i^2)}{N_z^2(\gamma_r^2 + \gamma_i^2) - 2N_z\gamma_r + 1} + 1 \tag{2.7a}$$

$$\mu_2 \approx -\frac{\gamma_i}{N_z^2(\gamma_r^2 + \gamma_i^2) - 2N_z\gamma_r + 1} \tag{2.7b}$$

where γ_r and γ_i are the scaled frequency and bandwidth shifts, respectively. An important verification is when $N_z = 0$ which gives 2.2a and 2.2b. Equations 2.7a and 2.7b can be used to measure samples of any known demagnetising shape factor. The case for a perpendicular field on different sample shapes is shown in Fig. 2.4.

Notice now that μ_1 and μ_2 are no longer exclusively related to frequency and bandwidth, respectively, as was given in 2.2a and 2.2b. The sensitivity of the measurement also becomes more dependent upon the sample as the demagnetisation factors increase. If

the samples, however, have low magnetic permeability and losses, then the relationship is approximately linear. The grid in 2.4 shows the case for the highest sensitivity where $N_z = 0$. Equation 2.7b can be used for any sample shape as long as the demagnetisation factor is known. Conversely, in theory if known materials of variable permittivity are machined into intricate shapes, the effective demagnetisation factors of these shapes can be obtained.

Hence this section shows that the highest sensitivity is achieved when there are minimal demagnetisation fields. Ends of a sample should be placed parallel to the applied field in the resonator. Next, we must determine what the fields look like in the resonator, so that we know where the sample needs to be placed. To understand what the field distributions look like and also what modes are useful for the measurement of materials, the field vectors need to be derived from Maxwell's equations. Each set of field vectors will be associated with a mode and hence a formula for the resonant frequency of the modes can be determined.

2.1.3 Cavity Wave Equations

To measure a material with microwaves through perturbation, it is important to understand how to create these controlled regions of microwave fields through cavity resonance. A resonating cavity space has an electromagnetic standing wave within its boundaries, containing both nodes and anti-nodes in the E and H-field depending upon the wavelength. For a rectangular space, the standing waves are dependent upon sinusoids, whereas curved spaces are dependent upon Bessel functions[123]. We can solve the resonant frequency of any space by using the Helmholtz equation. This derivation can be done for either the E or H field component depending on whether we are looking at a transverse magnetic (TM) wave, where $H_z = 0$ or transverse electric (TE) wave, where $E_z = 0$. For the derivation, the E or H field vector is considered arbitrarily as A_z. Since this thesis mainly uses a cylindrical cavity, the field components can be obtained using the Laplacian of a field along the cylindrical axis:

$$\nabla^2 A_z - k^2 A_z = \frac{1}{\rho}\frac{\partial A_z}{\partial \rho} + \frac{\partial^2 A_z}{\partial \rho^2} + \frac{1}{\rho^2}\frac{\partial^2 A_z}{\partial \phi^2} + \frac{\partial^2 A_z}{\partial z^2} - \frac{1}{c^2}\frac{\partial^2 A_z}{\partial t^2} = 0 \tag{2.8}$$

where ρ, ϕ and z are the cylindrical components and t is time. For an EM wave described by $e^{-j\omega t}$, the second order time derivative can be expressed as $-\omega^2$. To make this equation applicable for a cavity, we need to impose some metallic boundary conditions such as ensuring E-fields are not parallel to a metal surface and that H-fields must form loops. Multiplying by ρ^2 and defining the solutions to the partial differentials in the ϕ and z dimensions as k_ϕ and k_z respectively, we can arrive at Poisson's equation:

$$\rho\frac{\partial A_z}{\partial \rho} + \rho^2\frac{\partial^2 A_z}{\partial \rho^2} - \left(k_\phi^2 - \rho^2\left[k_z^2 - \frac{\omega^2}{c^2}\right]\right)A_z = 0 \tag{2.9}$$

where $-k_z^2$ and $-k_\phi^2$ are the solutions to $\frac{\partial^2 A_z}{\partial z^2}$ and $\frac{\partial^2 A_z}{\partial \phi^2}$ respectively. The radial component is the solution to Poisson's equation ($k_\rho^2 = [\omega/c]^2 - k_z^2$) and yields Bessel functions while the azimuth and length have sinusoidal solutions:

$$A_z(\rho) = \psi_1\, J_n(k_\rho \rho) + \psi_2\, Y_n(k_\rho \rho) \tag{2.10a}$$

$$A_z(\phi) = \begin{cases} \psi_3 \cos(k_\phi \phi) \\ \psi_4 \sin(k_\phi \phi) \end{cases} \tag{2.10b}$$

$$A_z(z) = \begin{cases} \psi_5 \cos(k_z z) \\ \psi_6 \sin(k_z z) \end{cases} \tag{2.10c}$$

where J_n and Y_n are Bessel's equations of the first and second kinds respectively and ψ_{1-6} are constants. First we deal with any mathematical inconsistencies. If $k_\rho\rho$ is equal to zero (on the axis of the cavity), then Y_n is infinite which is physically impossible thus ψ_2 must be equal to zero. Also, the field around the azimuth must be the same each revolution in space (i.e. periodic at 2π), thus k_ϕ must be an integer. Because of both sine and cosine solutions to the azimuthal component, there will be degeneracy (i.e. modes that have the same frequency) which have field distributions orthogonal to one another. For this derivation we will just consider the cosine case where $\psi_4 = 0$. Finally, the length component will depend upon whether the mode is a TE or TM mode (since E and H-fields have different boundary conditions). The spatially generic form of a cylindrical wave can

thus be given as:

$$A_z(\rho,\phi,z) = \psi_0 J_n(k_\rho \rho)\cos(k_\phi \phi) \begin{cases} \psi_5 \cos(k_z z) \\ \psi_6 \sin(k_z z) \end{cases} \tag{2.11}$$

where ψ_0 is a constant. This equation describes what the field in the z direction looks like. Using Maxwell's equations we can find out what the field looks like radially and on the azimuth:

$$\nabla \times \bar{E} = -j\omega\mu\bar{H} = -jkZ_0\bar{H} \tag{2.12a}$$

$$\nabla \times \bar{H} = j\omega\varepsilon\bar{E} = j\frac{k}{Z_0}\bar{E} \tag{2.12b}$$

Evaluating the curls, 2.12a and 2.12b give the generic forms of:

$$\begin{bmatrix} E_\rho \\ E_\phi \\ E_z \end{bmatrix} = -\frac{jZ_0}{k} \begin{bmatrix} \frac{1}{\rho}\frac{\partial}{\partial\phi}H_z - \frac{\partial}{\partial z}H_\phi \\ \frac{\partial}{\partial z}H_\rho - \frac{\partial}{\partial\rho}H_z \\ \frac{\partial}{\partial\rho}H_\phi - \frac{\partial}{\partial\phi}\frac{1}{\rho}H_\rho \end{bmatrix}, \qquad \begin{bmatrix} H_\rho \\ H_\phi \\ H_z \end{bmatrix} = \frac{j}{kZ_0} \begin{bmatrix} \frac{1}{\rho}\frac{\partial}{\partial\phi}E_z - \frac{\partial}{\partial z}E_\phi \\ \frac{\partial}{\partial z}E_\rho - \frac{\partial}{\partial\rho}E_z \\ \frac{\partial}{\partial\rho}E_\phi - \frac{\partial}{\partial\phi}\frac{1}{\rho}E_\rho \end{bmatrix} \tag{2.13}$$

whereby applying the appropriate boundary conditions, which depends on the supported modes of a structure (TM and TE for a cavity), gives equations describing the field in different directions. This is useful as it will allow us to find E and H field maxima and potentially useful characterisation modes.

2.1.4 TM Modes

For a TM mode, $A_z \equiv E_z$ and $H_z = 0$. The boundary conditions are that all E-fields parallel to a metal wall must equal zero and all E-fields must enter/exit perpendicular to a boundary. Therefore, the parallel E-field at the curved walls (E_z and E_ϕ) must be zero and the parallel E-field at the top and bottom plates (E_ρ and E_ϕ) must also equal zero. These E-field components can be determined from 2.13. Since $H_z = 0$ and $-k_z^2$, $-k_\phi^2$ and k_ρ^2 have already been defined as solutions to the second order derivatives of E_z, we can

substitute them into 2.13 to obtain:

$$\begin{bmatrix} E_\rho \\ E_\phi \\ E_z \end{bmatrix} = \begin{bmatrix} \frac{1}{k_\rho^2}\frac{\partial}{\partial\rho}\frac{\partial}{\partial z}E_z \\ \frac{1}{\rho k_\rho^2}\frac{\partial}{\partial\phi}\frac{\partial}{\partial z}E_z \\ E_z \end{bmatrix}, \qquad \begin{bmatrix} H_\rho \\ H_\phi \\ H_z \end{bmatrix} = \frac{j}{Z_0}\begin{bmatrix} \frac{k}{\rho k_\rho^2}\frac{\partial}{\partial\phi}E_z \\ -\frac{k}{k_\rho^2}\frac{\partial}{\partial\rho}E_z \\ 0 \end{bmatrix} \tag{2.14}$$

From 2.11, the radial variation of E_z is due to $J_n(k_\rho\rho)$, so in order for the E-field to be zero at the curved walls (at $\rho = a$), $J_n(k_\rho a) = 0$. Hence k_ρ must be equal to a root of J_n, or the m^{th} root of the n^{th} Bessel function of the first kind (α_{nm}) scaled by the radius ($k_\rho = \alpha_{nm}/a$). For the E-field to be zero at the top and bottom plates, E_ρ and E_ϕ must be dependent upon $\sin(z)$, thus $\psi_6 = 0$. The standing wave is satisfied by the cosine roots scaled by the height of the cavity ($\frac{p\pi}{l}$), leading to an equation for E_z for a TM wave:

$$E_z = E_0 J_n\left(\frac{\alpha_{nm}}{a}\rho\right)\cos\left(n\phi\right)\cos\left(\frac{p\pi}{l}z\right) \tag{2.15}$$

The azimuthal, radial and axial standing waves are given by n, m and p respectively.

TM Resonant Frequency

The solution to 2.9 is the solution to Poisson's equation which gives:

$$\left(\frac{\alpha_{nm}}{a}\right)^2 = \left(\frac{\omega}{c}\right)^2 - \left(\frac{p\pi}{l}\right)^2 \tag{2.16}$$

Rearranging yields the wave dispersion relation or resonant frequency equation for a cylindrical space bounded by a radius of a and height of l.

$$f_{\text{TM}} = \frac{c}{2\pi}\sqrt{\left(\frac{\alpha_{nm}}{a}\right)^2 + \left(\frac{p\pi}{l}\right)^2} \tag{2.17}$$

This relation determines the resonant frequency of a cylindrical space so that it can be measured on a VNA. This is an important result, showing that the resonant frequency of any air-spaced cylindrical cavity can be tuned by the height and radius for dielectric and magnetic measurements.

TM Field Distributions

The cylindrical components of the E and H field distributions can be obtained from 2.14:

$$\begin{bmatrix} E_\rho \\ E_\phi \\ E_z \end{bmatrix} = E_0 \begin{bmatrix} -\frac{k_z}{k_\rho^2} J_n'\left(\frac{\alpha_{nm}}{a}\rho\right)\cos(n\phi)\sin\left(\frac{p\pi}{l}z\right) \\ \frac{n}{\rho}\frac{k_z}{k_\rho^2} J_n\left(\frac{\alpha_{nm}}{a}\rho\right)\sin(n\phi)\sin\left(\frac{p\pi}{l}z\right) \\ J_n\left(\frac{\alpha_{nm}}{a}\rho\right)\cos(n\phi)\cos\left(\frac{p\pi}{l}z\right) \end{bmatrix} \tag{2.18a}$$

$$\begin{bmatrix} H_\rho \\ H_\phi \\ H_z \end{bmatrix} = -j\frac{E_0}{Z_0} \begin{bmatrix} \frac{n}{\rho}\frac{k}{k_\rho^2} J_n\left(\frac{\alpha_{nm}}{a}\rho\right)\sin(n\phi)\cos\left(\frac{p\pi}{l}z\right) \\ \frac{k}{k_\rho^2} J_n'\left(\frac{\alpha_{nm}}{a}\rho\right)\cos(n\phi)\cos\left(\frac{p\pi}{l}z\right) \\ 0 \end{bmatrix} \tag{2.18b}$$

This is an important result as we can use 2.18a and 2.18b, along with 2.17 to determine the field distributions of a mode and the frequency that it resonates at. Useful modes for dielectric characterisation have been identified in Fig. 2.5. Modes where $n = 0$ have been chosen due to the fact that J_0 Bessel functions have an E-Field anti node in the centre of the cavity. Practically for powders, the samples can be filled into thin tubes and placed axially in the cavity. The first mode of this nature is the TM_{010} mode which can be designed to excite at ≈ 2.5 GHz using 2.17.

TM Unloaded Quality factor

Since we are looking at the change in frequency and the change in Q factor, we need to know what the theoretical 'resolution' of the measurements is. The larger the Q factor, the more change that can be measured. The following is a derivation of the theoretical unloaded quality factor of a cylindrical cavity resonator which can be simplified to a function of geometry and the material it is constructed from. Stored energy is given by the volume of fields and energy lost is given by Joules conduction losses in the walls:

$$Q_0 = \frac{f_0}{BW_0} = \omega_0 \frac{\mu_0 \int_{V_{\text{cav}}} \bar{H}_{\text{cav}}^2 dV}{R_s \int_{S_{\text{cav}}} \bar{H}_{\text{cav}}^2 dS} = \omega_0 \frac{\mu_0 \int_{V_{\text{cav}}} \bar{H}_{\text{cav}}^2 dV}{P_{\text{plates}} + P_{\text{curved}}} \tag{2.19}$$

where BW_0 is the unloaded bandwidth, ω_0 is the angular resonant frequency of the TE or TM mode, R_s is the surface resistance of the cavity material, S_{cav} is the cavity surface area and P_{plates} and P_{curved} are the conduction losses in the end plates and curved walls, respectively. Surface resistance is defined as $R_s = \sqrt{\pi \mu_0 \rho_0 f_0}$ where ρ_0 is the electrical

resistivity of the cavity material. The frequency dependence arises from the skin depth phenomena.

For TM modes, the integral in the numerator of 2.19 can be expressed as:

$$\mu_0 \int_0^l \int_0^{2\pi} \int_0^a \bar{H}_{\text{cav}}^2(\rho,\phi,z)\rho d\rho d\phi dz = \begin{cases} \mu_0 U_{nmp} V_{\text{cav}} & , \quad p = 0 \\ \frac{1}{2}\mu_0 U_{nmp} V_{\text{cav}} & , \quad p \geq 1 \end{cases} \tag{2.20}$$

where U_{nmp} is the mode dependent filling fraction in the cavity and is not to be confused with G_{nmp} which includes the fraction of field at the sample location. For TM modes this can be determined using 2.18b which conveniently gives:

$$\begin{aligned} U_{nmp} &= \left(\frac{k}{Z_0 a}\right)^2 \int_0^a \left[\left(\frac{J_n'(k_\rho \rho)}{k_\rho^2}\right)^2 + \left(\frac{n}{\rho}\frac{J_n(k_\rho\rho)}{k_\rho^2}\right)^2\right] \rho d\rho \\ &= \frac{1}{2}\left(\frac{J_n'(\alpha_{nm})}{k_\rho^2}\right)^2 \left(\frac{k}{Z_0}\right)^2 \end{aligned} \tag{2.21}$$

For the denominator of 2.19, the power dissipated in the walls is dependent upon tangential H-fields since a time varying H-field gives rise to a current (Ampère's Law):

$$P_{\text{curved}} = aR_s \int_0^l \int_0^{2\pi} \bar{H}_{\text{cav}}^2(a,\phi,z) d\phi dz \tag{2.22a}$$

$$P_{\text{plates}} = 2R_s \int_0^{2\pi} \int_0^a \bar{H}_{\text{cav}}^2(\rho,\phi,l) \rho d\rho d\phi \tag{2.22b}$$

Using 2.18b, 2.22a and 2.22b become:

$$P_{\text{curved}} = \begin{cases} a\pi l R_s \left(\frac{J_n'(\alpha_{nm})}{k_\rho^2}\right)^2 \left(\frac{k}{Z_0}\right)^2 & , \quad p = 0 \\ \frac{a\pi l}{2} R_s \left(\frac{J_n'(\alpha_{nm})}{k_\rho^2}\right)^2 \left(\frac{k}{Z_0}\right)^2 & , \quad p \geq 1 \end{cases} \tag{2.23a}$$

$$P_{\text{plates}} = \pi a^2 R_s \left(\frac{J_n'(\alpha_{nm})}{k_\rho^2}\right)^2 \left(\frac{k}{Z_0}\right)^2 \tag{2.23b}$$

First, notice that the last parts of both 2.23a and 2.23b are equal to 2.21. Substituting these and R_s into 2.19 we can obtain the theoretical unloaded quality factor:

$$BW_{0,\mathrm{TM}} = \begin{cases} \sqrt{\frac{\rho_0 f_0}{\mu_0 \pi}} \left(\frac{1}{a} + \frac{1}{l}\right) & , \quad p = 0 \\ \sqrt{\frac{\rho_0 f_0}{\mu_0 \pi}} \left(\frac{1}{a} + \frac{2}{l}\right) & , \quad p \geq 1 \end{cases} \tag{2.24}$$

The convenient simplification using 2.21 gives a significant result, showing that the minimum theoretical bandwidth can be determined from just the frequency, material and the dimensions of the cavity without the need for numerical computation of the stored energy inside of the cavity. To ensure that this formula obtains the correct result, COMSOL simulations of ideal geometry are done in the next chapter in comparison with the measured results obtained in practice.

2.1.5 TE Modes

For TE modes, the same analogies in 2.11 can be used where in this instance $A_z \equiv H_z$ and $E_z = 0$ which makes 2.13 become:

$$\begin{bmatrix} H_\rho \\ H_\phi \\ H_z \end{bmatrix} = \begin{bmatrix} \frac{1}{k_\rho^2} \frac{\partial}{\partial z} \frac{\partial}{\partial \rho} H_\mathrm{z} \\ \frac{1}{\rho k_\rho^2} \frac{\partial}{\partial z} \frac{\partial}{\partial \phi} H_\mathrm{z} \\ H_z \end{bmatrix}, \qquad \begin{bmatrix} E_\rho \\ E_\phi \\ E_z \end{bmatrix} = jZ_0 \begin{bmatrix} \frac{-k}{\rho k_\rho^2} \frac{\partial}{\partial \phi} H_\mathrm{z} \\ \frac{k}{k_\rho^2} \frac{\partial}{\partial \rho} H_\mathrm{z} \\ 0 \end{bmatrix} \tag{2.25}$$

The same boundary conditions used for TM apply, where now only E_ρ must equal zero at the curved walls and E_ρ and E_ϕ must equal zero at the top and bottom plates. Since there is no z derivative in 2.25, $\psi_5 = 0$. The solutions k_z and k_ϕ are the same as for the TM case but k_ρ is set by E_ϕ. Notice from 2.25 that E_ϕ is determined by the differential of H_z with respect to ρ. Hence, k_ρ must be equal to the m^{th} root of the differential of the n^{th} Bessel function of the first kind (α'_{nm}) which is scaled by the radius ($k_\rho = \alpha'_{nm}/a$). The TE wave equation thus becomes:

$$H_z = H_0 J_n \left(\frac{\alpha'_{nm}}{a} \rho\right) \cos(n\phi) \sin\left(\frac{p\pi}{l} z\right) \tag{2.26}$$

TE Resonant Frequency

With the same approach for TM, the TE wave dispersion relation is:

$$f_{\mathrm{TE}} = \frac{c}{2\pi}\sqrt{\left(\frac{\alpha'_{nm}}{a}\right)^2 + \left(\frac{p\pi}{l}\right)^2} \tag{2.27}$$

The TE modes are also tuned by the radius and height of the cavity but will result in different resonant frequencies due to the dependence upon the roots of $J'_n(\rho)$.

TE Field Distributions

The field equations are derived in a similar way to TM yielding the following:

$$\begin{bmatrix} H_\rho \\ H_\phi \\ H_z \end{bmatrix} = \begin{bmatrix} \frac{1}{k_\rho^2}\frac{\partial}{\partial z}\frac{\partial}{\partial \rho}H_{\mathrm{z}} \\ \frac{1}{\rho k_\rho^2}\frac{\partial}{\partial z}\frac{\partial}{\partial \phi}H_{\mathrm{z}} \\ H_z \end{bmatrix}, \qquad \begin{bmatrix} E_\rho \\ E_\phi \\ E_z \end{bmatrix} = jZ_0 \begin{bmatrix} \frac{-k}{\rho k_\rho^2}\frac{\partial}{\partial \phi}H_{\mathrm{z}} \\ \frac{k}{k_\rho^2}\frac{\partial}{\partial \rho}H_{\mathrm{z}} \\ 0 \end{bmatrix} \tag{2.28}$$

with wave equations:

$$\begin{bmatrix} H_\rho \\ H_\phi \\ H_z \end{bmatrix} = H_0 \begin{bmatrix} \frac{k_z}{k_\rho^2}\, J'_n\left(\frac{\alpha'_{nm}}{a}\rho\right)\cos(n\phi)\cos\left(\frac{p\pi}{l}z\right) \\ -\frac{n}{\rho}\frac{k_z}{k_\rho^2}\, J_n\left(\frac{\alpha'_{nm}}{a}\rho\right)\sin(n\phi)\cos\left(\frac{p\pi}{l}z\right) \\ J_n\left(\frac{\alpha'_{nm}}{a}\rho\right)\cos(n\phi)\sin\left(\frac{p\pi}{l}z\right) \end{bmatrix} \tag{2.29a}$$

$$\begin{bmatrix} E_\rho \\ E_\phi \\ E_z \end{bmatrix} = jH_0Z_0 \begin{bmatrix} \frac{n}{\rho}\frac{k}{k_\rho^2}\, J_n\left(\frac{\alpha_{nm}}{a}\rho\right)\sin(n\phi)\sin\left(\frac{p\pi}{l}z\right) \\ \frac{k}{k_\rho^2}\, J'_n\left(\frac{\alpha_{nm}}{a}\rho\right)\cos(n\phi)\sin\left(\frac{p\pi}{l}z\right) \\ 0 \end{bmatrix} \tag{2.29b}$$

TE Unloaded Quality factor

Unfortunately, the simplifications that occur in TM modes do not occur for TE modes as the integration results are not as simple due to the added complexity of considering H_z as well as the fact that k_ρ is determined by α'_{nm}. Following the same procedure as for TM but using stored electrical energy:

$$\varepsilon_0 \int_0^l \int_0^{2\pi} \int_0^a \bar{E}^2_{\mathrm{cav}}(\rho,\phi,z)\rho d\rho d\phi dz = \frac{1}{2}\varepsilon_0 U_{nmp} V_{\mathrm{cav}} \quad , \quad p \geq 1 \tag{2.30}$$

where

$$\begin{aligned} U_{nmp} &= \left(\frac{kZ_0}{a}\right)^2 \int_0^a \left[\left(\frac{J_n'(k_\rho\rho)}{k_\rho^2}\right)^2 + \left(\frac{n}{\rho}\frac{J_n(k_\rho\rho)}{k_\rho^2}\right)^2\right]\rho d\rho \\ &= \frac{\mu_0}{\varepsilon_0}\frac{1}{2}\left(\frac{J_n(\alpha_{nm}')}{k_\rho^2}\right)^2 (\alpha_{nm}'^2 - n^2)\left(\frac{k}{a}\right)^2 \end{aligned} \tag{2.31}$$

For the plate losses from the tangential H-fields in the denominator of 2.19:

$$P_{\text{plates}} = R_s \pi k_z^2 \left(\frac{J_n(\alpha_{nm}')}{k_\rho^2}\right)^2 (\alpha_{nm}'^2 - n^2) \tag{2.32}$$

For the curved walls, the tangential H-field is from to H_ϕ and H_z, giving:

$$P_{\text{curved}} = R_s \frac{a\pi l}{2}\left(\frac{J_n(\alpha_{nm}')}{k_\rho^2}\right)^2 \left[\left(\frac{n}{a}k_z\right)^2 + k_\rho^4\right] \tag{2.33}$$

Substituting 2.31 into 2.30 and the result, 2.32 and 2.33 into 2.19 yields the theoretical unloaded bandwidth:

$$BW_{0,\text{TE}} = \left(\frac{R_s}{\pi\mu_0}\right)\left(\frac{k_z}{k}\right)^2 \left[\frac{2}{l} + \frac{1}{a}\left(n^2 + \left[\frac{ak_\rho^2}{k_z}\right]^2\right)(\alpha_{nm}'^2 - n^2)^{-1}\right] \tag{2.34}$$

which as a function of geometry becomes:

$$BW_{0,\text{TE}} = \sqrt{\frac{\rho_0 f_0}{\pi\mu_0}}\left(\frac{pc}{2f_0}\right)^2 \left[\frac{2}{l^3} + \frac{1}{a}\left(\left[\frac{n}{l}\right]^2 + \left[\frac{\alpha_{nm}'^2}{p\pi a}\right]^2\right)(\alpha_{nm}'^2 - n^2)^{-1}\right] \tag{2.35}$$

This result is not as simple as for the TM case but with this, it is clear that a similar relationship exits where bandwidth increases with the square root of the resistivity. This will be useful for the temperature dependent experiments in Chapter 4.

With the wave equations defined in cylindrical space for both the TM and TE modes, the field distributions can now be visualised and useful modes can be determined. The samples used in this thesis are placed on the axis of the resonator. Using, 2.18a, 2.18b, 2.29a and 2.29b visualisations of useful characterisation modes are given in Fig. 2.5, where the sample is placed axially in the cylindrical resonator. In this case, all of the TM_{0mp} modes have minimal depolarisation and hence high sensitivity due to the fields along the sample with the same true for TE_{0mp} modes for demagnetisation. Each of the modes will, however, have varying sensitivity due to the varying amplitude of the fields at the sample

location. With increasing mode number, the resonant frequency also increases, allowing measurements over a broad frequency range. In this way, frequency dependent dielectric and magnetic properties can be obtained in the GHz range.

With the appropriate modes defined, now there needs to be a practical way to measure them. In the next section we look at measuring the frequency response of the cavity which can be used in conjunction with 2.2a 2.2b, 2.7a and 2.7b.

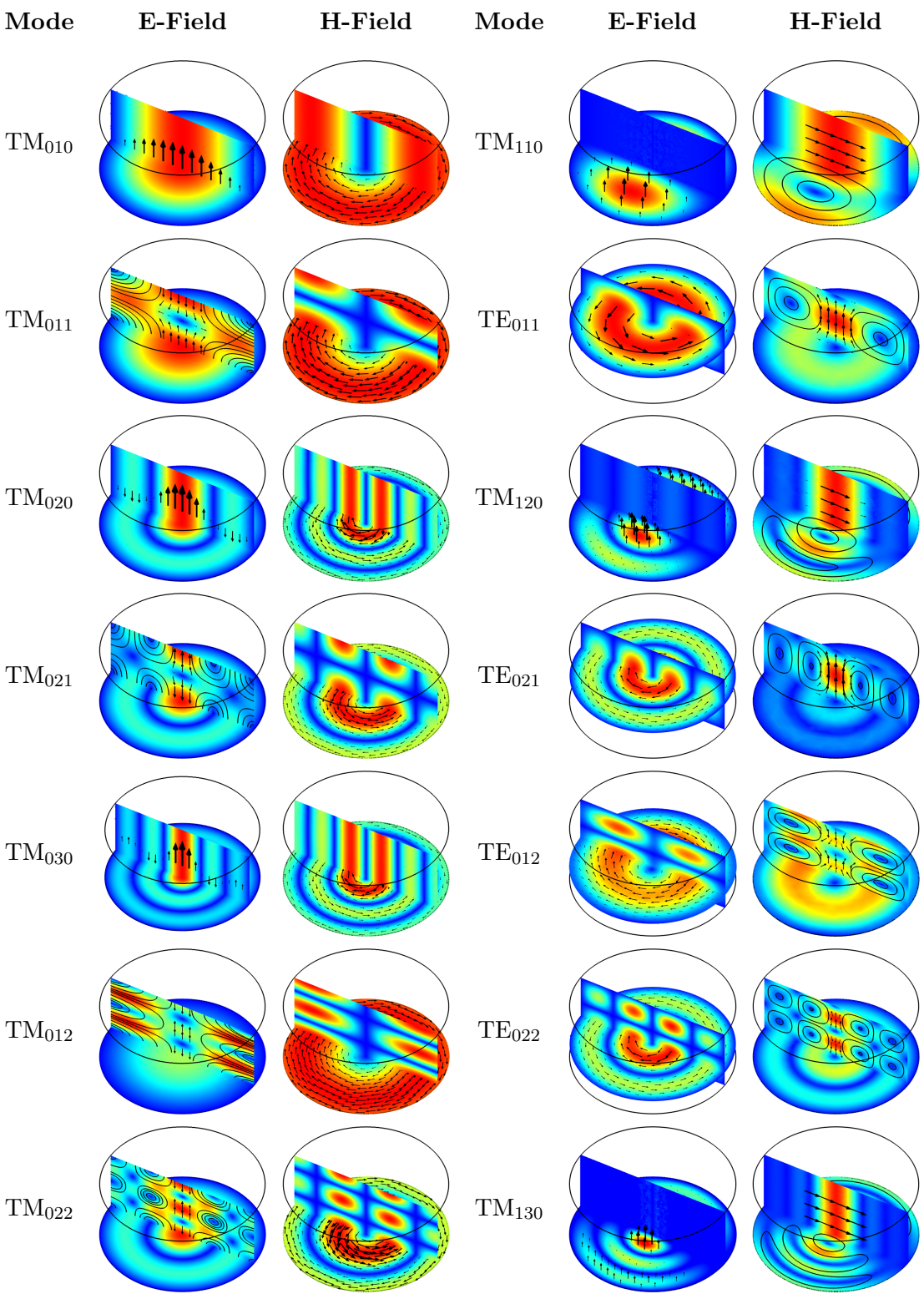

FIGURE 2.5: COMSOL Simulation of suitable modes for dielectric and magnetic characterisation for a tube of sample placed on the axis. The modes on the left are all in a minimal depolarising geometry, thus equations 2.2a and 2.2b can be used. The TE modes on the right also have minimal demagnetisation but the TM modes have finite demagnetisation hence equations 2.7a and 2.7b must be used.

2.2 Resonator Model

To measure the frequency response of a resonator, a swept microwave oscillator with a series of power detectors is used. This functionality is provided by a standard microwave VNA. Conventionally, excitation at frequencies close to resonance is provided at one port of the resonator, whilst the magnitude of the reflected power is measured. A second port can also be used to measure transmitted power. At resonance, power is transferred to the cavity and hence the magnitude of the reflection coefficient as a function of frequency exhibits a 'dip' at resonance. Similarly for transmission, the transmission coefficient exhibits a 'peak' at resonance. An RLC equivalent circuit is used to model the impedance of the cavity which is then translated into scattering parameters to model this power reflection/-transmission characteristic. This allows extraction of complex frequency to hence perform cavity perturbation measurements.

Fig. 2.6 shows a simplified RLC equivalent circuit of the cavity measurement system. The model consists of a one mode resonator ($Z_R(\omega)$) coupled using coaxial antennas (m_n) with excitation and power detection provided by a VNA (V_s with a source impedance of Z_0). The antennas used to excite the cavity will have a self-inductance (L_{xy}), which is a consequence of forming an inductor out of a loop of wire. Direct transmission between antennas can also occur ($Z_C(\omega)$) through crosstalk, effectively shunting the resonator. Coupling strength is controlled through the turns ratio (m_n), where n is the port number.

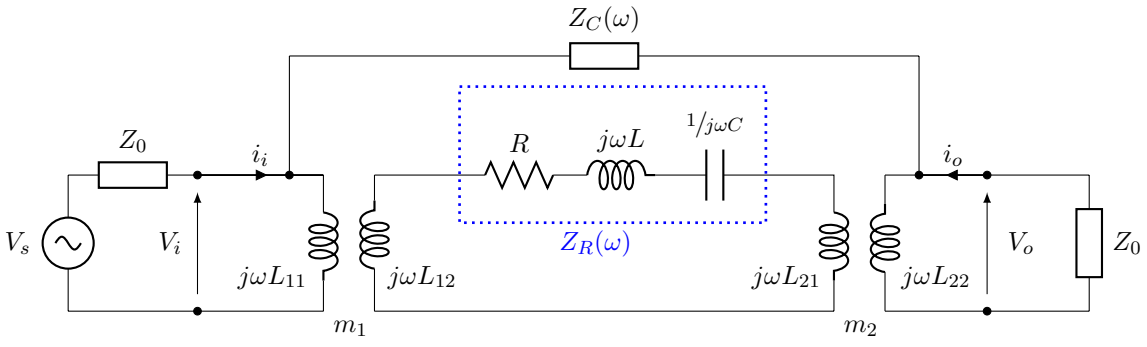

Figure 2.6: RLC circuit model of a cavity measurement system. $Z_R(\omega)$ represents the impedance of the resonator, where R are the resistive losses from the current in the cavity walls and L and C are the reactive components which are responsible for the resonance profile. $Z_C(\omega)$ represents crosstalk which shunts the resonator. The self inductance and coupling strength of the antennas are represented by L_{xy} and m_n respectively. V_s is the source voltage and Z_0 is the characteristic impedance of the system.

2.2.1 Cavity (Z_R)

Starting with just the impedance of the resonator $Z_R(\omega)$, the case for a high quality factor resonator is:

$$Z_R(\omega) = R + j\omega L - j\frac{1}{\omega C} \approx R\left[1 + j2Q_0\left(\frac{\omega - \omega_0}{\omega_0}\right)\right] \tag{2.36}$$

where Q_0 is the unloaded quality factor, ω_0 is the angular resonant frequency and R, L and C are the modelled resistive, inductive and capacitive components respectively. The reactive components are associated with the stored energy in the cavity whilst the resistance is associated with the power losses of the surface currents in the cavity walls. From the roots of 2.36, the most important notion of complex frequency can be determined which allows one to use the main cavity perturbation equations:

$$\omega \approx \omega_0 + j\frac{\omega_0}{2Q_0} \tag{2.37}$$

Hence any change in frequency of the resonator due to a sample perturbation can be represented as a complex frequency shift:

$$\frac{\Delta\omega}{\omega_0} \approx \frac{\omega_s - \omega_0}{\omega_0} + j\frac{1}{2}\left[\frac{1}{Q_s} - \frac{1}{Q_0}\right] \equiv \frac{f_s - f_0}{f_0} + j\frac{1}{2}\left[\frac{BW_s}{f_s} - \frac{BW_0}{f_0}\right] \tag{2.38}$$

where ω_s and Q_s are, respectively, the sample perturbed resonant frequency and quality factor. This is an important relation, stating that the real part is dominated by fractional frequency changes and the imaginary part to bandwidth or unloaded quality factor.

2.2.2 Antennas and Cross Coupling ($Z_C(\omega)$ and $j\omega L_{kl}$)

Complex resonant frequency can be obtained through coupling microwaves into the resonator using antennas, however, their use inherently adds loss to the system which affects the measurement of unloaded quality factor and to a lesser extent the resonant frequency. The antenna structures are designed to couple into either the electric or magnetic field component of the microwave standing wave; achieved with antenna probes or short-circuited loop antennas, respectively. Both of these components are modelled as impedance transforming networks with equivalent mutual capacitance and inductance. There are three main considerations for these antennas.

The first is crosstalk between the two antennas. Ideally, the coupled electromagnetic energy must be transferred to the receiving port *through* the cavity resonance (i.e. electromagnetic energy is 'tapped' in and out using the standing waves introduced by the cavity boundary conditions). In reality this is not a perfect exchange. The structures are, after all, antennas and radiate. Hence, shunt power transmission from one port to the other can occur (through the path denoted by $Z_C(\omega)$). This can be avoided by placing the antennas sufficiently far from one another and not in direct line of sight.

The second consideration is the extent to which the geometry of the antennas and port holes alter the standing wave patterns. If the antennas or port holes are large, we force different boundary conditions on the field patterns inside the resonator, therefore the assumption that the E or H-fields are uniform at the sample location may not be the case. A simple solution to this is to make the antennas and port holes small.

The last consideration is related to the impedance of the coupling antennas. Loading the system with lossy components affects the sensitivity of the measurement system and complicates the extraction of unloaded quality factor. To minimise the effects of the antennas, the resistances of the antenna conductors need to be minimised as well as their self-inductance/reactance. Again, a simple solution is to fabricate electrically small antennas out of high conductivity materials (e.g. short loops and rods made from copper or silver).

2.2.3 Impedance Matrix

A general impedance matrix can be derived using Kirchhoff's current law for the 2 port resonator given in Fig. 2.6.

$$\begin{pmatrix} V_i \\ V_o \end{pmatrix} = \begin{pmatrix} j\omega L_{11} + \frac{\omega^2 m_1^2}{j\omega(L_{12}+L_{21})+Z_R(\omega)} & \frac{\omega^2 m_1 m_2}{j\omega(L_{12}+L_{21})+Z_R(\omega)} \\ \frac{\omega^2 m_1 m_2}{j\omega(L_{12}+L_{21})+Z_R(\omega)} & j\omega L_{22} + \frac{\omega^2 m_2^2}{j\omega(L_{12}+L_{21})+Z_R(\omega)} \end{pmatrix} \begin{pmatrix} I_i \\ I_o \end{pmatrix} \tag{2.39}$$

The inclusion of $Z_C(\omega)$ into these equations is achieved in a different way which is considered in Section 2.2.5, hence in this model the antennas are placed appropriately such that crosstalk is insignificant ($Z_C(\omega) \approx \infty$). Also, in practice, it is assumed that the inductances of the loops are small ($L_{11} \approx L_{12} \approx L_{21} \approx L_{22} \approx 0$).

2.2.4 Scattering Parameters

Since in practice there will be excitation and detection from a VNA, it seems sensible to translate the impedance matrix to a scattering matrix which represents the system as a function of incident and reflected voltages at the ports of the resonator. Squaring these voltages gives the reflected and transmitted power at each of the ports which are used to measure the frequency response of the cavity.

The most stable method of measuring centre frequency and quality factor is to perform a transmission measurement across the two ports of the resonator. This reduces any error introduced due to the cables since the reflections and standing waves are not transmitted through the resonance. Taking the impedance matrix 2.39 and converting it into an S-parameter matrix, the power transmission coefficient can be obtained[123].

$$|S_{21}|^2 = \frac{4g_1g_2}{(g_1+g_2+1)^2 + 4Q_0^2\left(\frac{\omega-\omega_0}{\omega_0}\right)^2} \tag{2.40}$$

where g_n is defined as the coupling coefficient of the resonator:

$$g_n = \frac{\omega_0^2 m_n^2}{Z_0 Z_R} \approx \frac{\omega_0^2 m_n^2}{Z_0 R} \tag{2.41}$$

Equation 2.40, however, does not take into consideration the loaded quality factor which is what is observed in practice when measuring S_{21}. The relation between the loaded and unloaded quality factor is known as:

$$Q_L = Q_0(1-\sqrt{P_0}) \tag{2.42}$$

where P_0 is the power at resonance, when $\omega = \omega_0$:

$$P_0 = \frac{4g_1g_2}{(g_1+g_2+1)^2} \tag{2.43}$$

This shows that the power at resonance is a function of the coupling coefficients at each port and that increasing the coupling strength increases the peak resonance power. Increasing P_0 decreases the measured loaded quality factor implying that the impact from the losses of the coupling structures become prominent in the measurement. This is certainly not favourable as the system must be sensitive to the losses in the sample. One could argue

that since cavity perturbation is a differential measurement it is not as crucial to use unloaded quality factors, however, when the sample perturbs the cavity, the coupling also changes. If the coupling is strong, the measurements are more sensitive to these changes as opposed to the changes in the sample. Generally it is much easier to have weak coupling such that the loaded quality factor is almost representative of the unloaded. Substituting 2.43 into 2.40 yields the overall $|S_{21}|^2$ characteristic of the cavity:

$$|S_{21}|^2 = \frac{P_0}{1 + 4Q_L^2\left(\frac{\omega-\omega_0}{\omega_0}\right)^2} = \frac{P_0}{1 + 4Q_L^2 + 4Q_L^2\frac{f^2}{f_0^2} - 8Q_L^2\frac{f}{f_0}} = \frac{a_0}{1 + b_1 f + b_2 f^2} \tag{2.44}$$

where a_0, b_1 and b_2 are the coefficients of a Lorentzian resonance function which can be seen in blue in Fig. 2.7. Obtaining the complex frequency of the cavity can be achieved either through identifying the -3 dB points using markers or through non-linear curve fitting. Curve fitting is generally the better option since it allows one to minimise the number of points measured over a frequency span and hence the speed of measurement increases. This can be achieved using software such as National Instruments LabVIEW. Thus the measured $|S_{21}|^2$ trace obtained from the VNA can be fitted and the coefficents can be related to f_0, Q_L and P_0 through 2.44. The dynamic range in this measurement is limited to the peak power of the resonance and the noise floor of the power detectors (for typical VNA's, this can be as low as -80 dBm). This makes measurements of $|S_{21}|^2$ a very

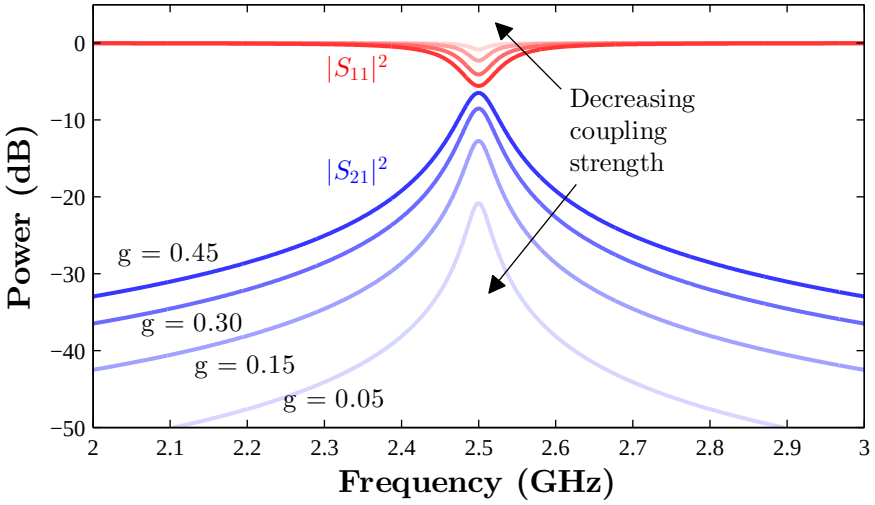

FIGURE 2.7: $|S_{21}|^2$ (blue) and $|S_{11}|^2$ (red) of a resonator with varying coupling strength where $f_0 = 2.5$ GHz and $Q_0 = 100$. This example assumes symmetrical coupling where $g = g_1 = g_2$. Notice that the -3 dB bandwidth becomes larger with increasing coupling strength, which is consequently very different to Q_0 as per 2.42.

sensitive method of measuring the complex frequency response of the cavity.

Let us consider a 1 port power reflection measurement of the 2 port resonator by using 2.39 to obtain $|S_{11}|^2$, and substituting in $Z_R(\omega)$ and g_n:

$$|S_{11}|^2 = \frac{(g_1 - g_2 - 1)^2 + 4Q_0^2\left(\frac{\omega-\omega_0}{\omega_0}\right)^2}{(g_1 + g_2 + 1)^2 + 4Q_0^2\left(\frac{\omega-\omega_0}{\omega_0}\right)^2} \tag{2.45}$$

Equation 2.45 is shown as the red lines in Fig. 2.7 which exhibits the dip at resonance. It is possible to extract the quality factor from this equation by negating the effects of the second coupling loop and thus perform perturbation measurements. Upon loading the resonator with a lossy dielectric, the reflected power will decrease as the sample dissipates electromagnetic energy within the cavity. As a result the minimum of the characteristic S_{11} dip will increase towards 0 dB, hence, the dynamic range of the measurement is limited to the initial coupling strength. Then it becomes clear that increasing coupling strength will increase dynamic range, however, this also inherently dumps more power into the sample which may cause heating through excitation of microwave loss mechanisms. Also to obtain a high quality factor and thus a high sensitivity of measurement, the coupling loading at the port must be small as given by 2.42. Finally, calibration to the plane of the resonator must be done to negate any standing waves and reflections introduced by the cables. From this it is clear that a two port transmission measurement is a much simpler method when compared to a one port reflection measurement.

2.2.5 Resonance Asymmetry

In the previous cases a 1 mode resonator has been assumed, however, cavity resonators are capable of supporting an infinite number of resonant modes. For the purpose of utilising multiple modes to provide partial spectral information, one must also consider that the measurement mode may produce an asymmetrical response, owing to the spectral presence of interfering modes. The resultant deformation may provide erroneous results as shown later. In this research, two main causes of an asymmetry or 'skew' have been identified.

The first type of skew is from another mode at higher mode numbers or where the resonant frequency solutions for TE and TM modes from 2.17 and 2.27 are very similar. This will create a distortion in the wanted measurement mode through the superposition of both

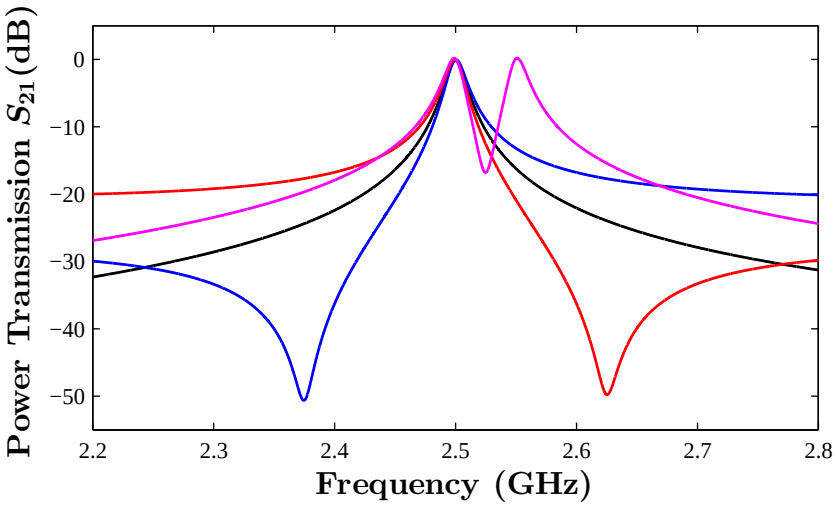

FIGURE 2.8: Example of different types of skew resonances at $f_0 = 2.5$ GHz. The main resonant peak is asymmetric depending upon the position of the interfering resonance or anti-resonance caused by the additional frequency dependent impedance. The original resonance is given in black. Red and blue show antenna related anti-resonance skew while magenta shows interference from another mode.

resonances in the frequency domain. Practically, this can be avoided by choosing the aspect ratio of the cylinder such that the wanted modes have clear spectral separation from the unwanted modes. As for degenerate TE and TM modes, one can use mode traps (explained in later sections) which separate the resonant modes. The second type of skew is a consequence of the antenna position, in particular directional antennas. When using one mode it is simple to find an optimum position for this loop to couple into the fields, however, when wanting to use multiple modes, this task becomes troublesome. This is especially the case for the TE_{011} and TE_{021} modes (see Fig. 2.5). At frequencies slightly off resonance, the field patterns distort in relation to the transmitting antenna position. At a critical frequency, this causes the receiving antenna to be in the presence of a node, making power transfer very small at this off resonance frequency. This consequently creates an anti-resonance in the frequency response and if the anti-resonance is deep enough, the wanted peak is drastically skewed.

Examples of skewed resonances are given in Fig. 2.8. In some cases, quality factors greater than their theoretical maxima can be observed if multiple modes are close enough. Errors in measurement occur when measurement is taken off of the -3 dB bandwidth or Lorentzian curve fitting is limited to the window of the peak. Also, the perturbation effects on both the wanted and unwanted modes may not shift in the same way, hence decoupling of the

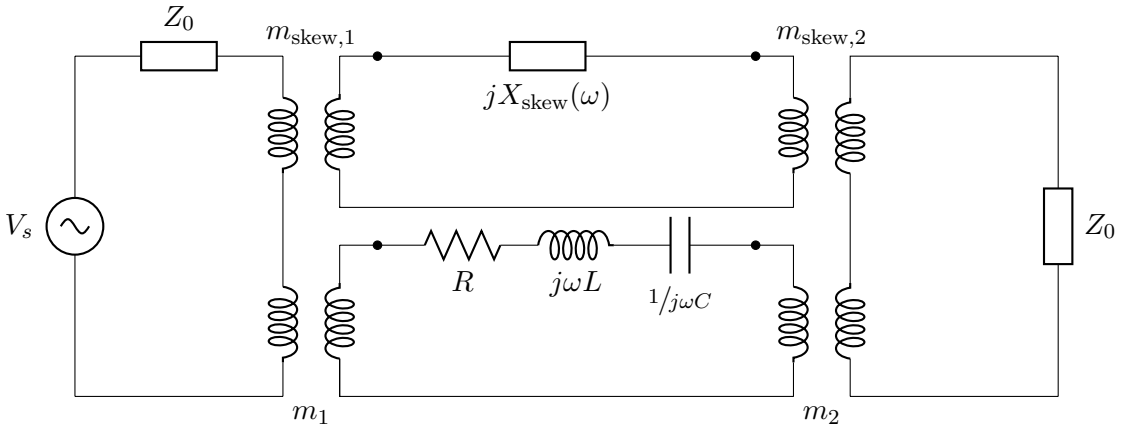

FIGURE 2.9: RLC circuit model of the resonator system with additional interference from a mode or crosstalk. The skew is caused by the reactance $X_{\text{skew}}(\omega)$ which varies the asymmetry of the main resonance. Coupling to this mechanism is represented by $m_{\text{skew},n}$.

peak resonance is paramount for correct complex frequency measurements.

Since it is easier to design a cavity with minimal TM and TE overlap from 2.17 and 2.27, the following considers skew caused by antenna positioning. This can be modelled using a shunt impedance across the whole resonator system, which is coupled into in the same way as a resonant mode as shown in Fig 2.9. The difference here is that the shunt impedance is not a resonator. There are essentially two variables that create a skew, which are coupling strength to this shunt impedance (g_{skew}) and the reactance (X_{skew}). To simplify the problem, the coupling coefficients can be made the same as the resonator ($g_{\text{skew}} = g_{\text{resonator}} = g$). This negates the need for a resistive component in the shunt impedance and simply distorts the resonance profile as a function of frequency based on the reactance. The main variable which controls the skew is the reactive component $jX_{\text{skew}}(\omega)$ since resistances are not functions of frequency.

Kirchhoff's Current Law can be applied to Fig 2.9 and the S_{21} response of the whole system can be derived. After rigorous simplification, whilst ignoring self-inductance, a general expression can be given for N resonances of a resonator:

$$S_{21,N} = \frac{2\sum_{i=1}^{N} \frac{g_i}{G_i(\omega)}}{1 + 2\sum_{i=1}^{N} \frac{g_i}{G_i(\omega)}} \tag{2.46}$$

where $G_i(\omega)$ is the intrinsic response of the i^{th} resonance. For a peak resonance:

$$G_{\text{res}}(\omega) = 1 + j2Q_0\frac{f - f_0}{f_0} \tag{2.47}$$

and for the skew impedance

$$G_{\text{skew}}(\omega) = j\frac{\omega L_{\text{skew}}}{R} = jX_{\text{sk}}(\omega) \tag{2.48}$$

where the reactance $X_{\text{sk}}(\omega)$ is the skew factor which influences the amount of skew on the resonance. This reactance can be an inductance (creates a skew upwards with frequency, blue trace in Fig. 2.8) or a capacitance (creates a skew downwards with frequency, red trace in Fig. 2.8)

Using 2.46, the following S_{21} equation can be obtained for a resonance with skew:

$$S_{21,\text{mix}} \approx \frac{2g\left(1 + \dfrac{G_{\text{res}}(\omega)}{G_{\text{skew}}(\omega)}\right)}{G_{\text{res}}(\omega) + 2g\left(1 + \dfrac{G_{\text{res}}(\omega)}{G_{\text{skew}}(\omega)}\right)} \tag{2.49}$$

In the limit where $G_{\text{res}}(\omega) \ll G_{\text{skew}}(\omega)$, the last term in the denominator can be neglected. This is analogous to saying that the shunt impedance must be much larger than the impedance of the resonator, otherwise no resonance will be observed. This yields the final simplified equation of:

$$|S_{21,\text{mix}}|^2 \approx \overbrace{\frac{P_0}{1 + 4Q^2\left(\dfrac{f - f_0}{f_0}\right)^2}}^{\text{resonator}} + \overbrace{\frac{P_0\dfrac{G^2_{\text{res}}(\omega)}{G^2_{\text{skew}}(\omega)} + 2P_0\dfrac{G_{\text{res}}(\omega)}{G_{\text{skew}}(\omega)}}{1 + 4Q^2\left(\dfrac{f - f_0}{f_0}\right)^2}}^{\text{skew}} \tag{2.50}$$

where, for brevity, excess terms in the numerator have not been expanded. Essentially, the original resonance can be identified as it is the only term without a frequency dependence in the numerator. Practically, any additional frequency dependent terms can be fitted to the following Lorentzian function with extra terms or 'skew' terms in the numerator:

$$|S_{21,\text{mix}}|^2 = \frac{a_0 + a_1 f + a_2 f^2 ...}{1 + b_1 f + b_2 f^2} \tag{2.51}$$

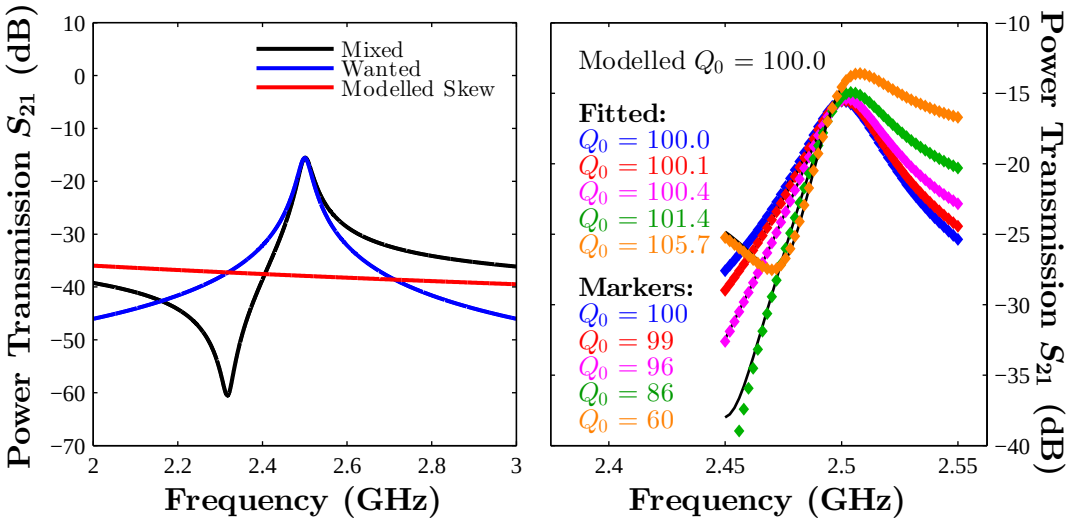

FIGURE 2.10: Example of a skewed mode (left) at 2.5 GHz. Blue shows the intrinsic resonance of the mode while red shows the response of the modelled cross talk reactance. Black shows the resultant convolution of the two impedances using 2.46. The convoluted resonance with skew varied by varying X_{skew} (right) is fitted using 2.51 and measured using -3 dB markers. Notice that using -3 dB markers produces a large error whilst skewed curve fitting mitigates this. Also notice that the crossing point between the skew trace and the wanted trace dictates where the anti-resonant dip occurs.

In this result, the two skew terms a_1 and a_2 can be used to account for any asymmetry in the peak resonance during curve fitting. Fig. 2.10 shows an example of a skewed response of a mode at 2.5 GHz (black line) caused by a modelled skew (red line). Skew was controlled by varying X_{skew} while -3 dB markers and non-linear curve fitting of 2.51 using the Levenberg-Marquadt algorithm in LabVIEW were used to measure the Q factor.

Notice that marker measurements produce a large error on the measured quality factor, while the skew fit remains within less than 6% error. Drastically skewed resonance modes are not favourable, but using this model it is possible to extract the intrinsic quality factor of the wanted mode with minimal error.

2.3 Cavity Measurement Procedure

2.3.1 Coupling Antennas

Excitation of the cavity is achieved with a coaxial line terminated with either a short or open circuit antenna for E or H field coupling respectively. Open circuit probe antennas radiate in a dome like fashion at the end of the cable. They are somewhat directional along the axis of the coaxial line and hence couple into fields where the E-field is along this axis. With this in mind, to couple to the E-field of a mode, the axis of the probe antenna should be pointing in the same direction as E-field of the mode. Short circuited loop antennas are also directional in that coupling is achieved by allowing the area of the loop to encompass the flux of the H-field of the mode. Hence, pointing the area of the loop in the direction of the H-field of the mode allows magnetic field coupling. It is also important that these antennas are placed at high field regions and not at nodes. This allows for greater control over coupling to the mode (to achieve coupling symmetry such that the RLC model for obtaining the complex frequency response is can be used).

2.3.2 VNA to provide S-Parameters

The measurements of $|S_{21}|^2$ were achieved using Keysight VNA systems. The VNA system mainly used throughout this work is a Keysight PNA N5232A system which has four 3.5 mm ports to perform S-parameter measurements. The oscillator and power detectors are capable of performing measurements in the frequency range of 300 kHz to 20 GHz with a maximum power output of +13 dBm and a noise floor approximately -100 dB. When unavailable, a Keysight ENA 5071C-2D5 system was used which has two 3.5 mm ports to perform S-parameter measurements. This system works between 300 kHz to 14 GHz with a maximum output power of +10 dBm and a noise floor at approximately -70 dB.

For measurements taken in this thesis, the 0.1 to 10 GHz range has been used for cavity and coaxial probe measurements. The excitation power used was 0 dBm though in practice this may be increased for resonator measurements to 10 dBm depending upon the coupling strength to the modes in the resonator. The IF bandwidth of the measurements is typically set at 1 kHz though for weakly coupled resonators and coaxial probe measurements, this

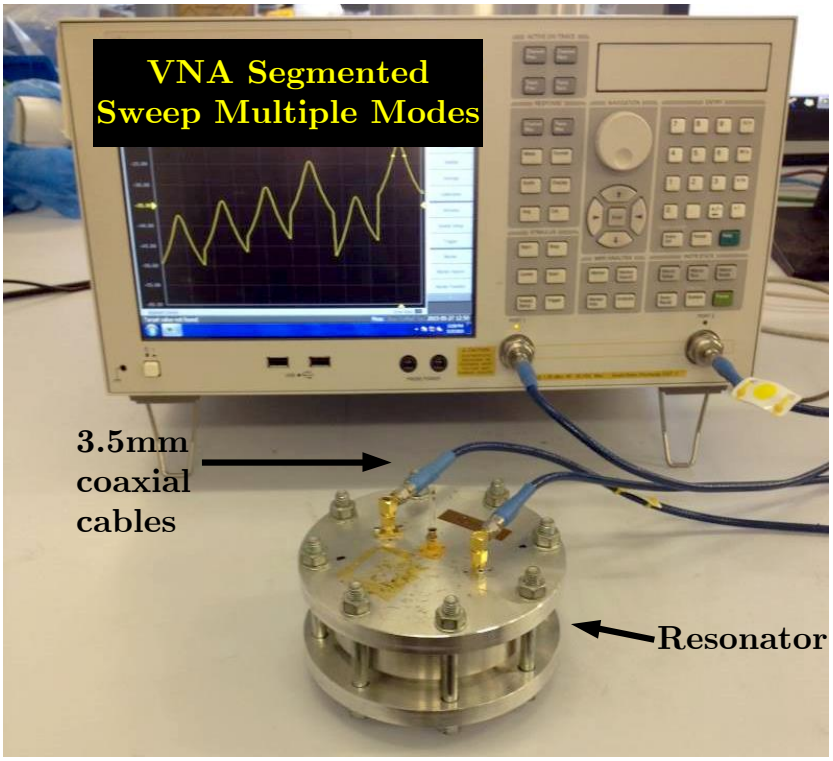

FIGURE 2.11: Typical VNA measurement set-up with cylindrical microwave cavity resonator. The VNA is set to perform a segmented sweep in order to capture the traces of multiple resonant modes in one measurement. These traces are acquired using a program written in National Instruments LabVIEW which performs fitting on the complex resonance and re-centres the peak when it changes. 3.5 mm coaxial cables provide excitation to the resonator.

may be reduced to 300 Hz to improve signal. The significance of the IF bandwidth is directly related to the acquisition speed and the quality of the measurement. This is because the quotient of the observed span over the IF bandwidth effectively yields the number of spectral acquisitions that the VNA has to perform. The quality of the signal is determined by the Fast Fourier Transform (FFT) of the time domain signal. In short, the main frequency span is made up of smaller spans (the IF bandwidth) where an FFT is performed on each of these windows and then the frequency domain signal is stitched back together. The smaller the window, the better the representation of the band as out of band products are ignored. However, this means that the VNA has more calculations to perform.

A meaningful measurement requires the frequency window to be tuned to the peak of the resonator such that the centre frequency and -3 dB bandwidth are clearly measurable.

The number of points used in a sweep is set to a low value of 31 per peak. This is because the measurement window is set to the order of the -3 dB bandwidth (i.e. for a mode with a resonant peak at 2.49 GHz with a bandwidth of approximately 100 kHz, the window will be centred at 2.49 GHz with a span of 200 kHz). Non-linear curve fitting is used, as explained previously, to extract the centre frequency and bandwidth, hence a large number of points is not required. The program is designed to perform a segmented sweep, such that multiple modes of the cavity resonator can be excited in one measurement. This allows fast measurement of broadband cavity perturbation measurements. In practice, the program measures the complex resonant frequency as a function of time with purpose to identify the temperature stability of the measurement since the resonant frequency is susceptible to the thermal properties of the cavity and the sample. The effects of the cavity can be accounted for as explained in a later chapter and so the time dependent responses are just used to determine sample stability.

2.3.3 Errors in measurement

There are numerous sources of error that must be recognised in conducting MCP measurements. Referring to 2.2a and 2.2b, notice that in order for permittivity and permeability measurements to be valid, there must be accurate measurement of resonant frequency, quality factor, sample volume, cavity volume and the effective scaling factor. The latter two, however, are effectively lumped together, where the cavity volume is assumed to be the manufactured value whilst any errors are passed onto the G_{nmp} value. The errors are broken down into the following:

$$\varepsilon_1 - 1 = 2 \times \overbrace{\frac{f_s - f_0}{f_0}}^{\text{Curve Fitting Error}} \times \underbrace{\frac{V_{\text{cav}}}{V_{\text{samp}}}}_{\text{Sample Preparation Error}} \times \overbrace{G_{nmp}}^{\text{Calibration Error}} \tag{2.52}$$

Since the experiment is based on a differential technique, the systematic errors in the cavity volume are effectively negated amongst the measurements. The error in G_{nmp} can be obtained from the cavity calibration procedure explained later in Chapter 3. The error in this measurement is, however, only 6%. The majority of the error falls onto the sample

preparation and the accuracy of extracting the resonant frequency and unloaded Q factor. The errors in the measurement of frequency are contributed by the VNA and the curve fitting process, though the VNA has a high frequency resolution of 1 Hz and an accuracy of ± 1 ppm. A typical measurement of complex frequency from curve fitting fluctuates by a maximum of 5 kHz. The majority of the error is therefore due to the variation in the sample preparation. To minimise the errors, multiple samples are prepared in the same way and measured using the cavity. The sample preparation involves filling the powders into a quartz tube and leaving them to settle on a vibrating stage.

2.4 Conclusions

In summary, an explanation on how a microwave cavity works is given. Details on how to obtain the resonant frequency and field distributions of a cylindrical space are presented which are paramount in understanding how to design systems for MCP. A circuit model is also presented to allow measurement of the resonator and thus perform MCP on samples. Finally, a brief outline on some of the measurement procedures is given, with emphasis on the sample preparation being the main source of error in these measurements.

CHAPTER 3

Methodology: Microwave Cavity Systems

The General Problem - Characterisation

MCP systems are required to measure the dielectric permittivity and magnetic permeability of materials. The properties need to be sensitively characterised at microwave frequencies to determine their efficacy and the limitations of these systems need to be evaluated.

The Approach

Simple powder MCP systems have been developed to measure microwave dielectric and magnetic properties in powders at Cardiff University. To test the systems, known microwave magnetic and non-magnetic materials are measured with varying concentrations of different materials to determine sole extraction of magnetic properties. *Both the dielectric and magnetic systems are presented in the EuMW 2014 and APMC 2014 Conference proceedings*[126, 127].

Key Findings

Measurements of powder mixtures with varying concentration of magnetic powders give increasing larger permeabilities with more magnetic powders. Fe_3O_4 gives a significantly large complex permeability, congruent with the literature. The ease of measurement demonstrates the effectiveness of the technique for researching materials for cancer hyperthermia and EMI absorbers.

3.1 Methods to measure microwave magnetism

Permeability is washed out at microwave frequencies because most magnetic phenomena is not able to keep up with the fast switching field. So what are the applications for materials which have this property? As stated in Chapter 1, the microwave magnetic permeability is a fundamental parameter in determining the absorbing performance of materials in hyperthermia and EMI. It can also be a figure of merit for detecting magnetism within a sample. In most cases, broadband microwave measurements are employed, whereby the sample is integrated into a transmission line structure.

Free-space Transmission Line techniques are generally suitable for looking at the specific absorbing properties of the final fabricated EMI absorbers since it best simulates the product conditions [28]. This is best suited for looking at tuning specific absorption frequencies through patterning effects[27, 28].

Coaxial and Waveguide techniques are employed for examining the microwave complex permeability[15, 19, 128, 129], which is the quantity that determines the absorbance. This is effective for producing broadband data, however, the values obtained often have small changes across the band until they are integrated into a polymer matrix where they show sharp absorption due to $\lambda/4$ resonances[27]. The repeatability of these techniques is often not mentioned and errors across the samples are generally ignored, possibly due to the complicated sample preparations. These techniques also have high susceptibility to calibration quality which again complicates the measurement.

3.2 A simpler approach: Multi-mode MCP

The proposal is to use MCP using magnetic field perturbations which sacrifices spectral resolution for high sensitivity at point frequencies in the band of interest. The intended modes to be used are the TE modes shown in Fig. 2.5. This technique can also be very simple in that the absorbing nanoparticles simply need be filled into a low microwave loss tube container and placed into the cavity for a measurement. This makes determination of suitable materials much faster than broadband techniques as it simplifies sample preparation. This approach has been attempted before using a rectangular cavity system[130], though in this thesis, the whole system is simplified and made smaller (to just a cylindrical cavity and a much simpler coupling mechanism). This type of system will form the basis of the rest of the work in this thesis and thus a thorough analysis on the design is provided.

To evaluate this concept, an already existing cylindrical cavity which was initially designed for dielectric characterisation was modified to excite modes for magnetic measurements, further referred to as Cyl-μ. The experiment to show that it measures microwave magnetic properties is to measure varying concentrations of magnetic powders mixed with non-magnetic materials which also exhibit dielectric and conducting properties. These non-magnetic materials should dilute the permeability measurement. The dielectric properties are measured using a dielectric measurement cavity, further referred to as Cyl-ε. This is to show that regardless of the dielectric property, the magnetic contribution can be extracted using the Cyl-μ system.

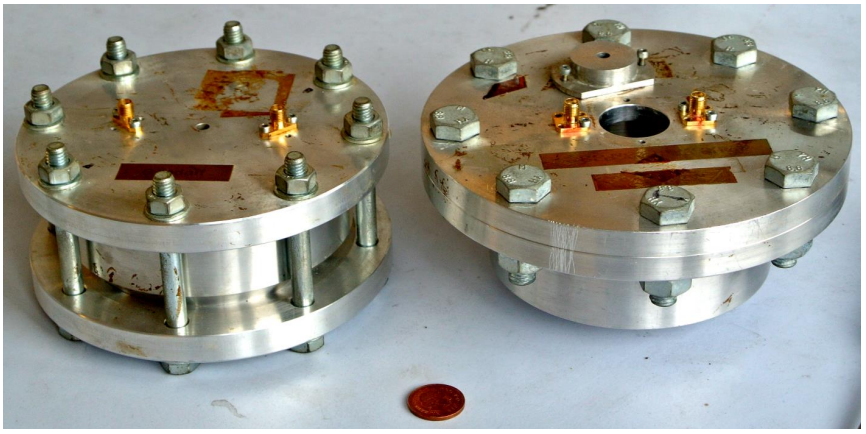

Figure 3.1: Dielectric measurement cavity Cyl-ε (left) and magnetic permeability measurement cavity Cyl-μ (right). The top plate of Cyl-μ has been removed to show the recess which is key to addressing mode degeneracy. Coin is a 1 pence piece.

3.3 Design of Cyl-μ and Cyl-ε Systems

To measure the dielectric and magnetic properties of a sample, the TM_{0mp} and TE_{0mp} modes shown previously in Fig. 2.5 are employed, respectively.

For Cyl-ε, the design is simpler than for Cyl-μ since degeneracy does not exist for the TM_{0mp} modes due to their symmetry about the azimuth. This system is needed to demonstrate that Cyl-μ is capable of singling out magnetic properties, regardless of the conducting or insulating mixture. This dielectric system is used for permittivity measurements used later in this thesis.

For Cyl-μ, the inherent degeneracy of the TE_{0mp} modes with the TM_{1mp} modes makes their usage troublesome for a cylinder. These modes have the same resonant frequency due to having the same Bessel root. This is partly shown in Fig. 3.2, where three modes overlap upon one another though are slightly separated due to the holes for the coupling antennas in the cavity. Using holes in specific places, or 'surface current mode traps', degeneracy can be broken. Furthermore, the TM_{1m0} demagnetising modes can also be used to provide more points in the spectrum.

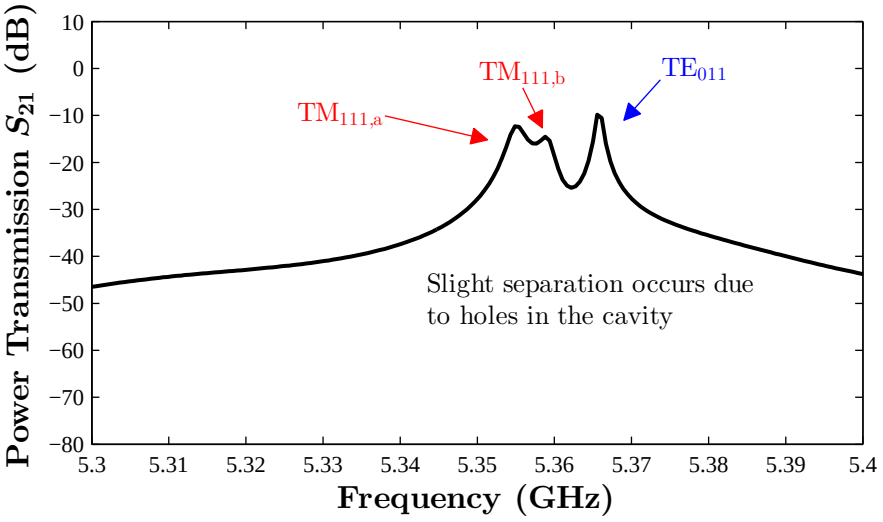

Figure 3.2: Measurement of the degenerate TM_{111} and TE_{011} modes using loop coupling on the top of a cylindrical cavity resonator. The only modifications to this cylindrical resonator are the port holes on the top (radius = 2.375 mm) and the sample holes on the top and bottom (radius = 2.5 mm). Two TM_{111} peaks are observed due to the orthogonal degeneracy of all TM_{1mp} modes given by 2.10b. The TE_{011} mode is higher in frequency since the holes have minimal impact on the surface currents of the mode (explained later).

3.3.1 Dielectric Measurement Modes

As stated previously, Cyl-ε is capable of using the TM_{0mp} modes to measure the dielectric properties of a tube sample placed on the axis. Though this cavity was originally designed to operate at only 2.5 GHz with TM_{010} and potentially 5.7 GHz with TM_{020}, there are in fact many other modes that can be used to calculate the permittivity at different frequencies to provide a better spread of data over the GHz range. This may be helpful in identifying frequency dependent behaviour such as contributions from static conductivity and space charge polarisation. The additional modes are TM_{011}, TM_{021}, TM_{012} and TM_{022} due to the fact that the radial 0^{th} order Bessel function has a maximum at $\rho = 0$. In these modes the E_z component has the only contribution on the axis, hence axial samples are always in a minimally depolarising field as shown in Fig. 2.5. Consequently, the H-field of these modes are dependent upon the derivative of the 0^{th} order Bessel function which results in a radial dependence on Bessel functions of at least the 1^{st} order. Practically this means that there will always be a minimum of H-field in the centre of the cavity for TM_{0mp} modes which is essential for assuming only E-Field perturbation as shown in Fig. 3.3.

The only issue is that with increasing mode number, interference becomes significant. Unfortunately, these are inevitable and it is hard to determine an ideal aspect ratio that separates them. Interference can be mitigated by using coupling structures that attempt to exclusively excite wanted modes. In practice, useful measurement modes can simply be identified by placing high dielectric materials at the sample location and examining

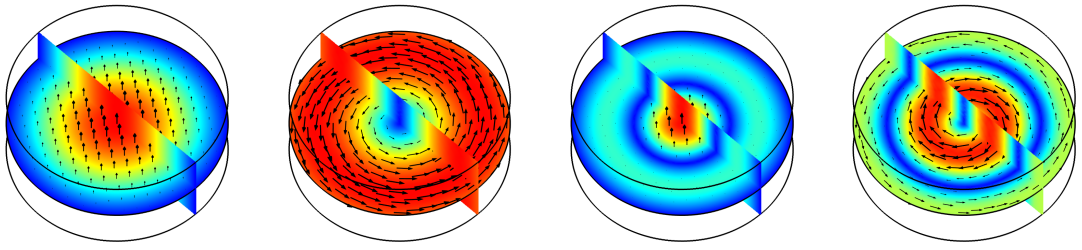

(a) TM_{010} E-Field (b) TM_{010} H-Field (c) TM_{020} E-Field (d) TM_{020} H-Field

Figure 3.3: Cylindrical cavity field distributions of the TM_{010} and TM_{020} modes. Notice that these modes have high E-field and low H-field on the axis, making them ideal for dielectric characterisation of a sample placed on the axis of the resonator. These modes are not degenerate with any other TM or TE mode due to their azimuthal symmetry.

the shift in frequency. Additionally, placing a metal rod at the sample location identifies minimal depolarising modes as these modes should vanish since an E-field cannot exist parallel to a metal surface.

3.3.2 Magnetic Measurement Modes

For the magnetic measurement cavity, there needs to be common regions of maximum H-field along the axis where there is no E-field and preferably minimal demagnetisation. Non-depolarising modes such as the TM_{010} mode which is conventionally used for dielectric measurements[102, 131, 132] cannot be equivalently realised for magnetic measurements since H-fields must be continuous (as given by Gauss' law $\nabla \cdot \bar{B} = 0$). It is possible, however, for the H-field to retain its continuity by circulating back out towards the walls (thus giving a spatially varying H_z). This is achieved with TE_{011} and TE_{0mp} modes with the former shown in Fig. 3.4c and 3.4d. As m increases, the field maxima on the axis starts to diminish, thus finite sample thickness must be considered. As p increases, standing waves are set-up across the sample with sections of parallel and anti-parallel vectors. Furthermore, as frequency increases, interference from other modes becomes important. As stated previously, TE_{0mp} modes (being degenerate) share a corresponding TM_{1mp} mode due to the wave dispersion relation shown in 2.17 and 2.27 (since $J_0'(x) = -J_1(x)$). These modes have a mixture of E and H fields along the axis, as shown in Fig. 3.4a and 3.4b which are useless for mutually exclusive electromagnetic measurements unlike the TE_{011} mode as shown in Fig. 3.4c and 3.4d. The scope of this section details suppression of the

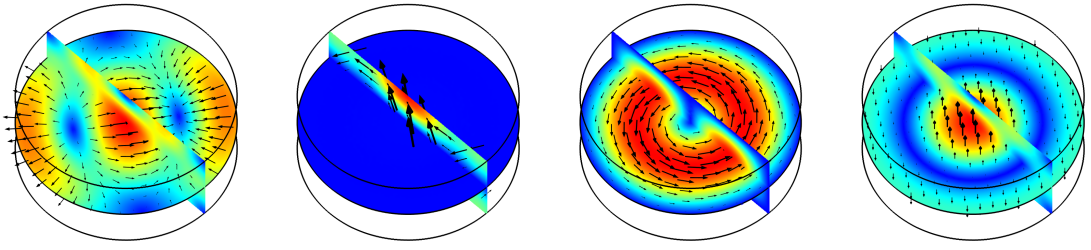

(a) TM_{111} E-Field (b) TM_{111} H-Field (c) TE_{011} E-Field (d) TE_{011} H-Field

Figure 3.4: Cylindrical cavity field distributions of the degenerate TE_{0mp} and TM_{nmp} modes. Notice that the in the TM_{111} mode, both the E and H-field are on the axis of the cavity making it useless for exclusive dielectric or magnetic characterisation. The TE_{011} mode, however, has a high H-field and low E-field in the centre, making it ideal for magnetic characterisation of a sample placed on the axis of the resonator.

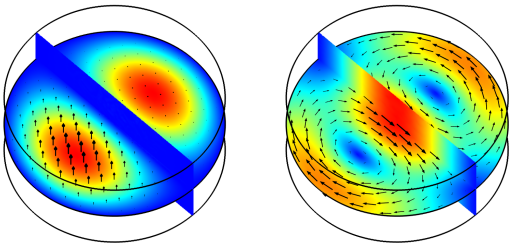

(a) TM_{110} E-Field (b) TM_{110} H-Field

FIGURE 3.5: Cylindrical cavity field distributions of the demagnetising TM_{1m0} mode. This mode is similar to the TE_{011} mode in that the H-field is large in the centre but the direction of the field is perpendicular to the sample as opposed to parallel to it.

TM_{111} mode with respect to the TE_{011} mode by creating a recess in the top and bottom plates of the cavity. This solution consequently spectrally separates all TE_{0mp} modes.

As well as the TE_{0mp} modes, there are also TM_{1m0} modes which have a high density H-Field on the axis of the cavity as shown in Fig. 3.5. In this configuration there is finite demagnetisation of the transverse H-field into the axial sample. In this case 2.2a and 2.2b cannot be used and instead 2.7a and 2.7b must be applied. Also, due the azimuthal standing wave, there must be a degenerate orthogonal mode (as per sine and cosine solutions to 2.10b). Practically this means that there will be two observed resonant peaks at the same frequency (much like the case for TM_{111} as shown in Fig. 3.2) which will overlap in the same fashion as in the multi-mode mixing model given in 2.46. Since the field maxima of these modes are clearly separated by $\pi/2$ along the azimuth, a simple approach to break this degeneracy is to orientate the coupling antennas in the direction of one of these modes. These demagnetising modes will be used where possible to add further points to the spectral magnetic measurement.

3.3.3 Breaking Degeneracy for Magnetic Modes

Conventionally, degeneracy is broken by positioning the antennas such that one mode is excited and the other is not. For TE_{0mp} modes, coupling can be achieved using short circuited loop antennas; as the E-Field is a circulating vector with no maxima on the edges, probe antennas cannot be used for this mode. Positioning the antennas on the top of the cavity with the loop facing the axis will provide strong coupling to the TE_{011} mode, however, the TM_{111} mode is still susceptible to excitation. Unfortunately, due to

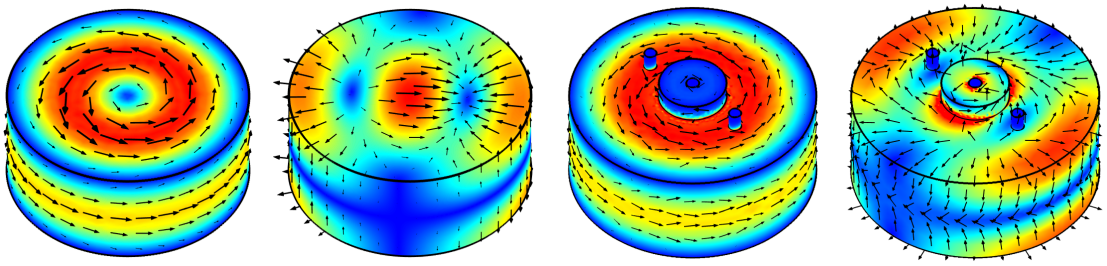

(a) TE_{011} (b) TM_{111} (c) TE_{011} Modified (d) TM_{111} Modified

FIGURE 3.6: COMSOL simulation of surface current density in the degenerate modes with and without recesses and port holes. When the recess is present, the surface current density of the TE_{011} mode is much less affected than the TM_{111} mode. This recess consequently affects the H-field distributions of the TM_{111} mode by imposing different boundary conditions on the space and changes the resonant frequency of the mode. The TE_{011} mode, however, is less affected by this.

the distribution of the fields in the TM_{111} mode, finding an ideal position is troublesome. At this stage, the induced *surface currents* in the cavity walls must be considered.

Referring to Fig. 3.6, the TE_{011} mode will have a circulating current on the top and bottom plates of the cavity with low surface current density at the centre. For the TM_{111} mode, note that there is a high induced surface current density across the centre. Hence, if this path is interrupted in some way, the resonance is also interrupted. This can be achieved by either replacing this section of metal with a low conductivity material, or by creating a hole or a dip. In this way, disruption of the TM_{111} mode can be achieved with minimal effect on the TE_{011} mode. This modification will also inevitably disrupt the TM_{110} mode to some extent since it has a similar surface current distribution. The recess can have any shape though for simplicity of manufacture a circular recess has been considered.

A COMSOL simulation was performed on the effect of the radius of a circular recess (shown in Fig. 3.7), where the depth is the typical thickness of the metal cavity walls (10 mm). Notice that with increasing hole size, the interference from TM_{111} decreases, however, when the ratio of the radius of the recess to the cavity is larger than 0.35, the interference becomes considerable. Also note that the wanted TE_{011} mode decreases in frequency, approaching TM_{210}. There reaches a point where the hole size is almost equivalent to the cavity radius which becomes the solution for a longer cylindrical cavity and hence the TM_{nm0} modes revert to their original values. TE_{111} also approaches TM_{110} and tends away at approximately 0.45. The effect on the TM_{110} mode is also shown where a decrease in resonant frequency is noticed. Due to the aspect ratio of the cavity, the only

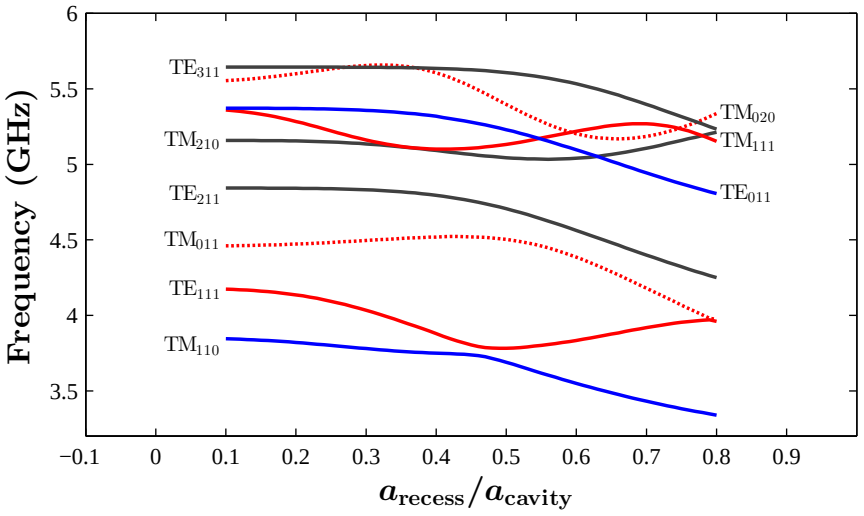

FIGURE 3.7: Effect of top and bottom recesses on the resonant frequency of cylindrical cavity modes from 3 to 6 GHz (radius = 47.5 mm, height = 40 mm). Solid lines show modes that can be excited using the loop coupling style while dotted show modes that will not be excited. Black lines show modes that will not change frequency upon perturbation, blue lines show the characterisation modes while red lines show interference modes.

interference this mode will encounter is the TM_{010} mode which is well below at 2.45 GHz. The significance of this simulation identifies a region between 0.15 and 0.45 for this ratio to sufficiently suppress the interfering TM_{111}.

3.3.4 Calibration and G_{nmp} of Cyl-μ

For Cyl-μ, to measure permeability using 2.2a and 2.2b, the G_{nmp} factor is required, which is the ratio of the amount of field in the cavity to the amount of field in the sample. These values have analytical solutions through integration of the field distributions, however, adding recesses to the cavity greatly alters the field distributions, especially those with high field intensity on the axis. To calibrate out these changes, an easy method would be to measure a sample of known magnetic permeability. There are not many materials with a well-known magnetic permeability at microwave frequencies. The alternative is to determine the filling factor through a metal rod perturbation. Consider the case where permittivity and permeability are large enough to screen out an incident applied field. This is the same as for a metal rod (assuming it is not perpendicular to the E-Field); hence, the resultant frequency and bandwidth perturbations represent the largest measurable values of permittivity and permeability. Consequently, with almost no H-field in the metal, the losses are minimal. The G_{nmp} factor for demagnetising modes can be obtained by

considering the limit where μ_1 is large and μ_2 is small, thus 2.6 can be simplified to:

$$G_{nmp} \approx \frac{1}{2N_z}\frac{f}{\Delta f}\frac{a_{\text{rod}}^2}{a^2} \tag{3.1}$$

Where a_{rod} is the radius of the metal rod. For non-demagnetising modes ($N_z = 0$), the frequency shift due to the sample tends towards infinity and hence a shape perturbation is considered instead. The rod essentially forces the field to zero, and hence the change in stored energy is equal to the total stored energy minus the stored energy when the rod is present. The change in stored energy results in a frequency shift, which can be related to G_{nmp}. Thus, G_{nmp} can be found from the frequency shift of a rod by:

$$G_{nmp} \approx \frac{1}{2}\frac{f}{\Delta f}\frac{a_{rod}^2}{a^2} \tag{3.2}$$

The introduction of the metal only slightly changes the field distribution of normal field modes if the diameter of the rod is small. For tangential fields, this calibration will only work for H-fields since tangential E-fields cannot exist on a metal.

3.3.5 Calibration and G_{nmp} of Cyl-ε

For Cyl-ε, there are no drastic geometrical modifications to the cavity, unlike Cyl-μ. However, the presence of the sample hole actually causes a large distortion in the E-Field along

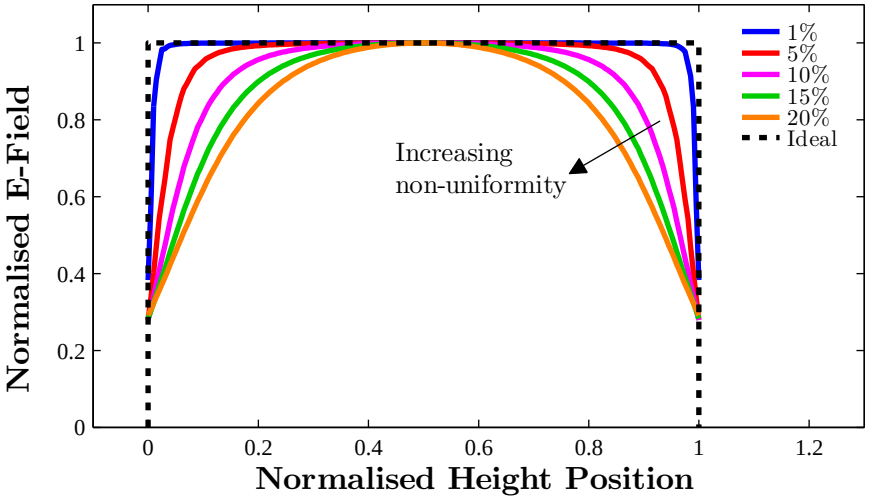

Figure 3.8: COMSOL simulation of the effect of the sample hole radius, as a percentage of the cavity radius, on the E-field uniformity along the axis of the TM_{010} mode. Normalised height position of 0 is at the bottom of the cavity while 1 is at the top.

the axis as shown in Fig. 3.8, hence calibration of Cyl-ε is required. This cannot be done with a metal rod perturbation for the reason stated at the end of the Section 3.3.4. A simple approach is to measure a material of known permittivity at microwave frequencies (such as Teflon where $\varepsilon_r \approx 2.1 - j0.001$) to determine the value of G_{nmp}. Previously, this cavity has been calibrated using spherical metal ball perturbations with 3.1 where $N_z = 1/3$[133]. This cannot be achieved easily for TM_{0mp} modes for $p \geq 1$ because of the spatially varying field along the axis.

There is a way around calibrating out the effects of the holes, and that is to consider that the reason the calibration is done is to determine *the strength of the E-field at the axially placed sample compared to the average field in the cavity.* The answer to this is that it is approximately the same as the analytical solution *but* there is a slight reduction caused by the sample holes at the top and bottom of the cavity.

In Fig. 3.8, notice that the E-Field distortion at the sample location only diminishies slightly at the edges depending on the hole size. Hence, as long as the solution to the case without the holes is known, we can simply multiply it by a scalar value dependent upon the hole size.

3.3.6 Construction

Both cavities are made from pieces of aluminium with their construction depicted in Fig. 3.9. Aluminium was chosen as a metal as it has a high electrical conductivity and is reasonably priced compared to copper. The Cyl-ε system was made by a previous MSc student[133] (radius of 46 mm and height of 40 mm). The Cyl-μ cavity was originally designed to measure dielectric properties using TM modes much like the Cyl-ε cavity, but has been modified to include recesses for the magnetic measurement modes (radius of 47.5 mm and height of 40 mm). Cyl-ε uses open circuit coaxial probes while Cyl-μ uses short circuited coaxial probes. These probes are to excite the different measurement modes mentioned previously.

The Cyl-ε system is machined out of three blocks of aluminium by sandwiching an aluminium tube with two cylindrical plates (held with steel bolts). The Cyl-μ system is an improved design with some advantages over the Cyl-ε cavity in that it is only machined out of two pieces and allows interchangeable recesses at the top and bottom plates of the

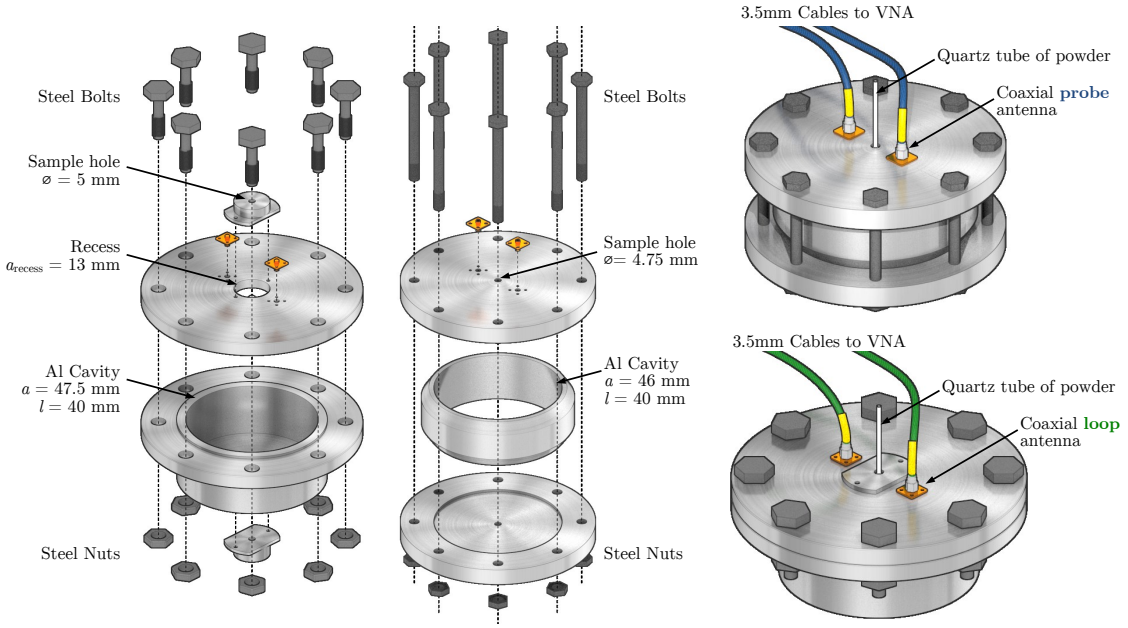

FIGURE 3.9: Exploded views of the Cyl-μ and Cyl-ε (left), and 3D view of cavity set-up (right).

cavity. For the latter case, this purpose is two-fold, allowing different sample hole sizes where needed and provides the mode traps discussed previously. This cavity is milled out of a solid block of aluminium and closed off with an aluminium plate. The plate is held in tightly using steel bolts to ensure a good electrical connection for TM modes, though for TE modes since the surface currents are transverse, this should have little effect on the Q factor. Coaxial SMA ports have been attached to the top for loop coupling in the appropriate orientation. The recess is formed with a hole down the axis of the cavity, and is closed off with an aluminium plate. A 5 mm axial hole is drilled for standard samples where additional sample collars are available for thinner samples.

The cavity was originally designed for a different application with large holes in the top and bottom plates to accommodate larger samples ($a_{\text{recess}} = 13$ mm which is 0.27 of the cavity radius). From Fig. 3.7, it is well within the suitable range to shift the unwanted modes and so metal plates were simply fixed over these holes to form the recess. The recesses have a depth of 7 mm and 10 mm for the top and bottom respectively. This diameter should significantly shift the TM_{111} mode away from the TE_{011} mode, and consequently free other TE_{0mp} modes. If needed, the diameter of this initial recess can be made smaller using metal plugs designed to fit in the resonator.

3.4 Experiment: Extraction of Magnetic Properties

3.4.1 Aims and Objectives

The aim of this experiment is to show that microwave magnetic permeability can be measured over a range of frequencies using multiple modes TE_{0mp} modes. To do this, Cyl-μ and Cyl-ε need to be calibrated and then materials with mixtures of dielectric and magnetic properties are measured to determine the extraction of magnetic properties.

3.4.2 Measured Resonant Frequency and Quality Factor

The analytical, simulated and measured values of the Cyl-ε cavity modes are given in Table 3.1. The values in the analytical column have been calculated using 2.17 with the ideal cavity dimensions. The values in the simulated column have been obtained with the dimensions of the machined cavity including the sample holes, port holes and the slight rounding at the corners of the cavity due to the milling process. It was found through simulation that the rounded edges were responsible for the slightly higher resonant frequencies given in Table 3.1. There are small differences between the analytical and the simulated quality factors but the measured values are much less than both of them. The reason for this is due to the electrical quality of the aluminium which is not pure and hence the modelled resistivity ($\rho_{\text{Al}} \approx 2.68 \times 10^{-8}$ Ωm) is very different. Using equation 2.24 with the values given in Table 3.1, the actual effective resistivity of the walls can be calculated giving $\rho_{\text{Al,real}} \approx 3.8 \pm 0.1 \times 10^{-8}$ Ωm. This slightly larger value is representative of the additional losses which take into account the surface roughness of the cavity (which inherently affects the surface current paths of the different modes) and the electrical quality of the aluminium.

The analytical, simulated and measured values of the Cyl-μ cavity modes are given in Table 3.2 with a similar procedure. This cavity, however, does not have any rounded edges due to the different construction procedure. The resultant differences in frequency are due to the recess. The measured resonant frequency is very similar to the simulated values with a maximum error of 2%. The measured Q factors are of the same order of magnitude with slightly lower values attributed to the surface roughness of the aluminium.

TABLE 3.1: Resonant frequencies and Q factors of the measurement modes in Cyl-ε

Mode	**Resonant Frequency (GHz)**			**Quality Factor**		
	Analytical	COMSOL	Measured*	Analytical	COMSOL	Measured
TM_{010}	2.494	2.500	2.501	13042	13260	10880 ± 180
TM_{011}	4.502	4.521	4.532	11416	11415	9390 ± 80
TM_{020}	5.729	5.734	5.746	19767	19751	15490 ± 70
TM_{021}	6.843	6.875	6.891	14075	14044	10610 ± 50
TM_{012}	7.899	7.931	7.946	15122	14990	12320 ± 80
TM_{022}	9.432	9.475	9.496	16524	12465	11950 ± 10

*measured with a maximum standard deviation of ±1 kHz.

TABLE 3.2: Resonant frequencies and Q factors of the measurement modes in Cyl-μ

Mode	**Resonant Frequency (GHz)**			**Quality Factor**		
	Analytical	COMSOL	Measured*	Analytical	COMSOL	Measured
TM_{110}	3.849	3.791	3.786	16464	9502	9240 ± 30
TE_{011}	5.372	5.362	5.357	25746	24965	20800 ± 20
TE_{021}	7.982	7.952	7.943	39525	37268	32700 ± 100
TE_{012}	8.425	8.396	8.387	25343	23899	20000 ± 70
TE_{022}	10.288	10.018	10.166	33804	28947	26800 ± 100

*measured with a maximum standard deviation of ±1 kHz.

TABLE 3.3: Resonant frequencies of the interfering degenerate modes of Cyl-μ

Mode	**Resonant Frequency (GHz)**		
	Analytical	Measured* Wanted	Measured* Degenerate
TM_{110}	3.849	3.800	-
TE_{011}	5.372	5.372	5.194
TE_{021}	7.982	7.952	7.885
TE_{012}	8.425	8.398	8.126
TE_{022}	10.288	10.18	10.03

*measured with a maximum standard deviation of ±1 kHz.

The reduction from simulation is not as profound in this cavity which may be explained by the fact that there are no joins interrupting surface currents for the TE modes while the TM_{110} mode is only disrupted by 1 join. The addition of the recess, however, reduces the Q factor of the TM_{110} mode dramatically.

The measured interference frequencies for Cyl-μ are given in Table. 3.3. With a recess diameter of 26 mm, the degenerate TM_{1mp} modes have shifted by at least 100 MHz providing a significant range for a the peak to shift. However, although this recess has

managed to move these modes away, due to the inherently crowded spectrum at higher mode numbers, a peak was noticed at 8.375 GHz, close to the TE_{012} mode at 8.398 GHz. This interference mode is only an issue if the shifts are significant and is monitored when taking measurements. Also the TE_{021} mode is slightly skewed due to the coupling mechanism which therefore requires skewed curve fitting.

3.4.3 Cavity Calibration for Permittivity and Permeability

The parameters required to perform permittivity measurements using 2.2a and 2.2b are given in Table 3.4. These values have been calculated using COMSOL by integrating the squared E-field over the cavity volume and dividing it by the average squared E-field on the axis. The calculated values have been obtained by measuring a solid rod of PTFE with a radius of 2.1 mm. The measured values are in good agreement with the simulated giving a maximum error of 6%. The measured and simulated values are very different to the analytical solutions with the main cause of this due to the sample holes creating distortions in the field distribution at regions of high field. Multiple COMSOL simulations of different hole radii are given in Fig. 3.8 where the uniform field of the TM_{010} mode (and consequently other TM_{0mp} modes) becomes distorted with increasing hole size. The hole lowers the E-field at the extremities which decreases the field the sample is exposed to and consequently decreases sensitivity; in Table 3.4 a lower G_{nmp} value means greater sensitivity due to larger shifts in fractional frequency.

Calculated and measured G_{nmp} values required for permeability measurements are given in Table 3.5. The calculated values have been obtained by measuring a solid copper rod with a radius of 1 mm. The values are in good agreement with the simulation, giving maximum discrepancies of 6% associated with minor imperfections in the cavity geometry and the coupling antennae. This demonstrates the effectiveness of the metal perturbation method for obtaining the G_{nmp} value. In comparison with the analytical solutions, the sensitivity has decreased for the TM_{110} and TE_{011} mode, however, for the higher modes, slight increases in sensitivity are noticed. This may be due to the fact that the H-field on the axis is actually spreading into the recess regions. The recess can be seen as a small section of wave guide attached to the top of the cavity with diameter that allows higher frequencies to propagate.

TABLE 3.4: G_{nmp} mode scaling factors for Cyl-ε

Mode	G_{nmp}		
	Analytical	Simulation	Measured
TM_{010}	0.2695	0.2898	$0.294 \pm 2 \times 10^{-3}$
TM_{011}	0.8776	0.9952	$0.962 \pm 6 \times 10^{-3}$
TM_{020}	0.1158	0.1247	$0.124 \pm 1 \times 10^{-3}$
TM_{021}	0.1654	0.1911	$0.183 \pm 1 \times 10^{-3}$
TM_{012}	2.7006	2.7435	$2.580 \pm 2 \times 10^{-2}$
TM_{022}	0.3140	0.3448	$0.332 \pm 2 \times 10^{-3}$

TABLE 3.5: G_{nmp} mode scaling factors for Cyl-μ

Mode	G_{nmp}		
	Analytical	Simulation	Measured
TM_{110}	0.325	0.414	$0.388 \pm 8 \times 10^{-3}$
TE_{011}	0.271	0.285	$0.285 \pm 1 \times 10^{-3}$
TE_{021}	0.108	0.105	$0.107 \pm 1 \times 10^{-3}$
TE_{012}	0.598	0.490	$0.494 \pm 3 \times 10^{-3}$
TE_{022}	0.162	0.126	$0.130 \pm 2 \times 10^{-3}$

3.4.4 SAMPLES AND PROCEDURE

For a proof of concept to show that this MCP system works, mixtures of a known magnetic material at microwave frequencies with different non-magnetic powders are measured to observe whether the magnetic property can be extracted. The weight concentrations of the magnetic material, magnetite (Fe_3O_4, Bayoxide® E8712) studied were 0, 40, 70 and 100% with silica (SiO_2), Iriotec® 9230 (I-9230) and graphite powders. The measurement procedure was conducted as given in Chapter 2. It is expected that at 0% weight concentration of Fe_3O_4, there should be no measurable complex permeability (hence a magnetic permeability of 1 and losses of 0), however, this will not be the case due to the fact that the E-field at the sample location is finite and not zero as described by the TM and TE wave equations. Any measurable response given is expected to be a perturbation in the E-field from the dielectric and conducting properties of the material. The mixtures are thus measured using the Cyl-ε dielectric measurement cavity to confirm their electrical properties.

3.4.5 Permittivity Measurements

The broadband permittivity measurements from the Cyl-ε cavity are shown in Fig. 3.10. It is clear that the varying weight concentrations (and thus volume concentrations) of SiO_2, I-9230 and graphite cause large differences in the measured permittivity. The measured results for the SiO_2 mixtures in Fig. 3.10a show that as the concentration of the magnetic powder Fe_3O_4 increases, the overall dielectric constant and losses increase over the 2 to 10 GHz range. This is simply because Fe_3O_4 has larger values of complex permittivity than SiO_2 owing to its semi-metallic nature. The conduction losses in this frequency range, however, do not show a $1/f$ dependence implying that the measured losses are not dominated by static conductivity, but some other polarisation loss or AC conductivity (more reasoning behind this phenomena is explained later in Chapter 5).

For the I-9230 mixtures given in Fig. 3.10b, the dielectric constant and losses are actually much larger than Fe_3O_4 and so the dielectric properties decrease with increasing concentration Fe_3O_4. This is simply due to the fact that I-9230 contains antimony doped tin oxide (Sb:SnO_2) which has applications as a transparent conducting oxide and therefore has a high conductivity[134]. This trait will be important in the permeability measurements as it demonstrates a clear difference in the dielectric properties. The dielectric constant and losses also decrease with increasing frequency. This characteristic is associated with a conduction mechanism (space charge polarisation owing to the decrease in both real and imaginary parts). Space charge is mainly present in mixed phases where I-9230 is a mixture of other products which cause this type of conduction. The full composition of I-9230 is not known due to the confidentiality of the substance, however, it is known that it is non-magnetic with semi-conducting Sb:SnO_2. This is all that is desired to compare insulating and conducting mixtures with Fe_3O_4.

For the graphite samples given in Fig. 3.10c, the measured dielectric constant had large variations across the samples and was immeasurable using TM_{010} and TM_{020} due to the large perturbations. The measurement was also troublesome at other frequencies owing to the extremely absorbing nature of sp^2 and amorphous carbon at microwave frequencies[82]. The absorption mechanism seems to be contributed by a static conduction loss mechanism as the losses have a decreasing trend with frequency, while the measurable dielectric constant does not change by the same magnitude. This is most likely due to

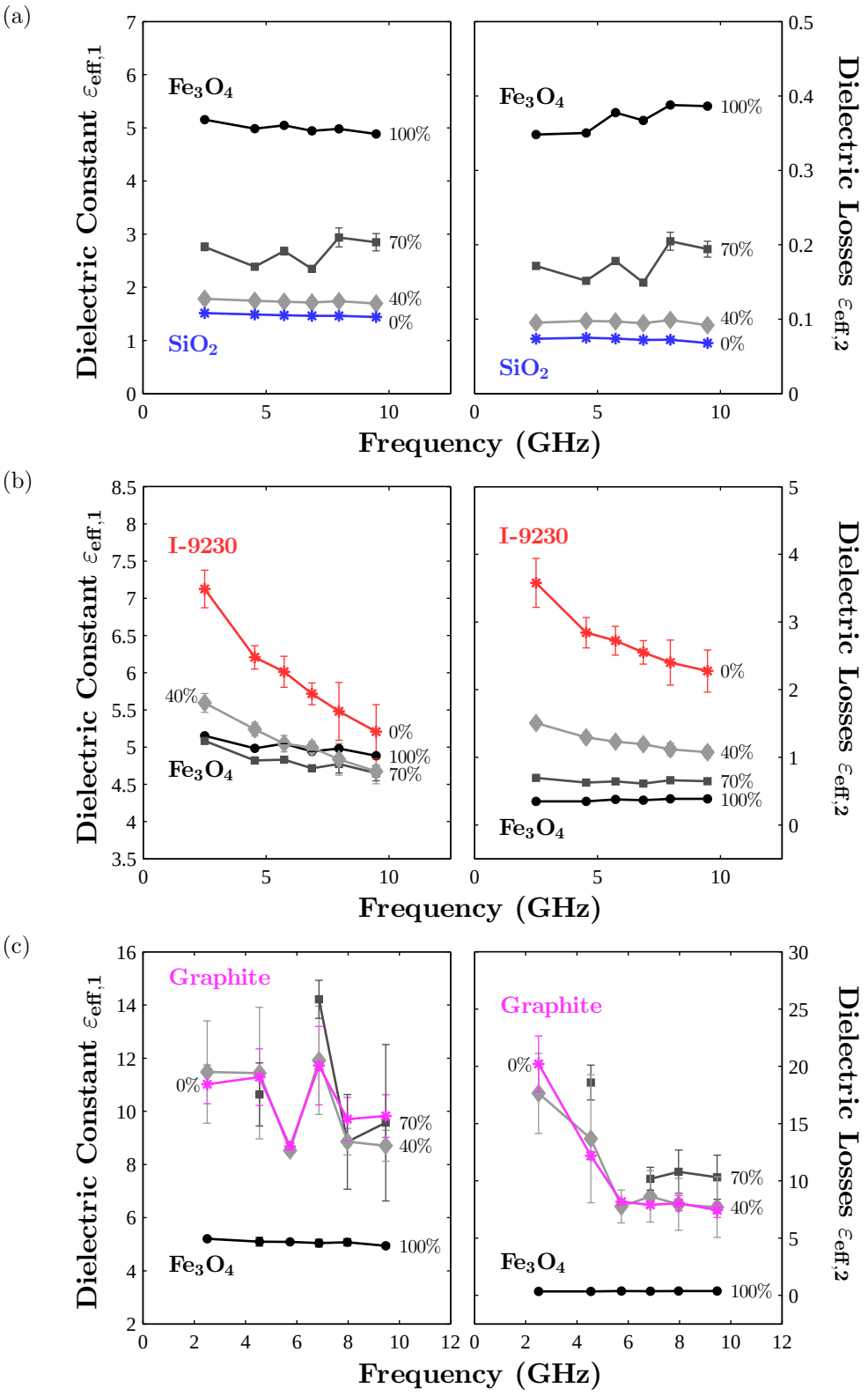

FIGURE 3.10: Measured effective complex permittivity of (a) Fe_3O_4 and SiO_2, (b) Fe_3O_4 and I-9230 and (c) Fe_3O_4 and graphite mixtures in varying weight concentrations (100% = •, 70% = ■, 40% = ♦, 0% = ∗). Error bars given show the standard deviations across different prepared samples. Notice that increasing the concentration of SiO_2 decreases the complex permittivity whereas the opposite is noticed for the I-9230 and graphite mixtures. Also, at 70% weight concentration of Fe_3O_4 and graphite, the complex permittivity could not be measured due to the large perturbation.

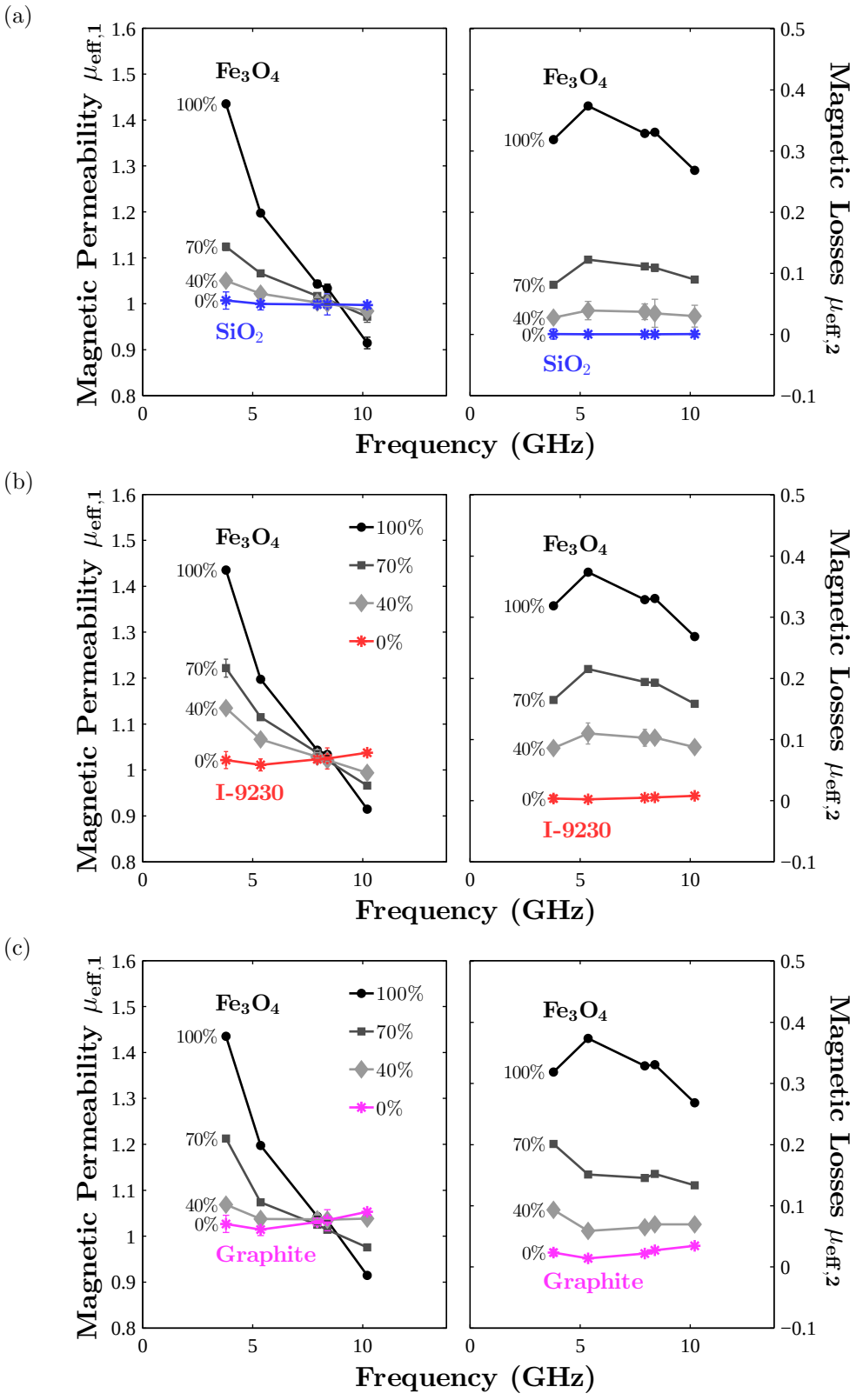

FIGURE 3.11: Measured effective complex permeability of (a) Fe_3O_4 and SiO_2, (b) Fe_3O_4 and I-9230 and (c) Fe_3O_4 and graphite mixtures in varying weight concentrations (100% = •, 70% = ■, 40% = ♦, 0% = ∗). Error bars given show the standard deviations across different prepared samples. Notice that increasing the concentration of Fe_3O_4 increases the complex permeability of all of the mixtures. Also, at 0% weight concentration of Fe_3O_4, an erroneous magnetic permeability is found for the I-9230 and graphite mixtures.

the de-localised electrons in the p orbitals of sp^2 bonded carbon which gives rise to electron conductivity along the plane of the hexagonal lattice (more reasoning behind this phenomena is explained later in Chapter 6). Nevertheless, this measurement again shows that there is a large difference in dielectric properties compared with the SiO_2 and I-9230 mixtures.

3.4.6 Permeability Measurements

For the SiO_2 results shown in Fig. 3.11a, there is a noticeable difference in the bulk magnetic permeability and losses as the concentration of Fe_3O_4 varies. With a decreasing concentration of Fe_3O_4 the measured magnetic permeability at all frequencies tends towards 1 for and the magnetic losses tend towards 0, which is consistent with a bulk material with decreasing concentrations of magnetic content. The frequency dependence of the real part for the pure Fe_3O_4 shows a decreasing trend with frequency which reaches values less than 1 at frequencies approaching 10 GHz. These features are congruent with what is found in the literature for more invasive measurement systems[7, 16, 18], and so there is high confidence that the measurement is giving a correct response, however, some attempt as to the explanation behind this 'negative' permeability has often been avoided. There are two explanations for this. It is either related to conductivity or a magnetic resonance phenomenon.

If the particles have metallic conductivity (Fe_3O_4 is known to have electron hopping conduction mechanisms, more on this explained in Chapter 5), then the particle is capable of screening the magnetic field resulting in a shape perturbation (which results in an increase in the resonant frequency, and hence a measured permeability of less than 1). In this scenario, the magnetic properties are not being probed but the conductivity. However, now consider the case where a material with a higher conductivity is measured using these modes. By this logic, the frequency should shift by at least the same magnitude as what was achieved with the Fe_3O_4 particles. As we can see in Fig. 3.11, this is not the case, since I-9230 contains Sb:SnO_2 which has a much higher conductivity than Fe_3O_4 and the response at high frequencies tends to a slightly larger value than 1. This means that the response measured is most likely due to a ferromagnetic resonance phenomena with a broad peak over the GHz range.

TABLE 3.6: COMSOL simulated percentage of E-Field for a 1 mm diameter sample on the axis of the cavity

Mode	$\bar{H}^2_{\text{cav}}/\bar{E}^2_{\text{cav}}$	Percentage of E-Field
TM_{110}	58.4	1.68%
TE_{011}	2630.1	0.04%
TE_{021}	1195.6	0.08%
TE_{012}	1088.75	0.09%
TE_{022}	739.73	0.13%

For the I-9230 mixtures shown in Fig. 3.11b, a similar decrease in the measured magnetic permeability and losses is noticed implying that the TE modes are able to solely measure the magnetic property of the mixture. Slightly different values are measured at the same weight concentration of Fe_3O_4, but this is simply because of the difference in density between SiO_2 and the I-9230 particles. Also, the packing density of the dielectric materials may have a difference in air gaps. The results can be normalised to the same effective packing density by weighing the samples and dividing this by its per unit volume, but for the purposes of this measurement, all that is required is a varying concentration of magnetic material inside different mixtures with dielectrics such that magnetism can be extracted. Hence, the I-9230 results show a similar trend as for the SiO_2 samples, in that with increasing concentration of magnetic materials, the complex permeability increases.

For the graphite mixtures shown in Fig. 3.11c, the response is very similar to those shown in Fig. 3.11a and 3.11b again showing that these modes are capable of extracting magnetic properties from mixtures. However, notice that at 0% weight concentration, the frequency and bandwidth appear to have shifted resulting in an erroneous measurable magnetic permeability for both M-230 and graphite. This is incorrect since both of these materials consist of non-magnetic components, thus a limitation has been identified for this system in the measurement of very high dielectric loss and conducting materials. This is mainly due to the radius of the sample perturbing the E-field as explained previously. TE_{0mp} modes are less affected, which can be explained by considering the volume ratio of $\bar{H}^2_{\text{cav}}$ to $\bar{E}^2_{\text{cav}}$ at the sample location. The volume integrals of the squared E and H fields were calculated in COMSOL and are given in Table 3.6. This shows that the sample has a greater exposure to the E-field of the TM_{110} mode in comparison to the TE_{0mp} modes. As p increases, the sample perturbation into the E-Field also increases marginally which is congruent with the results for the pure I-9230 and graphite samples.

The reason the TM_{110} mode is more susceptible to E-Field perturbation is just because the stored E-field energy at the sample location is larger. In any case, the measurement of a highly conducting material identifies a measurement limit of approximately 1.05 for permeability and 0.01 for losses for the demagnetising TM_{1m0} mode and a smaller error of approximately 0.005 for both permeability and losses measured using the TE_{0mp} modes.

3.5 Conclusions

This chapter details the principles and design of the dielectric (Cyl-ε) and magnetic (Cyl-μ) MCP systems that are primarily used in this thesis. The requirement of these systems is to provide the complex permittivity and permeability at microwave frequencies (2 to 10 GHz). This has been achieved using multiple TM_{0mp} modes for permittivity measurements and multiple TE_{0mp} modes (with an extra TM_{110} mode) for permeability. This study concludes that it is possible to provide a partial spectrum of complex permittivity and permeability, however, when working with mixtures of different densities, this must be taken into account if comparisons need be drawn across different sample mixtures for a *specific* volume concentration of the magnetic component. For this study it is not required and only a varying quantity within different concentrations of other dielectrics is required.

The extremely variant dielectric properties of the SiO_2, Iriotec® 9230 and graphite powders proved to have minimal influence on the measured magnetic response with discrepancies caused by marginal E-field perturbations. The TM_{110} mode is, however, more sensitive to E-Field perturbations for 1 mm diameter samples and therefore care must be taken for samples with larger radii if the dielectric contribution is significant. To determine accuracy of the Cyl-μ magnetic measurements, complementary dielectric measurements with Cyl-ε should be performed, especially if graphitic carbon samples are used.

The significance of this experimental result for applications demonstrates that extraction of the magnetic properties of the materials at microwave frequencies is possible, and very simple. For the investigation of new magnetic materials for microwave EMI, this would mean that material scientists can simply synthesise a magnetic oxide, fill it into a tube and place it into the cavity to determine its efficacy.

CHAPTER 4

Methodology: Microwave Cavity for Temperature Dependent Properties

The General Problem - Characterisation

The powders used for microwave absorption may be used at varying temperatures for example in EMI absorbers on devices which may get warm or in hyperthermia as particles get irradiated. The magnetic and dielectric properties need to be sensitively **characterised as a function of temperature** to ensure that their performance is not affected.

The Approach

An MCP system has been developed to measure the temperature dependent dielectric permittivity and magnetic permeability at microwave frequencies. This uses the same systems as previously, however, a nodal cylindrical mode approach has been used to correct for systematic errors as temperature changes. Empty and quartz ramps are conducted to demonstrate the procedure.

Key Findings

The TM_{310} and TE_{311} modes are highlighted as effective nodal modes to provide correction of systematic errors caused by small temperature fluctuations in the cavity. The quartz tube holders have minimal temperature dependence and thus minimal impact on sample measurements.

4.1 Measuring temperature dependent dielectric and magnetic properties

In Chapter 3 we have looked at using the MCP techniques to characterise different *static* material properties and have demonstrated its sensitivity to insulating and conducting samples. This technique, however, can be extended to measure the *temperature dependent* dielectric and magnetic properties in-situ by simply changing the conditions of the sample; examples include varying the temperature or pressure of the atmosphere inside of the cavity. This has been investigated in-situ using a 100W system by applying microwave heating whilst also measuring the frequency response of the cavity to obtain dielectric properties[135]. Laser heating of a sample inside a rectangular microwave cavity has also been investigated with procedures to correct for temperature using other rectangular modes[136]. Furthermore, the measurement of gases under varying pressure using a cylindrical cavity resonator has been investigated[137].

The cavity method, however, is very sensitive to changes in temperature. Complex permittivity and permeability are temperature dependent properties which consequently shift the complex frequency of a resonator when a sample is inside a region of microwave field. The resonance can also be affected by the environment due to the natural thermal expansion of the cavity metal (given that the unperturbed resonant frequency and bandwidth are functions of the cavity geometry). Thus, when temperature becomes a dependent variable, intrinsic material properties need to be decoupled from system fluctuations. Attempts have been made to correct for temperature by realising that the empty cavity is a function of temperature and thus subtracting the linear thermal coefficients from the data achieves correction[138, 139]. Attempts have also been made to monitor other modes of the cavity resonator to offset any ambient fluctuations; Pohl et al. for example used rectangular modes where the E-Field is zero and Ewing et al. used the cylindrical TM_{011} and TM_{110} modes to correct for ambient changes while measuring the dielectric properties of gases.

4.2 A Novel Approach: Using Nodal modes for Temperature Correction

In this study, temperature correction is achieved by in-situ monitoring of modes where the sample provides minimal perturbation in *both* the E and H-field of the standing wave by exploiting modes with radial variation based on higher order Bessel functions. This idea was identified at the end of the thesis by a previous PhD student at Cardiff University, though experiments had not been conducted yet[140]. This technique is in contrast to previous studies since rectangular modes are dependent upon sinusoids and the TM_{011} and TM_{110} modes have, respectively, finite E-field and H-field on the axis of the resonator. For the measurement of magnetic materials, TM_{110} cannot be used for correction. A cylindrical cavity becomes advantageous in measuring temperature dependent properties of axial samples because with increasing mode number (and thus Bessel function order), the field maxima tend towards the edges of the cavity. The higher the mode, the less sensitive the mode is to the sample. With these modes unaffected by the sample, they can thus be used to correct systematic fluctuations. This is also different to the mentioned studies which use dielectric resonators, where nodal modes are not possible since the sample may be the resonator or perturb a larger portion of it[138, 139]. Three cylindrical cavity resonators have been used to demonstrate multi-mode correction. The Cyl-ε and Cyl-μ cavities mentioned in Chapter 3 have been used as well as a copper cavity similar to Cyl-ε, further referred to as Cyl-Cu.

Given that the cavity perturbation method already offers such high sensitivity and minimal sample requirements, the aim of this study is to demonstrate the measurement of temperature dependent properties in-situ, in a temperature varying environment. A number of challenges exist with this approach as it is clear that even though the cavity is mechanically sturdy, it is prone to the effects of thermal stress and temperature dependent electrical conductivity; as well as changes in antenna geometry and coupling symmetry. These systematic errors will offset the sample resonant frequency measurements. Some of these effects can be monitored by looking also at S_{11} reflection measurements but there is no way to clearly decouple the thermal expansion effects by only looking at one mode.

4.3 Analysis

4.3.1 Temperature Dependence of Frequency

In a static permittivity measurement we assume the cavity to have a fixed volume, though in the event where the sample is changing temperature and potentially radiating heat, the resultant convection will inevitably create a temperature increase at the cavity walls. This process depends upon the temperature of the sample, the thermal properties of the cavity medium and the thermal properties of the conducting walls of the cavity.

We can further examine the effect of temperature on the cavity by looking at the wave dispersion relation of a cylindrical cavity resonator derived previously. For TM modes, if we include a temperature dependence on the geometrical dimensions 2.17 becomes:

$$f_0(T) = \frac{c}{2\pi}\sqrt{\left(\frac{\alpha_{nm}}{a(T)}\right)^2 + \left(\frac{p\pi}{l(T)}\right)^2} \tag{4.1}$$

where $a(T)$ and $l(T)$ are the temperature dependent radius and height of the cavity respectively. In this instance we assume an air filled cavity and therefore any temperature dependence of the medium is negated, hence the phase velocity is simply the speed of light c. The change in the cavity dimensions due to a temperature increase (ΔT) can be described by a linear thermal expansion approximation:

$$a(T) \approx a(1 + \alpha_c \Delta T) \tag{4.2a}$$

$$l(T) \approx l(1 + \alpha_c \Delta T) \tag{4.2b}$$

where a and l are the initial dimension lengths and α_c is the linear thermal expansion coefficient of the cavity material. Using first order partial derivatives, the change in resonant frequency due to an increased temperature can be given by:

$$\frac{\partial f}{\partial T} \approx \frac{\partial f}{\partial a}\frac{\partial a(T)}{\partial T} + \frac{\partial f}{\partial l}\frac{\partial l(T)}{\partial T} \approx \alpha_c\left(\frac{\partial f}{\partial l}l + \frac{\partial f}{\partial a}a\right) \tag{4.3}$$

Evaluating each partial derivative and taking discrete measurements of frequency and temperature we find that:

$$\frac{\Delta f}{f_0} \approx -\frac{\alpha_c}{f_0^2}\left(\frac{c}{2\pi}\right)^2\left(\left[\frac{\rho_{nm}}{a}\right]^2+\left[\frac{p\pi}{l}\right]^2\right) \approx -\alpha_c \Delta T \tag{4.4}$$

This shows that the fractional increase in frequency is just the linear thermal expansion coefficient of the cavity material. Therefore, any change in temperature that the cavity experiences results in a change in frequency with slope equal to $-\alpha_c f_0$. Correction of TM_{010} measurements simply involves removing this slope.

4.3.2 Temperature Dependent Bandwidth

Next, a derivation of an expression for the temperature dependent bandwidth for TM modes using 2.24 is given. Identifying the components which have a dependence on temperature yields:

$$BW_{0,\mathrm{TM}}(T) = \begin{cases} \sqrt{\dfrac{\rho(T)f(T)}{\mu_0\pi}}\left(\dfrac{1}{a(T)}+\dfrac{1}{l(T)}\right) & , \quad p=0 \\ \sqrt{\dfrac{\rho(T)f(T)}{\mu_0\pi}}\left(\dfrac{1}{a(T)}+\dfrac{2}{l(T)}\right) & , \quad p\geq 1 \end{cases} \tag{4.5}$$

Using the same approach as the temperature dependent frequency derivation:

$$\frac{\partial BW}{\partial T} \approx \frac{\partial BW}{\partial a}\frac{\partial a}{\partial T}+\frac{\partial BW}{\partial l}\frac{\partial l}{\partial T}+\frac{\partial BW}{\partial f}\frac{\partial f}{\partial T}+\frac{\partial BW}{\partial \rho}\frac{\partial \rho}{\partial T} \tag{4.6}$$

The partial derivatives give the following equation dependent upon geometrical expansion and resistivity:

$$\frac{\Delta BW}{BW_0} \approx \frac{1}{2}\left(\beta_c - 3\alpha_c\right)\Delta T \approx \frac{\beta_c}{2}\Delta T \tag{4.7}$$

where β_c is the linear coefficient of resistivity. Thus, as temperature increases, the theoretical unloaded bandwidth of the TM modes linearly increases due to resistivity and decreases due to geometrical expansion. Typically for metals, the coefficient of resistivity is 3 orders of magnitude greater than the thermal expansion coefficient hence the contribution from α_c is assumed negligible. For the temperature dependent bandwidth of TE modes this is convenient, since 2.34 is far more complicated in deriving a partial derivative over temperature. This equation, however, does not take into account effects due to

coupling strength into the resonator and its symmetry. The coupling strengths are also complicated functions of temperature since the geometry of the antennas will expand and change resistance. These effects may be negated when unloaded bandwidth is extracted using P_0. However, for loop coupling, the expansion of the loop and the physical connection to the cavity may have a much larger role. In the following experiments modified loop antennas are used for TE modes, such that these effects can be negated, while still providing coupling. The disadvantage of this, however, is that TE_{021} and TE_{022} are now no longer coupled.

4.3.3 Nodal Modes

The change in resonant frequency of all of the modes is linked through thermal expansion and the change in bandwidth to both thermal expansion and resistivity through 4.4 and 4.7, all resonant frequencies of the cavity will drift up and down with temperature by the same fractional amount. Hence, we cannot simply measure a quartz tube at room temperature and then perform a sample measurement at another temperature. Correction for temperature is simply achieved through subtraction of the fractional frequency shift of another mode from the measurement mode. This can be done using a mode with minimal sample perturbation or a 'nodal mode'. There are numerous modes which have a node in the centre. This can be realised by recalling that all E and H field components in

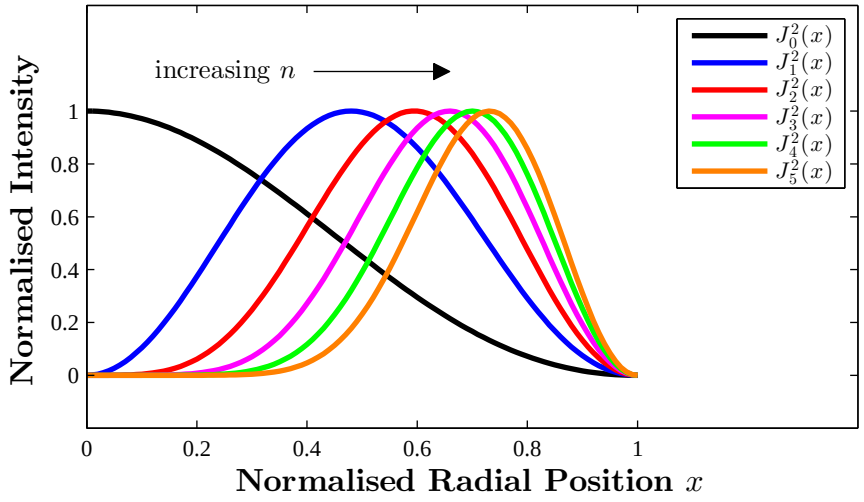

Figure 4.1: Normalised radial field components of modes with increasing Bessel function order. With increasing n, the field maxima tends away from the axis of the resonator. Higher order Bessel function modes are, therefore, less sensitive to the sample.

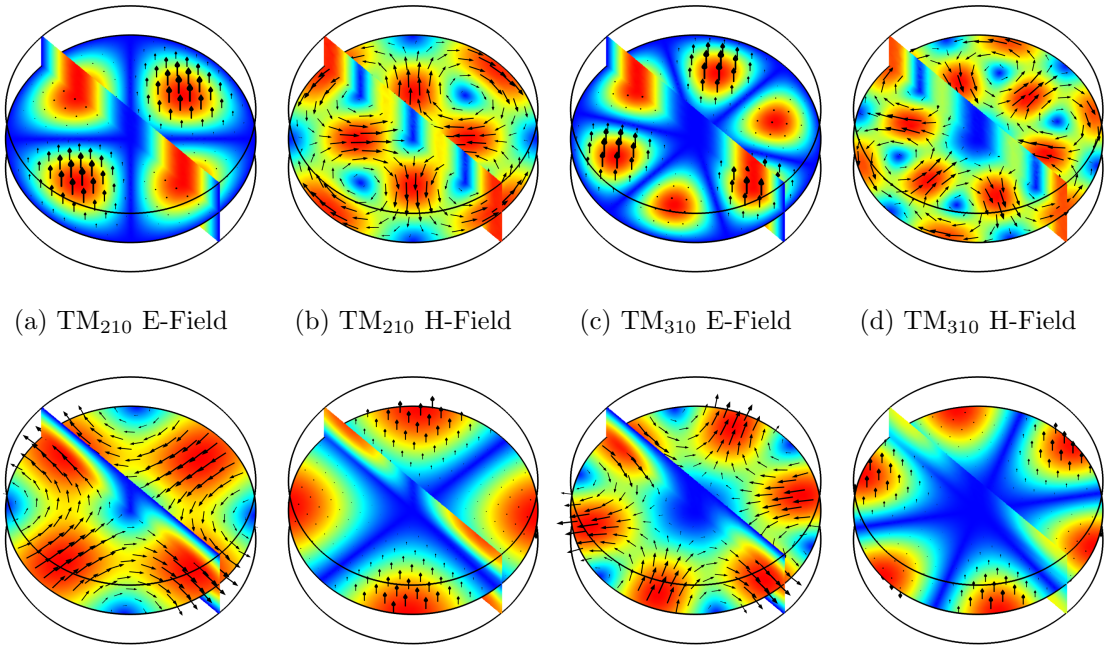

(a) TM_{210} E-Field (b) TM_{210} H-Field (c) TM_{310} E-Field (d) TM_{310} H-Field

(e) TE_{211} E-Field (f) TE_{211} H-Field (g) TE_{311} E-Field (h) TE_{311} H-Field

FIGURE 4.2: Field distributions of the E and H fields of potential nodal modes. Notice that at the sample location in the centre of the cavity, the net E and H field is zero in both. Also, the node spot gets larger with increasing n.

cylindrical modes are dependent on n^{th} order Bessel functions of the first kind (shown in Fig. 4.1) as given in 2.18a, 2.18b, 2.29a and 2.29b in Chapter 2. Hence any mode where n is non-zero will yield a possible nodal measurement mode. Examples of these modes are shown in Fig. 4.2. As n increases, the central node spot gets wider and is therefore less sensitive to the sample. This aspect is available to cylindrical cavities and not rectangular ones (since they are sinusoidally dependent), giving cylindrical cavities a distinct advantage over rectangular ones. Although, as mode number increases, interference from other modes starts to become considerable.

These nodal modes depend upon whether the current cavity coupling antennas excite them. If the coupling antennas are located on the side of the cavity (i.e. coaxial loop antennas for magnetic field coupling to TM_{010}) then this configuration will most certainly excite the nodal modes since the maxima tend towards the edges of the cavity. It is, however, much easier to achieve symmetrical coupling using open circuit coaxial probes on the top and bottom plates of the cavity. This coupling style will not excite TE nodal modes and will only excite lower order nodal TM modes. The first two nodal modes of the antenna

coupled cavity are the TM_{210} and TM_{310} modes. For the loop coupled cavity, the first two nodal modes are the TE_{211} and TE_{311} modes, shown in Fig. 4.2.

4.3.4 Method for Applying Correction

Let us first consider what the change in frequency is actually showing us. The contributions to frequency shift are from the sample and the cavity:

$$\frac{\Delta f_{011}}{f_{011}}(T) \approx \frac{\Delta f_{011,\mathrm{s}}}{f_{011,\mathrm{s}}}(T) + \frac{\Delta f_{011,\mathrm{c}}}{f_{011,\mathrm{c}}}(T) \tag{4.8}$$

where s and c denote the sample and cavity contributions respectively. So it makes sense that we can perform a quartz tube ramp and a sample ramp and then subtract the two from one another through linear interpolation at each temperature. The disadvantage of this, however, is that we assume that $\frac{\Delta f_{011,\mathrm{c}}}{f_{011,\mathrm{c}}}$ is the same each time, and that the cavity has the exact same temperature profile each time it is heated. For a sturdy aluminium block, it is a reasonable assumption, however, if the changes in the sample as a function of temperature are very small (of the order of any minute creaking or expanding of the cavity which differs each time), this may lead to erroneous measurements. The way to avoid this is to realise that the fractional shifts in frequency are all linked with slightly different slopes but linked linearly through geometry and resistivity. Thus, by using a nodal mode to subtract another fractional shift, we obtain:

$$\frac{\Delta f_{011}}{f_{011}}(T) \approx \frac{\Delta f_{011,\mathrm{s}}}{f_{011,\mathrm{s}}}(T) + \frac{\Delta f_{011,\mathrm{c}}}{f_{011,\mathrm{c}}}(T) - \frac{\Delta f_{211,\mathrm{c}}}{f_{211,\mathrm{c}}}(T) \approx \frac{\Delta f_{011,\mathrm{s}}}{f_{011,\mathrm{s}}}(T) + \kappa_{011-211}(T) \tag{4.9}$$

where κ is the difference in slopes between the nodal and the measurement modes. Now, when we do the interpolation of the quartz and sample ramps, the minute effects between each temperature ramping experiment can be accounted for.

4.4 Experiments

4.4.1 Aims and Objectives

The aim of this experiment is to show that the temperature dependent properties of microwave magnetic and dielectric materials can be measured in-situ using the microwave cavity perturbation technique. First, system experiments were conducted with Cyl-ε and Cyl-μ as well as an additional copper cavity. The copper cavity was only included to demonstrate the measurements of the thermal expansion and resistivity coefficients for different materials. This cavity has a radius of 33 mm and a height of 15 mm. The first experiment is the rod perturbation which determines the sensitivity of certain modes. The second experiment is the drift experiment which demonstrates how the resonant frequencies of these cavities are linked through geometry via minute drifts in room temperature. The final experiments are the quartz ramp experiments to demonstrate that the containers have minimal effect on the measurement modes.

4.4.2 Node Perturbation

First, to test the effectiveness of the nodal modes a copper rod with a diameter of 3 mm was placed at the sample location of the aluminium cavities. The change in resonant frequencies of the two cavities are given in Table 4.1. For the TM cavity, this perturbation essentially destroys the resonance of the TM_{010} mode as the maximum field in the centre of the cavity is forced to zero. The field distribution is also vastly altered since an E-field cannot exist parallel to a metal interface. For the TE cavity, the field in the TE_{011} mode is forced to zero but the distribution is not grossly affected. In this case, the perturbation actually represents a material with permeability high enough to screen the field, thus the resulting

Table 4.1: Fractional frequency shifts of nodal modes in Al cavities.

Mode	$\Delta f/f_0$	$\Delta BW/BW_0$
TM_{210}	-5.2×10^{-5} $\pm1\times10^{-6}$	1×10^{-3} $\pm2\times10^{-3}$
TM_{310}	-4×10^{-7} $\pm2\times10^{-7}$	3×10^{-3} $\pm2\times10^{-3}$
TE_{211}	9.8×10^{-6} $\pm4\times10^{-7}$	-1×10^{-3} $\pm3\times10^{-4}$
TE_{311}	4×10^{-7} $\pm3\times10^{-7}$	-2×10^{-3} $\pm2\times10^{-3}$

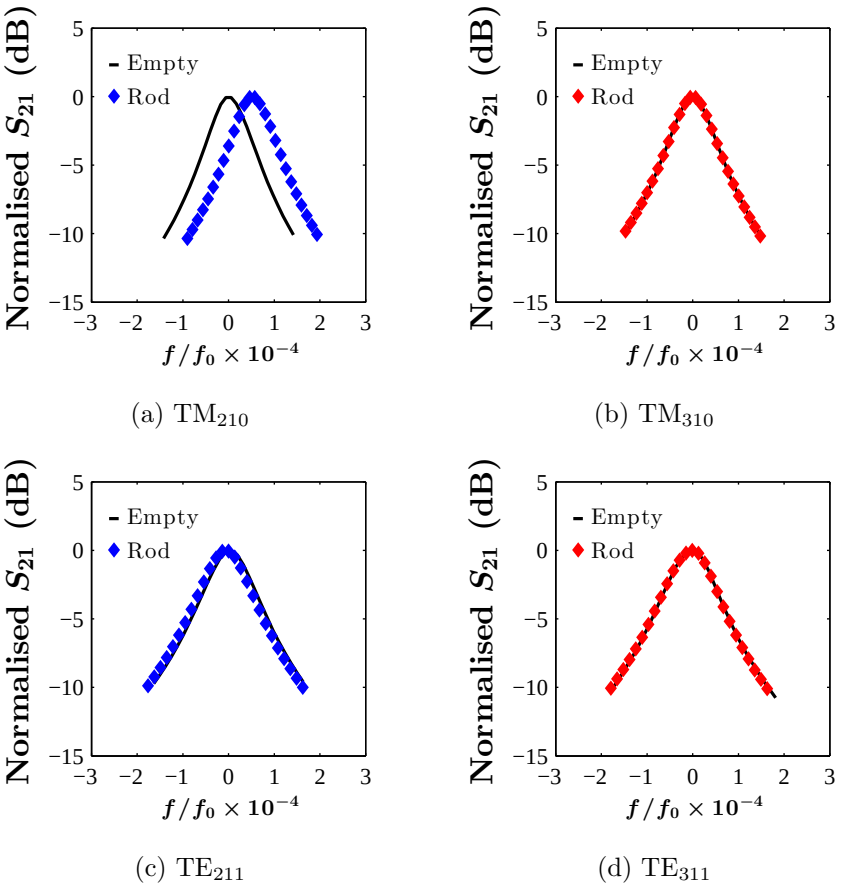

(a) TM_{210} (b) TM_{310}

(c) TE_{211} (d) TE_{311}

FIGURE 4.3: Normalised power transmission traces against fractional frequency of nodal modes with and without the copper rod perturbation ($a_{\text{rod}} = 3$ mm). As anticipated, the modes for higher values of n are less sensitive to the metal rod at the sample location.

change in resonant frequency due to the rod represents the maximum perturbation possible in this mode. The effect on the nodal modes, however, should be minimal.

The results show that TM_{210} is partially perturbed although this is only a maximum fractional shift of -5.2×10^{-5}. This shift is also upwards, implying that the H-field is perturbed, which is expected due to Fig 4.2. The change, however, in TM_{310} is much less affected by the sample at only an upward fractional shift of 4×10^{-7}, making it a much better mode for correction of TM_{010}. The TE_{211} and TE_{311} modes yield downward shifts of 9.8×10^{-6} and 4×10^{-7} respectively. This implies a slight perturbation into the electric field. Again, the higher mode has a much smaller shift hence showing how the resonant frequencies of these modes are very insensitive to the sample location. The fractional changes in bandwidth are more sensitive to the sample though with errors still much less than 1%.

Hence, this experiment shows that even if the sample has very high conductivity (and therefore will produce a large perturbation in the sample location), these nodal modes are insensitive to the sample location.

4.4.3 Ambient Temperature Drift

The Cyl-Cu, Cyl-μ and Cyl-ε (not shown) were measured over periods of 4 hours on separate occasions in the laboratory to look at the effects of the ambient temperature on all modes that the cavity could excite from 3 to 10 GHz. The results show that for a given cavity, all modes drift with the same fractional frequency shift with temperature. This

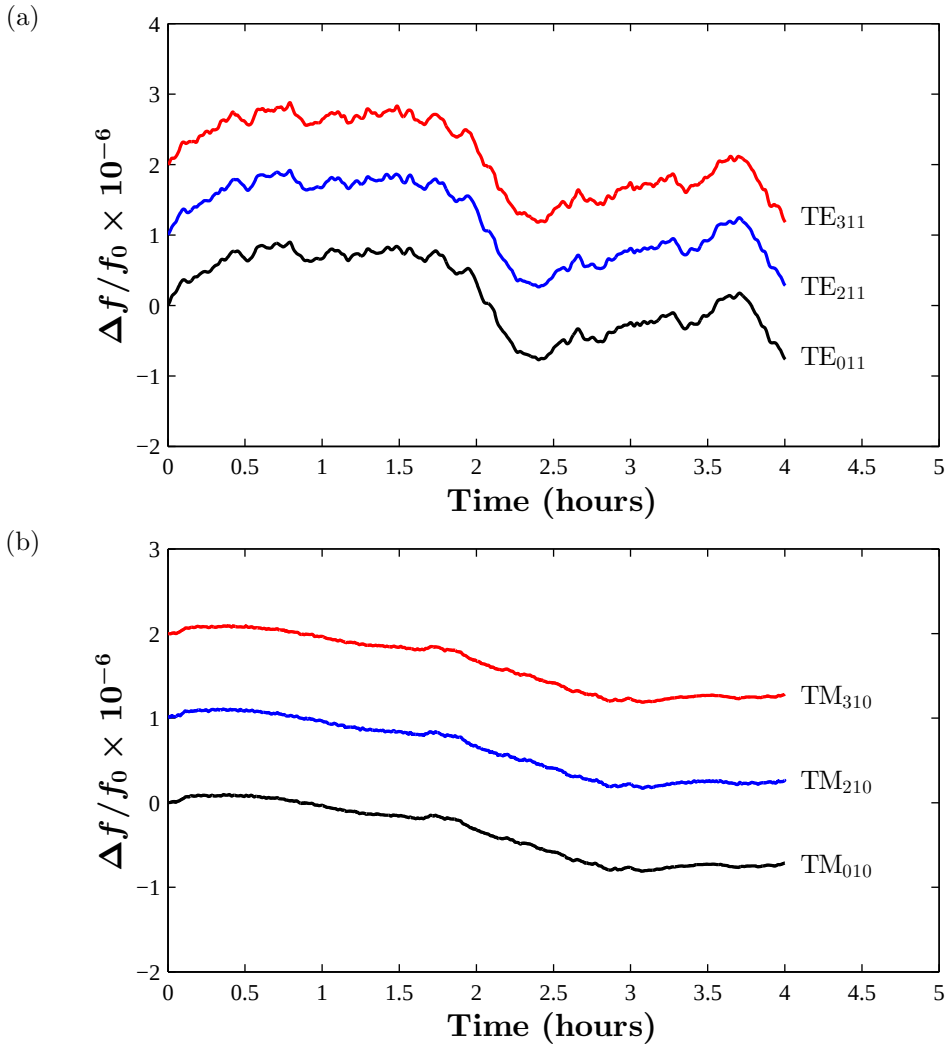

Figure 4.4: Fractional frequency shifts of cavities in the laboratory for 4 hours of Cyl-μ 4.4a and Cyl-Cu 4.4b. Traces have been separated by 1×10^{-6} for visibility. Notice that all of the modes drift up and down with the minute changes in temperature of the laboratory.

means that even for room temperature measurements, fluctuations in the conditions can be detected and accounted for. This also demonstrates how a cavity resonator is a very good temperature sensor, though much larger than commercial RTD devices. The bandwidth drift was below the noise floor of the measurements and yielded a stable response (not shown). This is because the sensitivity is much less as the fractional variations are with respect to kHz as opposed to GHz (making the cavity suitable for measuring ambient temperature resolutions of 1 ppm). The temperature differences are also very small and thus the resistivity of the inner cavity walls will not change by much. This experiment demonstrates the sensitivity of the frequency measurement and that all of the resonant frequencies are inherently linked through geometrical expansion as described in 4.4.

4.4.4 Empty Temperature Ramp

Each of the cavities was placed inside a varying temperature environment. Temperature ramps were achieved by placing the cavity inside of a Memmert UF30 laboratory oven with a hole for temperature sensors and the 3.5 mm coaxial cables provided by Huber and Suhner. The resonant frequency and bandwidth was recorded using the set-up described in Chapter 2. Temperature was measured using PT100 RTDs provided by Omega interfaced to a National Instruments C-DAQ. These were placed on the cavity metal to monitor the temperature. A temperature ramp profile of 30-80 °C at 1 °C per minute was used. Stepped ramps were also performed by leaving the cavity at set temperatures for at least 1 hour. The ramp results presented here correlated with the stepped results.

Table 4.2: Calculated thermal expansion coefficients from each cavity mode.

Mode	**Cavity Material**	**Frequency (GHz)**	$\boldsymbol{\alpha_c}$ **($\times 10^{-6}$m/°C)**
TM_{010}	Al	2.49	19.3
TM_{210}	Al	5.33	21.3
TM_{310}	Al	6.61	21.6
TM_{010}	Cu	3.49	16.2
TM_{210}	Cu	7.45	15.6
TM_{310}	Cu	9.26	16.4
TE_{011}	Al	5.36	22.5
TE_{211}	Al	4.83	22.6
TE_{311}	Al	5.64	22.7

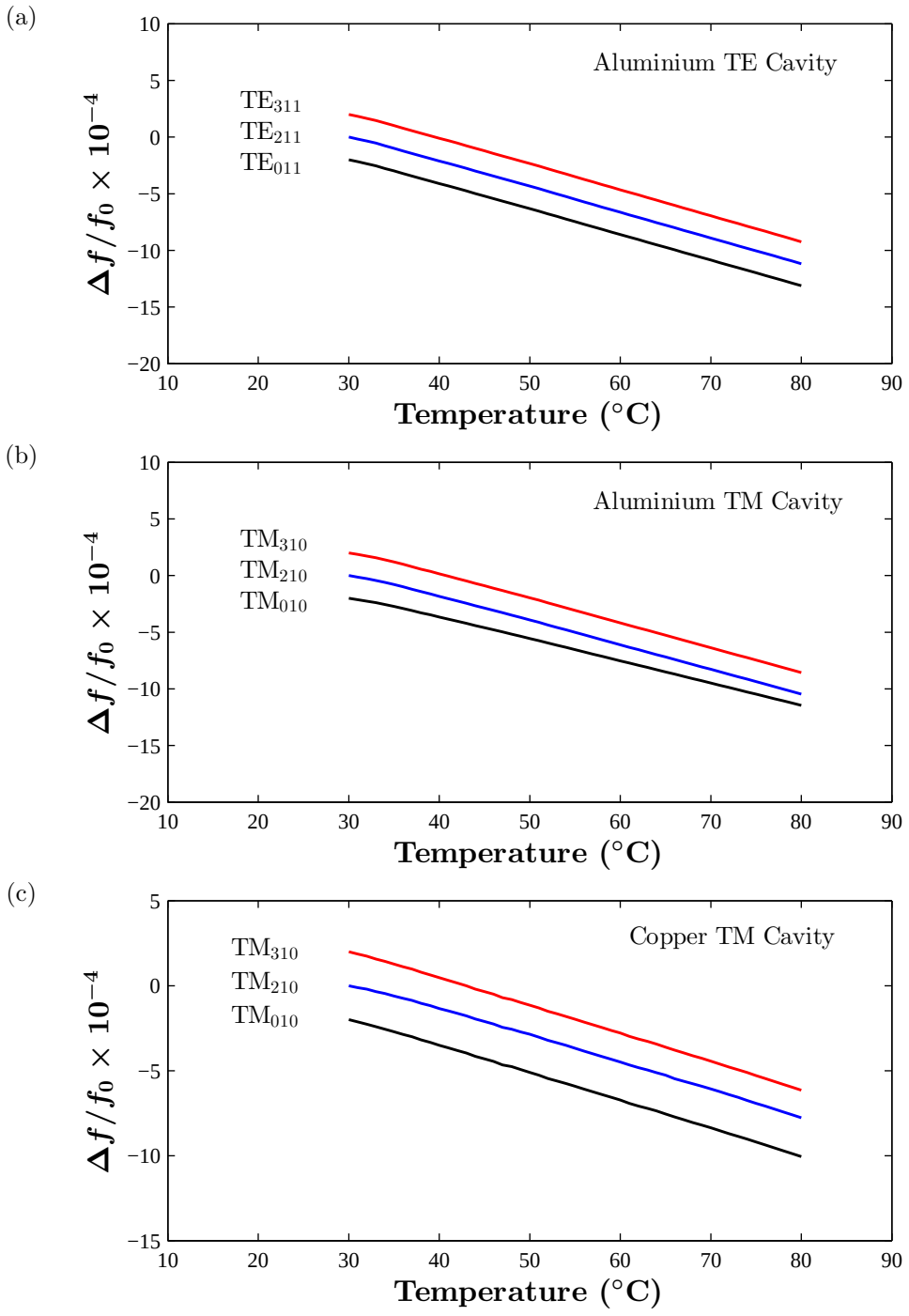

FIGURE 4.5: Fractional frequency shifts of the cavities as a function of temperature. Traces have been separated by 2×10^{-4} for visibility. All modes have a linear temperature dependence though there are minute differences in their slopes. This means that for correction purposes, this difference must also be taken into account.

Table 4.2 shows the results of the temperature ramping experiments. The gradients show approximate values for the linear thermal expansion coefficients of their respective materials as expected from (5). The TM_{010} mode of the Al TM cavity has a slightly smaller than

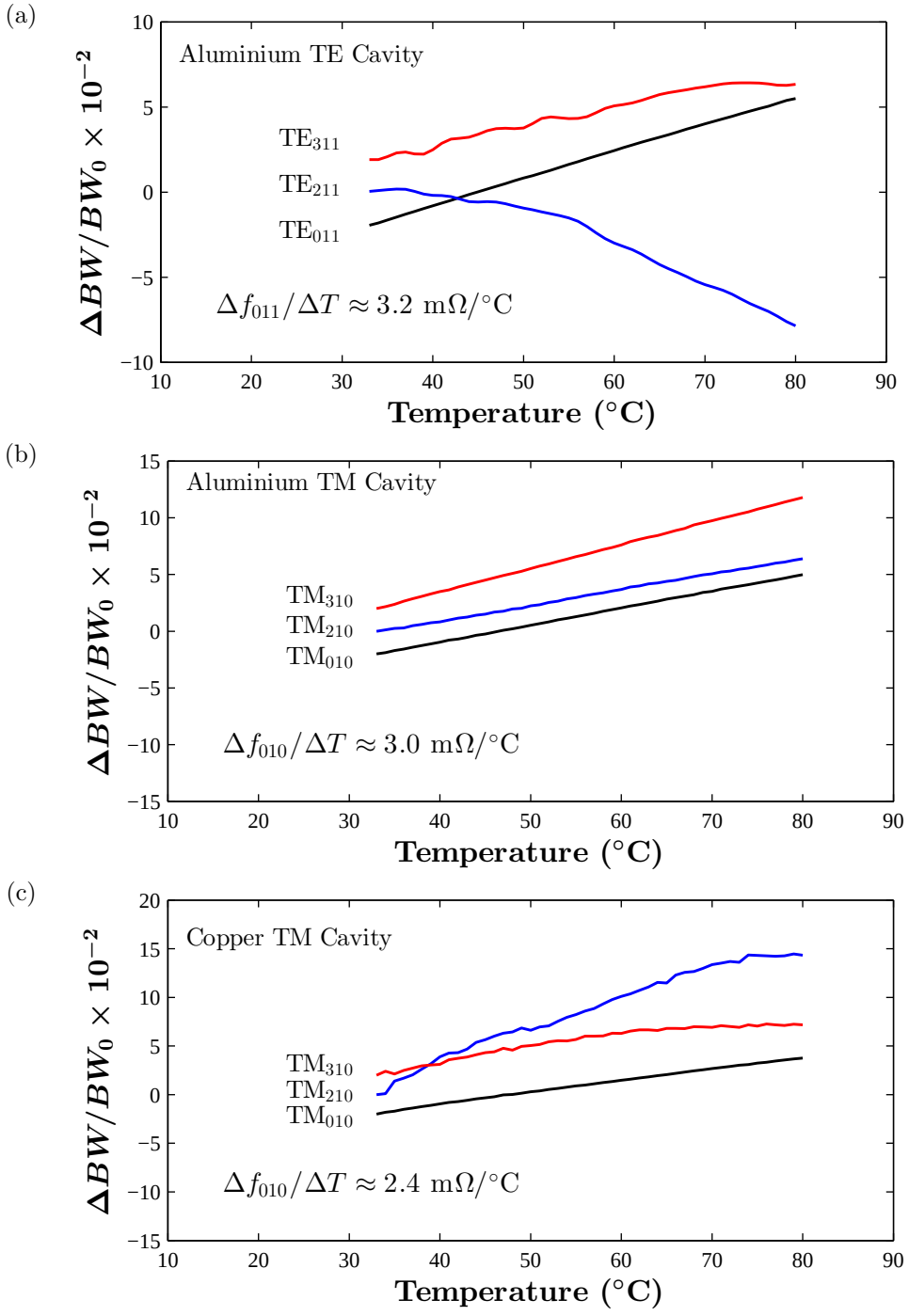

FIGURE 4.6: Fractional bandwidth shifts of the cavities as a function of temperature. Traces have been separated by 2×10^{-2} for visibility. The sample measurement mode has a linear temperature dependence though the nodal modes have much more variation as compared to the frequency measurements, emphasising that differences between the modes must be taken into account for any correction procedures using these modes.

expected of approximately 19.3×10^{-6}m/ °C, though a relationship between this slope and those of the nodal modes can be established to cancel this offset. The TM_{210} and TM_{310} modes yield gradients much closer to typical values. There is also a discrepancy in

the Cyl-Cu cavity measurements where the gradient of TM_{210} is much smaller than the others. This is most likely due to this mode having a slightly skewed resonance as a result of a third port hole on this cavity. This offset can be calibrated out and does not affect the general conclusions of this work. Interestingly, the Al Cyl-μ cavity has minimal difference amongst all of the modes. This may be due to the simpler two piece design of the cavity as opposed to the three piece design of the Al Cyl-ε cavity which also has rounded edges. This experiment demonstrates the linear relationship between frequency and temperature and also the measurement of thermal expansion of different cavity materials. It also shows that the different modes yield marginally different slopes for the thermal expansion coefficient, hence just conducting a sample ramp (without conducting the tube ramp) will yield an offset error dependent upon the difference of the slopes.

The effects of the different modes are most profound in the bandwidth measurements shown in Fig. 4.6. The reason for the large variance in the temperature dependent behaviour is due to the effects of the temperature dependent coupling. The geometry of the coupling antennas play a large role in the coupling strength of the resonator (and thus the bandwidth). Interestingly, the probe coupled Cyl-ε cavity has the least variance amongst the modes with temperature. This may be due to the simple design of coaxial probes as opposed to loop antennas where their coupling strength is dependent upon the area of the loop and the electrical contact to the outer walls of the cavity.

Nevertheless, this experiment demonstrates that there is a large difference in the temperature dependent bandwidth amongst the modes, however, this relationship is *constant* amongst the modes and is repeatable on multiple ramps. Therefore, it is important to first measure a quartz tube ramp as well as the sample ramp to decouple the effects of both temperature and the systematic error from the coupling.

4.4.5 Sample Holder Ramps

Next sample container ramps were conducted using Cyl-ε and Cyl-μ. The containers used were the fused quartz tubes used for some of the static measurements (outer diameter = 2.4 mm, inner diameter = 2 mm). The tube was placed in the sample location and the ramp was performed with the same settings used in the previous experiments. The difference between the uncorrected and corrected TM measurements is simply the thermal expansion

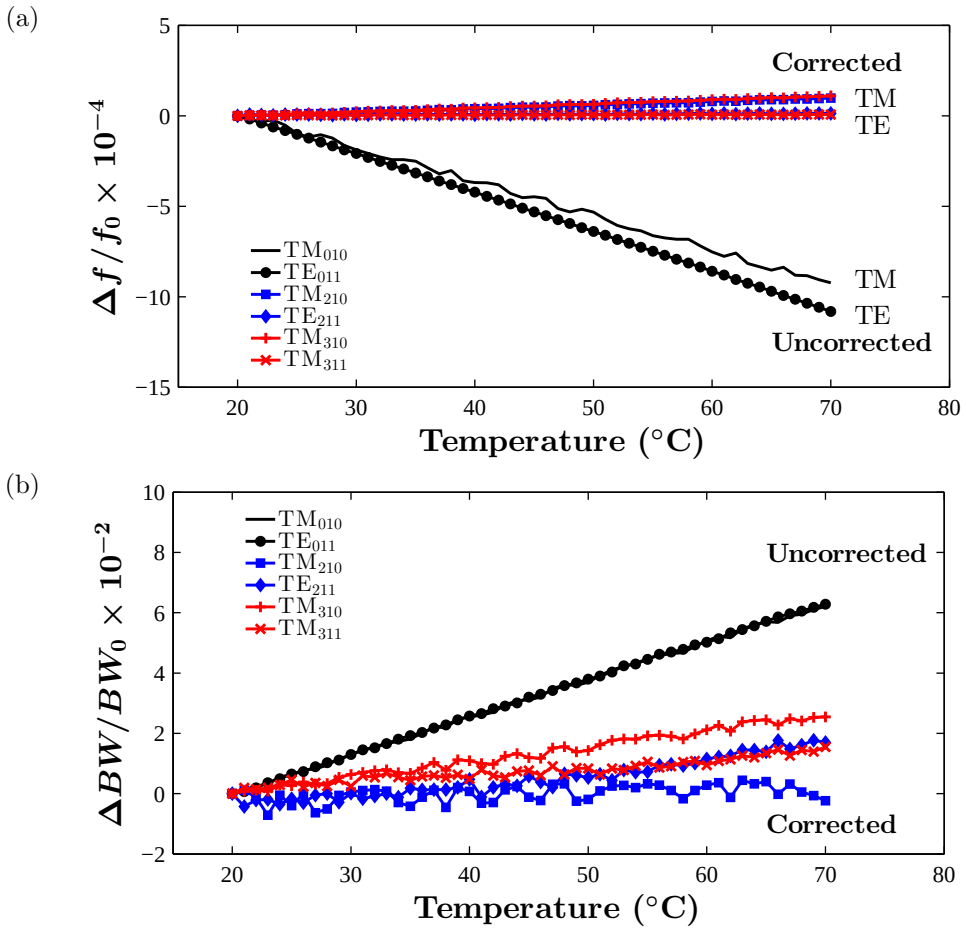

FIGURE 4.7: Measured temperature dependent properties of quartz tubes from 20 to 70 °C. The black lines show uncorrected measurements. The coloured lines show the corrected temperature dependent responses using the nodal modes.

coefficient of the cavity. Notice that after correction, the response in the TE mode is essentially a flat line, however, there is still a slight increase in the TM_{010} measurement. The corrected TM_{010} slopes given in Fig. 4.7 are approximately 2.1×10^{-6} m/ °C which are consistent with the gradient offsets between TM_{010} and the nodal TM_{n10} modes given in Table 4.2. The bandwidth measurements for Cyl-μ show that the relationship between TE_{211} and TE_{011} and TE_{311} and TE_{011} are almost the same due to their similar slopes. For Cyl-ε however, TM_{210} and TM_{310} both have different slope relationships with TM_{010}. Practically this means that correction of measurement data must always be with the same mode.

4.5 Conclusions

This chapter shows the potential to use the two MCP measurement systems used in Chapter 3 to measure the temperature dependent magnetic and dielectric properties of materials at microwave frequencies. The TM_{210} and TM_{310} modes have been investigated to correct TM_{010} measurements due to their insensitivity to the axial sample. The measurements show that the cavity modes are all linked geometrically through linear thermal expansion, though these slopes can vary across the modes and offsets may be noticed especially in the bandwidth changes. Being aware of this, quartz tube sample ramps must be conducted to offset this error. Quartz tubes can be used effectively as a sample container in the 20 to 70 °C temperature range, showing minimal temperature dependent properties. These results demonstrate that the nodal correction method can effectively account for any external influences on the cavity during perturbation measurements which is important for decoupling any systematic errors between different measurements (i.e. removing the errors in the quartz tube ramp and those in the sample ramp which may not be the same).

The significance of this study demonstrates the potential for this technique to observe temperature dependent electrical processes and opens doors to high temperature dynamic measurements, allowing the real-time monitoring of the complex permittivity of samples during phase changes or other chemical processes, without disturbing the environment.

CHAPTER 5

Study:
Microwave Characterisation of the Magnetite to Maghemite Transition

The General Problem - Synthesis

Magnetic nanoparticles are used in targeted delivery such that an external magnetic field can focus the drugs at tumour locations[49,141,142]. There is a need for sensitive determination of **synthesised** stable magnetic nanoparticles through oxidation of unstable ones.

The Approach

It is proposed to use MCP to identify the transition from magnetite (Fe_3O_4) to the more stable form of maghemite (γ-Fe_2O_3) through ex-situ annealing at temperatures from 60 to 300 °C. The transition to γ-Fe_2O_3 was identified using standard techniques (XRD, XPS and VSM). MCP is proposed to see if it is capable of determining the change and further analysis on why this is possible is given through temperature dependent measurements. *This work is presented in Journal Physics: Condensed Matter, 2016.*

Key Findings

MCP permittivity measurements are very sensitive to the change, allowing confident determination of the transition. MCP permeability measurements show small changes. It is shown that MCP is very sensitive to the interactions of Fe^{2+} and Fe^{3+}cations, allowing determination of the transition and demonstrates the potential for MCP to examine other Fe^{2+} rich materials.

5.1 Synthesis and Characterisation of γ-Fe_2O_3

Magnetic particles have gained great interest recently in applications ranging from electromagnetic absorbers[7, 17, 25, 143] to numerous biomedical applications including targeted magnetic drug delivery[4, 49, 141, 142] and treatment of hyperthermia[144, 145]. In particular, Fe_3O_4 and γ-Fe_2O_3 have been highlighted as suitable candidates for these applications due to the simplicity of their synthesis, biocompatibility and non-toxicity[44, 146]. Fe_3O_4 can be synthesised through coprecipitation of iron salts. Synthesis of γ-Fe_2O_3 is most commonly through subsequent oxidation of Fe_3O_4, with the exception of the dehydration of iron oxide-hydroxides such as lepidocrocite ($\gamma-$FeOOH) or goethite ($\alpha-$FeOOH)[147, 148]. Oxidation of Fe_3O_4 in air at temperatures around 200-300 °C induces the phase change to γ-Fe_2O_3[149–151]. These two oxides are of interest due to their structural similarity but γ-Fe_2O_3 is the more thermally and chemically stable of the two[52, 53].

Current standard techniques to determine γ-Fe_2O_3 include X-Ray Diffraction (XRD) [152], X-Ray Photoelectron Spectroscopy (XPS), X-Ray Absorption Near Edge Spectroscopy (XANES) [153], Vibrating Sample Magnetometry (VSM), Raman and Infrared (IR) Spectroscopy [154, 155], and Mössbauer Spectroscopy[145, 150]. The most effective method is Mössbauer Spectroscopy since it specifically probes the oxidation state of the irons from the sextet caused by Zeeman splitting from the different nuclear spin moments. XRD works by changes in lattice constant but since both oxides have the same inverse spinel lattice, identifying γ-Fe_2O_3 after oxidation is by no means trivial. The lattice constant of γ-Fe_2O_3 (8.34Å) is slightly smaller than Fe_3O_4 (8.39Å), resulting in a marginally shifted 2θ Bragg diffraction pattern for Fe_3O_4. A difference can be identified though from the shift in the (511) plane[156]. For a multi-phase material, a convolution of two peaks with intensities dependent upon the concentrations of Fe_3O_4 and γ-Fe_2O_3 have be seen. XPS probes a difference in binding energy of the Fe 2p core electrons, as well as characteristic satellite peaks caused by particular iron oxidation states. This technique is a very effective surface probe, but is less sensitive to the bulk. Raman Spectroscopy is able to identify the material phases through distinct differences in phonon scattering of the A1g, Eg and T2g modes[154, 155]. However, due to the nature of the measurement it can induce the phase change to hematite, caused by the laser heating and thus great care must be taken to measure these materials[155, 157, 158]. Though phase identification can be achieved,

there are some drawbacks to all of these methods, including complicated analysis, low sensitivity, invasive (to the point of destruction) and the demand for complex, expensive equipment which sometimes involve ionising radiation.

5.2 A Novel Approach: MCP to measure oxidation state

Since the materials differ by their cations with unpaired electron spins, polarisation (via permittivity and permeability) measurements may offer a complementary insight to the transformation. This is due to the exchange interactions present in Fe_3O_4 which gives rise to conductivity and magnetism (shown in Fig. 5.1). γ-Fe_2O_3, however, does not exhibit the double exchange interaction and hence its conductivity is inferior in comparison. Measurement of this can be achieved through impedance spectroscopy and magnetometry[159]. For the former this requires powdered samples to be compressed, shaped and physically built into the measurement system. Though this method infers the conductivity, repeatability becomes a problem as well as system contamination due to contact. For magnetic measurements, high precision field probes with large magnets or superconducting detectors require controlled cooling to support large fields. This present study explores whether the conversion of Fe_3O_4 to γ-Fe_2O_3 can be observed using non-invasive dielectric and magnetic probing techniques, in particular MCP. The MCP approach may offer a more simple and highly sensitive measurement system for oxidation analysis, which could be applied to many other materials systems apart from iron oxides.

MCP is a non-contact electromagnetic probe through the simple perturbation of high density fields as opposed to contact measurements at DC (or low frequencies) and subsequent measurement of impedance through voltage and current. As explained in previous chapters, in MCP, the powder of interest is simply poured into a low microwave loss container and placed into the anti-node of the appropriate standing wave (electric or magnetic) of a microwave cavity resonator. The greatest advantages of this approach are the non-contact nature of the measurement, as well as low power requirements (generally it uses input power levels of approximately 1 mW, with typically less than 10 μW dissipated in the sample). Microwave systems have been explored to measure some iron oxides through Electron Spin Resonance (ESR) where a sample perturbs a microwave cavity resonator whilst subject to a DC magnetic field (often modulated by Helmholtz coils to increase the

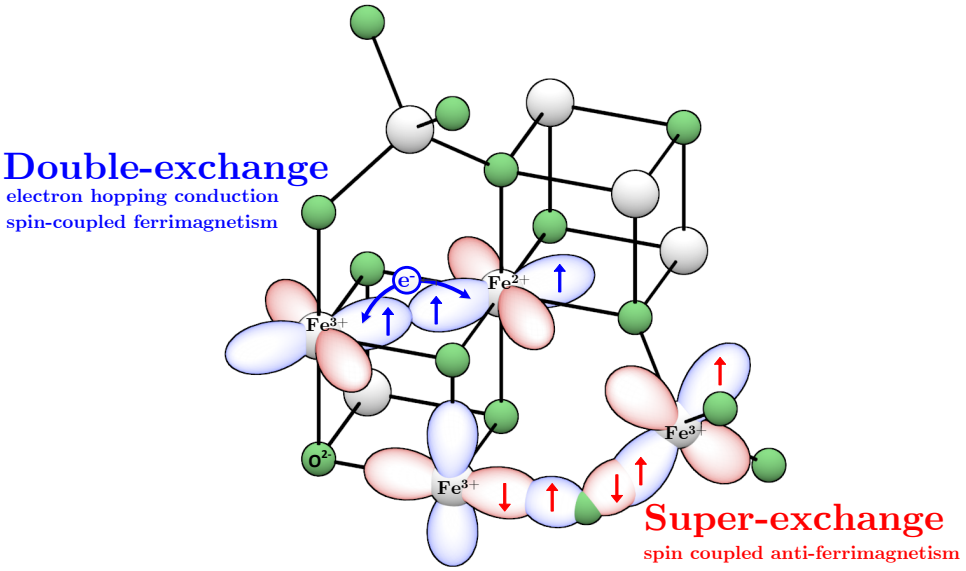

FIGURE 5.1: Conceptual representations of double and super-exchange interactions in Fe_3O_4 through d orbitals of Fe^{2+} and Fe^{3+} cations. Double-exchange interactions are responsible for electron transport where the delocalised electron seemingly hops through the material. Super-exchange results in anti-parallel Fe^{3+}_{tet} and Fe^{2+}_{oct} resulting in a net magnetic moment.

signal to noise ratio using lock-in amplifiers). The DC field aligns the electron spins parallel and anti-parallel, creating Zeeman splitting where the equivalent energy level difference lies in the microwave region through the Einstein relation $E = hf$. Maximum absorption occurs when the microwave frequency of the resonator matches that of the energy difference E. It has been shown that Fe_3O_4 and γ-Fe_2O_3 give different ESR responses, with γ-Fe_2O_3 giving a narrower linewidth at absorption[160–162]. However, if the differences in the materials' properties can be expressed in a simple change in cavity resonance alone, there is no need for the additional instrumentation imposed by ESR. Hence we move from probing spin resonance to simple bulk complex permittivity and permeability measurements, which eliminates the need for a large DC electromagnet, field calibration procedures and other added complexities, reducing the system to just a resonator and a means of interrogating it such as a VNA or a swept oscillator with a broadband power detector.

The main drawback of the MCP technique is that measurements can only be performed at spot frequencies defined by the cavity dimensions. The measurement is also volumetric, and thus an accurate determination of sample volume is required. Powders will have some air gaps and hence the measured quantity is not intrinsic unless the packing density

is known. This is coupled with the uncertain depolarisation factors associated with the specific shapes of the individual powder grains. Finally, the definite identification of an unknown material is very challenging since many materials may have a similar absorption response at these frequencies.

These weaknesses, however, can be addressed. The sparse data points in the frequency domain are not so much an issue since microwave relaxation phenomena such as Debye type behaviour are not expected as dipolar molecules do not exist. Frequency dependent data will only provide qualitative analysis on conduction mechanisms. The packing density and particle shape are dealt with by quoting an effective value of both permittivity and permeability which are less than the intrinsic values due to the volume of air gaps and field depolarisation. Also, weighing of samples allows appropriate comparison measurements of materials with different densities. Finally, for the identification issue, in this application it is the characterisation of a known precursor material and determination of a different product; a simple before and after experiment. The MCP technique in this respect is a much simpler and non-invasive method when compared to the aforementioned techniques.

5.3 Experiment: MCP measurements of annealed Fe_3O_4

5.3.1 Aims and Objectives

The aim of this experiment is to determine whether the Fe_3O_4 to γ-Fe_2O_3 transition can be measured through differences in the microwave permittivity and permeability. A selection of samples are annealed at different temperatures in an attempt to create partially oxidised magnetite and fully oxidised γ-Fe_2O_3. The properties of each of these samples are then measured as a function of annealing temperature. Following this, an investigation into the loss mechanisms of Fe_3O_4 is achieved with temperature dependent dielectric and magnetic MCP measurements.

5.3.2 Samples and Procedure

The starting powder (Bayoxide® E8712) initially exhibited a solid black colour consistent with Fe_3O_4. The particle sizes of this sample are quoted at less than 0.3 μm. 500 mg of the powder was filled into an open vial and placed into a laboratory oven. Ten separate vials were prepared with each one annealed for 1 hour at a different temperature, ranging from 60 to 300 °C, to vary the amount of oxidation. The resultant powder changed to a brown colour which was initially subjectively identified as γ-Fe_2O_3. The identification of this phase was carried out using XRD, XPS, VSM and MCP measurements. XRD was conducted using Cu Kα radiation at 1.545Å from 10 to 80°. Offsets were removed and Gaussian curve fitting was applied at the relevant peaks in the data to match the materials. XPS spectra were collected using a Kratos Axis Ultra DLD system with monochromatic Al Kα X-ray source operating at 144 W. Data was collected with pass energies of 160 eV for survey spectra and 40 eV for high resolution scans. Due to the magnetic nature of the samples under analysis, the system was operated in the electrostatic operation mode with an acquisition area of approximately 300 × 700 μm^2. Spectra were analysed using CasaXPS (v2.3.17) with sensitivity factors supplied by the instrument manufacturer. All spectra were calibrated to the C1s line for adventitious carbon at 284.8 eV. Magnetic hysteresis loops were measured at room temperature using a LakeShore® 7400 Series VSM System calibrated to a 3 mm nickel ball standard. The maximum applied field on the samples was 8 kOe. The samples were dispersed at a fixed weight concentration of

10% inside a non-magnetic adhesive (Unibond super glue) and left to dry in semi-spherical silicone moulds approximately 3 mm in diameter.

5.3.3 XRD

First, XRD was carried out on the precursor and a selection of the annealed particles. This is so that the powders can be identified as Fe_3O_4 transitioning to γ-Fe_2O_3. Additional information can also be obtained on the crystallite size and strain. Diffraction patterns from 20 to 80° were collected, with data cropped to the significant peaks shown in Fig. 5.2. The diffraction patterns of the starting magnetite powder and powders annealed around the inferred transition temperature from the microwave results were obtained. The pattern of the starting powder was matched to Fe_3O_4 in the Inorganic Crystal Structure Database (ICSD), with a strong (311) peak at approximately 35.9° accompanied with the (220), (400), (422), (511) and (440) planes of the cubic cell at 30.5, 43.6, 53.9, 57.5 and 63.1°, respectively. These peaks are in agreement with other XRD studies on Fe_3O_4 particles[152, 163, 164]. The same planes are evident for the annealed samples, but are shifted upward with increasing temperature indicating that structurally these materials have a spinel cubic lattice but with a changing lattice constant.

The average calculated lattice constant (with standard deviations) from the higher diffraction angles of planes (511) and (440) yielded, 8.394 ± 0.002Å and 8.368 ± 0.007Å for the starting Fe_3O_4 and the 260°C annealed samples, respectively. These shifts are somewhat smaller than some values given in the literature, which may be an instrumentation offset error, however, there is a large variation of the reported lattice constant of γ-Fe_2O_3 from 8.36Å[165,166] to as low as 8.34Å[167]. The trend in decreasing lattice constant is evident as shown in Fig. 5.3. An explanation behind this is that the decreasing lattice constant is due to the ionic radii of the Fe^{2+} and Fe^{3+} cations. Since Fe^{2+} cations have a larger ionic radius, the Fe-O spacing is greater. In γ-Fe_2O_3 the conversion of these cations to Fe^{3+}, along with the formation of vacancies, decreases the spacing which results in the shifted 2θ pattern.

It is also noticed in Fig. 5.3 that the lattice constant decreases at 240 °C and increases back up again at 260 °C. In conjunction with this, the average full width half maximum, increases and then decreases. The changes in FWHM can be indications of a changing

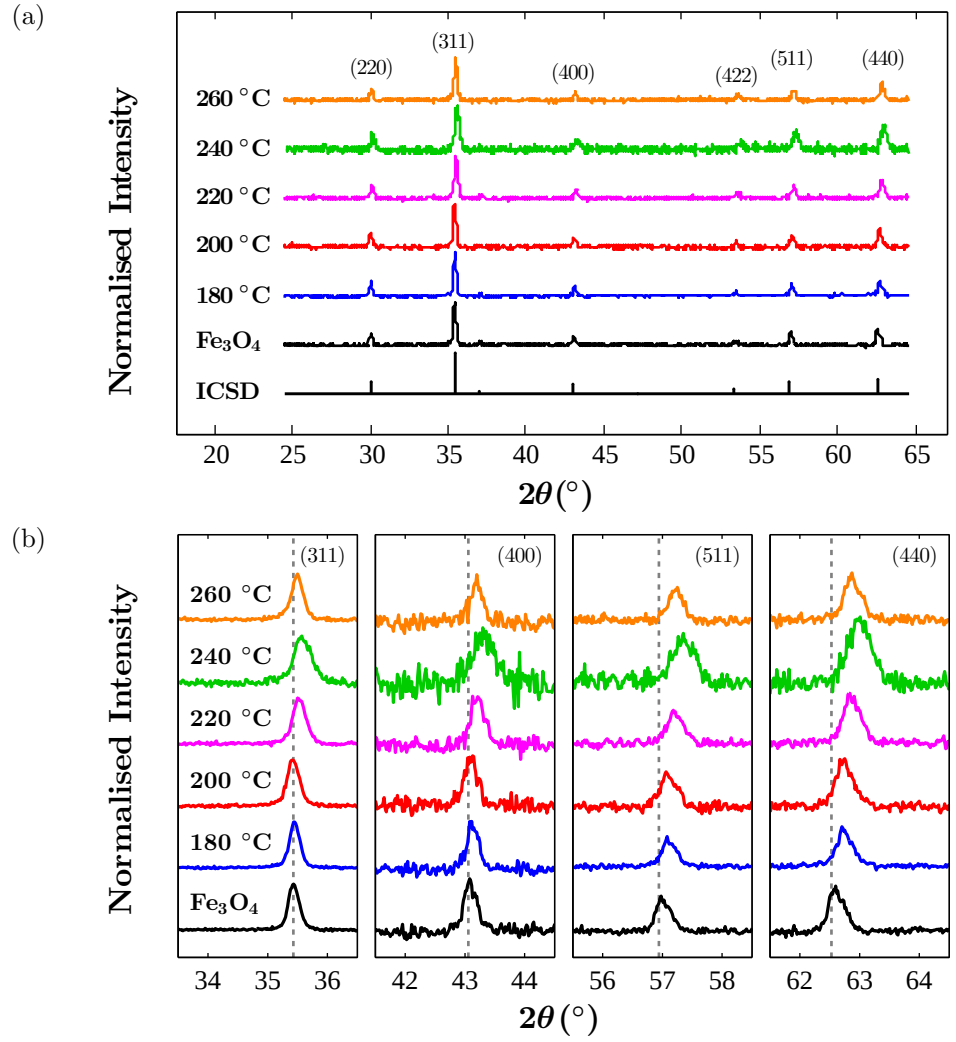

FIGURE 5.2: XRD patterns of the starting Fe_3O_4 powder and subsequent annealed powders at 180, 200, 220 and 240 °C. Full scan (a) and close inspection of the relevant peaks (b) show upward shifts with increasing annealing temperature which is indicative of the phase change to γ-Fe_2O_3.

crystallite size (D) through what is known as the Scherrer equation[168]:

$$D = \frac{K\lambda}{B_\theta \cos(\theta)} \tag{5.1}$$

where K is the shape factor of the sample (approximated to 0.9 for cubic iron oxide materials[169–171]), λ is the X-ray wavelength in metres, B_θ is the FWHM in radians and θ is the Bragg angle. Crystallite size is inversely proportional to FWHM, which means that smaller sizes show a broader response. However, increasing FWHM also may mean an increase in disorder for a particle of the same size.

This behaviour suggests that at this point in the annealing process a peak in disorder

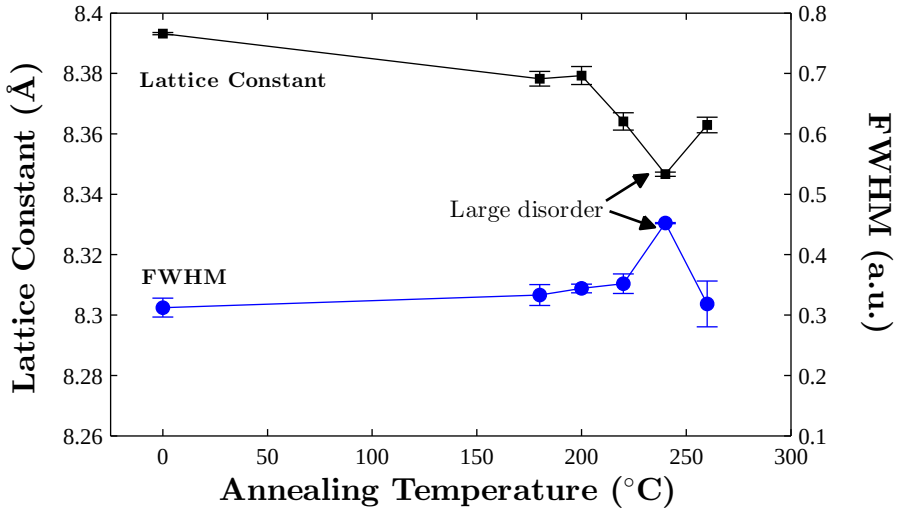

FIGURE 5.3: Calculated lattice constant of annealed Fe_3O_4 using the (511) and (440) peaks. The higher angle peaks were used since the lattice constant equation is dependent upon $1/\sin(\theta)$, thus errors in the Bragg angle measurement are minimised with the higher angles approaching $n\pi$.

may be occurring where the crystalline structure is disrupted. This may be explained by a number of vacancies formed in the lattice which are not being substituted by Fe^{3+} cations. Since the Fe^{3+} cation diffusion process is thermally assisted, upon quenching to room temperature, the vacancies do not get filled and hence the diffusion is impeded. This does not occur when annealing at higher temperatures since the higher thermal energy accelerates the oxidation and thus the diffusion process allowing the Fe^{3+} cations to fill the vacancies.

The overall result is congruent with the transformation to maghemite as given in the aforementioned literature[152, 164]. However, a convolution of two peaks for the (511) plane, as reported by Kim et al. (2012), was not noticed in this material. This may be more of a consequence of the low resolution from the Cu Kα line as well as increased background fluorescence, as opposed to the presence of an intermediate phase. From these results we can qualitatively conclude that structurally the phase change occurs at a temperature of at least 200 °C.

5.3.4 XPS

Survey and high resolution XPS spectra of the C1s, O1s and Fe2p peaks are shown in Fig. 5.4 and Fig. 5.5. The wide scan shows an overview of the elements present in the sample,

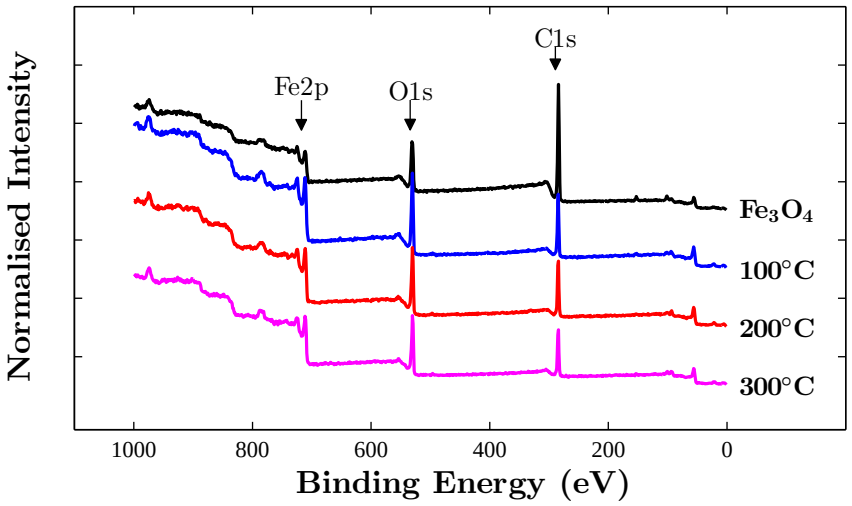

FIGURE 5.4: XPS Survey spectra of annealed magnetite powders. This scan shows the initial identification of iron, oxygen and carbon on the surfaces of the particles.

with binding energies matched to those found in Fe containing samples.

The adventitious carbon peaks at approximately 285 eV were used as charge references for the other spectra; all other spectra have been corrected to a C1s at 285 eV. These peaks show minimal difference across the annealed samples and are only necessary for calibration since the difference in binding energy between the two phases is small. This peak is associated with carbon contamination on the samples due to exposure to ambient air atmospheres.

For the Fe_3O_4 starting material, the $Fe2p_{3/2}$ peak shown in Fig. 5.5b is centred at 711.1 eV and is due to the convolution of both Fe^{2+} and Fe^{3+} signals in magnetite, Fe_3O_4[172]. Since magnetite comprises of both Fe^{2+} and Fe^{3+} the resultant peaks are a convolution of electron energies in both oxidation states and whilst the Fe^{3+}:Fe^{2+} ratio can be obtained through rigorous curve fitting, for this experiment only a qualitative identification of the γ-Fe_2O_3 phase is required.

Annealing reveals a change in the O1s spectra, with loss of organic contamination and the development of clear oxide and hydroxide peaks, the latter coming from exposure of the samples to air during transfer to the vacuum chamber for analysis. More importantly, the Fe2p region exhibits a slight downward shift in energy to 710.7 eV and the development of a Fe^{3+} 'shake-up' satellite peak at approximately 719 eV. This peak is present in γ-Fe_2O_3 but it is less noticeable in Fe_3O_4. There is also a Fe^{2+} satellite peak at 715 eV but this peak is less prominent and is generally hidden by the main peak at 711 eV. The Fe^{3+}

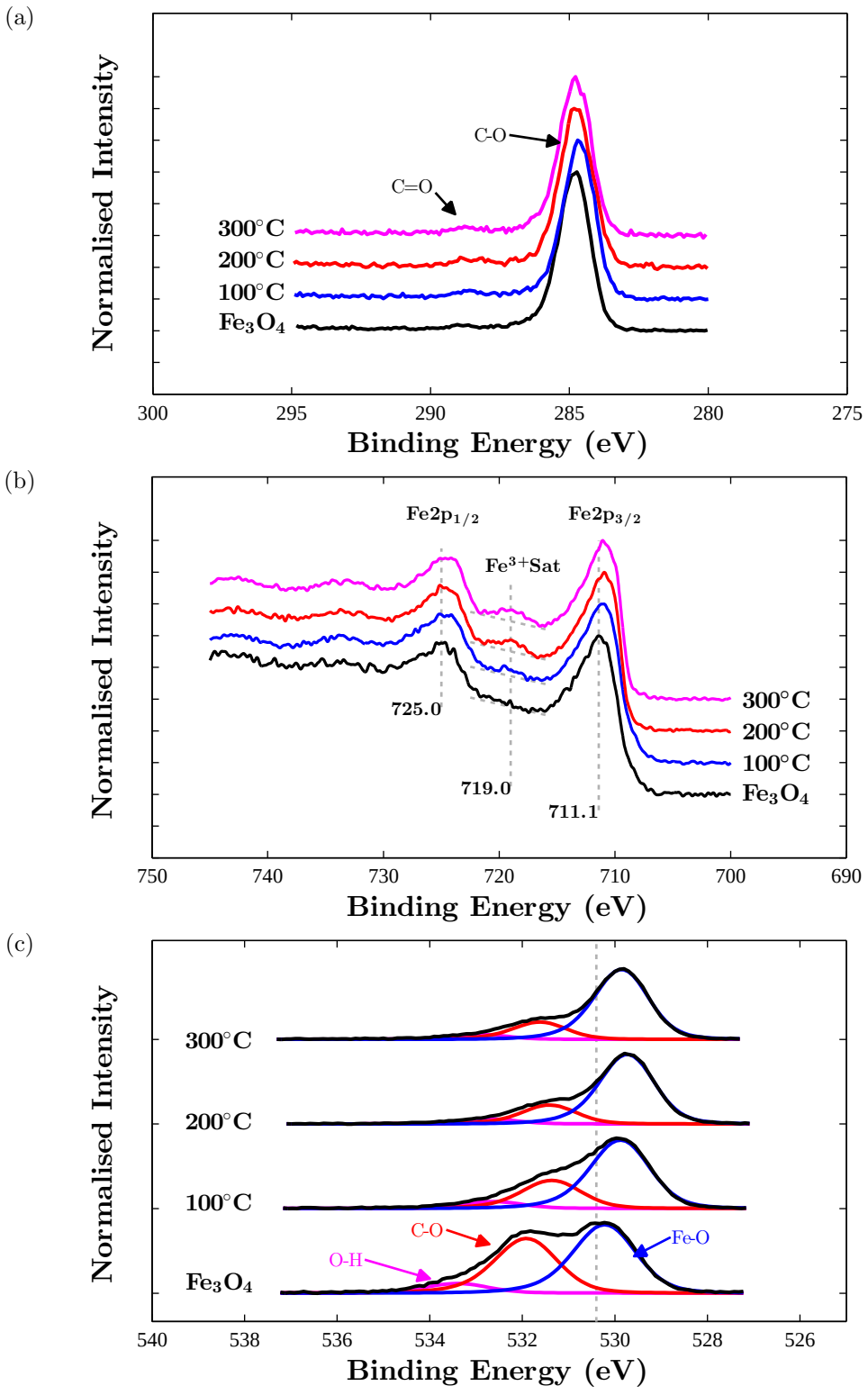

FIGURE 5.5: High resolution XPS spectra of the annealed magnetite powders. The C1s peak (a) shows carbon contaminants and is used as a charge reference. The Fe2p spectra (b) implies the iron oxidation states present. At 200 and 300°C there are slight shifts in the Fe2p peaks but more prominently, there is a peak at 719 eV which is characteristic of γ-Fe_2O_3. The O1s spectra (c) shows any other surface contamination from the atmosphere.

satellite peak starts to grow with annealing samples and is most prominent in the samples annealed at 200 and 300 °C. Hence, one can conclude that the starting material is Fe_3O_4, progressing to the removal of small contamination with some formation of Fe^{3+} at 100 °C and finally at 200-300 °C to the formation of the γ-Fe_2O_3 phase.

The O1s peaks at approximately 530 eV provide information on the surface terminations of the particles via the O^{2-} anions in the lattice. In the starting Fe_3O_4 material, presence of hydrogen and carbon is noticed as given by the C-O and O-H peaks in Fig. 5.5c. This is due to atmospheric contamination. At 100 °C, these peaks decrease while the Fe-O peak remains prominent. There is also a noticeable shift downwards in the Fe-O peak, which is vaguely implicit of some vacancy formation; when a vacancy is formed, the O^{2-} anion is no longer influenced by the Fe cation hence O^{2-} p orbital electrons lower in binding energy. After annealing at 200 and 300 °C, the hydrogen and carbon presences diminish with no further shift in binding energy implying no further effects on the surface. The $Fe2p_{1/2}$ and $Fe2p_{3/2}$ peaks at 725 and 711 eV, respectively, are congruent with binding energies for Fe_3O_4. The annealed samples give a slight shift downwards in binding energy. This shift may be explained by the fact that the peak in γ-Fe_2O_3 has a smaller binding energy than the Fe^{3+} present in Fe_3O_4 but the shifts are very small.

5.3.5 VSM

Magnetic hysteresis curves of the annealed Fe_3O_4 samples are given in Fig 5.6 with numerical calculations given in Table 5.1. The calculated saturation magnetisation (M_s) for the starting Fe_3O_4 phase is 92 emu/g, which is in agreement to values reported in the literature[8] of 92 emu/g. As the powder is annealed at higher temperatures, M_s decreases to approximately 60 emu/g which is slightly less than measured values of 74 emu/g for γ-Fe_2O_3[53] . The decrease in saturation is congruent with the change to the γ-phase and

TABLE 5.1: Measured magnetic properties obtained by VSM

	0°C Fe_3O_4	**200°C**	**300°C**
Hysteresis Area $\times 10^3$ (emu Oe/g)	30 ± 10	20 ± 30	8 ± 1
Coercivity, H_c (Oe/m)	120 ± 10	128 ± 6	140 ± 10
Magnetisation, M_s (emu/g)	92 ± 2	87 ± 9	60 ± 3
Remanence, H_r (Oe)	9 ± 2	13 ± 9	10 ± 4
Squareness, M_r/M_s	0.10 ± 0.03	0.2 ± 0.2	0.2 ± 0.1

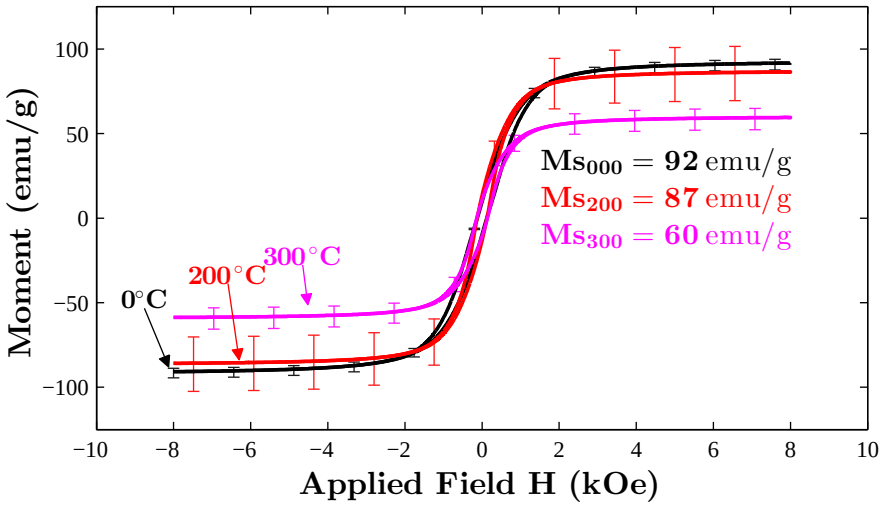

FIGURE 5.6: Hysteresis curves obtained from VSM of the starting Fe_3O_4 powder and subsequent annealed powders at 200 and 300 °C. Standard deviation given for 3 samples. The decrease in saturation as the material is annealed is indicative of the phase change of Fe_3O_4 to γ-Fe_2O_3.

not the α-phase (since the saturation of hematite is 2 orders of magnitude less[8]). Coercivity (H_c) after annealing has very little change; starting at approximately 120 Oe/m and increasing to 140 Oe/m (see Table 5.1 for the associated errors). The significance of the measurement of H_c is that it may infer the average particle size[97]. In this instance, it does not change by much during the phase transition since the particles retain their overall shape and simply decrease in magnetic moment. The main characteristic obtained from coercivity measurements is the extent to which these particles are super-paramagnetic, since this should be zero for super-paramagnetic particles. From the traces shown in Fig. 5.6, the particles are clearly not super-paramagnetic and therefore have a domain structure. The magnetic losses inferred by the integrated areas of the hysteresis curves show a large decrease with annealing temperature. Relating this magnetic loss property intrinsically to Fe_3O_4 and γ-Fe_2O_3 is not easy as it varies greatly with particle size and shape[173]. However, Fe_3O_4 has been shown to have larger magnetic losses than γ-Fe_2O_3 for micron sized particles[145].

The difference in magnetism between the two materials is a consequence of the cations in the inverse spinel lattice. For Fe_3O_4, ferrimagnetism exists through two main mechanisms, which is shown in Fig. 5.1. The first is the anti-ferromagnetic super-exchange interactions between the Fe^{3+}_{oct} and Fe^{3+}_{tet} cations through the O^{2-} anions[174]. The spin-up 5d electrons in the Fe^{3+}_{oct} couple with the overlapping 2p orbitals in the O^{2-} making

them spin-down. The other 2p electron is thus spin-up which makes the Fe^{3+}_{tet} 5d electrons spin-down. Thus Fe^{3+}_{oct} and Fe^{3+}_{tet} are antiparallel and cancel out each other's unpaired spin magnetic moments. The second factor is related to the aforementioned double-exchange interaction[175]. The spin-down electron can only hop from Fe^{2+}_{oct} to Fe^{3+}_{oct} if the majority spins are the same. Hence they are coupled and aligned parallel. Therefore, all the Fe^{2+} cations contribute to the magnetic moment while all Fe^{3+} cations cancel each other out. However in γ-Fe_2O_3, the conversion of 2/3 of the Fe^{2+}_{oct} to Fe^{3+}_{oct} balances some of the Fe^{3+}_{tet} cations but not all of them since the rest are turned into vacancies, resulting in a finite magnetic moment. When calculated, Fe_3O_4 has a larger magnetic moment[56] which is implied in Table 5.1, thus providing more evidence that the phase change has occurred.

5.3.6 MCP Permittivity

MCP traces of two modes are given in Fig. 5.7. It is clear that the microwave properties of Fe_3O_4 change as it is annealed at different temperatures. This is shown by the changes in complex frequency, with the maximum in dielectric loss occurring at an annealing temperature of 200 °C. Taking the centre frequency and bandwidth of each trace of each

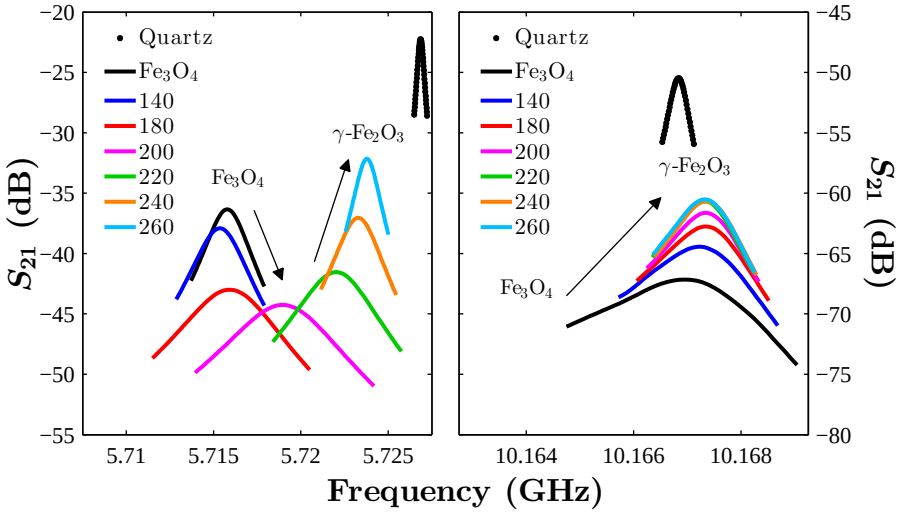

Figure 5.7: Examples of MCP traces, with the TM_{020} mode (left) used to measure permittivity and TE_{022} (right) for permeability. The TM_{020} trace shifts to the right and increases indicating a decrease in both the dielectric constant and losses. There is also a minimum at 200 °C indicating a dielectric loss peak for a given volume mixture of Fe^{3+} and Fe^{2+}. The TE_{022} trace also shifts to the right and increases indicating a decrease in magnetic permeability and losses.

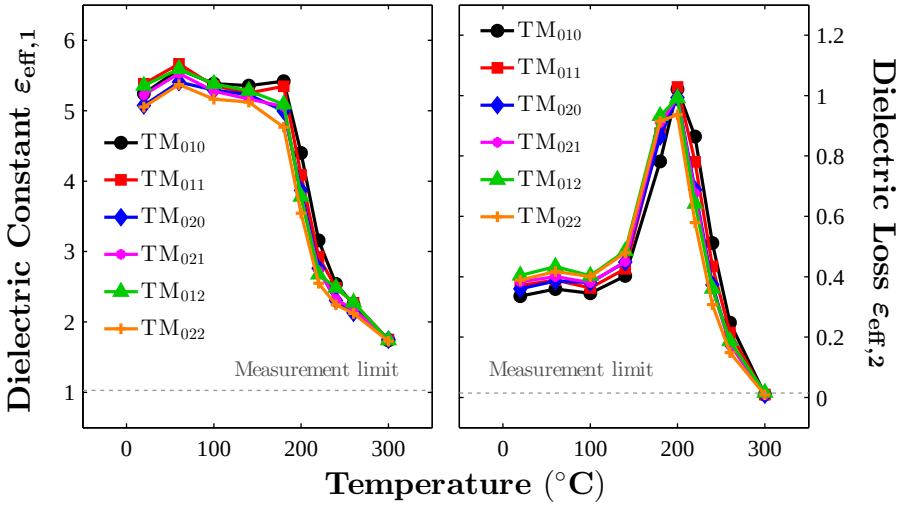

FIGURE 5.8: Calculated complex permittivity of annealed Fe_3O_4 samples using 6 different modes of the resonator as a function of annealing temperature. The dielectric constant and losses decrease with annealing temperature but the losses exhibit a peak at 200 °C. There is also minimal frequency dependence as all of the measurements from different modes are overlapping.

resonant mode, the complex permittivity (thus conductivity) and permeability can be calculated at each resonant frequency.

The complex permittivity is given in Fig. 5.8. At temperatures below 180 °C both the effective dielectric constant and losses show minimal change. At higher temperatures, the dielectric constant decreases greatly while the losses increase to a peak and then decrease to effectively zero. There is also very little frequency dependence, as implied by all of the different resonant modes being superimposed upon one another. As more of the Fe^{2+} cations are oxidised to Fe^{3+} the dielectric constant decreases, so showing that the presence of Fe^{2+} cations provides a significant contribution to the polarisation mechanism at microwave frequencies in Fe_3O_4. With the assumption that only Fe^{3+} cations exist in the samples annealed above 200 °C as inferred by XPS, the permittivity measurements show that Fe^{3+} cations have less polarisation at microwave frequencies.

A similar decrease is noticed in the losses, which reduce from approximately 0.4 to approximately 0, as shown in Fig. 5.8. A very large loss peak, however, is exhibited around 200 °C, which intriguingly is not noticeable in any of the other measurement techniques. This can be explained by a consequence of measuring a multiphase mixture in a microwave electric field if the difference in complex permittivity between the two phases is significant. Consider a medium (ε_b) that consists of multiple spherical particles of radius b representing

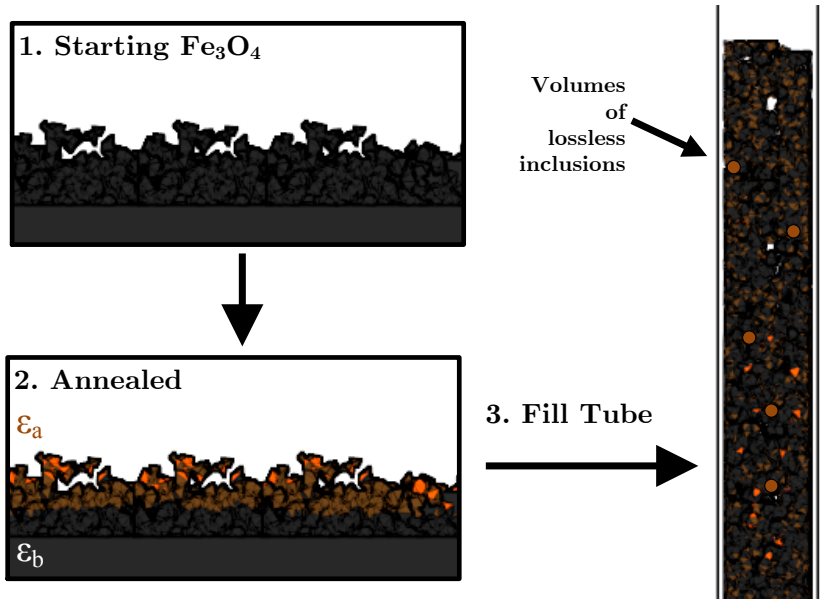

FIGURE 5.9: Abstract representation of the annealing process resulting in a multi-phase mixture with volumes of the low loss phase dispersed inside the bulk mixture.

the Fe_3O_4 phase. After annealing, the powders are filled into the tube with a fraction of the Fe_3O_4 now converted to γ-Fe_2O_3. This can be represented as a spherical volume (ε_a) with radius a growing within the main volume. This volume is not actually growing *inside* the individual Fe_3O_4 particles since the oxidation process is expected to permeate from the edges but represents a low loss volume growing within the bulk volume. The reason why the model has been considered in this way is because models for a lossy core and a low loss shell particle do not take into account the local field effects from other particles. In this model, the volume of the mixture remains the same hence $a \leq b$. Eventually, all of the Fe_3O_4 phase disappears and the result is the γ-Fe_2O_3 phase or the low loss phase now occupies the volume of the original particle so that $a \to b$. If this material is placed in an applied E-Field (E_0), then the dipole moment (P_i) of one of these inclusions can be described using the following formula[79]:

$$P_i = 4\pi\varepsilon_0 b^3 E_0 \frac{(\beta+2)(\alpha-1)\gamma^3 - (\alpha+2)(\beta-1)}{(2\beta-1)(\alpha+2) - 2(\beta-1)(\alpha-1)\gamma^3} \tag{5.2}$$

where $\alpha = \varepsilon_a/\varepsilon_b$, $\beta = \varepsilon_m/\varepsilon_a$, $\gamma = a/b$. In this instance it is assumed that the particle is in air space (hence $\varepsilon_m = 1$). This formula can be incorporated into the well-known Maxwell-Garnett mixing law for multiple particles in a dielectric medium[79]:

$$\varepsilon_{\text{eff}} = \varepsilon_m \left(\frac{1 + 2\delta_i P_i}{1 - \delta_i P_i} \right) \tag{5.3}$$

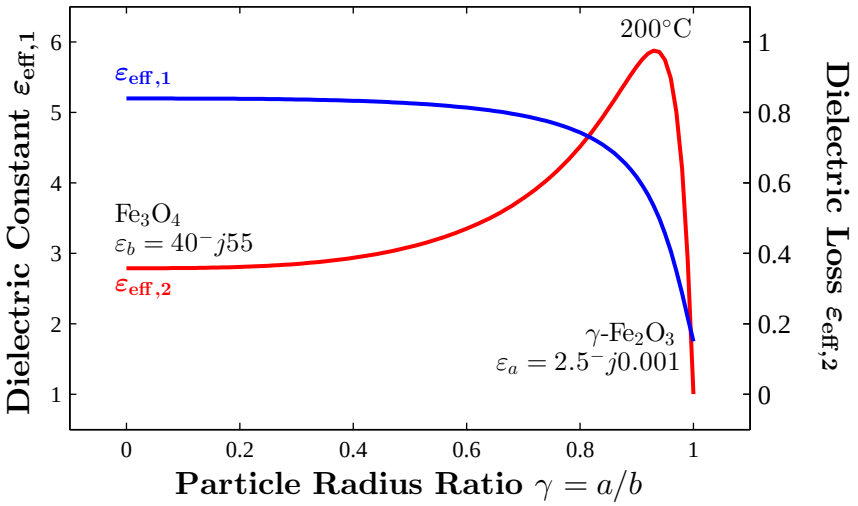

FIGURE 5.10: The effective permittivity of a dielectric mixture ($\delta_i = 0.6$) as a function of particle radius ratio. This model explains the large loss peak noticed in the dielectric measurements where a critical volume ratio of the low loss and lossy material creates this effect.

where δ_i is the volume fraction of the particles in the tube. It is clear that if P_i is equal to 1 for a volume fraction of 1, that the the permittivity tends to infinite which is the case for a metal. In the case of a lossy particle with an increasing volume of a low loss dielectric, a loss peak can be exhibited at a certain volume fraction, as shown in Fig. 5.10. This loss peak only occurs, however, if the difference in permittivity between the materials is significant. Hence, microwaves may be a very useful tool for looking at dramatic phase changes in materials and these materials may have excellent microwave absorbing properties at certain volume fractions.

Since Fe_3O_4 is a multi-valence oxide, it has a significant electrical conductivity which has been explained as a consequence of electron hopping from double exchange interactions through a chain of Fe^{2+}_{oct} and Fe^{3+}_{oct} cations[175]. This occurs because, being high spin[176, 177], the cations only differ by one spin down electron, which is effectively delocalised due to minor overlapping between t_{2g} orbitals. In the transformation to γ-Fe_2O_3, 2/3 of the Fe^{2+}_{oct} cations are oxidised to Fe^{3+} while the remaining 1/3 diffuse of out of the lattice leaving behind vacancies[178]. The hopping dependent conductivity effectively explains why γ-Fe_2O_3 is an inferior conductor when compared to Fe_3O_4, as the conduction path through the cations is disrupted by the presence of vacancies and, assuming that the spin states in γ-Fe_2O_3 are high[52], there is no longer a delocalised spin-down electron. Hence, it is seemingly a case of one phase showing electron hopping conductivity and the other

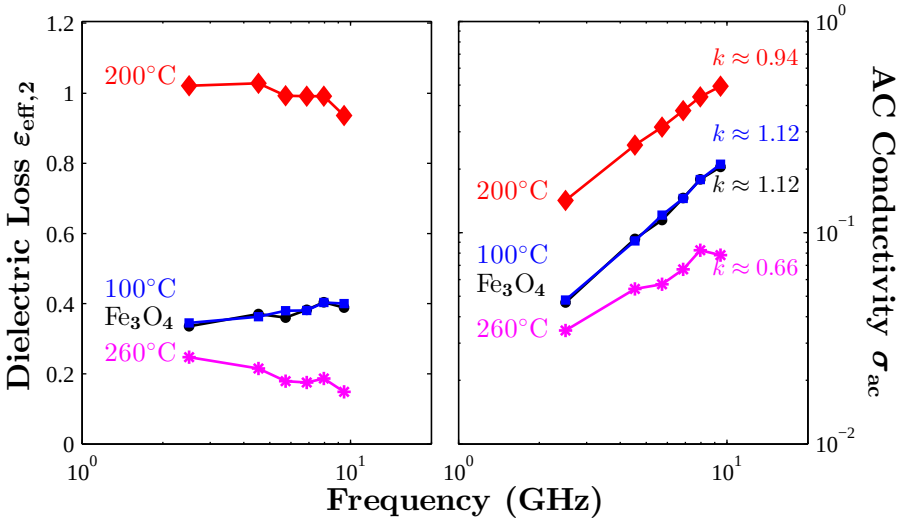

FIGURE 5.11: Calculated dielectric losses and AC conductivity of annealed Fe_3O_4 samples using 5 TM_{0mp} modes of Cyl-ε as a function of frequency. As the Fe_3O_4 powder is annealed, the slope for the Jonscher power law decreases indicating that the density of AC conduction paths are decreasing. Therefore, the AC contribution from any electron hopping mechanisms are disappearing.

showing none.

As for the microwave measurements, the hopping conduction mechanism will contribute to the loss with both a static electron conduction component and an AC component. It is already clear that the static component is not the result of the large losses since the frequency dependence is minimal. The observed losses is thus due to the AC component of the electron hopping loss, which does not rely upon a DC percolating pathway through the material. Recall the Jonscher power law (JPL) for hopping conduction[92] shown previously in 1.10 whilst omitting the DC conductivity:

$$\sigma_{\text{Jonscher}}(\omega) \approx \sigma_{\text{ion,dc}} + \sigma_{\text{ion,ac}} \approx \psi_{\text{ion,ac}}\omega^{k} \tag{5.4}$$

Typically, in the regular form of this law $0 < k \leq 1$, while larger values indicate a super-linear power law (SLPL). Since static electron conductivity is not measured (no $1/f$ dependence in the loss), the result is from $\varepsilon_{\text{eff},2} \approx \psi_{\text{ion,ac}}\omega^{k-1}/\varepsilon_0$. The measured slopes are given in Fig. 5.11 where Fe_3O_4 gives a SLPL in this frequency range with an exponent k of approximately 1.12. For γ-Fe_2O_3 (annealed at 300 °C) the dielectric loss (and hence hopping conductivity) is effectively zero at microwave frequencies. Taking the slopes of the 200 and 260 °C annealed samples one finds that the SLPL tends towards a regular JPL with k values of 0.94 and 0.66 respectively. Therefore, this implies that the Fe_3O_4

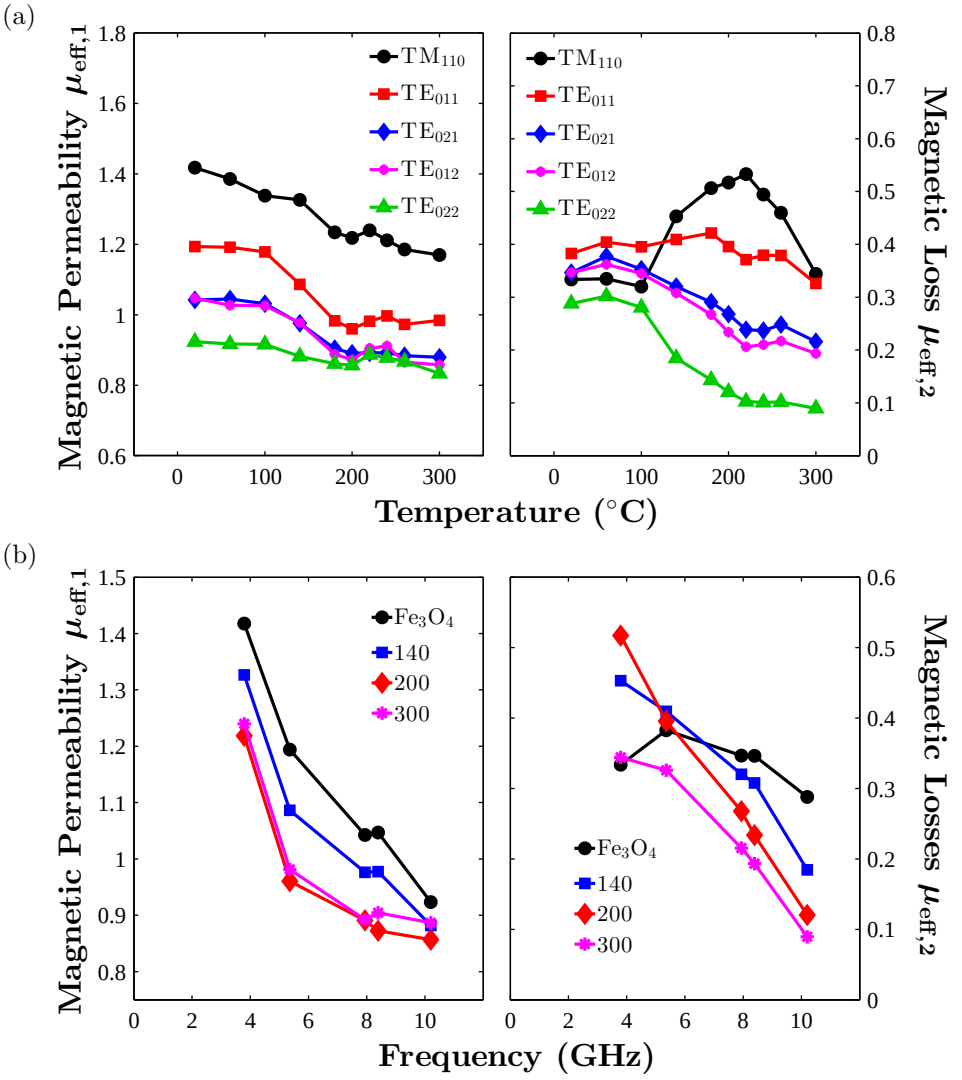

FIGURE 5.12: Calculated effective complex permeability of annealed Fe_3O_4 as a function of (a) annealing temperature and (b) frequency. Overall, the effective complex permeability decreases as the material is annealed which is expected since Fe_3O_4 has a larger magnetic moment than γ-Fe_2O_3. The broad loss peak over the GHz range seemingly shifts and increases in peak value to frequencies lower than can be measured.

has a SLPL characteristic at microwave frequencies which is most likely due to the Fe^{2+}_{oct} and Fe^{3+}_{oct} electron hopping mechanism[81].

5.3.7 MCP PERMEABILITY

The complex permeability or magnetic permeability and losses are given in Fig. 5.12. From Chapter 3, the microwave magnetic permeability of Fe_3O_4 decreases with frequency while the losses have a broad peak over the 5.0 to 8.5 GHz range. As the powder is annealed, the overall magnetic permeability decreases with frequency, congruent with the

VSM measurements. The losses, however, increase in the lower GHz range while decreasing in the higher range. This implies that the broad peak may have either disappeared, or has shifted to lower frequencies. The magnetic permeability is merely a tail of ferromagnetic resonance peaks occurring at lower frequencies as given by the negative slopes. The greatest differences occur in the TM_{110} (3.8 GHz) and TE_{022} (10.2 GHz) modes in the losses. In the permeability, the greatest difference is in the TE_{011} mode (5.4 GHz) as shown in Fig. 5.12. From the TM_{110} mode, the losses give a similar response as for the permittivity measurements, with a decrease in the real part and a large loss peak at 200 °C. Contrary to the permittivity measurements, the losses at 300 °C do not go to zero and are of similar values to the starting material. This may be explained by the fact that in Fe_3O_4 the dielectric and magnetic loss mechanisms are a consequence of the double and super exchange interactions respectively (i.e. the electron hopping gives rise to the dielectric loss and the ferrimagnetism from coupled electron spins will have an associated magnetic alignment loss with an applied field). With the diffusion of Fe^{2+} cations and the formation of vacancies, the dielectric loss mechanism is eliminated but the magnetic mechanism remains. This is because of the imbalance of tetrahedral Fe^{3+} and octahedral vacancies, hence the losses are associated with this. The TE_{022} mode shows little changes in the real part but a large decrease in loss from 140 °C. The TE_{011} mode shows some change in the losses but larger changes in the real part, again occurring at 140 °C. The transition is somewhat less clear-cut than for the permittivity measurements, but when looking at the frequency dependent data the change can be clearly seen.

Thus it has been demonstrated that MCP measurements corroborate the phase change of Fe_3O_4 to γ-Fe_2O_3 observed using standard material characterisation techniques. The results here show that dielectric MCP measurements give a clearer indication of the phase change. Magnetic MCP measurements, however, give clearer indications when measured as a function of frequency.

5.4 Experiment: MCP Temperature Dependent Mechanisms of Fe_3O_4

Now that it has been determined that MCP can measure the change, the question is, *what is it actually measuring?* Further investigation of the microwave loss mechanisms can be achieved by realising that both ionic hopping conductivity and magnetic resonance phenomena are dependent on temperature. From Fig. 5.8, an ionic hopping conductivity contribution is assumed, as opposed to a static percolating conductivity, due to the minimal frequency dependence. This hopping process is known to be activated by an energy threshold [179–181]. This energy threshold can potentially be measured at microwave frequencies by measuring the dielectric properties as a function of temperature and using 1.9.

The magnetic properties showed some frequency dependence where a broad peak over the GHz range in Fig. 5.12 was noticed and the decrease in the magnetic permeability to less than 1 implied a resonance phenomenon. This peak then seemingly disappeared or potentially shifted to lower frequencies with annealing temperature. It is not clear what the resonance phenomenon could be a contribution from. Since Fig. 5.6 shows that the particles have some coercivity and remanence, the particles are certainly not superparamagnetic and therefore have a multi-domain structure. This means that resonance phenomena could be from domain wall resonance or natural resonance. However, it is known that the natural resonance of Fe_3O_4 is supposedly just below the GHz range as opposed to the observed peak which is around 5 to 6 GHz[96]. If a domain wall resonance is assumed, this process is also known to be a temperature activated process[182], whereby an energy barrier (E_{dom}) represents the energy required to flip the spin of a domain to move the wall.

This experiment also holds significant relevance for hyperthermia applications in that it is important to determine the temperature dependent absorption of the material. This is to ensure that at elevated heating, the material continues to absorb the RF radiation.

5.4.1 Aims and Objectives

The aim of this experiment is to further show that the microwave dielectric loss mechanism is related to an ionic hopping conductivity and that the microwave magnetic losses may be represented by a magnetic resonance peak. To do this the temperature dependent dielectric and magnetic properties need to be measured using Cyl-μ and Cyl-ε.

5.4.2 Samples and Procedure

Measuring the temperature dependent properties of Fe_3O_4 is not a trivial task since it easily undergoes oxidation to γ-Fe_2O_3 with signs appearing at 180 °C and 100 °C in the dielectric and magnetic responses, respectively, in Sections 5.3.6 and 5.3.7. It is possible to disperse the particles into a matrix such as a lacquer or an oil to avoid any air contamination, however, dispersion must be taken into account. Maintaining homogeneity of the sample whilst the cavity is measuring the properties in the oven is difficult especially if the viscosity and dielectric properties of the host matrix are temperature dependent. As a preliminary proof of concept study, to approach this, the pure Fe_3O_4 phase has been ramped up and down several times from 10 to 70 °C, where the results presented here include the initial ramp and the final ramp a few days after to allow for the material to oxidise to a certain point. The ramp profile was an increase in temperature of 1 °C per minute with a wait of 1 hour at the ending temperature before decreasing at 1 °C per minute back to the starting temperature.

5.4.3 Temperature dependent MCP permittivity of Fe_3O_4

The temperature dependent microwave permittivity is shown in Fig. 5.13. The temperature dependence over a broad range is shown. After partial oxidation, the dielectric constant has a linear relationship with temperature. As determined in Chapter 5, the frequency dependence is minimal, showing essentially the same linear trend with temperature at all measurement modes.

The explanation behind this temperature dependence of the dielectric constant has been ascribed to impurities in the material which were determined by XRD[183]. The XRD patterns given in Chapter 5 gave no signs of any impurity phases. Although the experimental

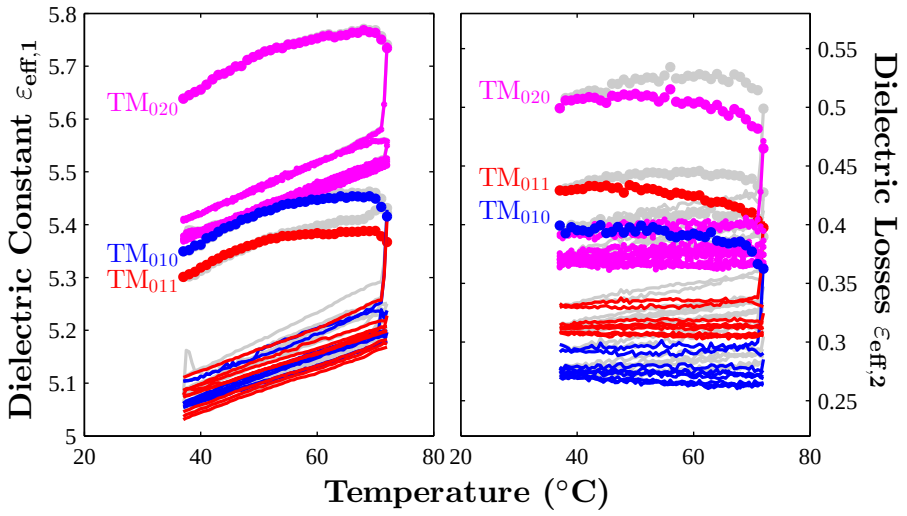

FIGURE 5.13: Measured temperature dependent properties of 3 ramps of Fe_3O_4 over 30 to 70 °C. The grey lines show uncorrected measurements, calculated through linear interpolation of the quartz and sample ramps. The coloured lines show the corrected temperature dependent response using the TM_{310} mode.

set-up is similar to Ansar et al., the independence of the dielectric constant implies that it is not impurity related and something intrinsic to Fe_3O_4. Other studies have looked at the temperature dependence towards the Verwey transition (which is far below the temperatures we are considering here), nevertheless, with increasing temperature from DC to kHz ranges, the dielectric constant steadily increases whilst the low frequency conductivity starts to plateau[184]. Also with increasing frequency, Svindrych et al. showed that the temperature dependence of the dielectric constant decreases.

Interestingly, the dielectric losses show almost no temperature dependence once partially oxidised, however, this is due to the temperature dependence of the hopping conductivity. It has been shown that electron exchange interactions in Fe^{3+} and Fe^{2+} in Fe_3O_4 and similar materials are very temperature dependent[185, 186] and can be explained by 1.9. Whilst ignoring the DC and additional atomic polarisation losses, which are more dominant at lower and higher frequencies respectively, recall that the temperature dependent ionic conductivity is influenced by the dielectric loss in the following way:

$$\sigma_{\text{eff}}(T) \approx \omega\varepsilon_0\varepsilon_{2,\text{eff}}(T) \approx \frac{\psi_{\text{ion,ac}}}{T}\exp\left(-\frac{E_c}{k_BT}\right) \tag{5.5}$$

Taking logs of both sides, the more familiar form of an Arrhenius equation can be obtained:

$$\ln\left[\sigma_{\text{eff}}(T)T\right] \approx -\frac{E_c}{k_BT} + \ln\left[\psi_{\text{ion,ac}}\right] \tag{5.6}$$

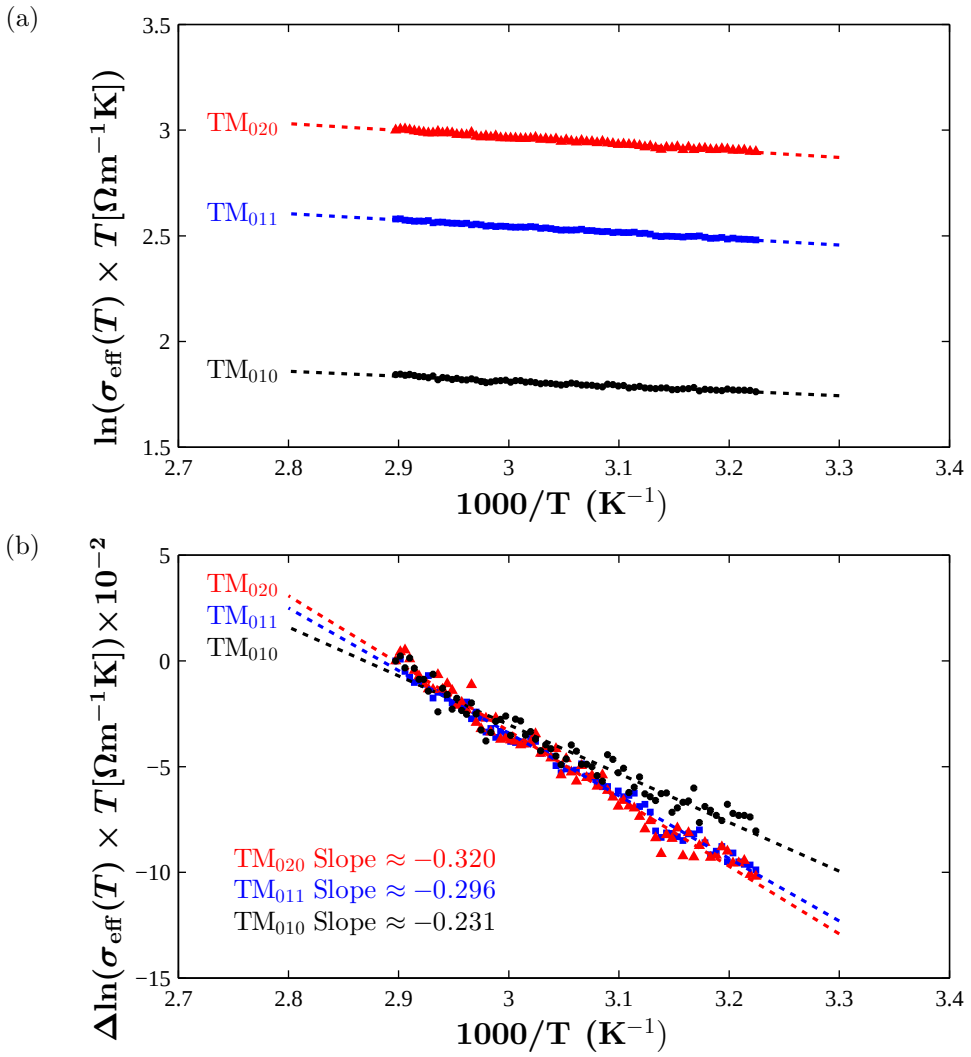

FIGURE 5.14: Arrhenius plots obtained from temperature dependent properties of Fe_3O_4. 5.14a shows the absolute plots whilst plots in 5.14b have been shifted (hence are denoted as Δ) to allow visibility of the slopes. The values of these slopes imply the activation energies for electrical hopping processes.

In this form, plotting $\ln[\sigma_{\text{eff}}(T)T]$ against $1000/T$ allows extraction of the activation energy in eV for hopping conduction assuming that the temperature range provides thermal energy to induce conduction[179, 185]. This is shown in Fig. 5.14 where the extracted linear slopes give an average $E_c \approx 0.28 \pm 0.05$ eV. This value is what some term as the band gap of Fe_3O_4 since it is the energy required to excite an electron (or the Fe^{2+} ion) into a mobile and an effective conducting state. These values are in a similar low eV range to those obtained from different techniques in the literature including the four point probe method giving 0.12 eV[179], temperature dependent UV-VIS giving 0.91 eV[180] and scanning tunnelling spectroscopy 0.6 eV[181].

Thus, this measurement strongly correlates with a thermally activated ionic hopping conduction mechanism at microwave frequencies in Fe_3O_4. Practically, over small temperature ranges, the dielectric absorption has minimal difference which is favourable for applications in EMI and hyperthermia, however, in the latter case the temperature range presented here may not be representative of the temperatures that the particles experience when subject to RF radiation to achieve an average temperature at the site of ≈ 45 °C.

5.4.4 Temperature dependent permeability of Fe_3O_4

The effective temperature dependent microwave magnetic permeability is shown in Fig. 5.15. The results show that without correction of the minute changes in cavity temperature, the resultant response yields both erroneous magnetic permeability and losses as a function of temperature. The difference between the upward and the downward ramp is due to the partial oxidation of the material during the dwell time at 70 °C. The corrected response shows that the effective magnetic permeability is almost invariant with temperature, with a slight decrease in the real part. The losses, however, show clear temperature dependent behaviour with the lower TM_{110} mode (3.8 GHz) showing an increase, the mid-band TE_{011} mode (5.35GHz) showing a small decrease and the higher TE_{012} (8.38 GHz) and TE_{022} (10.16 GHz) modes showing a larger decrease. This may be implicit of a

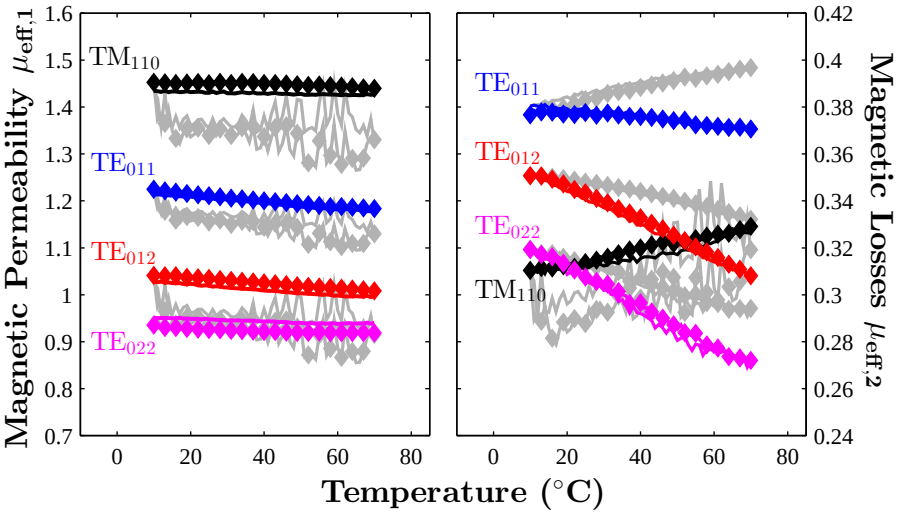

Figure 5.15: Measured temperature dependent magnetic properties of Fe_3O_4 over 10 to 70 °C. The grey lines show uncorrected measurements, calculated through linear interpolation of the quartz and sample ramps. The coloured lines show the corrected temperature dependent response using the TE_{311} mode. Diamonds show the initial ramp whereas the lines show the downward ramp.

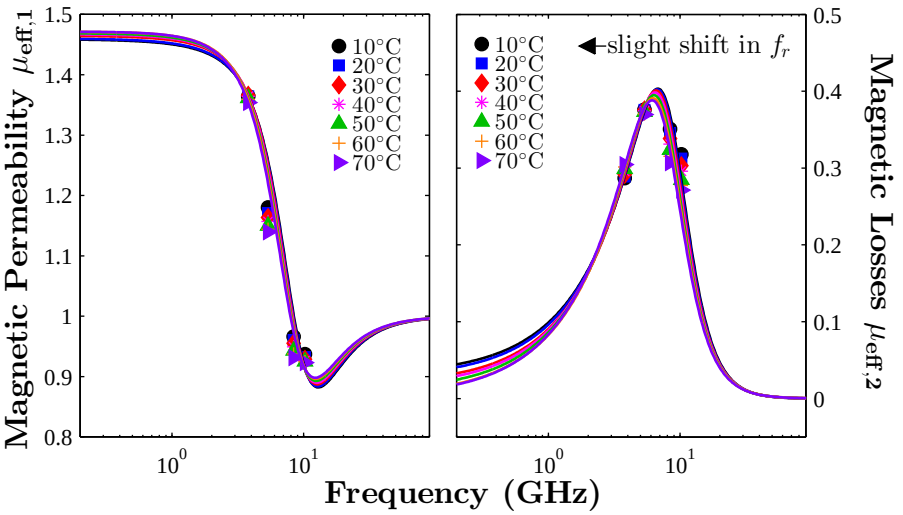

FIGURE 5.16: Temperature data fitted to a Lorentzian resonance in steps of 10 °C. While all points are fitted in the same way, the lack of measured points only provides a qualitative view of the resonance as a function of temperature. It is noticed that the resonant frequency decreases with increasing temperature.

magnetic resonance peak moving towards lower frequencies as a function of temperature. Of course, this approach depends upon whether this phenomenon is actually a resonance (since there are so few points in the frequency spectrum).

Microwave magnetic losses in Fe_3O_4 have been ascribed to a Néel related relaxation involving the reversal of the magnetic moments (or spin orientation of the collections of unpaired d orbital electrons in the Fe^{2+} and Fe^{3+} cations[187]). Thus, microwaves constantly excite this magnetic moment flipping which results in magnetic losses. However, the particles used in this study are not super-paramagnetic (are simply ferrimagnetic). This means that Néel relaxation may not be a mechanism and the contributions are from a combination of natural ferromagnetic resonance from precessing spins and additionally domain wall resonance from the multi-domain particles.

Domain wall resonance is considered with a relaxation frequency in the GHz range. Recall that magnetic resonance is modelled using a Lorentz function[79,80] which is shown in 1.4. This model fits the room temperature Fe_3O_4 results since it allows permeability values to be less than 1 as explained in Chapter 3. Also, domain wall resonance is a thermally activated process, explained by a characteristic resonance frequency shown in 1.13.

$$f_r(T) = \frac{1}{\tau_0}\exp\left(-\frac{\Delta E_{\text{dom}}}{k_B T}\right) \tag{5.7}$$

where f_r is the resonance frequency and ΔE_{dom} is the energy required to reverse a spin to move the domain wall. Notice that an increasing temperature results in a decrease in f_r. Again, using the same approach as for the hopping conductivity, taking logs of both sides yields:

$$\ln\left[f_r(T)\right] = -\frac{\Delta E_{\text{dom}}}{k_B T} + \ln\left[\frac{1}{\tau_0}\right] \tag{5.8}$$

Fitting the Lorentzian resonator given in 1.4 to the measured complex magnetic permeability as a function of temperature yields Fig. 5.16. A slight decrease is noticed in the modelled resonant frequency which results in a linear trend in the Arrhenius plot given in Fig. 5.17. The slope value of 0.17 eV is of the same order of magnitude for domain wall activation energies[188].

It is also possible that this particular resonance is due to the natural resonance frequency of the material through the Kittel formula in 1.14. In this case, either the gyromagnetic ratio (γ) or the effective applied field (H_{eff}) is temperature dependent. It is assumed that the gyromagnetic ratio is constant, since it is related to the intrinsic magnetic moment of an electron spin, and hence the anisotropic field is temperature dependent. With increasing temperature, random motion increases, thus, at any instance in time the net magnetic moment is less than it would be when $T = 0$. With H_{eff} decreasing with increasing temperature, the natural resonance frequency decreases.

Nonetheless, this experiment demonstrates that through temperature dependent measurements of the dielectric and magnetic properties of Fe_3O_4, the ionic hopping conductivity and magnetic resonance phenomena can be identified through extraction of activation energies using an Arrhenius model. The permeability of Fe_3O_4 at microwave frequencies is fairly invariant with small changes in loss. In applications for EMI, this is significant showing that at elevated temperatures (which may be caused by extreme environments or radiation from the device), there is minimal change in the microwave magnetic absorption at lower GHz frequencies. At higher frequencies however, the absorption performance decreases. With this system, temperature and upper microwave frequency limits of magnetic absorbing EMI materials can be identified. In hyperthermia applications the result is also

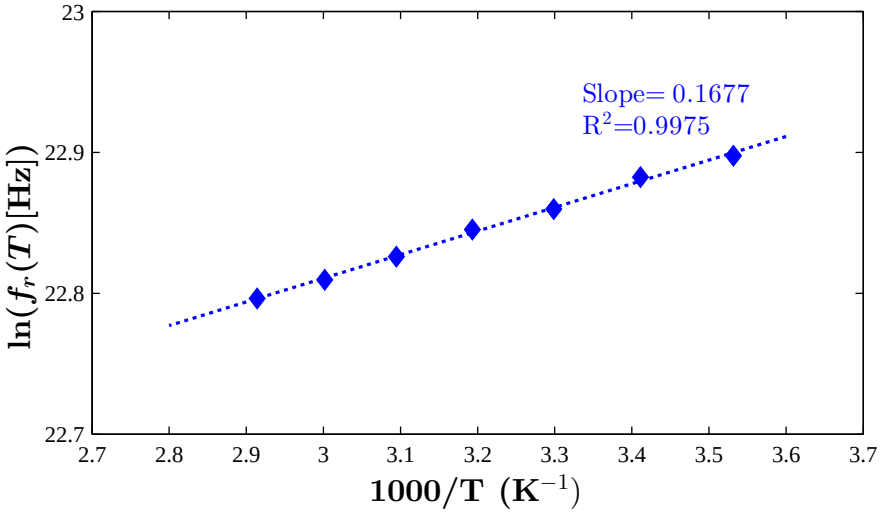

FIGURE 5.17: Arrhenius plot obtained from the modelled temperature dependent resonance in the complex magnetic permeability of Fe_3O_4. The fitted resonance decreases with increasing temperature, providing a slope and therefore an activation energy of approximately 0.17 eV.

significant as it shows that when the particles elevate in temperature, the microwave absorption has minimal change. However, this does not take into account the dependency on field and any additional losses caused by large microwave fields.

5.5 CONCLUSIONS

This chapter shows that the MCP method is excellent for high-sensitivity, non-invasive materials characterisation for the Fe_3O_4 to γ-Fe_2O_3 transition in annealed powders. Data has been presented from the standard methods of XRD, XPS and VSM on these powders to corroborate the findings found with MCP. Each technique bears its own figure of merit for the characterisation of the phase change. XRD results indicated the changing lattice constant from the upward shifting pattern in 2θ. XPS showed differences in binding energy caused by the different Fe cations at the surface of the material. Also Fe^{3+} satellite peaks associated mainly with γ-Fe_2O_3 verified the change. VSM measurements provided hysteresis curves which showed that the starting material had a saturation magnetisation very similar to Fe_3O_4, which decreased as the sample was annealed, again congruent with the change since γ-Fe_2O_3 is less magnetic. MCP measurements gave large frequency dependence for the effective permeability, with 3.8 and 10.2 GHz giving the most sensitive results, but with opposite behaviours of increasing and decreasing trends, respectively,

with increased annealing temperature. Looking over a broad microwave frequency range provides a better indication of the change qualitatively. Complex permittivity measurements, however, showed no frequency dependence, implying that the loss mechanism was not due to any static electron conduction. The key result was that very large changes in both dielectric constant and loss were observed. One cavity mode is sufficient for measuring the changes at microwave frequencies. Fitting the results to a hopping model reveals that the powders showed a SLPL which is due to the double-exchange hopping conduction caused by Fe^{2+}_{oct} and Fe^{3+}_{oct} cations. A loss peak was found at 200 °C, a consequence of field being focused at locations of inhomogeneity due to a multi-phase core-shell mixture. This insinuates that the phase change may occur around this temperature, with full transformation being reached at 300 °C. γ-Fe_2O_3 has a smaller dielectric constant and negligible microwave losses when compared to Fe_3O_4.

Furthermore, the temperature dependent absorbing properties of magnetite are evaluated from room temperature to 70 °C. It is shown that the variations in permeability could be due to a temperature dependence of a resonance (natural or domain wall), which may be observed through multi-mode temperature dependent measurements, however, only four modes were used in this study due to coupling issues thus giving low spectral resolution. In principle, coupling as many modes as possible allows better resolution of temperature dependent resonance phenomenon. The temperature dependent permittivity is linear in the real part and constant in the imaginary part. This is attributed to the temperature dependence of the ionic hopping conductivity. The activation energies of these processes are extracted using temperature dependent MCP technique, giving values similar to those found in the literature.

The significance of this experiment shows that the exchange interactions that Fe^{2+} cations take part in can be probed very effectively using MCP and Fe^{3+} rich materials are likely to give minimal response. The presence of the loss peak in permittivity is a significant result for the applications of EMI materials and hyperthermia, as high loss tangents can be achieved through simple annealing of Fe_3O_4 at this temperature. This result shows that microwave dielectric measurements for all intents and purposes provide highly sensitive characterisation of this oxidation process. Researchers can simply anneal their Fe_3O_4 to a certain degree and use the MCP method to determine how oxidised they are using the effective dielectric constant.

CHAPTER 6

Study: Microwave Determination of Impurities in Nanodiamond

The Problem - Purity

Diamonds have emerged as a promising drug delivery platform for doxorubicin[63, 189] where their efficacy lies in the **purity** of their surfaces[69]. There is a need to study the purity of nanodiamond surfaces of bulk nanopowders with fast and simple techniques.

The Novel Approach

The novel idea is to use MCP and MBCP to measure this, due to a difference in microwave absorption between the impurity phases and the wanted diamond phase. A selection of conventional methods are also used to verify this and corroborate the MCP findings. *This work is presented in Carbon Journal and IEEE Transactions on Microwave Theory and Techniques, 2015*[190, 191].

The Outcome

The MCP results show an increase in dielectric loss in the smaller particles, interpreted as being due to a larger volume fraction of surface impurities (smaller particles have a larger surface area and thus have more impurities). XRD and FESEM confirm these varying sizes while Raman confirms the presence of sp^2 and amorphous carbon on the surface. MBCP confirms any frequency dependence in the multi-mode MCP data, implying that the reason for this response is not related to static electron conduction.

6.1 Characterisation of Nanodiamond Purity

Determination of nanodiamond impurities can be achieved using a wide variety of techniques. They tend to be split into detection of either carbon based impurities or hydrogen and oxygen related functional groups.

Raman spectroscopy is capable of measuring carbon based impurities. Identification of the characteristic phonon peaks for diamond at 1,332 cm^{-1}, amorphous carbon at 1350 cm^{-1} and graphitic or sp^2 carbon at 1580 cm^{-1} gives qualitative information on the allotropes present[192].

X-Ray Diffraction (XRD) is also capable of measuring sp^2 carbon content by identifying the strong (111) plane for diamond at a 2θ of approximately 44° and the (002) plane in graphite at a 2θ of approximately 25°. This technique is again qualitative since the (100) and (101) planes of graphite have similar diffraction angles to the (111) plane and the diamond peak can thus be heavily convoluted by the impurities[193].

Fourier Transform Infrared (FTIR) spectroscopy can be used to look at surface functional groups. With this method, spreads of the spectrum can be attributed to the various terminations; including but not limited to hydrocarbon bonds (C-H) at 2750-3000 cm^{-1}, carboxyl and hydroxyl groups (-COOH and -OH) at 1640-1660 cm^{-1}, and carbonyl (C=O) groups at 2700-3000 cm^{-1}[194].

Nuclear Magnetic Resonance (NMR) spectroscopy is considered one of the most appropriate methods as it measures both carbon and hydrogen impurities. Also, unlike Raman and FTIR, it is sensitive to the bulk as opposed to specific points. NMR is capable of quantifying the sp^2 to sp^3 carbon ratio through deconvolution of peaks attributed to the carbon allotropes, where diamond has a chemical shift peak at approximately 36 ppm and sp^2 carbon has a peak at approximately 143 ppm[195]. This is achieved with ^{13}C NMR spectroscopy while functional groups are measured with ^{1}H NMR spectroscopy.

X-Ray Photoelectron Spectroscopy (XPS) is also able to identify both carbon and the hydrogen and oxygen related functional groups. For the latter, this can be achieved by observing shifts in the C1s and O1s peaks. For sp^2 carbon related impurities, there are six different methods that use different regions of the XPS spectra including the C1s peaks, the derivative of the C KVV spectra and the valence band region[196–199].

Of course all of these methods offer insight to the intrinsic properties of a material, but they generally require large and complicated systems.

6.2 A Novel approach: MCP to measure impurities

The MCP method could be useful in characterising impurities due to the contrast in DC electrical properties, however, it will only work if the impurities have a significant difference in microwave permittivity to the bulk sp^3 phase. Carbon black (which is almost fully sp^2 hybridised) is well-known to exhibit a large microwave absorption[13,200]. From Chapter 3, the dielectric loss measurements of graphite were extremely troublesome with the resonance response reaching the noise floor. This is due to the conducting sp^2 hybridised carbon. The cubic covalent bond structure of fully sp^3 hybridised carbon has very different electrical properties. Since all four valence electrons participate in bonding as shown in Fig. 6.1, the electron conductivity is much smaller and hence it is anticipated that the dielectric losses should be lower in comparison to sp^2. It is this difference in absorption that makes microwave spectroscopy useful to quantify the volume of sp^2 carbon.

In this chapter the MCP technique will be used to provide a point frequency measurement of complex permittivity at 2.5 GHz using the TM_{010} mode. This measurement will then be extended to look at other modes as well as using MBCP to determine any frequency dependence which may infer optimum characterisation frequencies and explanation of the loss mechanisms; in particular, investigating whether the measurement is percolating static electron conduction as opposed to polarisation loss from disorder and localised charges.

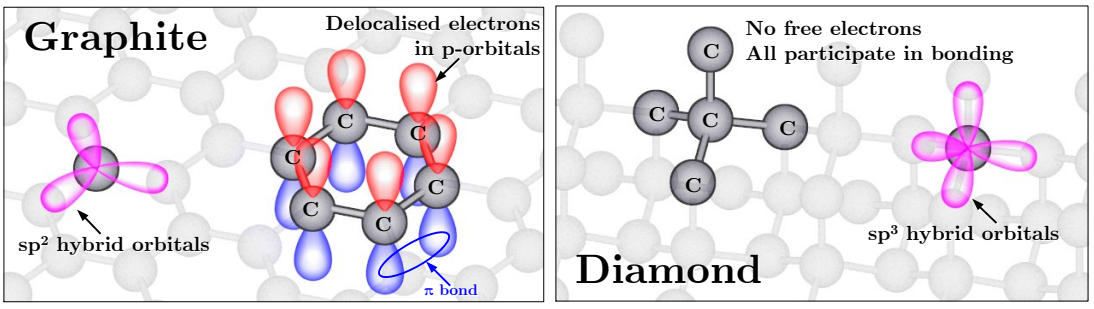

Figure 6.1: Differences in bonding structures of sp^2 and sp^3 carbon. The atoms in sp^2 carbon are hexagonally arranged whereas the atoms in sp^3 carbon are tetrahedrally arranged. The electrical difference between these materials is that sp^2 carbon is a good conductor (due to the p orbital electrons) and sp^3 carbon is an insulator (no free electrons).

6.3 Experiment: Determination of impurities with MCP

6.3.1 Aims and Objectives

The aim of this experiment is to determine whether MCP measurements can be used to infer the amount of surface impurities on the particles through verification with other techniques. To do this, samples with varying impurity concentrations are needed. This can be realised by measuring nanodiamonds of varying size. By varying the average sizes of the particles, the surface area of the powder can be controlled and thus the surface impurities. The TM_{010} mode of the Cyl-ε measurement system is used in conjunction with Raman (to determine surface impurities), XRD (to measure impurities, identify diamond and determine a varying size) and Field Emission Scanning FESEM (to determine a varying in size).

6.3.2 Samples and Procedure

The particles under study were various sizes of the Syndia SYP nanodiamond range provided by Van Moppes Geneva, Switzerland. This particular range of nanodiamonds exhibit block-like particle shapes which are specialised for polishing. The advertised size bands of 0-0.03 µm, 0-0.05 µm, 0.5-1 µm and 1-2.25 µm were used. The first two powders exhibited a solid black colour, the third showed a dark grey colour while the final two showed very light grey colours.

The Raman measurements were conducted using a Renishaw inVia Raman microscope with a 514 nm argon ion laser. The sample was illuminated with 100 laser pulses with a period of 1 second and a power of 25 mW. A spot diameter of 0.65 mm was used to provide an appropriate average over the volume of the particles as well as irradiation at numerous sites in the powder to ensure repeatability. XRD was conducted using the same Cu $K_{\alpha 1}$ X-ray wavelength of 0.15405 nm used in Chapter 5. Field Emission Scanning Microscopy (FESEM) of the powders was done using a Philips XL-30 FESEM. In this set-up, the particles were spread over a silicon surface to avoid charging. Multiple images were taken to calculate the average particle sizes. MCP measurements were conducted using Cyl-ε detailed in Chapter 3. The sample powders were poured into quartz tubes (outer and

inner diameters of 2.4 mm and 2.0 mm respectively) and left to settle on a vibrating stage for 10 minutes. Quartz was chosen as a tube material as it has very low dielectric loss and thus minimal effect on the unloaded centre frequency and bandwidth. Packing in the tubes was quantified by measuring the mass of the empty and filled tubes whilst taking into account the volume of the filled powder. With mass and volume, the effective packing density in the tube can be obtained. The quotient of the tube density and the intrinsic density yields the effective packing density.

6.3.3 Raman Spectroscopy

Raman was conducted across a wavenumber spectrum of 800 to 1700 cm^{-1}. Due to the highly absorbing nature of graphitic carbon, the sensitivity of the measurement is reduced for the smaller particles sizes. This is because Raman looks at the difference in wavelength of the incident and emitted photon (or Stoke's shift); since most of the laser energy is absorbed, converted into phonons and lost as heat, the emitted photon intensity is low. In some instances, nanodiamond has been detected via other means (XRD for example) but no diamond peak in Raman has been found simply because of the large volume of carbon impurities on the surface[65]. This is evident in the results given in Fig 6.2, where the noise floor is very high for the smaller sizes.

There are three main features noticed in the Raman spectra shown in Fig 6.2. The first is the sharp resonance peak at 1332 cm^{-1} which is a characteristic of the presence of sp^3 carbon, verifying that the materials being measured are diamonds[201]. This peak is most prominent in SYP_{050} and SYP_{125} which diminishes in intensity with SYP_{015}, SYP_{005} and SYP_{003}. This decrease is actually due to an increasing background from the absorption of the surface impurities. A slight shift in the diamond peak is also noticed in the less pure samples which may be due to the small size of the particles[202, 203]. Osswald et al. reported that smaller nanodiamonds produce shifts in the main diamond peak due to phonon confinement effects. Since the 1332 cm^{-1} T_{2g} line is for a bulk diamond material, the phonon vibrational mode is intense for large particles. As the size diminishes, the volume of the absorbing impurities is far more significant and thus the observed phonon mode becomes a convoluted effect from both stretching of the sp^3 bonds and the impurity bonds.

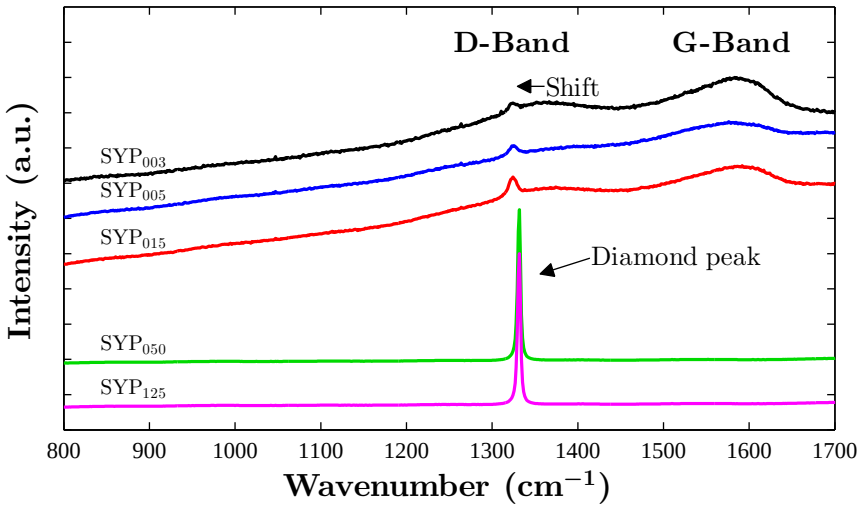

FIGURE 6.2: Raman Spectra of nanodiamond from 800 to 1700 cm^{-1}. For $SYP_{003-015}$, the D-band at approximately 1350 cm^{-1} is convoluted with the diamond peak at 1332 cm^{-1}. The G-band at approximately 1580 cm^{-1} is clear evidence of non-diamond carbon for smaller sizes. For SYP_{050} and SYP_{125} the diamond peak is completely dominating the spectrum.

The second and third features are the two broad peaks at approximately 1600 cm^{-1} and 1350 cm^{-1} which correspond to the G-Band and the D-Band, respectively. The G-Band refers to the presence of sp^2 hybridised carbon and is associated with the stretching of the carbon bonds in the hexagonal 2D lattice structure[204]. This band is most prominent in SYP_{003} (which is the smallest size) and diminishes slightly in SYP_{005} and SYP_{015}. Finally, it is unobservable in the largest sizes, SYP_{050} and SYP_{125}. This confirms diminishing levels of sp^2 carbon from the smallest to the largest size. The D-Band refers to disorder carbon which has no crystalline structure. A significant D-band implies that there are high number of defects on the surfaces of the particles. This type of carbon again follows a similar trend to the sp^2 carbon impurities; scaling in intensity with decreasing size, however, for SYP_{005} the D-band is very shallow.

Raman Spectroscopy has shown a reasonable qualitative measurement of the presence of surface impurities on the nanodiamond particles, with the smallest sizes being the most impure as expected. Moreover both sp^2 carbon and disorder carbon impurities were detected. The intensity of the G-Band in SYP_{003}, however, is much larger than the D-Band. However, a sensitive quantifiable figure of merit is unobtainable. It is also worth noting at this point that after irradiation, dark spots were left on the largest powder size, demonstrating that this technique is somewhat destructive even at low power levels.

6.3.4 XRD

The XRD results given in Fig. 6.3 exhibit intense peaks at 2θ angles of 43.9, 75.2 and 91.4°which are consistent with the (111), (220) and (311) planes for an sp^3 hybridised carbon lattice. This pattern was matched to: *bort, carbonado diamond* (00-006-0675). Since XRD probes collective excitations of repeating crystal planes, it is not sensitive to the identification of spurious contributions of disorder and sp^2 carbon. If, however, there is a significant contribution, a very broad Bragg peak may be observed at a 2θ of approximately 25°[65]. In Fig. 6.3 there are some signs of a peak at 25°but the FWHM is large possibly due to the trace volumes. There are, however, traces of silicon carbide (SiC) and silicon dioxide (SiO_2) in SYP_{125} and SYP_{050}. This could be due to the processing method of the HPHT nanodiamond, and possibly introduced in the sieving procedures to obtain specific particle sizes. These are additional impurities that were not detected in the Raman measurements. The addition of these impurities in the larger sizes was not expected and may have some affect on the MCP measurements. This is because while measurements of SiO_2 performed in Chapter 3 showed that their dielectric constant and losses were small (even in large concentrations), SiC is often used as an 'auxiliary' absorbent in microwave absorbing materials to boost attenuation in other materials[205, 206]. Therefore, it may have a significant dielectric constant and loss, potentially greater than diamond. This means that any losses observed in these larger particles can potentially be due to SiC, though their trace amounts are expected to have minimal effect.

As used in Chapter 5, the FWHM of the peaks is related to the crystallite size (D) through the Scherrer formula:

$$D = \frac{K\lambda}{B_\theta \cos(\theta)} \tag{6.1}$$

where K is the shape factor of the grains (normally approximated to 0.9 for diamond[207]), λ is the wavelength of the X-Rays in metres ($\lambda = 0.15419$ nm), B_θ is the FWHM in radians and θ is the observed Bragg angle. The smallest FWHM is observed in SYP_{125} which increases with decreasing particle size. This is in agreement with 6.1 in that the larger advertised particles exhibit a narrower FWHM. The logarithmic scale shown in Fig. 6.3, is an unconventional presentation of an XRD pattern, however, the regular spacing between the different samples clearly shows that the intensity (and thus the FWHM) varies

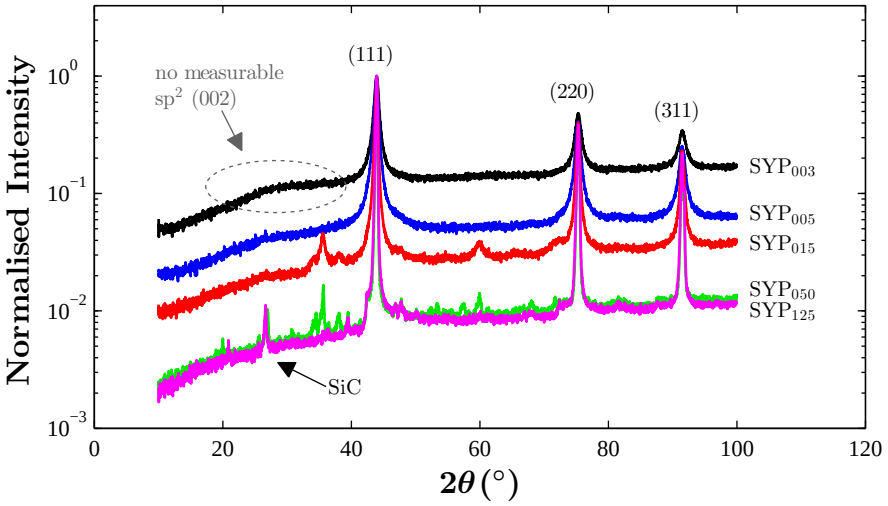

FIGURE 6.3: XRD of the nanodiamond particles $SYP_{003-125}$ over a 2θ diffraction angle range of 10 to 100°. The (111), (220) and (311) peaks are indicative of an sp^3 carbon diamond phase. The arrow pointing to the region from 20 to 30°shows some signs of SiC impurities. The (002) peak at approximately 25° for crystalline sp^2 carbon phases is not noticed, though a broad peak is noticed in SYP_{003}.

logarithmically. This is owing to the $1/B_\theta$ relationship shown in 6.1. If these particles are assumed mono-crystalline nanodiamond then, consequently, the diffraction pattern shows that the average particle size decreases from SYP_{125} to SYP_{003} in a logarithmic fashion. The calculated average crystallite sizes are given in Table 6.1 and are discussed in comparison to the FESEM data in the following section.

XRD has thus shown that the materials measured are made of diamond, however, there were no detectable signs of sp^2 carbon impurities (due to their spurious contributions) but some signs of Si related ones. The average crystallite size also decreases from $SYP_{125-003}$ which is in agreement with the Raman results in that surface purities scale with the smaller particle sizes.

6.3.5 FESEM

Sample FESEM micrographs are given in Fig. 6.4. There is a clear variance in size across the samples as anticipated. Multiple images were taken to provide average values of particle size given in Table 6.1. The average particle sizes are similar to those given in the datasheet with perhaps slightly larger particle sizes observed due to measurement error. Comparing the datasheet sizes, SEM sizes and XRD crystallite sizes, evidence suggests

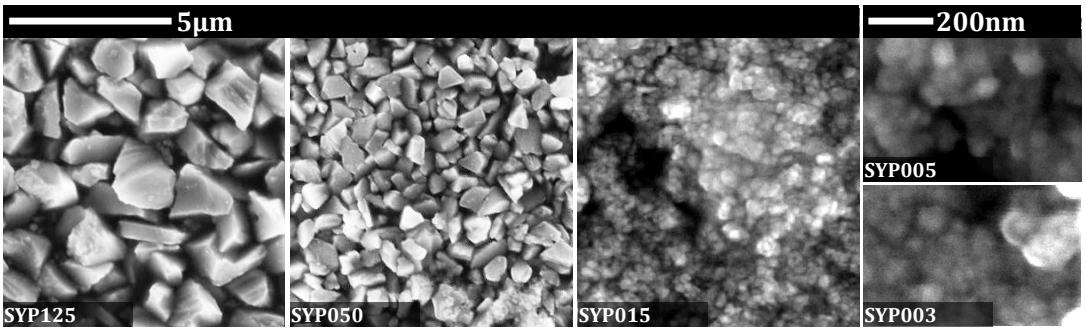

FIGURE 6.4: Sample SEM Micrographs of all nanodiamond samples used in this study. The scale for $SYP_{125-015}$ is shown at 5 µm while the scale for SYP_{005} and SYP_{003} is shown at 200 nm. It is clear that the average particle sizes of the different powders vary, therefore, any surface impurities will scale with the surface area.

that on average, these particles are in fact polycrystalline, more similar to that of ultra-dispersed diamond (UDD), even though they are advertised as mono-crystalline. The impact this has on the MCP measurements to determine *surface* impurities is that there may be an additional bulk polarisation and loss from whatever is at the dislocations. If, for example, the nanodiamond has a crack inside the particle resulting in a small concentration of disorder or sp^2 carbon, then the overall losses of the material is expected to increase. As well as the losses from the surface impurities, there will be an additional loss from the 'grain boundary impurities'. These concealed carbon impurities may be conducting in nature and interfacial polarisation may amplify the dielectric properties of the particle, as explained in Chapter 1. Hence, impurities may exist within the grain boundaries; most likely of the carbon variety if they are simply fractured (introduced in the milling process). Determination of the origin of this potentially erroneous crystallite size is not trivial since it requires a method to look *through* the particles. This can be achieved with High Resolution Transmission Electron Microscopy (HRTEM) and is highlighted as future work for investigating the effects of the polycrystallinity on the MCP results.

FESEM has shown that the average particle sizes vary which signifies that the surface area and thus surface impurities vary. This measurement in isolation, however, yields no direct information regarding sp^2 and disorder carbon impurities and is only used to prove that the surface area varies.

TABLE 6.1: Particle sizes with standard deviations, crystallite sizes and effective complex dielectric properties of nanodiamond powders measured at 2.5 GHz using TM_{010}.

Sample	**Datasheet Size (nm)**	**FESEM Size (nm)**	**XRD Crystallite Size (nm)**	**MCP at TM_{010}**	
				$\varepsilon_{\mathbf{eff,1}}$	$\varepsilon_{\mathbf{eff,2}}$
SYP_{003C}	18	30±5	10.5	6.8±0.3	$0.574\pm7\times10^{-3}$
SYP_{005C}	25	50±10	12.4	6.4±0.1	$0.501\pm2\times10^{-4}$
SYP_{015C}	75	160±30	23.8	4.9±0.1	$0.140\pm4\times10^{-4}$
SYP_{050C}	710	740±270	58.3	4.9±0.2	$0.017\pm2\times10^{-3}$
SYP_{125C}	1680	1750±320	78.0	5.2±0.1	$0.0189\pm2\times10^{-4}$

6.3.6 MCP

Table 6.1 shows the calculated complex permittivity at 2.5 GHz using TM_{010} with values normalised to the intrinsic density of 3.5 kg/cm^3 (as given by the datasheet) by taking into account the packing density (achieved subtracting the mass of the quartz tube from the powder filled tube to obtain an effective mass and thus an effective density in a known volume). The samples denoted with a 'C', refer to a cavity measurement (whereas later, probe measurements are denoted with a 'P' for comparison). Fig. 6.5 shows the MCP traces for the characterisation mode of TM_{010}. It is clear that there is a difference in microwave absorption across the samples at approximately 2.5 GHz. Recall that the real part of permittivity is associated with frequency shift and the imaginary part with bandwidth or Q factor. An increase in dielectric loss is observed with particles of smaller sizes which is indicative of an increasing volume concentration of an absorbing substance (surface sp^2 and disorder carbon). The measurements of the effective dielectric constant, however, are not as sensitive as the measurements of the effective losses. The relative changes from pure to impure is approximately 1.5× for the real part as opposed to approximately 20× for the imaginary part.

One could argue that the observed results merely show a size dependent dielectric constant and loss (for example $\varepsilon_{\text{large}}$ when the particle is big and $\varepsilon_{\text{small}}$ when the particle is small). Consider a large particle in an E-Field. A net build-up of charge occurs on the surfaces which focuses field in locations at the surfaces normal to the applied field. By this logic, this focuses the field onto the surfaces of adjacent particles, thereby making the measurement of surface species far more sensitive. This means that the effect of particle size on the microwave measurements merely increases sensitivity for surface impurities.

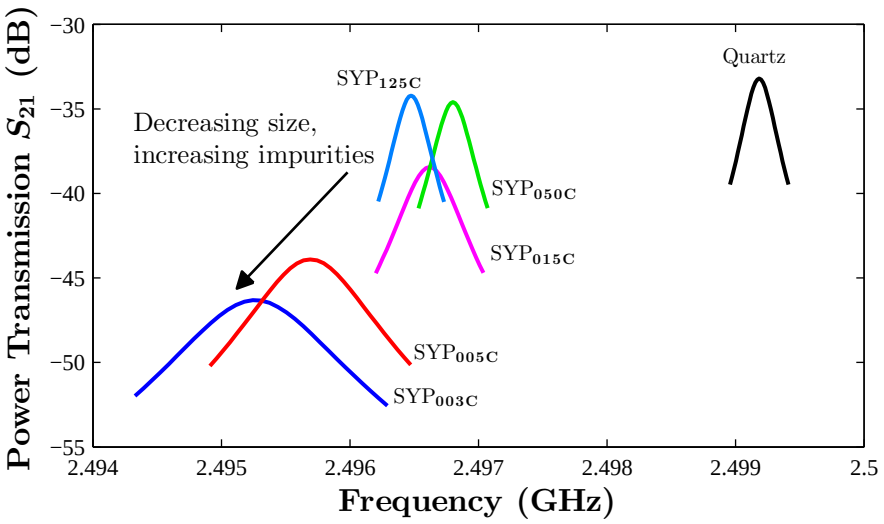

FIGURE 6.5: MCP traces of the TM_{010} mode for the $SYP_{003-125}$ nanodiamond powders. The decrease in Q factor on decreasing the particle size is evident, implying that the dielectric losses of the powder are increasing. The difference in frequency amongst the samples is small and therefore the dielectric constant does not change by a large amount.

Also, for this size dependence the largest size must have the smallest effective dielectric constant and loss, which is not the case. The effective dielectric constant of SYP_{125C} is slightly larger than SYP_{050C}, although this may be due to the larger concentration of SiC impurities in SYP_{125C}, identified by XRD previously. Since SiC has some loss, but a much larger dielectric constant than diamond, then this reasoning is plausible in that only a change is noticed in the real part.

If the increased losses are assumed to be due to the increasing amorphous and sp^2 carbon concentration, then the complex permittivity can again be modelled using the core-shell model. However, with no observable non-linear behaviour (such as the loss peak measured in the Fe_3O_4 to γ-Fe_2O_3 transition in the Chapter 5), a simple surface area to volume ratio model can be assumed. Since the lossy substance is distributed on the surfaces of the powder particles, it is expected that the volume of the impurities is proportional to the total surface area. In these experiments the total powder volume (which is almost all sp^3 carbon) is fixed. Hence, for a powder with N spherical particles each of radius a_i, the effective value of loss can be expressed by the following proportionality equation:

$$\varepsilon_{\text{eff},2} \propto \frac{V_{sp^2}}{V_{sp^3}} \propto \frac{\sum_{i=1}^{N} 4\pi a_i^2}{\sum_{i=1}^{N} \frac{4}{3}\pi a_i^3} \propto \frac{\langle a^2 \rangle}{\langle a^3 \rangle} \tag{6.2}$$

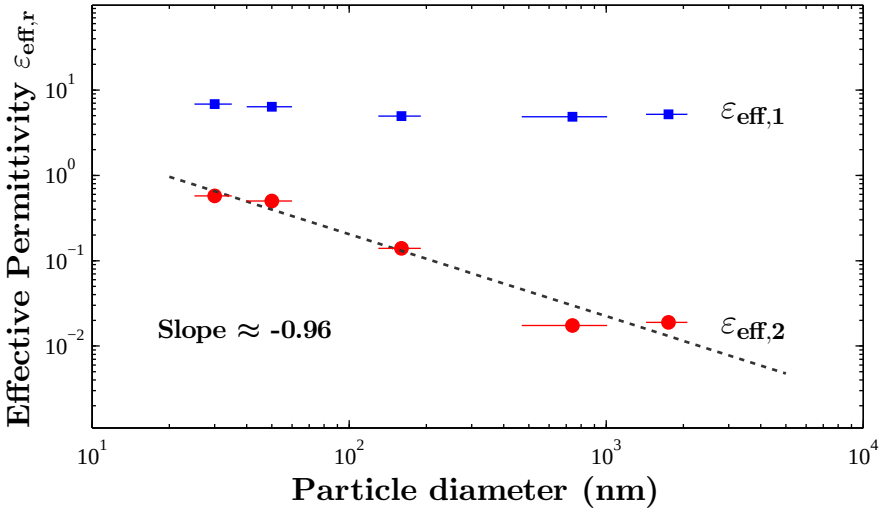

FIGURE 6.6: Calculated dielectric measurements at 2.49 GHz using the TM_{010} mode. Effective dielectric constant (top) and losses (bottom) are plotted against average particle size from SEM. An expected straight line relationship on a logarithmic scale is shown due to the losses effectively scaling by $\langle a^2\rangle/\langle a^3\rangle$.

where $\langle a^2\rangle$ and $\langle a^3\rangle$ are the averages of the squared and cubed radii respectively. Thus it is expected that the microwave loss is to be inversely proportional to the mean particle size. The dielectric loss is plotted against the mean particle size in Fig. 6.6. The $\langle a^2\rangle/\langle a^3\rangle$ relationship is clearly demonstrated by the almost straight line relationship on the log-log plot of the losses as a function of average particle size, with the gradient close to the expected value of -1. The fact that the observed gradient is not equal to -1 is to be expected from the weighted averages imposed by 6.2. Larger particles within the powder distributions will have disproportionately larger effects on the measured results, making the loss values lower than expected.

Thus it has been demonstrated that MCP measurements using TM_{010} strongly correlate with other measurements of determining the surface sp^2 and disorder carbon impurities present in nanodiamond powders. The results here show that a simple one mode MCP set-up at 2.5 GHz is capable of producing comparable results to more the standard material characterisation techniques.

6.4 Experiment: Frequency Dependence and Loss Mechanisms

The Cyl-ε cavity supports a range of other measurement frequencies which can provide some information on the loss mechanisms and the reason why the impurities are absorbing at these frequencies. Also the characterisation frequency of 2.5 GHz may not be the best frequency in the GHz range and higher frequencies may offer better results.

One of the main facts which underpins this preliminary experiment is that *sp^2 carbon has a high conductivity which gives rise to loss*, which is certainly true at microwave frequencies for the graphite samples shown in Chapter 3 and in other studies[128] and graphene based materials such as carbon nanotubes[208, 209]. However, this is only for regular repeating structures of the hexagonal sp^2 lattice. The delocalisation of the π orbital electrons is what gives rise to the long mean free paths of graphene and ballistic conduction of carbon nanotubes. Regular macroscopic structures allow percolating conductivity through the whole material; or if one is capable of attaching electrodes to the material, a DC current may pass through it. For nanodiamonds however, there are only trace amounts of sp^2 with almost no regularity, hence the π orbital electron may conduct but will be impeded by numerous defects resulting in space charge relaxation at lower frequencies. The π orbital electron may even be trapped or localised to a particle. Hence the static conduction mechanism, which is apparent in graphite and graphene, may be frozen out or even absent at microwave frequencies due to no suitable percolating pathways. The reason for the losses at microwave frequencies may simply be due to the polarisation losses of irregularly distributed carbon impurities. In this case, to microwaves, sp^2 and amorphous carbon are essentially the same thing in that they both lose energy through *polarisation* (as opposed to freely moving charge through the material).

Determination of whether the electrons in the sp^2 carbon impurities are in fact free to conduct can be qualitatively investigated by measuring the frequency dependence of the effective dielectric losses. Recall that in Chapter 1, electron conduction mechanisms arise in the dielectric losses through a $1/f$ dependence. The broadband MCP measurements can be corroborated with other broadband methods such as the microwave broadband coaxial probe (MBCP). This technique will be able to provide high resolution measurements over

the low to high GHz region. The sensitivity of MBCP is, however, not as good as the MCP method and requires contact, thus, consistent powder packing is far more problematic.

6.4.1 Aims and Objectives

In this experiment, the aim is to examine the frequency dependent dielectric properties of the impurities to try and understand the mechanism which gives rise to the large microwave absorption of nanodiamond impurities at 2.5 GHz (percolating conduction or polarisation related). To do this the multi-mode technique is used to extend these measurements over frequency with verification from the MBCP technique.

6.4.2 Analysis of MBCP

The MBCP system has been researched by a previous PhD student[140]. For the purposes of this experiment, an overview of this technique is now presented. The probe consists of an open ended coaxial cable, achieved using an Anritsu K-connector embedded in a brass flange, such that the electric field disperses evanescently at the half-plane at the probe's end, as shown in Fig. 6.7. The aperture of the probe is the active region which has an outer diameter of 1.6 mm with an inner conductor with a diameter of 0.3 mm. The sample is simply placed at the end of the probe, where there is a maximum of E-field (owing to the open circuit boundary condition). Complex permittivity can be calculated by measuring the reflection coefficient Γ of the probe using the following equation[140]:

$$\Gamma = \frac{1 - Z_0 Y_L}{1 + Z_0 Y_L} e^{j\theta} \tag{6.3}$$

where Y_L is the admittance of the end of the probe, θ is the equivalent phase difference introduced due to the length of the probe and Z_0 is the impedance of the system (50Ω). Since the probe has a standard K-connector which will interface with standard 3.5 mm microwave coaxial cables, the probe can be calibrated to the port to account for any standing waves in the reflection measurement. However, calibration to the sample plane can only be accomplished by designing perfect open, short and load terminations for the probe. A simpler approach to account for the phase difference across the probe is to first measure the probe when air-spaced (subscript 'a' below) and then measure with a sample

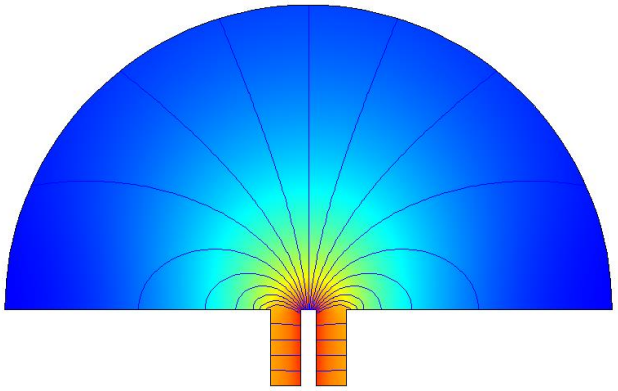

FIGURE 6.7: COMSOL simulation of logarithmic electric field distribution of an open ended coaxial probe in the GHz frequency range. The active sample region of the probe is at the tip of the probe where the E-field evanescently disperses into the air atmosphere. The change in impedance of the domed space when perturbed with a dielectric results in a change in the complex reflection coefficient.

load (subscript 'L' below), then forming a ratio:

$$\frac{\Gamma_L}{\Gamma_a} = \frac{1 - Z_0 Y_L}{1 + Z_0 Y_L} \frac{1 + Z_0 Y_a}{1 - Z_0 Y_a} \tag{6.4}$$

The admittance at the end of the probe can be modelled as two capacitors in parallel giving[210–212]:

$$Y_L = j\omega(\varepsilon_0 \varepsilon_{\text{eff}}(C_0 + C_f) \approx j\omega(\varepsilon_0 \varepsilon_{\text{eff}}(C_0) \approx Y_a \varepsilon_0 \varepsilon_{\text{eff}} \tag{6.5}$$

where C_0 is the capacitance when terminated in free space, C_f is the fringing capacitance. The two capacitances can be found by measurement of a known sample (for example a block of PTFE) and verified by simulation. Equations 6.4 and 6.5 can be used to deduce an approximate expression for the complex permittivity valid at lower frequencies:

$$\varepsilon_{\text{eff}} \approx \left(\frac{1}{j\omega\varepsilon_0 C_0 Z_0}\right)\left(\frac{1 - \Gamma_L/\Gamma_a}{1 + \Gamma_L/\Gamma_a}\right) \tag{6.6}$$

6.4.3 Samples and Procedure

The nanodiamond samples are the same as those used in the previous experiment. The multi-mode MCP measurements were repeated in the same way as the TM_{010} measurements. The permittivity in the MBCP measurements is also quoted as effective, as for the

MCP measurements, due to the finite air spaces between the particles. The packing in this method may, however, be different to the packing in the quartz tubes. Hence the effective packing density is calculated through mass and volume measurements (within experimental error) to allow comparison between MBCP and MCP measurements. For the MBCP measurements, the sample is compressed onto the end of the coaxial flange as shown in the system in Fig. 6.8. To calculate the packing density of the powders, they were packed into a separate jig with the same compression system. These samples occupied a cylindrical space with a diameter of 8 mm and a height of 1 mm. In this configuration, the mass was measured and thus the effective density was extracted. In a similar fashion to the sample tubes, taking this as a fraction of the material's intrinsic density as given by the datasheet of 3.5 kg/cm^3, the effective packing density can be determined, and this is typically about 0.3. This is mainly important for comparison with the MCP results.

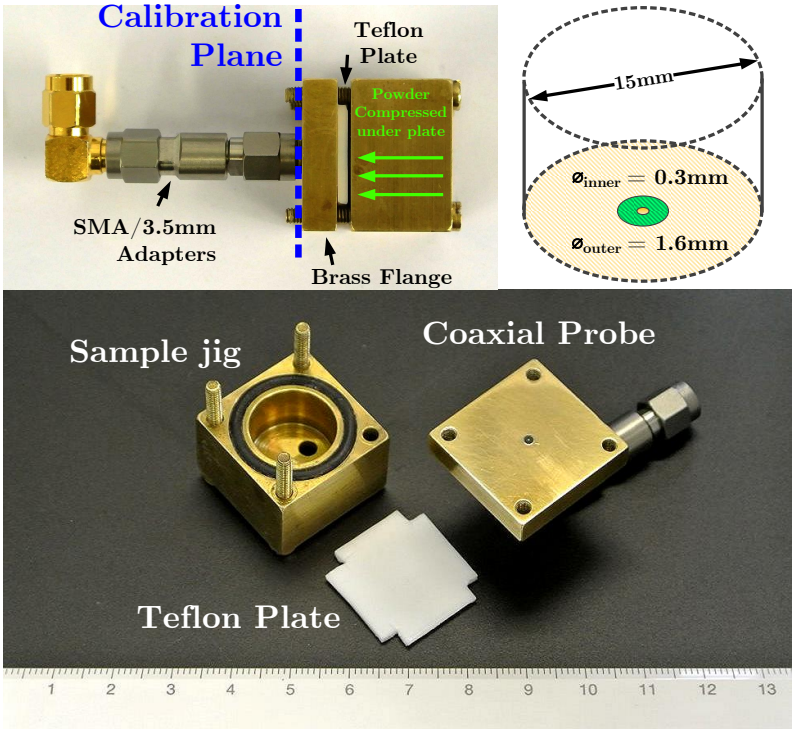

FIGURE 6.8: MBCP used for this experiment showing the calibration plane and the sample jig (top-left). Dimensions of the aperture and enclosure are given (top-right). Disassembled system (bottom) showing the aperture of the probe (the ruler numerals are every 1 cm). The PTFE sample used for the calibration covered an area of approximately 20 mm × 20 mm with a thickness of 1.5 mm.

6.4.4 Broadband MCP and MBCP

Overall, the complex permittivity measurements obtained with the coaxial probe correlate well with the cavity measurements. The errors in the MCP measurements are less than the sizes of the markers whereas for the MBCP measurements there is, however, a notably large variation in the real part across each of the powders, as shown by the shaded regions of the standard deviation in Fig. 6.9. In comparison, the cavity measurements yielded much smaller errors across the samples. The sample errors for the real parts in the cavity measurements were less than the errors for the probe data. This is most likely associated with the subtle differences in powder packing between the measurements. The errors in the loss measurements are again largest in the probe measurements compared to the cavity. The sample errors in between 0.1 to 1 GHz (further referred to as the low GHz range) are much larger than in between 1 to 10 GHz (further referred to as the high GHz range).

Table 6.2: Calculated complex permittivity of nanodiamond powders using multiple cavity modes. Error bars given as standard deviations.

Mode	**Frequency (GHz)**	**Dielectric Constant $\varepsilon_{\mathbf{eff,1}}$**				
		SYP$_{003C}$	**SYP$_{005C}$**	**SYP$_{015C}$**	**SYP$_{050C}$**	**SYP$_{125C}$**
TM_{010}	2.503	6.8 ±0.3	6.4 ±0.1	4.9 ±0.1	4.9 ±0.2	5.2 ±0.1
TM_{011}	4.532	6.7 ±0.2	6.3 ±0.1	5 ±0.2	4.9 ±0.1	5.3 ±0.1
TM_{020}	5.746	6.8 ±0.3	6.3 ±0.1	5 ±0.1	5 ±0.2	5.3 ±0.1
TM_{021}	6.891	6.7 ±0.2	6.3 ±0.2	5 ±0.2	5 ±0.2	5.3 ±0.1
TM_{012}	7.946	6.6 ±0.4	6.3 ±0.2	5 ±0.1	5 ±0.1	5.4 ±0.04
TM_{022}	9.496	6.5 ±0.3	6.2 ±0.2	4.9 ±0.1	5 ±0.2	5.3 ±0.1

Mode	**Frequency (GHz)**	**Dielectric Loss $\varepsilon_{\mathbf{eff,2}}$**				
		SYP$_{003C}$	**SYP$_{005C}$**	**SYP$_{015C}$**	**SYP$_{050C}$**	**SYP$_{125C}$**
TM_{010}	2.503	0.574 $\pm 7\times10^{-3}$	0.501 $\pm 2\times10^{-4}$	0.140 $\pm 4\times10^{-4}$	0.017 $\pm 2\times10^{-3}$	0.0189 $\pm 2\times10^{-4}$
TM_{011}	4.532	0.542 $\pm 5\times10^{-3}$	0.478 $\pm 1\times10^{-3}$	0.146 $\pm 4\times10^{-4}$	0.019 $\pm 2\times10^{-3}$	0.0208 $\pm 3\times10^{-4}$
TM_{020}	5.746	0.572 $\pm 6\times10^{-3}$	0.502 $\pm 4\times10^{-4}$	0.1525 $\pm 2\times10^{-5}$	0.016 $\pm 2\times10^{-3}$	0.0192 $\pm 3\times10^{-4}$
TM_{021}	6.891	0.555 $\pm 4\times10^{-3}$	0.491 $\pm 2\times10^{-3}$	0.151 $\pm 4\times10^{-4}$	0.016 $\pm 2\times10^{-3}$	0.0196 $\pm 4\times10^{-4}$
TM_{012}	7.946	0.56 ±0.01	0.496 $\pm 4\times10^{-3}$	0.157 $\pm 6\times10^{-4}$	0.015 $\pm 2\times10^{-3}$	0.0191 $\pm 2\times10^{-4}$
TM_{022}	9.496	0.55 ±0.01	0.494 $\pm 4\times10^{-3}$	0.1562 $\pm 5\times10^{-5}$	0.015 $\pm 2\times10^{-3}$	0.0196 $\pm 5\times10^{-4}$

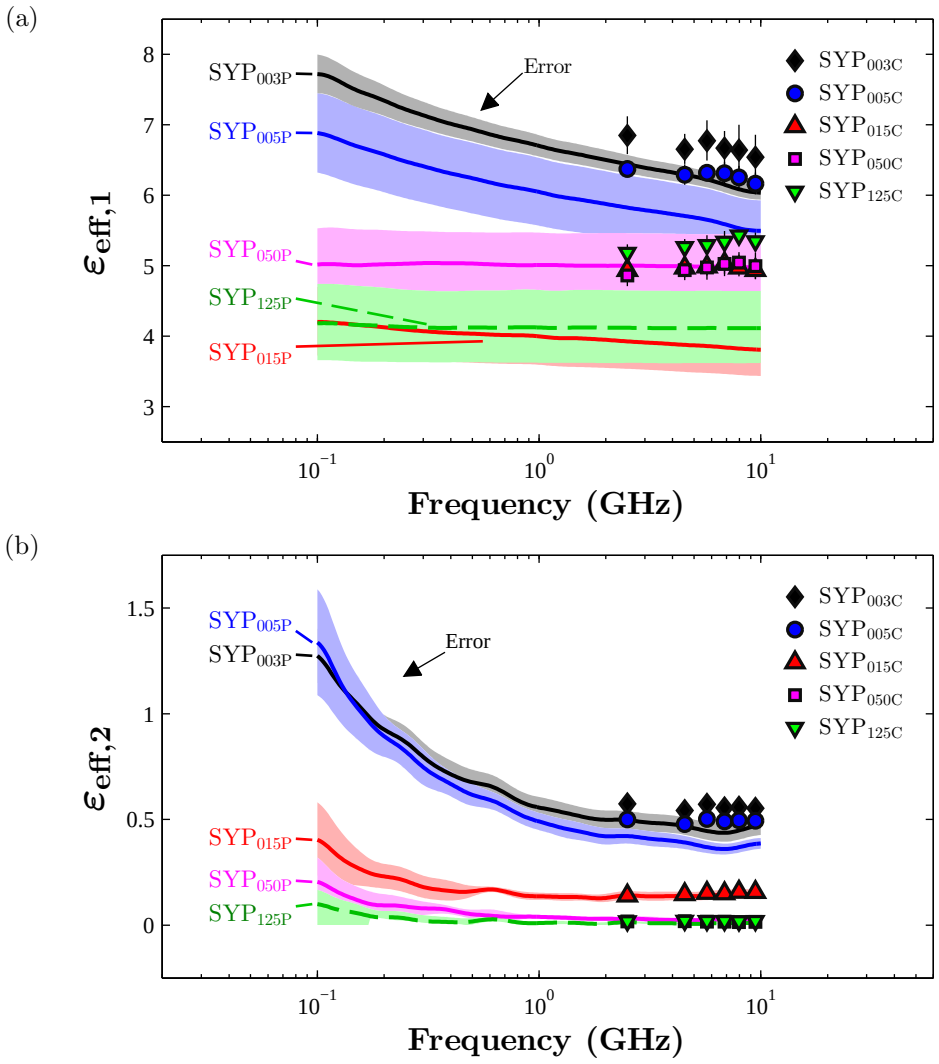

FIGURE 6.9: Measured permittivity of nanodiamond samples: (a) real and (b) imaginary. The lines represent values calculated with the probe method (denoted 'P') while the marked points show those achieved with the cavity method (denoted 'C'). Shaded regions show the standard deviation obtained across the samples. All values are normalised to the intrinsic density of 3.5kg/cm^3 to allow for sample and method comparison.

The model for the coaxial probe assumes that the material occupies the full, infinite half-space at the end of the probe. The extent to which this field radiates diminishes as materials with larger permittivities are placed at the aperture. In this instance we are probing a low permittivity material with notable differences in loss, but since the real part is low, the evanescent fields may not be contained wholly within the sample. Thus some fields penetrate into the jig and effectively 'probe' the sample holder. This causes the measurements of the real part to skew. Since the PTFE plate is a low loss material this does not greatly affect the loss measurements, but at lower frequencies penetration is greater and may radiate further. To avoid this, much larger volumes are required, greater

than the jig can support and that are practically available. For the purposes of this measurement system as a sensor for sp^2 impurities, this creates a large level of uncertainty for measurements of the real part. This is not so much a problem since it has already been ascertained from previous cavity results that the real parts show minimal correlation regarding sp^2 and amorphous impurities. Also the MBCP system is only meant to provide a qualitative estimation of the frequency dependence of the losses.

6.4.5 Microwave Loss Mechanism

Starting with the losses, Fig. 6.9a shows that they are largest in the least pure samples as expected. $SYP_{003-015}$ all had large concentrations of surface sp^2 and amorphous carbon and $SYP_{050-125}$ had undetectable amounts. The notable contribution in this study is that both the MCP and MBCP measurements show similar frequency dependent responses which corroborate the initial findings of disorder related loss mechanisms at microwave frequencies. Moreover, the broader band measurement of MBCP reveals significant frequency dependent behaviour in the losses in the low GHz range and also across the whole range in the real part for $SYP_{003-015}$.

The decrease in loss with frequency in the low GHz range is implicit of either free electron conductivity or space-charge polarisation, both of which are mechanisms related to conduction. To establish the potential cause, we must look at the measurements of the real part as well. Free electron conductivity appears in just the losses with a $1/f$ dependence. Space-charge polarisation appears in both the real and imaginary parts of permittivity. Due to the inertia of the movement of large areas of charge, relaxation occurs at low frequencies. This mechanism can therefore be identified by a decrease in both the real and imaginary parts as frequency increases[88]. From Fig. 6.9a and 6.9b, for less pure samples, a negative slope with increasing frequency emerges in both parts, however, the real part continues to decrease even when the losses appear to be frequency independent. Due to this, a clear determination of space charge cannot be reached.

An approximate representation for the net contribution to loss is shown in Fig. 6.10 where at lower frequencies, static conductivity and space-charge polarisation dominate (where $\varepsilon_{\text{eff},2}(\omega) \propto \sigma_{\text{dc}}/\omega$ and atomic and electronic relaxation frequencies $\omega_\tau \gg 1$ GHz) and at higher frequencies, polarisation related losses dominate from localised electrons and

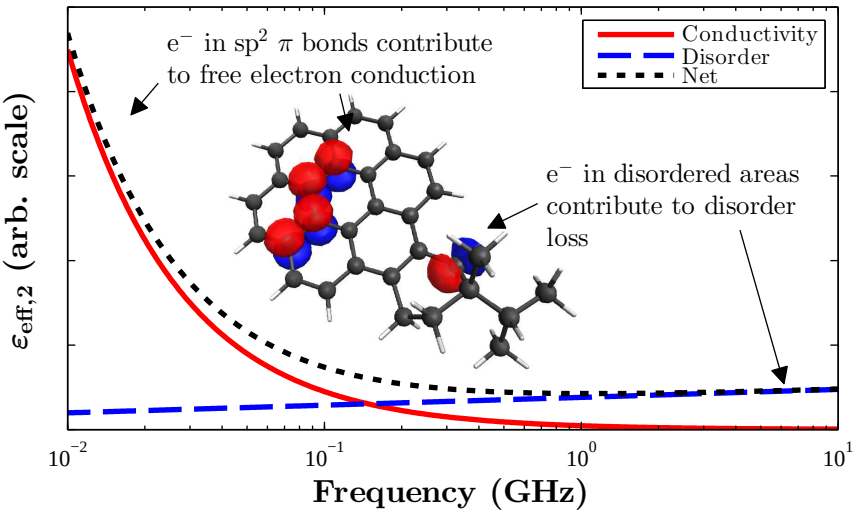

FIGURE 6.10: Simplified contributions to dielectric loss from delocalised electrons (i.e. conductivity and space-charge) and polarisation related loss mechanisms[79]. Inset shows the delocalised electrons in the p orbitals in sp^2 carbon which gives rise to electron conductivity and representative disorder loss created using Avogadro, GAMESS and MacMolPlt[213–215].

disordered carbon. The frequency dependence of this mechanism is, however, unknown and is depicted as a relatively constant loss with an increasing gradient that eventually approaches the atomic relaxation peaks which occur at THz frequencies as shown in Fig. 1.4.

The losses can be modelled as an independent free-electron conduction mechanism using the $1/f$ divergence at low frequencies shown in 1.5. Taking the average values over the measurement and fitting to this equation, the effective values of conductivity can only be estimated, since the errors in the low frequency region are large. Table 6.3 shows the estimated values for the effective contribution from free electron conductivity and the disorder related dielectric loss mechanisms. The loss mechanism measured with the original MCP method is therefore most likely not caused by free electron conduction and must be some disorder polarisation related mechanism. This disordered dielectric loss mechanism has been reported in sp^2 carbon allotropes, where these highly free electron conducting materials exhibit an additional loss at GHz and THz frequencies[216] (the $\varepsilon_{\text{eff,2,d}}$ offset in Table 6.3). This loss mechanism may be attributed to junctions and defects on the surface where charges are localised[217] which is congruent with losses associated with the disordered nature of the carbon impurities on the nanodiamond; note that disorder related effects may occur from both spurious fractions of amorphous and sp^2

TABLE 6.3: Estimated contributions of static electron conduction to the dielectric losses of nanodiamonds at 2.5 GHz

Sample	**R^2 on Fit**	**σ_{dc} (mS/m)**	**$\varepsilon_{2,d,eff}$**	**Contribution at 2.5 GHz**
SYP_{003P}	0.98	5.0	0.45	7%
SYP_{005P}	0.99	5.4	0.38	9%
SYP_{015P}	0.94	1.5	0.11	9%
SYP_{050P}	0.96	1.0	0.02	26%
SYP_{125P}	0.91	0.4	0.005	37%

carbon as opposed to just the concentration of disorder/amorphous carbon. Interestingly, a larger contribution from σ_{eff} is noticed in SYP_{050} and SYP_{125} implying that disorder related effects start to decay with decreasing sp^2 concentration. There may even be a threshold of sp^2 concentration as to when this starts to dominate. Also, from a quality control perspective, the results show that the high GHz range is more appropriate for looking at nanodiamond purity in with MCP and MBCP methods due to its approximately constant and consistent response. Assuming that an appropriate microwave source and power detector can be obtained at high GHz frequencies, this means that implementation of an MCP sensor system can be achieved with a much smaller resonator than Cyl-ε.

6.5 CONCLUSIONS

In conclusion, is has been demonstrated that MCP is capable of measuring the amount of surface sp^2 and amorphous carbon of varying sized nanodiamond powders. Raman spectroscopy was able to detect surface sp^2 and amorphous carbon on smaller particle sizes, though at larger sizes it is undetectable and only gives the diamond response. Regarding quantifying sp^2 carbon, MCP is capable of producing a numerical figure of merit (effective dielectric loss or conductivity). XRD has been used to detect the crystallite size of the nanodiamond proving that the crystallite sizes are much smaller than the measured particle sizes. The sizes of the particles can be inferred from the diamond (111) peak in XRD though no signs of non-diamond carbon were detected due to its nominal levels and non-crystalline nature.

This chapter shows that the MCP method is excellent for high-sensitivity, non-invasive materials characterisation of non-diamond carbon impurities on nanodiamond particles. Data has been presented from Raman Spectroscopy which detected surface sp^2 and amorphous carbon on smaller particle sizes, though at larger sizes it is undetectable and only

gives the diamond response. Regarding quantifying sp^2 carbon, MCP is capable of producing a numerical figure of merit (effective dielectric loss). XRD has been used to detect the crystallite size of the nanodiamond proving that the crystallite sizes are much smaller than the average measured particle sizes. The sizes of the particles can be inferred from the diamond (111) peak in XRD though no signs of non-diamond carbon were detected due to its nominal levels and non-crystalline nature. Broadband complex permittivity measurements at microwave frequencies can be achieved using both MCP and MBCP, with the MCP method giving a much higher sensitivity over a broad range but MBCP provided insight into the loss mechanisms active at microwave frequencies. This experiment also showed that the MBCP method corroborates the frequency dependent behaviour found with the MCP measurements, in that the dielectric losses of the sp^2 and amorphous carbon phases have minimal frequency dependence in the low GHz range. The loss mechanism providing the figure of merit for impurity at microwave frequencies is inferred as due to polarisation losses linked to the disordered nature of the surface sp^2 and amorphous carbon impurities, though the exact mechanism has not yet been determined.

The significance of this experiment shows that nanodiamonds or any pure insulating materials can be probed for impurities (very effectively using MCP) especially if the impurities are highly absorbing at microwave frequencies (such as graphitic or amorphous carbon). This would mean that material scientists can simply fill the insulating powder into a tube and place it into the cavity to determine their purity.

CHAPTER 7

Study: Photo-reactivity of Titania Powders

The General Problem - photo-reactivity

In air purification[218] and light induced drug delivery[75], photo-reactive titania (TiO_2) is needed to decompose pollutants or release antibiotics while the opposite is required in pigmentation to avoid 'chalking'. Thus, a simple way to measure *photo-reactivity* is of interest.

The Approach

In this section it is proposed to use the MCP method to measure the photo-reactivity of materials of different TiO_2 powders. The MCP method is sensitive enough to measure minute changes in dielectric properties where some materials exhibit what is known as a photo-dielectric or photo-conductive effect which can infer the photo-reactivity.

Key Findings

Preliminary results show Anatase TiO_2 has a large photo-dielectric response with long lifetimes congruent with the excitation of trapped electrons. Rutile shows a null response implying that the improved photocatalytic nature of anatase when compared to rutile may be linked to the density of electron traps. This demonstrates that MCP is a highly sensitive method for examining the photocatalytic properties of anatase TiO_2.

This is an ongoing study, where only ***preliminary*** *results are presented. In light of this research, further work for a new PhD student at Cardiff University has been initiated.*

7.1 Characterising photo-reactivity

Photocatalysis is an important field of research for looking at destroying organic species in various atmospheres. Titania (TiO_2) has been highlighted as an effective photo-catalyst which can be used in the purification of water and air through the adsorption and subsequent decomposition of volatile species such as carbon monoxide pollutants and bacteria[72,73,75,219]. TiO_2 has many phases, some of which are far superior as photo-catalysts than others. Brookite is said to be one of the better photo-catalysts[220], however, its natural occurrence is rare while its synthesis procedures are still under research. Anatase and rutile, however, are naturally abundant with the former displaying slightly better photo-reactivity than rutile[71]. Explanation behind this has been given by Lutrell et al. whereby the surface chemistry and structure play large roles in this. One explanation is that anatase is a semiconductor with an indirect band gap smaller than its direct gap[71] and therefore has phonon assisted recombination[221]. This subsequently causes the excess charge carriers to have a longer lifetime due to an increased density of trapped states. Rutile, however, also has an indirect band gap but is similar to the direct band gap thus electrons may recombine easily[71].

TiO_2 is a photo-catalyst in that UV excited excitons contribute to surface reactions with adsorbed molecules. These excitons can separate creating mobile electron hole pairs which migrate to the surface. The generated electron reduces atmospheric O_2 to superoxide O_2^- and the hole oxidises surface oxygen to create two hydroxyl radicals in the presence of H_2O[222]. These reactive species then decompose pollutants and bacteria. If the excitons recombine, then they do not create any reactive species, hence probing the lifetime of excess charge carriers and thus the density of trapped states may infer the photo-reactive nature of the material.

The methods for determining photo-reactivity can be divided into two types. The first is detection of reactive surface species such as reactive oxygen species (ROS) and hydroxyl radicals. The more reactive species detected, the more likely the TiO_2 powder is to react with organic species. The second is the measurement of generated free charges (photo-conductivity) and bound charges (photo-dielectric). Since the creation of reactive species at the surface is dependent upon how many charge carriers reach the surface (dependent

upon their lifetime), detection of these evaluates the *potential* of a powder to be photo-reactive.

Electron Spin Resonance (ESR) techniques are generally used to measure the surface reactivity through in-situ photo-excitation of a sample inside of a microwave cavity whilst subject to a DC magnetic field. The increasing concentration of unpaired spins from the reactive species creates a characteristic ESR response[223–225]. Since, the dark state of TiO_2 has no magnetic moment from unpaired spins, this makes measurement simple through observation of a characteristic peak in the ESR response. This is different to the dielectric MCP approach in that the material is placed in the H field standing wave with a large DC magnet applied to align the unpaired spins of the free radicals.

AC and DC Conductivity measurements with in-situ photo-excitation is the approach to measure the photo-conductivity [226]. But, since DC and low frequency impedance measurements require contact, this method is not favourable for powders in assessing conductivity. RF and microwave systems are an obvious choice for non-invasive in-situ photo-excitation measurements of TiO_2 powders. The first and most famous studies are those by Hartwig and Hinds [227–229] which laid the foundations for using microwave cavities by looking at photo-dielectric and photo-conductive effects through changes in resonance using power reflection. This led to the development of transient microwave photo-conductivity (TMP) measurements and the advanced method of transient microwave photo-conductivity (AMTMP). The former involved measuring the reflection of a cavity resonator at a single frequency, but through very fast time scales. The disadvantage of this approach is that the measured amplitude could be a consequence of either a changing bandwidth or a changing resonance frequency. AMTMP accounts for this by measuring the whole resonance at slightly slower speeds. Attempts have been made to measure the photo-dielectric and photo-conductive responses using waveguides[230] and microwave cavity systems[231–233] with Janes et al. using MCP in reflectance mode with a 150W xenon arc source for long periods. The ambient conditions were controlled carefully (temperature and humidity) using chambers.

7.2 A Novel approach: Improved Nodal MCP Method

This approach uses the AMTMP method but the difference with this study is that now that it is possible to very accurately measure temperature using the nodal modes of the cavity, any systematic effects can be negated and the whole system can be simplified to a desktop resonator with an LED attached. Also, due to the abundance of semiconducting LED technology, monochromatic radiation can be achieved using high power LED's (with their radiative effects on the cavity negated using nodal modes). Also, in some studies, the dielectric properties are alluded to through changes in microwave parameters, but sample depolarisation and placement (as given in Chapter 2) is seemingly ignored; where the sample is placed in a maximum depolarising orientation[231]. In this approach, an attempt is made to simplify the system with aim to develop a compact and easy solution, which is capable of offering the same information as well as utilising temperature correction with nodal modes.

7.3 Analysis

7.3.1 Photo-excitation

There are numerous processes that occur in a semiconductor upon absorption of a photon with sufficient energy (larger than the band gap or trap level). These include: exciton generation resulting in electron hole pair creation, band gap recombination, excitation of charges to trap levels followed by recombination, and Auger recombination where conduction electrons transfer energy to other conduction electrons.

Electron hole pair generation is the excitation of valence band electrons to the conduction band and holes to the valence band for a finite time before recombining. These charge carriers are *mobile* and cause the conductivity to increase and the dielectric constant to decrease when in the excited state. Upon recombination, the material relaxes to its 'dark' state. The Auger recombination process may increase the conductivity momentarily as energy is transferred to relaxing electrons.

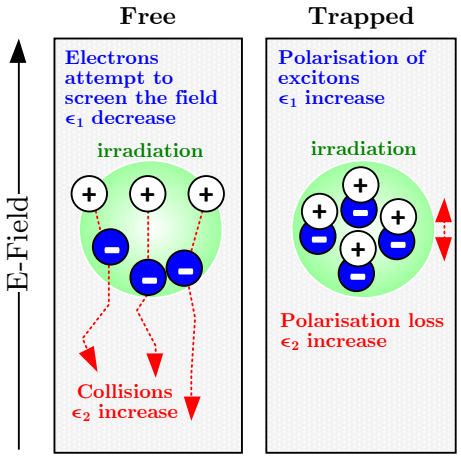

FIGURE 7.1: Abstract representation of free and trapped electron photo-dielectric effects. Free electrons attempt to screen the field from the material thus limiting the number of dipoles which react with the field. This hence decreases the dielectric constant. The movement of the electrons creates heat and thus dielectric loss. Trapped charges simply displace and any losses are associated with the time required for this to occur.

Electrons can also be excited to traps in-between the valence and conduction band where they are not as free as those in the conduction band. Since these charge carriers are effectively not mobile, this does not increase conductivity but instead increases the dielectric constant as charge displacement occurs. This is almost like a *trapped* charge carrier state, however, if the density of traps is high, these charge carriers can effectively diffuse through the material by hopping to other trap levels through thermal excitation before relaxing (similar to thermally induced ionic conductivity).

Thus, in the general case there are *free* and *trapped* charge carrier mechanisms. Grabtchak and Cocivera proposed a collection of formulae to relate free and trapped charge carrier kinetics to the photo-conductivity and photo-dielectric response of a semiconductor through microwave measurements[234]. The change in the complex permittivity can be modelled by:

$$\Delta\varepsilon_{\text{eff}} = \Delta\varepsilon_{\text{free}} + \Delta\varepsilon_{\text{trap}} + \Delta\varepsilon_{\text{plasma}} \tag{7.1}$$

where $\Delta\varepsilon_{\text{plasma}}$ is plasma depolarisation and is an additional effect due to very large concentrations of excess carriers in a small space such that the polarisation in the rest of the material creates a restoring force to maintain equilibrium. This results in an increase in both $\varepsilon_{\text{eff},1}$ and $\varepsilon_{\text{eff},2}$, however, for the non-depolarising geometry, these effects have been shown to be negligible[234].

Thus, the main contributions are due to free and trapped charges shown in Fig. 7.1. Free electron effects are described using the Drude-Zener model[230] which is given in 1.7. This means that an increase in photo-conductivity results in an increase in $\varepsilon_{\text{eff},2}$ but a decrease in $\varepsilon_{\text{eff},1}$. This decrease in the real part is attributed to the free electrons screening the field[230] while the increase in losses is due to the generation of heat from the collisions of the electrons. The decrease in the real part may also be explained by the fact that these electrons are no longer localised and therefore distortions of their electron cloud around their local atom no longer contributes. Trapped electrons are those which become localised in lattice sites for some time upon irradiation. A trapped charge can contribute to displacement polarisation resulting in an increase in $\varepsilon_{\text{eff},1}$ and an increase in $\varepsilon_{\text{eff},2}$. With this knowledge certain phenomena can be identified, though a convolution of both effects may be present.

7.3.2 Carrier Lifetime

A good a photo-catalyst requires a long carrier lifetime to reach the surface and stay active at the surface. It is known that carrier lifetimes in anatase far exceed those in rutile and this is the supposed reason as to why the former is a much better photo-catalyst[71]. Trapped charges (as the name suggests) have a much longer lifetime compared to free charges since they are impeded in the recombination process. Because of this, these generated charge carriers have a longer time to diffuse to the surface through trap hopping or even excitation from trap levels to the conduction band. Thus long lifetimes are favourable for photocatalysis as it gives time for more charges to diffuse to the surface to create more reactive species. In general, a large photo-dielectric or photo-conducting response implies a better photo-catalyst.

7.4 Experiment: Photo-reactivity of Anatase and Rutile

7.4.1 Aims and Objectives

The aim of this experiment is to determine whether photo-dielectric MCP measurements can infer the photocatalytic properties of TiO_2 powders. Anatase and rutile powders are tested where anatase is expected to be more photo-reactive. To achieve this, first the band gap is estimated in the TiO_2 powders using UV-VIS spectroscopy and then the MCP nodal correction method given in Chapter 4 is used for the photo-dielectric and photo-conducting response. This study aims to contribute to the reasoning of why anatase is better than rutile through photo-dielectric measurements.

7.4.2 Samples and procedure

The TiO_2 samples used in this study were provided by Kronos. One anatase (Kronos 3000) and two rutile pigments (Kronos 3025 and 2900) were measured denoted respectively as TiO_2-A1, TiO_2-R1 and TiO_2-R2. The Kronos 3000 and 3025 powders are branded as coarse powders without any pigmentary properties. The applications of these powders are to increase UV absorption in glasses as well as improving their electrical properties. The Kronos 2900 powder is a pigment grade rutile powder, used for road markings and emulsion paints. It is anticipated that this pigment should show little photo-reactivity since it is designed as a pigment whereas the other two should show some response as UV photons are absorbed and converted into excitons and phonons.

All powders were filled into the fused quartz tubes (outer diameter = 2.4 mm, inner diameter = 2 mm) used in previous experiments. As well as a suitable low loss microwave dielectric container, it also allows UV wavelengths as low as 300 nm into the sample specimen. The samples were placed on the axis of the resonator and measured continuously in time in the TM_{010} mode at 2.49 GHz. Temperature correction was achieved using the TM_{210} mode at 5.33 GHz in the same way as explained in Chapter 4. The samples were irradiated on separate occasions with the four monochromatic sources with 10 pulses at a frequency of 0.1 Hz with 50% duty cycle. The maximum sampling speed of the continuous LabVIEW acquisition program was 5 Hz. In this configuration speed is sacrificed for

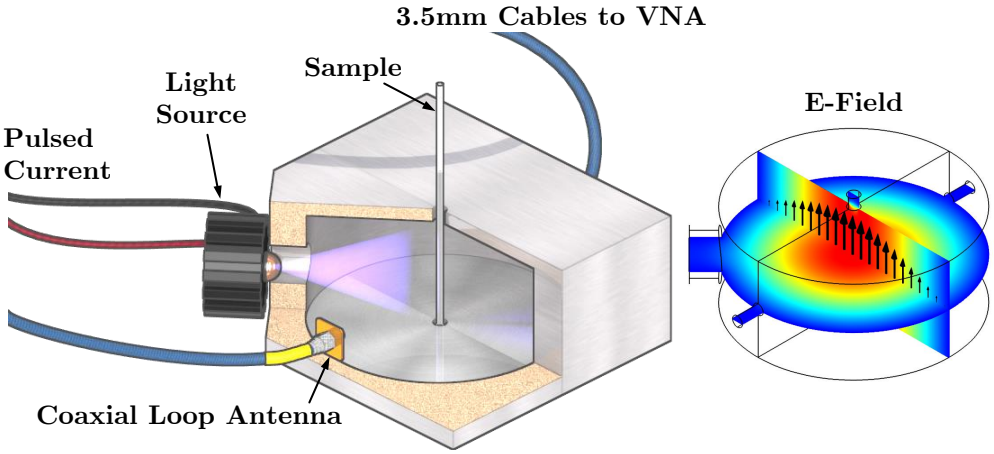

FIGURE 7.2: Cut section of Cyl-ι set-up for monochromatic photo-excitation. The light source is exchanged for different LED's to vary the wavelength of excitation. The TM_{010} mode is shown on the right, which demonstrates that the large hole for the light source has minimal effect on the field distribution.

greater resolution where the errors in frequency and bandwidth measurements were less than 1 kHz. Multiple modes are used for correction purposes, which again limits the speed of a measurement but this allows the correction of systematic errors. This was chosen because the changes in dielectric property are expected to be small.

The cavity used in this study (referred to as Cyl-ι) excites similar modes to the Cyl-ε cavity, however, the construction is different in that it is split along the axis into two aluminium pieces (2 'D shaped' cavities in the aluminium blocks). Full details on of the design of this style cavity was introduced by a previous PhD student[140], with a representation shown in Fig. 7.2. Although the split is down the centre, the current paths of the TM_{0mp} modes are not disrupted, since they flow along the split. TM_{1m0} and TE_{0mp} modes, however, are disrupted since the current flows along the gap minimising interference on the dielectric measurement modes. Cyl-ι is excited through short circuited loop coupling on the sides of the cavity meaning that considerable interference from higher order modes occurs (since these propagate along the curved walls of the resonator and are less affected by the split), hence only the TM_{010} mode is used for measurements with nodal correction provided by TM_{210} in this set-up.

The hole for the LED will cause small distortions in the TM_{010} field distribution hence calibration has been conducted with a PTFE rod in the method described in the previous Chapter 3. This gave a value of $G_{nmp} \approx 0.296$ which, interestingly, is not that different to Cyl-ε. Photo-excitation of the axial sample is achieved with LED's designed by LED

Engin, California, USA. Red (625 nm), green (523 nm) and blue (462 nm) excitation was achieved using an LZC-A0MA00 multi-colour LED while UV (365 nm) excitation was achieved using an LZ1-10U600 LED. To normalise the output power of the LED's, the DC voltage applied across the LED was varied such that the same relative intensity could be achieved as given using the information provided in the datasheet (current of approximately 700 mA). As further work to continue this research, characterisation of the output intensities as well as verification of the wavelengths of the LED's would be favourable, however, for the purposes of this study, it is recognised that the variation in output power would give differences in quantum yield and comparisons across different sources may not be extremely accurate. Pulsed current was provided by a Maxim 16820 driver circuit controlled by a square wave generator with a maximum rated frequency of 20 kHz, though the frequencies used in this study are less than 10 Hz.

7.4.3 UV-VIS

UV-Visible Spectroscopy was first performed using a Jenway 6000 series Spectrophotometer which uses a combination of a tungsten halogen lamp and a deuterium lamp to provide excitation wavelengths in the range of 250 to 800 nm. This range was chosen such that the approximate bandgap energy of 3 to 3.2 eV (approximately 390 - 415 nm) could be

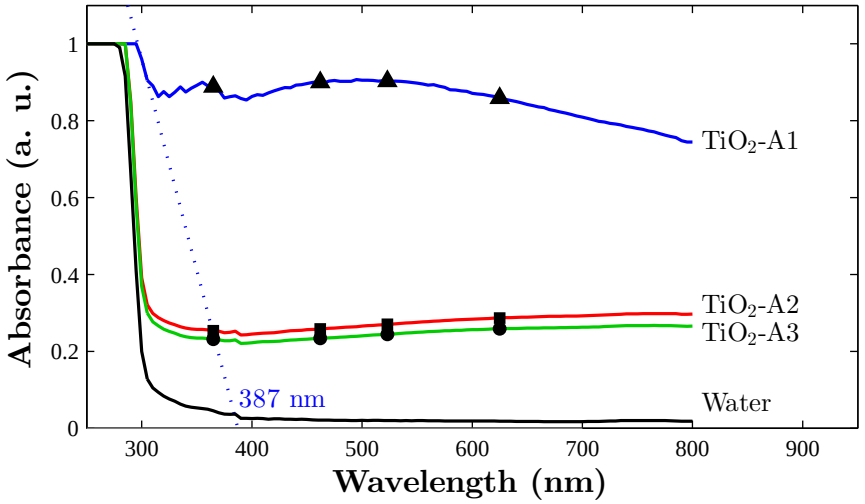

FIGURE 7.3: Measured UV-VIS Spectra of TiO_2 powders. Black markers show the points where the wavelength matched the LED's used for the MCP photo-reactivity study. Extrapolation of the absorption edge yields an estimation of the band gap of the material. For TiO_2-A1, excitation of wavelengths less than 387 nm can induce free electron conduction.

determined for the materials[72]. The samples were dispersed at 0.1% weight concentration in deionised water such that visible light transmission through the sample could be achieved.

The results are shown in Fig. 7.3 for the three powders. The band gap can be found through extrapolation of the absorption edge in the measurable region. This could only be extracted from TiO_2-A1 since a distinguishing absorption edge between the water reference and the sample could not be seen for TiO_2-R1 and TiO_2-R2. This could be due to the poor dispersive properties of all of these granular products. A band gap value of 387 nm which is approximately 3.2 eV was found for TiO_2-A1 which is congruent with those found in the literature[71]. This implies that any free electron conduction caused by electron hole pair generation should in theory only be seen upon irradiation with the UV LED at 365 nm, however, if there is a high density of electron traps below the conduction band, then excitation of electrons in these states will also result in photo-conduction. Also notice that the absorption across the band is also fairly constant showing that any photon scattering phenomena is constant.

Hence, UV-VIS spectroscopy has provided some information on the band gap of one of the materials. It is thus expected that excitation from wavelengths lower than 387 nm should give much higher losses than excitation wavelengths below the band gap (owing to an increase in conductivity from electron-hole pair generation). This measurement is important for MCP measurements in distinguishing free electron photo-conductivity from trapped electron photo-dielectric effects.

7.4.4 MCP Photo-excitation

The photo-excitation results of the anatase TiO_2-A1 sample are shown in Fig. 7.4 while the results for the rutile TiO_2-R1 and TiO_2-R2 samples are shown in Fig. 7.5. There is a noticeable change in frequency and bandwidth of the TiO_2-A1 as the sample is irradiated, however, these changes were not measured for the rutile samples. This implies that there is a distinct photo-dielectric difference between these phases. As stated, it is expected that anatase is a much better photo-catalyst[71], and there are some differences in the photo-dielectric behaviour[232], however, the changes witnessed in those experiments were no where near as drastic as the results presented here. Edge et al. did, however, conduct

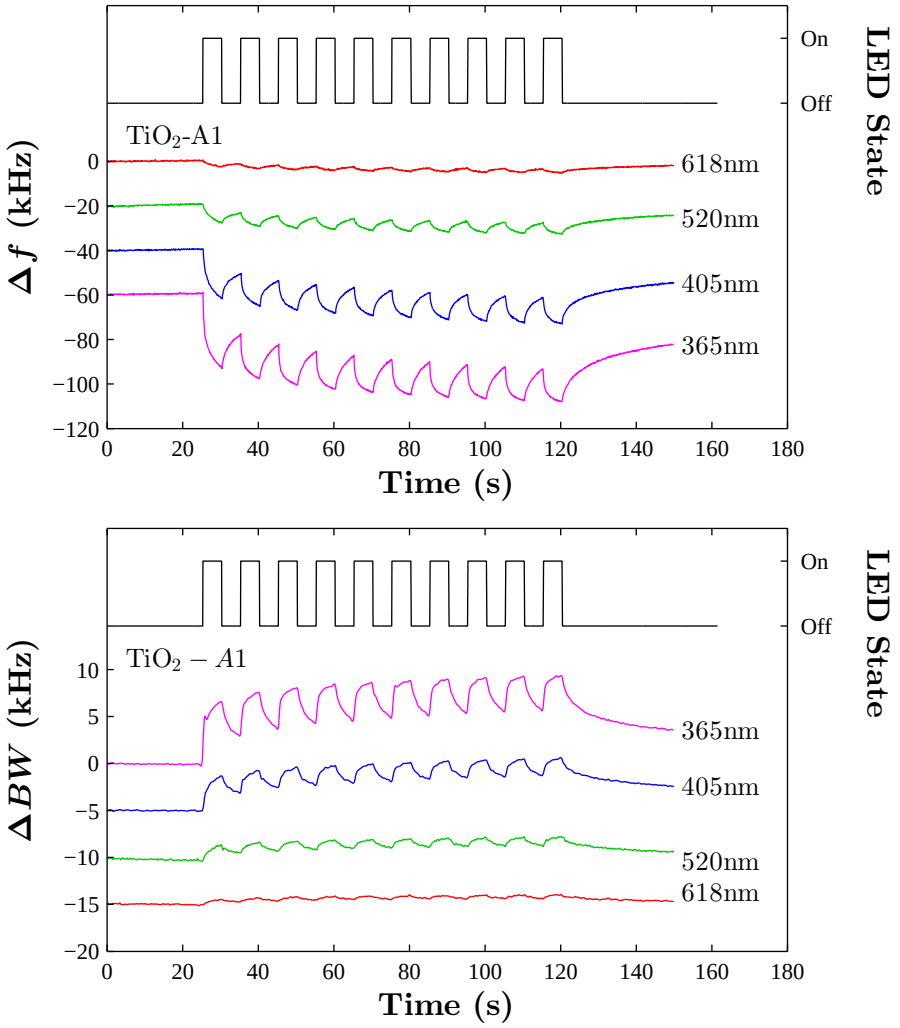

FIGURE 7.4: Changes in the resonant frequency and bandwidth of TiO_2A1 from excitation from various light sources. It is clear that with decreasing wavelength, the photo-dielectric response increases in both the change in resonant frequency and bandwidth.

their measurements with a 250 W tungsten light source which exhibited power dependent excitation. They found that excitation power of less than 200 W resulted in no photo-dielectric response which may be the case for these results. Practically, this makes the observation of photo-dielectric responses in rutile much more challenging and less feasible for this set-up. This may be one of the reasons as to why rutile is less photo-active.

The change in dielectric constant can be calculated by using 2.2a assuming $G_{nmp} \approx 0.296$. For a reference of scale in Fig. 7.4, a 20 kHz shift constitutes to $\Delta\varepsilon_{\text{eff},1} \approx 0.01$ which is the approximate amplitude of the oscillation for the 365 nm irradiation. For TiO_2-A1, the decrease in resonant frequency and increase in bandwidth implies an increase in

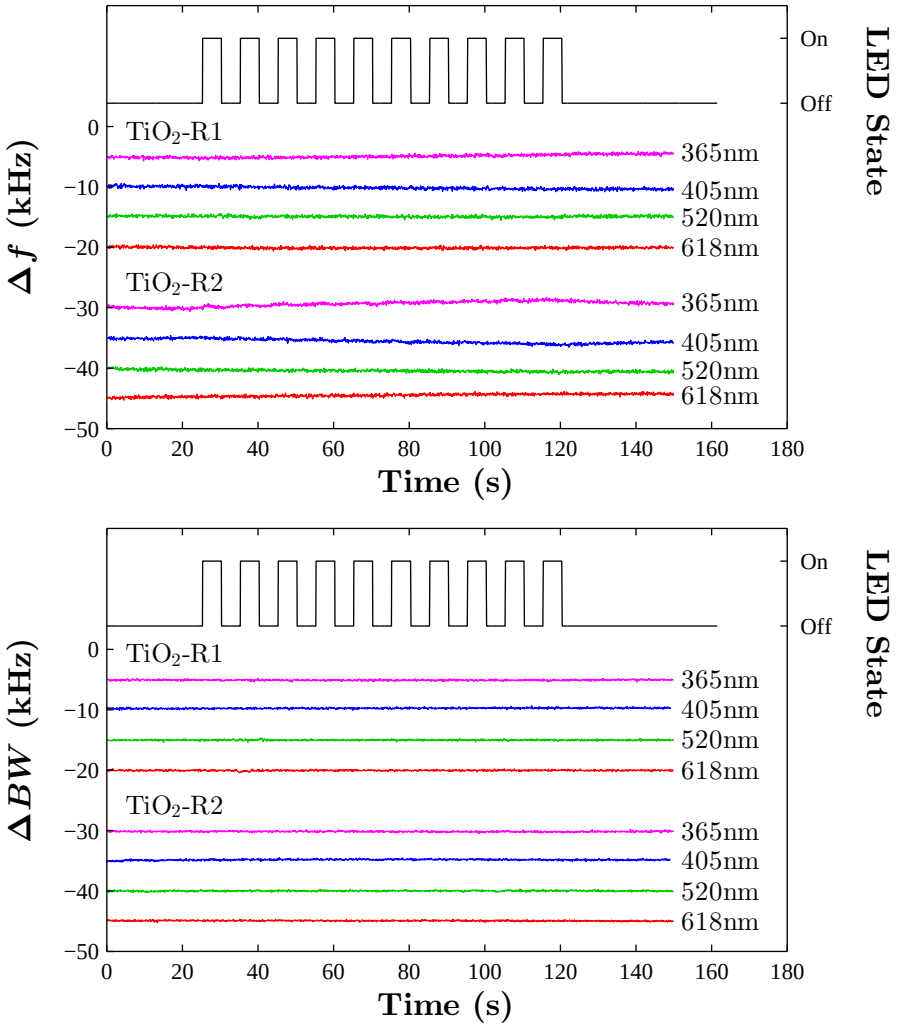

FIGURE 7.5: Changes in the resonant frequency and bandwidth of the TiO_2-R1 and R2 excitations from various light sources. It is clear that these rutile materials are not affected by photo-excitation from wavelengths from 365 to 618 nm.

polarisation and losses. This response is indicative of the excitation of trapped charge carriers as explained previously.

Also a photo-dielectric response is noticed at wavelengths much larger than the band gap wavelength of approximately 387 nm. This means that the response is most probably not due to band gap photo-conductivity. The dielectric constant should decrease (frequency increase) as per 1.6 with a more profound response at 365 nm. This may be happening at 365 nm and the presented result may be a convolution of both free and trapped electron effects.

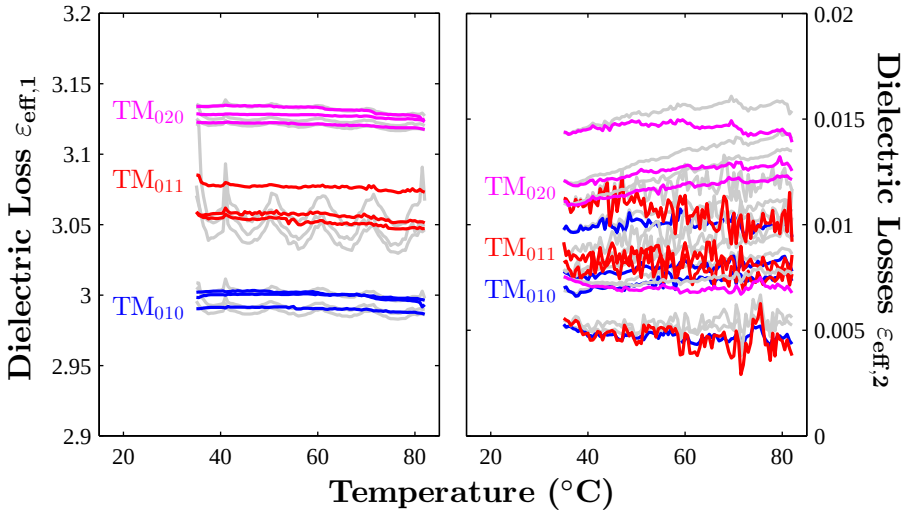

FIGURE 7.6: Measured temperature dependent dielectric properties of TiO_2-A1. 3 different ramps were conducted over 30 to 80 °C. The grey lines show uncorrected measurements, calculated through linear interpolation of the quartz and sample ramps. The coloured lines show the corrected temperature dependent response. using the TM_{310} mode.

7.4.5 MCP - TEMPERATURE

One could also argue that this slow increase may be caused by an increase in temperature of the sample due to thermal convection from the LED and the response is due to some remarkable thermal absorbing capability. As soon as the LED draws current in the photon generation process, it dissipates energy which might be radiating towards the sample. Though the TM_{210} correction procedure is capable of calibrating out effects on the cavity from LED radiation, it is not able to calibrate out changes in temperature at the sample location from an external influence. A simple way to verify this phenomenon is to conduct the same experiment with a temperature sensor on the sample, which was achieved using a pyrometer showing no noticeable increase. To verify this further, the temperature dependent properties of the sample can be measured to determine the equivalent rise in temperature for a change in dielectric constant of approximately $\Delta\varepsilon_{\text{eff},1} \approx 0.01$.

The results of three temperature ramps are given in Fig. 7.6. The results again demonstrate the effectiveness of the correction procedure in removing systematic fluctuations from the ramp. The dielectric constant is almost invariant with temperature while the measured losses of each ramp are also fairly constant with temperature although given their small values, the errors are quite large. The changes shown in Fig. 7.4 give $\Delta\varepsilon_{\text{eff},2} \approx 0.002$

which are much greater than the variations in Fig. 7.6 and do not indicate any change in dielectric property as a function of temperature. Thus, from this experiment the radiation effects of the pulsing LED are negligible and the resultant photo-dielectric response is intrinsic to the dielectric properties of sample. It is, however, worth noting that long term pulsed exposure (> 5 minutes) from the LED did result in a measurable temperature rise of a TiO_2-A1 sample at the sample location (verified by the pyrometer).

7.4.6 Trapped charges

Now that the result is determined to be a photo-dielectric effect, the excitation mechanism can now be considered as a mechanism related to the charge carriers. Consider the case where excitons are generated upon absorption of photons less than the band gap energy. The electron and hole never separate since they never reach the conduction or valence band respectively, but they do, however, reach a trap at an energy level in-between. If the absorbed photon has energy greater than the trap level, excess energy is lost to the lattice in the generation of phonons. As wavelength decreases, more electrons are excited to traps at different energy levels resulting in an increased loss due to phonons. Also these trapped excitons are polarisable constituents which increase the dielectric constant. This also means that their characteristic time to polarise contributes to the losses. This provides a plausible explanation as to why a resulting increase in polarisation and losses is observed upon radiation and also why an increased response occurs at lower wavelengths.

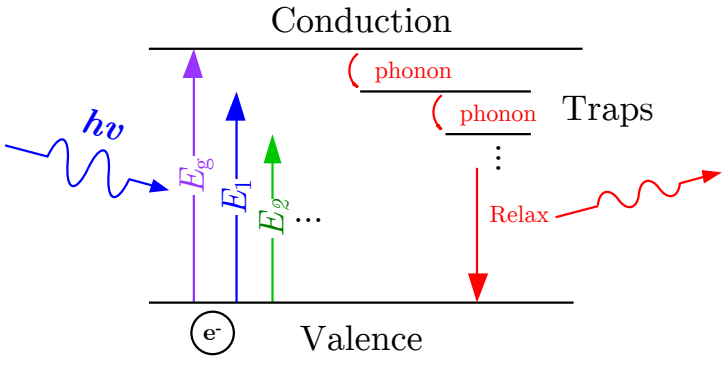

Figure 7.7: Abstract representation of the electron traps. With increasing photon energy, more electrons are excited to different traps resulting in polarisation increases. Losses are generated from the electron colliding with the lattice to reach the trap as well as dissipating the excess energy through the relaxation process.

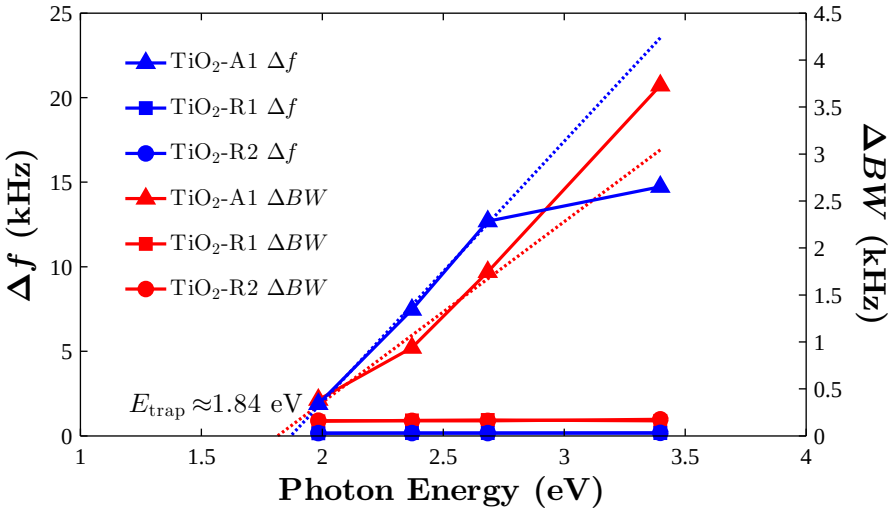

FIGURE 7.8: The average peak to peak of the complex frequency shifts of the different TiO_2 samples which imply the photo-dielectric and photo-conductive effects as a function of photon excitation energy. Dotted line shows the linear fit of the excitations below the estimated band gap of the material, providing an estimate of trap levels.

The average peak to peaks of each cycle for each wavelength shown in Fig. 7.4 are plotted in Fig. 7.8. At lower photon energies (higher wavelengths), the change in dielectric constant follows a linear trend whereas UV excitation does not. The reason for this may be due to differences in output power of the multi-colour and UV LEDs but may also be due to the fact that the response given at UV may be a convolution of both free and trapped electron effects (as alluded to earlier) since the energy here exceeds the band gap. From 1.6, recall that the change in frequency is opposite to the trapped case whereas the change in bandwidth is the same. This will result in a smaller change in frequency and a larger change in bandwidth which is shown in Fig. 7.8, meaning that UV excitation above the band gap excites both photo-dielectric and photo-conductive effects.

Since the wavelengths larger than the band gap are less affected by photo-conduction, an estimation of the energy required to excite a trapped charge can be determined through extrapolation of these effective photo-dielectric response shown in Fig. 7.8 where a value of approximately 1.84 eV can be obtained; though again this value is subject to the errors of the excitation power. In comparison to the band gap energy of approximately 3.2 eV, these trap levels are 1.36 eV below the conduction band and may be associated with electron and hole traps on oxygen atoms[235]. This assumes, however, that the excited charge carriers are initially in the valence band. These deep traps have been reported to contribute to large excess carrier lifetimes[236].

7.4.7 Lifetime

Another noticeable feature in Fig. 7.4 is that when the light is switched off, the excited charge carriers do not relax instantaneously and there is a finite carrier lifetime. These time constants are shown in Table 7.1. These seemingly increases with time, implying that with continuous excitation, a steady state could be achieved. Practically, this experiment cannot be realised because longer periods cannot be measured since the radiation onto the sample from the LED becomes more significant (verified using a pyrometer). The time constants are also extremely long, much longer than the recombination rate of electrons which is of the order of ns to ps[237]. The slowest process, however, is the reduction process of an electron and O_2 to create hydroxyls and superoxides which occurs on the ms scale, thus implying that combinations of long lived carriers may be participating in this process. For this to be true the generated excitons must separate their electron and hole and conduct to the surface to participate in this. This would result in a photo-conducting response which is seemingly not measured here. Instead, it can be interpreted as a combination of both trapped charges at the surfaces of the TiO_2, which do not migrate, and slow diffusing excitons through hopping processes.

Consider the case of an electron excited to a trap. Its movement through the lattice however, is not achieved by reaching the conduction band but instead through 'hopping' to other traps via thermal energy, hence the screening effect from free electron conductivity never occurs and the increased polarisation caused by the trapped electron remains. This supports the fact that the observed photo-dielectric measurement is due to an electron trapping processes. As future work to further examine this process, photo-excitation in varying temperature environments would be the way to examine this phenomenon in a similar way to examining the thermally activated conduction process in Fe_3O_4 in Chapter 4.

The decreasing time constant is implicit of a decreasing number of available trap levels[238]. Ke et al. reported very long carrier lifetimes in photo-excited titania, measured using EPR. This was attributed to the increasing concentration of electrons in deep traps. Also, their results showed that long irradiation led to a plateau. This is congruent with the results presented here in that the decreasing time constant with long pulsed exposure is implicit of the decreasing numbers of unoccupied trap levels. Trapping electrons relies on

TABLE 7.1: Estimated time constants of long term photo-dielectric lifetimes of TiO_2-A1

Cycle	**UV (s)**		**Blue (s)**		**Green (s)**	
	from Δf	from ΔBW	from Δf	from ΔBW	from Δf	from ΔBW
1	2.66	1.73	1.87	2.52	1.33	2.83
2	4.02	2.35	2.72	4.04	1.51	2.70
3	4.55	2.71	3.75	3.86	2.69	3.21
4	4.99	3.07	3.81	4.11	3.39	3.37
5	5.57	3.77	4.10	4.49	3.52	3.46
6	5.82	3.70	4.42	5.13	3.72	3.51
7	6.24	4.06	4.74	5.26	3.77	3.65
8	6.91	4.34	4.96	5.83	4.25	3.67
9	6.86	4.26	5.07	5.86	4.59	3.55
10	8.38	4.94	5.63	6.37	4.71	3.71

unoccupied trap states and if the electrons have long lifetimes before recombining, then another electron is unable to occupy that state. This results in the plateau and hence a decrease in time constant.

7.5 CONCLUSION

This chapter shows a simple demonstration of the photo-reactivity of the two most popular polymorphs of TiO_2 (anatase and rutile) using a simplified MCP system utilising the strict temperature monitoring procedures detailed in Chapter 4. UV-VIS spectroscopy was used to determine the band-gap of the materials, however, only the band gap of the anatase sample could be obtained. The MCP results show that the anatase powder gives a dominating photo-dielectric response at wavelengths from 625 nm to 365 nm with an increasing response with decrease wavelength. A photo-conducting response was not apparent, however, it may be present in the 365 nm excitation but dominated by the photo-dielectric response. Practically, the type of plot shown in Fig. 7.8 provides a means to evaluate the photo-reactive behaviour as a function of wavelength.

The significance of this experiment supports the argument that trap density plays a large role in the photo-reactive nature of TiO_2 in that microwave photo-dielectric measurements detect long lived carriers (due to traps). It also provides a simple desktop system to measure photo-reactivity in anatase TiO_2 pigments.

CHAPTER 8

Final Conclusions

Literature Survey: MCP Principles

Chapter 1 gives a survey of the applications and properties of Fe_3O_4, nanodiamond and TiO_2. The initial proposal of this research is to design and build MCP systems to measure different properties of these materials. The features which are characterised are the dielectric and magnetic absorption of Fe_3O_4 (for EMI and hyperthermia), the phase change from Fe_3O_4 to γ-Fe_2O_3 (for hyperthermia and drug delivery), the surface impurities on nanodiamonds (for bio-labelling and drug delivery) and the photo-reactivity of TiO_2 (for pigmentation and photo-catalysis).

Analysis: MCP Principles

Chapter 2 gives an explanation on the MCP systems and how they work. Placing samples in non-depolarising fields yields the highest sensitivity of measurement, however, an equation has been derived for different depolarising geometries. The relevant equations for the MCP method are presented, with an original expression for the theoretical bandwidth for TM and TE modes. A variety of different modes with different frequencies have been identified for measuring the frequency dependent dielectric and magnetic properties. A circuit model is also presented which is important for understanding how to take measurements, as well as a procedure for handling skewed resonance profiles.

Methodology

Chapter 3 details the principles and design of the two main MCP systems, Cyl-ε and Cyl-μ, for dielectric and magnetic measurements, respectively. This study shows that multi-mode MCP can be used to estimate the microwave dielectric and magnetic absorption spectra

in the 2 to 10 GHz range. Cyl-ε uses TM_{0mp} modes whereas Cyl-μ uses TE_{0mp} modes (which can only be used with carefully designed mode traps). Additional demagnetising modes can be used with Cyl-μ though samples may be prone to perturbing the E-field.

Chapter 4 gives an explanation of how to use Cyl-ε and Cyl-μ to measure the temperature dependent dielectric and magnetic properties of samples. A novel procedure for the correction of systematic temperature fluctuations using higher order cylindrical modes is detailed. Analytically, the temperature dependent resonant frequency and bandwidth of all modes are linked, respectively, through the thermal expansion coefficient and the coefficient of resistivity. In practice, offsets in these coefficients exist across the modes. The relationship between each of the modes, however, is constant and thus this procedure should only be used to remove systematic fluctuations in the conducted experiment.

Experiments

The initial questions about functional powders at the beginning of this thesis are recalled and briefly addressed:

Magnetite (Fe_3O_4)

What are the features that need to be characterised?

For Fe_3O_4 particles used in hyperthermia and EMI, it is the temperature dependent dielectric and magnetic permeability in the frequency band which needs to be measured. This allows the material to convert EM waves into heat to kill tumours or absorb interference.

Can this be measured easily using microwaves?

The two MCP systems in Chapter 3 have been shown to have high measurement accuracy for Fe_3O_4. Even when this oxide is mixed with other semiconducting materials, the two MCP systems are capable of solely extracting the dielectric and magnetic contributions to the absorption. The measurements of the temperature dependent absorption of Fe_3O_4 using the approach given in Chapter 4 show small changes over the 10 to 70 °C range. Additionally, through these measurements, activation energies of the microwave loss mechanisms can be extracted, including the double-exchange interaction which results in ionic hopping conduction losses and magnetic resonance phenomena.

Maghemite (γ-Fe_2O_3)

What are the features that need to be characterised?

γ-Fe_2O_3 is another magnetic material that may be considered for the above applications where its improved resilience to oxidation over Fe_3O_4 makes it useful (particularly in biomedical applications). However, due to its structural similarities to Fe_3O_4, determination of γ-Fe_2O_3 after oxidation of Fe_3O_4 can be troublesome, leading to characterisation procedures with complex systems.

Can this be measured easily using microwaves?

Chapter 5 details this specific study. Through varying the ratio of Fe_3O_4 to γ-Fe_2O_3 by annealing separate Fe_3O_4 samples, it is demonstrated that MCP measurements provide an effective way of characterising the oxidised end product. Dielectric measurements have been shown to be very sensitive to the Fe^{2+}-Fe^{3+}double-exchange interaction in Fe_3O_4, while γ-Fe_2O_3 has a much smaller dielectric constant and losses. It was discovered that an intermediate multi-phase stage of Fe_3O_4 and γ-Fe_2O_3 may result in a much larger complex permittivity which is significant for absorbing applications if it can be contained. Magnetic measurements show a less dramatic response owing to a lower magnetic permeability, however, the frequency dependent data reveals clear differences in the starting Fe_3O_4 and the end product of γ-Fe_2O_3.

Nanodiamond

What are the features that need to be characterised?

Nanodiamonds are useful particles for drug delivery and bio-labelling, however, this depends on the volume of their surface impurities. High concentrations of surface impurities causes agglomeration and quenching of fluorescence.

Can this be measured easily using microwaves?

Chapter 6 details this specific study. Through varying the ratio of diamond to non-diamond surface impurities by using different particle sizes, it is demonstrated that MCP measurements provide an effective way of characterising the bulk concentration of disordered carbon impurities on the surfaces of nanodiamonds. This is achieved since diamond gives rise to low microwave losses whereas non-diamond carbon (disordered and sp^2 carbon) gives rise to finite microwave losses. The microwave loss mechanism is determined to be related to the polarisation loss of the disordered nature of the non-diamond carbon as opposed to any static electron conductivity normally attributed to sp^2 or graphitic carbon.

Titania (TiO_2)

What are the features that need to be characterised?

Titania is useful as a photo-catalyst and a pigment and characterisation of the photo-reactivity is important for both applications, where the former requires high photo-reactivity and the latter requires the opposite.

Can this be measured easily using microwaves?

Chapter 7 details this specific study. Through photo-dielectric measurements of anatase and rutile pigments, it was demonstrated that in-situ photo-excitation MCP measurements can give insight into the density of deep electron traps in anatase powders. Rutile powders showed no response to band gap photo-excitation.

8.1 Further Work

Towards the end of this research, attempts have been made to measure the Fe_3O_4 to γ-Fe_2O_3 transition in-situ through the temperature dependent MCP technique. This has been highlighted as future work since repeatability became an issue which is believed to be due to the extremely thin quartz tubes and therefore the amount of atmospheric oxygen which permeates into powder is strongly dependent upon sample preparation. Thin samples are required for separation of E and H fields to ensure isolated electric or magnetic perturbations and so challenges arise in creating an appropriate sample container to examine this chemical reaction in-situ.

The discovery of significant photo-reactivity in just the anatase TiO_2 powder also came towards the end of this research, where the intention to continue this work is apparent in the next PhD student. While a plethora of different material characterisation methods are utilised for the Fe_3O_4 and nanodiamond studies, these should also be employed for the TiO_2 powders; in particular compositional characterisation with XRD, surface characterisation using XPS and photoluminescence studies should be carried out to examine these apparent deep level traps.

The nanodiamond studies should also be extended, with further investigation onto the effects of polycrystallinity on the microwave absorption. Dislocations within the crystal may cause formations of non-diamond carbon. To see this, HRTEM would need to be

used in conjunction with MCP measurements. Also, the application of bio-labelling with nanodiamonds involves NV^- centre rich powders in order to fluoresce. An investigation into the effects of proton bombardment to create these NV^- centres may be an interesting way to quantify it.

8.2 Closing Statement

Being an electronic and electrical engineer, one finds that although the microwave cavity perturbation technique has existed for at least half a decade, there are still many avenues which may benefit from this technique. This research aims towards bridging the gap between microwave engineering and material science. I hope that the studies investigated here enrich the minds of other inquisitive engineers to explore similar paths towards the exciting realms chemistry has to offer.

Bibliography

[1] L. Xiao, J. Li, D. F. Brougham, E. K. Fox, N. Feliu, A. Bushmelev, A. Schmidt, N. Mertens, F. Kiessling, M. Valldor, B. Fadeel, and S. Mathur, "Water-soluble superparamagnetic magnetite nanoparticles with biocompatible coating for enhanced magnetic resonance imaging," *ACS Nano*, vol. 5, pp. 6315–6324, Jul. 2011.

[2] C. Y. Haw, F. Mohamed, C. H. Chia, S. Radiman, S. Zakaria, N. M. Huang, and H. N. Lim, "Hydrothermal synthesis of magnetite nanoparticles as MRI contrast agents," *Ceram. Int.*, vol. 36, pp. 1417–1422, Mar. 2010.

[3] N. P. Martínez Vera, R. Schmidt, K. Langer, I. Zlatev, R. Wronski, E. Auer, D. Havas, M. Windisch, H. Von Briesen, S. Wagner, J. Stab, M. Deutsch, C. Pietrzik, F. Fazekas, and S. Ropele, "Tracking of magnetite labeled nanoparticles in the rat brain using MRI," *PLoS One*, vol. 9, pp. 20–24, Mar. 2014.

[4] S. Bucak, B. Yavuztürk, and A. D. Sezer, "Magnetic nanoparticles: synthesis, surface modifications and application in drug delivery," in *Recent Adv. Nov. Drug Carr. Syst.* (A. D. Sezer, ed.), ch. 7, pp. 165–200, InTech, 2012.

[5] M. F. Silva, A. A. Winkler Hechenleitner, D. M. F. de Oliveira, M. Agüeros, R. Peñalva, J. M. Irache, and E. A. G. Pineda, "Optimization of maghemite-loaded plga nanospheres for biomedical applications," *Eur. J. Pharm. Sci.*, vol. 49, pp. 343–51, Jun. 2013.

[6] V. Dediu, E. Arisi, I. Bergenti, A. Riminucci, M. Murgia, and G. Ruani, "Magnetite films grown directly on organic semiconductor layers," in *IEEE Int. Magn. Conf.*, vol. 184, p. 374, May. 2006.

[7] Z. Wang, L. Wu, J. Zhou, W. Cai, B. Shen, and Z. Jiang, "Magnetite nanocrystals on multiwalled carbon nanotubes as a synergistic microwave absorber," *J. Phys. Chem. C*, vol. 117, pp. 5446–5452, Mar. 2013.

[8] R. M. Cornell and U. Schwertmann, *The Iron Oxides*. Wiley, 2003.

[9] S. E. Lapinsky and A. C. Easty, "Electromagnetic interference in critical care," *J. Crit. Care*, vol. 21, pp. 267–270, Sep. 2006.

[10] I. H. Hahn, D. Schnadower, R. J. Dakin, and L. S. Nelson, "Cellular phone interference as a cause of acute epinephrine poisoning," *Ann. Emerg. Med.*, vol. 46, pp. 298–299, Sep. 2005.

[11] D. M. Witters and P. S. Ruggera, "Electromagnetic compatibility (EMC) of powered wheelchairs and scooters," in *Proc. Rehabil. Soc. North Am. Annu. Conf. Tuning to 21st Century Through Assist. Technol.*, pp. 359–360, Nov. 1994.

[12] Elsevier, "Mobile phones and hospital equipment," *Evidence-Based Healthc. Public Heal.*, vol. 9, p. 173, Apr. 2005.

[13] F. Qin and C. Brosseau, "A review and analysis of microwave absorption in polymer composites filled with carbonaceous particles," *J. Appl. Phys.*, vol. 111, p. 061301, Mar. 2012.

[14] V. B. Bregar, "Advantages of ferromagnetic nanoparticle composites in microwave absorbers," *IEEE Trans. Magn.*, vol. 40, pp. 1679–1684, May. 2004.

[15] X. Liu, S. Wing Or, C. Ming Leung, and S. L. Ho, "Microwave complex permeability of Fe_3O_4 nanoflake composites with and without magnetic field-induced rotational orientation," *J. Appl. Phys.*, vol. 113, p. 17B307, Apr. 2013.

[16] C. Zhao, A. Zhang, Y. Zheng, and J. Luan, "Electromagnetic and microwave-absorbing properties of magnetite decorated multiwalled carbon nanotubes prepared with poly(n-vinyl-2-pyrrolidone)," *Mater. Res. Bull.*, vol. 47, pp. 217–221, Feb. 2012.

[17] I. Kong, S. H. Ahmad, M. H. Abdullah, D. Hui, A. N. Yusoff, and D. Puryanti, "Magnetic and microwave absorbing properties of magnetite-thermoplastic natural rubber nanocomposites," *J. Magn. Magn. Mater.*, vol. 322, pp. 3401–3409, Nov. 2010.

[18] Y. Chen, Y. Zhang, G. Xiao, T. Wang, Y. Ma, C. Zhu, and P. Gao, "Controlled synthesis and shape-dependent electromagnetic wave absorption characteristics of porous Fe_3O_4 submicro particles," *Sci. China Physics, Mech. Astron.*, vol. 55, pp. 25–32, Dec. 2011.

[19] H. S. Cho and S. S. Kim, "M-hexaferrites with planar magnetic anisotropy and their application to high-frequency microwave absorbers," *IEEE Trans. Magn.*, vol. 35, pp. 3151–3153, Sep. 1999.

[20] S. Padhy, S. Sanyal, A. Bose, R. Chatterjee, and R. S. Meena, "Development and characterisation of (Mg, Mn) U-type microwave absorbing materials and its application in radar cross sections reduction," *IET Microwaves, Antennas Propag.*, vol. 8, pp. 165–170, Feb. 2014.

[21] S. Ozah and N. S. Bhattacharyya, "Nanosized barium hexaferrite in novolac phenolic resin as microwave absorber for X-band application," *J. Magn. Magn. Mater.*, vol. 342, pp. 92–99, Apr. 2013.

[22] P. Chen, R. X. Wu, T. Zhao, F. Yang, and J. Q. Xiao, "Complex permittivity and permeability of metallic magnetic granular composites at microwave frequencies," *J. Phys. D. Appl. Phys.*, vol. 38, pp. 2302–2305, Jul. 2005.

[23] L. Liu, Y. Duan, S. Liu, L. Chen, and J. Guo, "Microwave absorption properties of one thin sheet employing carbonyl-iron powder and chlorinated polyethylene," *J. Magn. Magn. Mater.*, vol. 322, pp. 1736–1740, Dec. 2010.

[24] O. Akman, H. Kavas, A. Baykal, M. S. Toprak, A. Çoruh, and B. Aktaş, "Magnetic metal nanoparticles coated polyacrylonitrile textiles as microwave absorber," *J. Magn. Magn. Mater.*, vol. 327, pp. 151–158, Sep. 2013.

[25] A. M. Gama, M. C. Rezende, and C. C. Dantas, "Dependence of microwave absorption properties on ferrite volume fraction in MnZn ferrite/rubber radar absorbing materials," *J. Magn. Magn. Mater.*, vol. 323, pp. 2782–2785, Nov. 2011.

[26] D. Yuping, M. He, L. Xiaogang, L. Shunhua, and J. Zhijiang, "The microwave electromagnetic characteristics of manganese dioxide with different crystallographic structures," *Phys. B Condens. Matter*, vol. 405, pp. 1826–1831, Apr. 2010.

[27] W. Li, T. Wu, W. Wang, P. Zhai, and J. Guan, "Broadband patterned magnetic microwave absorber," *J. Appl. Phys.*, vol. 116, pp. 044110–1–7, Jul. 2014.

[28] H. B. Zhang, L. W. Deng, P. H. Zhou, L. Zhang, D. M. Cheng, H. Y. Chen, D. F. Liang, and L. J. Deng, "Low frequency needlepoint-shape metamaterial absorber based on magnetic medium," *J. Appl. Phys.*, vol. 113, Jan. 2013.

[29] W. Li, X. Qiao, Y. Luo, F. X. Qin, and H. X. Peng, "Magnetic medium broadband metamaterial absorber based on the coupling resonance mechanism," *Appl. Phys. A Mater. Sci. Process.*, vol. 115, pp. 229–234, Oct. 2014.

[30] A. Porch, D. Slocombe, and P. P. Edwards, "Microwave absorption in powders of small conducting particles for heating applications," *Phys. Chem. Chem. Phys.*, vol. 15, pp. 2757–63, Feb. 2013.

[31] J. A. Pearce, J. R. Cook, P. J. Hoopes, and A. Giustini, "FEM numerical model study of heating in magnetic nanoparticles," in *Proc. SPIE*, vol. 7901, pp. 1–6, Feb. 2011.

[32] T. Motomura, K. Ueda, S. Ohtani, E. Hansen, L. Ji, K. Ito, K. Saito, Y. Sugita, and Y. Nose, "Evaluation of systemic external microwave hyperthermia for treatment of pleural metastasis in orthotopic lung cancer model," *Oncol. Rep.*, vol. 24, pp. 591–598, Sep. 2010.

[33] S. N. Kale, R. Rajagopal, S. Arora, K. R. Bhayani, J. M. Rajwade, K. M. Paknikar, D. C. Kundaliya, and S. B. Ogale, "Microwave response of $La_{0.7}Sr_{0.3}MnO_3$ nanoparticles for heating applications," *J. Biomed. Nanotechnol.*, vol. 3, pp. 178–183, May. 2007.

[34] A. Hervault and N. T. K. Thanh, "Magnetic nanoparticle-based therapeutic agents for thermo-chemotherapy treatment of cancer," *Nanoscale*, vol. 6, pp. 11553–11573, Aug. 2014.

[35] H. S. Huang and J. F. Hainfeld, "Intravenous magnetic nanoparticle cancer hyperthermia," *Int. J. Nanomedicine*, vol. 8, pp. 2521–2532, Jul. 2013.

[36] S. Dutz and R. Hergt, "Magnetic particle hyperthermia - a promising tumour therapy?," *Nanotechnology*, vol. 25, p. 452001, Oct. 2014.

[37] J. L. Kirschvink, "Microwave absorption by magnetite: a possible mechanism for coupling nonthermal levels of radiation to biological systems," *Bioelectromagnetics*, vol. 17, no. 3, pp. 187–194, 1996.

[38] J. F. Bakker, M. M. Paulides, A. H. Westra, H. Schippers, and G. C. Van Rhoon, "Design and test of a 434 MHz multi-channel amplifier system for targeted hyperthermia applicators," *Int. J. Hyperth.*, vol. 26, pp. 158–170, Jan. 2010.

[39] Y. Nikawa and F. Okada, "Selective heating for microwave hyperthermia using ferrimagnetic resonance," *IEEE Trans. Magn.*, vol. 23, pp. 2431–2433, Sep. 1987.

[40] I. Santoso, T. S. Widodo, A. Susanto, and M. Tjokronagoro, "Spatial temperature pattern of a non-invasive 2.45 GHz microwave hyperthermia device," *ARPN J. Eng. Appl. Sci.*, vol. 9, pp. 2131–2134, Nov. 2014.

[41] M. Converse, E. J. Bond, B. D. Van Veen, and S. C. Hagness, "A computational study of ultra-wideband versus narrowband microwave hyperthermia for breast cancer treatment," *IEEE Trans. Microw. Theory Tech.*, vol. 54, pp. 2169–2180, May. 2006.

[42] R. R. Shah, T. P. Davis, A. L. Glover, D. E. Nikles, and C. S. Brazel, "Impact of magnetic field parameters and iron oxide nanoparticle properties on heat generation for use in magnetic hyperthermia," *J. Magn. Magn. Mater.*, vol. 387, pp. 96–106, Mar. 2015.

[43] T. K. Jain, M. A. Morales, S. K. Sahoo, D. L. Leslie-Pelecky, and V. Labhasetwar, "Iron oxide nanoparticles for sustained delivery of anticancer agents," *Mol. Pharm.*, vol. 2, pp. 194–205, Apr. 2005.

[44] Q. A. Pankhurst, J. Connolly, S. K. Jones, and J. Dobson, "Applications of magnetic nanoparticles in biomedicine," *J. Phys. D. Appl. Phys.*, vol. 36, pp. R167–R181, Jun. 2003.

[45] V. V. Mody, A. Cox, S. Shah, A. Singh, W. Bevins, and H. Parihar, "Magnetic nanoparticle drug delivery systems for targeting tumor," *Appl. Nanosci.*, vol. 4, pp. 385–392, Apr. 2013.

[46] R. Hergt, S. Dutz, and M. Röder, "Effects of size distribution on hysteresis losses of magnetic nanoparticles for hyperthermia," *J. Phys. Condens. Matter*, vol. 20, p. 385214, Aug. 2008.

[47] A. Z. Wilczewska, K. Niemirowicz, K. H. Markiewicz, and H. Car, "Nanoparticles as drug delivery systems," *Pharmacol. Reports*, vol. 64, pp. 1020–1037, Dec. 2012.

[48] S. Abdeen, "Diagnostics and treatment of metastatic cancers with magnetic nanoparticles," *J. Nanomedine. Biotherapeutic Discov.*, vol. 3, Aug. 2013.

[49] U. O. Häfeli, J. S. Riffle, L. Harris-Shekhawat, A. Carmichael-Baranauskas, F. Mark, J. P. Dailey, and D. Bardenstein, "Cell uptake and in vitro toxicity of magnetic nanoparticles suitable for drug delivery," *Mol. Pharm.*, vol. 6, pp. 1417–1428, May. 2009.

[50] E.-J. Park, H. Umh, D.-H. Choi, M. Cho, W. Choi, S.-W. Kim, Y. Kim, and J.-H. Kim, "Magnetite- and maghemite-induced different toxicity in murine alveolar macrophage cells," *Arch. Toxicol.*, vol. 88, pp. 1607–1618, Feb. 2014.

[51] H. L. Karlsson, J. Gustafsson, P. Cronholm, and L. Möller, "Size-dependent toxicity of metal oxide particles-a comparison between nano- and micrometer size," *Toxicol. Lett.*, vol. 188, pp. 112–118, Mar. 2009.

[52] R. Grau-Crespo, A. Y. Al-Baitai, I. Saadoune, and N. H. De Leeuw, "Vacancy ordering and electronic structure of γ-Fe_2O_3 (maghemite): a theoretical investigation," *J. Phys. Condens. Matter*, vol. 22, p. 255401, Jun. 2010.

[53] C. J. Serna and M. P. Morales, "Maghemite (γ-Fe_2O_3): A versatile magnetic colloidal material," in *Surf. Colloid Sci.* (E. Matijevic and M. Borkovec, eds.), vol. 17, pp. 27–81, Springer US, 2004.

[54] A. U. Gehring, H. Fischer, M. Louvel, K. Kunze, and P. G. Weidler, "High temperature stability of natural maghemite: A magnetic and spectroscopic study," *Geophys. J. Int.*, vol. 179, pp. 1361–1371, Sep. 2009.

[55] Q. A. Acton, *Issues in Earth Sciences, Geology, and Geophysics.* ScholarlyEditions, 2012.

[56] M. Chirita and I. Grozescu, "Fe_2O_3 - nanoparticles, physical properties and their photochemical and photoelectrochemical applications," *Chem. Bull. Politeh. Univ. Timisoara*, vol. 54, pp. 1–8, May. 2009.

[57] A. S. Barnard, "Diamond standard in diagnostics: nanodiamond biolabels make their mark," *Analyst*, vol. 134, pp. 1751–64, Sep. 2009.

[58] N. Mohan, Y.-K. Tzeng, L. Yang, Y.-Y. Chen, Y. Y. Hui, C.-Y. Fang, and H.-C. Chang, "Sub-20-nm fluorescent nanodiamonds as photostable biolabels and fluorescence resonance energy transfer donors," *Adv. Mater.*, vol. 22, pp. 843–7, Mar. 2010.

[59] M. Bevilacqua, A. Chaudhary, and R. B. Jackman, "The influence of ammonia on the electrical properties of detonation nanodiamond," *J. Appl. Phys.*, vol. 106, p. 123704, Dec. 2009.

[60] E. K. Chow, X.-Q. Zhang, M. Chen, R. Lam, E. Robinson, H. Huang, D. Schaffer, E. Osawa, A. Goga, and D. Ho, "Nanodiamond therapeutic delivery agents mediate enhanced chemoresistant tumor treatment," *Sci. Transl. Med.*, vol. 3, pp. 1–10, Mar. 2011.

[61] G. Xi, E. Robinson, B. Mania-Farnell, E. F. Vanin, K.-W. Shim, T. Takao, E. V. Allender, C. S. Mayanil, M. B. Soares, D. Ho, and T. Tomita, "Convection-enhanced delivery of nanodiamond drug delivery platforms for intracranial tumor treatment," *Nanomedicine nanotechnology, Biol. Med.*, vol. 10, pp. 381–91, Feb. 2014.

[62] A. K. Mallik, S. Bysakh, K. S. Pal, N. Dandapat, B. K. Guha, S. Datta, and D. Basu, "Synthesis and characterisation of freestanding diamond coatings," *Indian J. Eng. Mater. Sci.*, vol. 20, pp. 522–532, Dec. 2013.

[63] J. Xiao, X. Duan, Q. Yin, Z. Zhang, H. Yu, and Y. Li, "Nanodiamonds-mediated doxorubicin nuclear delivery to inhibit lung metastasis of breast cancer," *Biomaterials*, vol. 34, pp. 9648–9656, Sep. 2013.

[64] V. N. Mochalin, O. Shenderova, D. Ho, and Y. Gogotsi, "The properties and applications of nanodiamonds," *Nat. Nanotechnol.*, vol. 7, pp. 11–23, Dec. 2011.

[65] V. Pichot, M. Comet, E. Fousson, C. Baras, A. Senger, F. Le Normand, and D. Spitzer, "An efficient purification method for detonation nanodiamonds," *Diam. Relat. Mater.*, vol. 17, pp. 13–22, Jan. 2008.

[66] L. Lai and A. S. Barnard, "Modeling the thermostability of surface functionalisation by oxygen, hydroxyl, and water on nanodiamonds," *Nanoscale*, vol. 3, pp. 2566–2575, Jun. 2011.

[67] B. M. Chang, H. H. Lin, L. J. Su, W. D. Lin, R. J. Lin, Y. K. Tzeng, R. T. Lee, Y. C. Lee, A. L. Yu, and H. C. Chang, "Highly fluorescent nanodiamonds protein-functionalized for cell labeling and targeting," *Adv. Funct. Mater.*, vol. 23, pp. 5737–5745, Jul. 2013.

[68] M. A. Zurbuchen, M. P. Lake, S. A. Kohan, B. Leung, and L.-S. Bouchard, "Nanodiamond landmarks for subcellular multimodal optical and electron imaging," *Sci. Rep.*, vol. 3, p. 2668, Sep. 2013.

[69] R. Kaur and I. Badea, "Nanodiamonds as novel nanomaterials for biomedical applications: Drug delivery and imaging systems," *Int. J. Nanomedicine*, vol. 8, pp. 203–220, Jan. 2013.

[70] F. Delgado-Vargas and O. Paredes-Lopez, *Natural Colorants for Food and Nutraceutical Uses*. Food Science and Technology, CRC Press, 2002.

[71] T. Luttrell, S. Halpegamage, J. Tao, A. Kramer, E. Sutter, and M. Batzill, "Why is anatase a better photocatalyst than rutile? - model studies on epitaxial TiO_2 films," *Sci. Rep.*, vol. 4, p. 4043, Feb. 2014.

[72] K. Nakata and A. Fujishima, "TiO_2 photocatalysis: Design and applications," *J. Photochem. Photobiol. C Photochem. Rev.*, vol. 13, pp. 169–189, Jun. 2012.

[73] K. Hashimoto, H. Irie, and A. Fujishima, "TiO_2 photocatalysis: A historical overview and future prospects," *Jpn. J. Appl. Phys.*, vol. 44, pp. 8269–8285, Jul. 2006.

[74] Z. W. Wicks, F. N. Jones, S. P. Pappas, and D. A. Wicks, *Organic Coatings: Science and Technology*. Wiley, Feb. 2007.

[75] T. Wang, H. Jiang, L. Wan, Q. Zhao, T. Jiang, B. Wang, and S. Wang, "Potential application of functional porous TiO_2 nanoparticles in light-controlled drug release and targeted drug delivery," *Acta Biomater.*, vol. 13, pp. 354–363, Nov. 2015.

[76] H.-J. Xiang, L. An, W.-W. Tang, S.-P. Yang, and J.-G. Liu, "Photo-controlled targeted intracellular delivery of both nitric oxide and singlet oxygen using a fluorescence-trackable ruthenium nitrosyl functional nanoplatform," *Chem. Commun.*, vol. 51, pp. 2555–2558, Dec. 2015.

[77] X. Sun, C. Wang, M. Gao, A. Hu, and Z. Liu, "Remotely controlled red blood cell carriers for cancer targeting and near-infrared light-triggered drug release in combined photothermal-chemotherapy," *Adv. Funct. Mater.*, pp. 2386–2394, Feb. 2015.

[78] E. K. Akdogan, M. R. Leonard, and A. Safari, "Size effects in ferroelectric ceramics," in *Handb. Low High Dielectr. Constant Mater. Their Appl.* (H. Nalwa, ed.), ch. 2, pp. 61–112, Burlington: Academic Press, 1999.

[79] A. H. Sihvola, *Electromagnetic Mixing Formulas and Applications*. IET, illustrate ed., 1999.

[80] L. F. Chen, C. K. Ong, C. P. Neo, V. V. Varadan, and V. K. Varadan, *Microwave Electronics*. Chichester, UK: John Wiley & Sons, Ltd, Mar. 2004.

[81] P. Lunkenheimer and A. Loidl, "Response of disordered matter to electromagnetic fields," *Phys. Rev. Lett.*, vol. 91, p. 207601, Nov. 2003.

[82] M. Hotta, M. Hayashi, M. T. Lanagan, D. K. Agrawal, and K. Nagata, "Complex permittivity of graphite, carbon black and coal powders in the ranges of X-band frequencies (8.2 to 12.4 GHz) and between 1 and 10 GHz," *ISIJ Int.*, vol. 51, pp. 1766–1772, Nov. 2011.

[83] Y. Poo, R.-x. Wu, X. Fan, J. Q. Xiao, and B.-b. Jin, "An experiment study of gold nanofilm's conductivity at microwave and terahertz frequencies," in *2010 Asia-Pacific Microw. Conf.*, vol. 2, pp. 1452–1454, Dec. 2010.

[84] J. Wilson and J. F. B. Hawkes, *Optoelectronics*. Prentice Hall Europe, 3rd ed., 1998.

[85] T. Zhang, M. Wu, S. Zhang, J. Wang, D. Zhang, F. He, and Z. P. Li, "Influence of the various doping elements on the microwave dielectric loss of silica," *J. Alloys Compd.*, vol. 509, pp. 9279–9283, Jun. 2011.

[86] V. Mane and V. Puri, "Microwave conductivity and permittivity of moisture laden soybean seed," in *2008 Int. Conf. Recent Adv. Microw. Theory Appl. Microw. 2008*, vol. 1, (Jaipur), pp. 168–170, Nov. 2008.

[87] B. Marinho, M. Ghislandi, E. Tkalya, C. E. Koning, and G. de With, "Electrical conductivity of compacts of graphene, multi-wall carbon nanotubes, carbon black, and graphite powder," *Powder Technol.*, vol. 221, pp. 351–358, Jan. 2012.

[88] J.-Y. Kim, J. Lee, W. H. Lee, I. N. Kholmanov, J. W. Suk, T. Kim, Y. Hao, H. Chou, D. Akinwande, and R. S. Ruoff, "Flexible and transparent dielectric film with a high dielectric constant using chemical vapor deposition- grown graphene interlayer," *ACS Nano*, vol. 8, pp. 269–274, Dec. 2014.

[89] M. Gupta and E. Wai Leong Wong, "Microwave-material interactions," in *Microwaves Met.*, pp. 43–63, John Wiley & Sons (Asia) Pte Ltd, 2007.

[90] P. Lunkenheimer, V. Bobnar, A. V. Pronin, A. I. Ritus, A. A. Volkov, and A. Loidl, "Materials with colossal dielectric constant: Do they exist?," *Condens. Matter*, pp. 1–4, Aug. 2002.

[91] M. Eichelbaum, R. Stößer, A. Karpov, C.-K. Dobner, F. Rosowski, A. Trunschke, and R. Schlögl, "The microwave cavity perturbation technique for contact-free and in situ electrical conductivity measurements in catalysis and materials science," *Phys. Chem. Chem. Phys.*, vol. 14, p. 1302, Nov. 2012.

[92] A. K. Jonscher, "The 'universal' dielectric response," *Nature*, vol. 267, pp. 673–679, Jun. 1977.

[93] A. N. Papathanassiou, I. Sakellis, and J. Grammatikakis, "Universal frequency-dependent AC conductivity of conducting polymer networks," *Appl. Phys. Lett.*, vol. 91, pp. 2–5, Sep. 2007.

[94] J. Ye, Y. Liu, J. Zhang, X. Chen, and M. Yao, "Preparation and electromagnetic wave absorption properties of core-shell structured Fe_3O_4-polyaniline nanoparticles," *J. Magn. Magn. Mater.*, vol. 335, pp. 32–35, Oct. 2013.

[95] M. Wu, Y. D. Zhang, S. Hui, T. D. Xiao, S. Ge, W. A. Hines, J. I. Budnick, and G. W. Taylor, "Microwave magnetic properties of $Co_{50}/(SiO_2)_{50}$ nanoparticles," *Appl. Phys. Lett.*, vol. 80, p. 4404, Jun. 2002.

[96] N.-N. Song, H.-T. Yang, H.-L. Liu, X. Ren, H.-F. Ding, X.-Q. Zhang, and Z.-H. Cheng, "Exceeding natural resonance frequency limit of monodisperse Fe_3O_4 nanoparticles via superparamagnetic relaxation," *Sci. Rep.*, vol. 3, p. 3161, Nov. 2013.

[97] M. Ma, Y. Wu, J. Zhou, Y. Sun, Y. Zhang, and N. Gu, "Size dependence of specific power absorption of Fe_3O_4 particles in AC magnetic field," *J. Magn. Magn. Mater.*, vol. 268, pp. 33–39, May. 2004.

[98] A. G. Gurevich, *Ferrites at microwave frequencies.* Consultants Bureau, 1963.

[99] W. Jasinski and J. A. Berry, "Measurement of refractive indices of air, nitrogen, oxygen, carbon dioxide and water vapour at 3360 Mc/s," in *Proc. IEE - Part III Radio Commun. Eng.*, vol. 101, pp. 337–343, Mar. 1954.

[100] I. G. MacBean, "The measurement of complex permittivity and complex tensor permeability of ferrite materials at microwave frequencies," in *Proc. IEE - Part B Radio Electron. Eng.*, vol. 104, pp. 296–306, Oct. 1957.

[101] J. F. Rouleau, J. Goyette, T. K. Bose, and M. F. Frechette, "Sensitivity of a microwave differential technique for the measurement of contaminants in gases," in *Electr. Insul. Dielectr. Phenomena, 1999 Annu. Rep. Conf.*, (Austin), pp. 411–414 vol.1, Oct. 1999.

[102] T. Ikeda and M. Danno, "Diagnostics of TM_{010}-mode microwave cavity discharges in CO_2-n2-he laser gas mixtures. I. Measurement of dielectric constant," *Quantum Electron. IEEE J.*, vol. 31, pp. 1525–1532, Aug. 1995.

[103] H. Yoshikawa and A. Nakayama, "Measurements of complex permittivity at millimeter-wave frequencies with an end-loaded cavity resonator," *IEEE Trans. Microw. Theory Tech.*, vol. 56, pp. 2001–2007, Aug. 2008.

[104] H. S. M. Nazarat, Y. Kobayashi, and Z. Ma, "Frequency dependence measurements of complex permittivity of a dielectric plate by using TE_{0m1} modes in a circular cavity," in *APMC 2009 - Asia Pacific Microw. Conf. 2009*, (Singapore), pp. 421–424, Dec. 2009.

[105] G. Zhang, S. Nakaoka, and Y. Kobayashi, "Millimeter wave measurements of temperature dependence of complex permittivity of dielectric plates by the cavity resonance method," in *Proc. 1997 Asia-Pacific Microw. Conf.*, vol. 3, pp. 913–916, Dec. 1997.

[106] T. Shimizu, S. Kojima, and Y. Kogami, "Accurate evaluation technique of complex permittivity for low-permittivity dielectric films using a cavity resonator method in 60-GHz band," *IEEE Trans. Microw. Theory Tech.*, vol. 63, pp. 279–286, Jan. 2015.

[107] B. L. Givot, J. Krupka, and K. Derzakowski, "Split-post dielectric resonator for complex permittivity measurements at 20-25 GHz," in *Microwaves, Radar Wirel. Commun. 2002. MIKON-2002. 14th Int. Conf.*, vol. 2, pp. 401–403 vol.2, 2002.

[108] H.-X. Zheng, "Measurements of complex permittivity using dielectric resonator at 60 GHz," in *Antennas, Propag. EM Theory, 2006. ISAPE '06. 7th Int. Symp.*, (Guilin), pp. 1–4, Oct. 2006.

[109] J. Mazierska, J. Krupka, M. V. Jacob, and D. Ledenyov, "Complex permittivity measurements at variable temperatures of low loss dielectric substrates employing split post and single post dielectric resonators," in *IEEE MTT-S Int. Microw. Symp. Dig.*, vol. 3, pp. 1825–1828 Vol.3, 2004.

[110] A. A. Abduljabar, D. J. Rowe, A. Porch, and D. A. Barrow, "Novel microwave microfluidic sensor using a microstrip split-ring resonator," in *Microw. Theory Tech. IEEE Trans.*, vol. 62, pp. 679–688, Mar. 2014.

[111] H. Choi, J. Nylon, S. Luzio, J. Beutler, and A. Porch, "Design of continuous non-invasive blood glucose monitoring sensor based on a microwave split ring resonator," in *RF Wirel. Technol. Biomed. Healthc. Appl. (IMWS-Bio), 2014 IEEE MTT-S Int. Microw. Work. Ser.*, (London), pp. 1–3, Dec. 2014.

[112] B.-H. Kim, Y.-J. Lee, H.-J. Lee, Y. Hong, J.-G. Yook, M. H. Chung, W. Cho, and H. H. Choi, "A gas sensor using double split-ring resonator coated with conducting polymer at microwave frequncies," in *SENSORS, 2014 IEEE*, pp. 1815–1818, Nov. 2014.

[113] M. N. Afsar, A. Sharma, and M. Obol, "Microwave permittivity and permeability properties and microwave reflections of micro/nano ferrite powders," in *2009 IEEE Intrumentation Meas. Technol. Conf. I2MTC 2009*, pp. 274–278, May. 2009.

[114] Y. Wang, M. N. Afsat, and R. Grignon, "Complex permittivity and permeability of carbonyl iron powders at microwave frequencies," in *Antennas Propag. Soc. Int. Symp. 2003. IEEE*, vol. 4, (Columbus), pp. 619–622 vol.4, Jun. 2003.

[115] B. Kang, J. Cho, C. Cheon, and Y. Kwon, "Nondestructive measurement of complex permittivity and permeability using multilayered coplanar waveguide structures," *IEEE Microw. Wirel. Components Lett.*, vol. 15, pp. 381–383, May. 2005.

[116] A. Boughriet, Z. Wu, H. Mccann, and L. E. Davis, "The measurement of dielectric properties of liquids at microwave frequencies using open-ended coaxial probes," in *1st World Congr. Ind. Process Tomogr.*, pp. 318–322, Apr. 1999.

[117] D. Misra and S. Member, "On the measurement of the complex permittivity of materials by an open-ended coaxial probe," *IEEE Microw. Guid. Wave Lett.*, vol. 5, pp. 161–163, May. 1995.

[118] A. Raj, W. Holmes, and S. Judah, "Wide bandwidth measurement of complex permittivity of liquids using coplanar lines," *IEEE Trans. Instrum. Meas.*, vol. 50, pp. 905–909, Aug. 2001.

[119] A. Cunliffe and L. E. S. Mathias, "Some perturbation effects in cavity resonators," in *Proc. IEE - Part III Radio Commun. Eng.*, vol. 97, pp. 367–376, Apr. 1950.

[120] S. K. Chatterjee, "Microwave cavity resonators. some perturbation effects and their applications," *Radio Eng. J. Br. Inst.*, vol. 13, pp. 475–484, Jul. 1953.

[121] R. A. Waldron, "Perturbation theory of resonant cavities," *Proc, Inst. Elec. Eng.*, vol. 107C, pp. 272–274, Apr. 1960.

[122] R. F. Harrington, *Time-Harmonic Electromagnetic Fields*. McGraw-Hill, 1961.

[123] D. M. Pozar, *Microwave Engineering*. Wiley, 2004.

[124] D. J. Rowe, A. A. Abduljabar, A. Porch, D. A. Barrow, and C. J. Allender, "Improved split-ring resonator for micro fluidic sensing," *IEEE Trans. Microw. Theory Tech.*, vol. 62, pp. 1–11, Mar. 2014.

[125] R. Boca, *Theoretical Foundations of Molecular Magnetism*. Elsevier, 1999.

[126] J. A. Cuenca, E. Thomas, S. Mandal, O. Williams, and A. Porch, "Broadband microwave measurements of nanodiamond," in *Microw. Conf. (APMC), 2014 Asia-Pacific*, (Sendai), pp. 441–443, Nov. 2014.

[127] J. A. Cuenca, S. Klein, R. Rüger, and A. Porch, "Microwave complex permeability of magnetite using non-demagnetising and demagnetising cavity modes," in *Microw. Conf. (EuMC), 2014 44th Eur.*, (Rome), pp. 128–131, Oct. 2014.

[128] X. Ji, "Microwave absorption properties of flake graphite and carbonyl-iron particles filled aliphatic polyurethane resin," *Adv. Mehcanical Eng. its Appl.*, vol. 3, pp. 294–298, Apr. 2012.

[129] S. Vinayasree, M. A. Soloman, V. Sunny, P. Mohanan, P. Kurian, and M. R. Anantharaman, "A microwave absorber based on strontium ferrite-carbon black-nitrile rubber for s and X-band applications," *Compos. Sci. Technol.*, vol. 82, pp. 69–75, Apr. 2013.

[130] M. Lin, Y. Wang, and M. N. Afsar, "Precision measurement of complex permittivity and permeability by microwave cavity perturbation technique," in *Infrared Millim. Waves 13th Int. Conf. Terahertz Electron.*, vol. 1, pp. 62–63, Sep. 2005.

[131] H. Choi, J. Cuenca, G. Attard, and A. Porch, "A novel concentration detection method of hydrogen peroxide using microwave cavity perturbation technique," in *Microw. Conf. (EuMC), 2014 44th Eur.*, no. 1, (Rome), pp. 632–635, Oct. 2014.

[132] P. Kanpan, E. Khansalee, N. Puangngernmak, and S. Chalermwisutkul, "TM_{010} mode cylindrical cavity for complex permittivity measurement of liquid using field analysis technique," in *Electr. Eng. Comput. Telecommun. Inf. Technol. (ECTI-CON), 2012 9th Int. Conf.*, pp. 1–4, 2012.

[133] D. Okhiria, *TM_{010} Cylindrical Microwave Cavity Resonator for Material Measurements*. MSc Dissertation, Cardiff University, 2010.

[134] L. Luo, D. Bozyigit, V. Wood, and M. Niederberger, "High-quality transparent electrodes spin-cast from preformed antimony-doped tin oxide nanocrystals for thin film optoelectronics," *Chem. Mater.*, vol. 25, pp. 4901–4907, Dec. 2013.

[135] Y. Guan and Y. Nikawa, "Measurement of temperature-dependent complex permittivity for materials using cylindrical resonator under microwave irradiation," *Electron. Commun. Japan (Part II Electron.*, vol. 90, pp. 1–8, Nov. 2007.

[136] V. Pohl, D. Fricke, and A. Muhlbauer, "Correction procedures for the measurement of permittivities with the cavity perturbation method," *J. Microw. Power Electromagn. Energy*, vol. 30, pp. 10–26, Nov. 1994.

[137] M. Ewing and D. Royal, "A highly stable cylindrical microwave cavity resonator for the measurement of the relative permittivities of gases," *J. Chem. Thermodyn.*, vol. 34, pp. 1073–1088, Jul. 2002.

[138] B. Riddle, J. Baker-Jarvis, and J. Krupka, "Complex permittivity measurements of common plastics over variable temperatures," *IEEE Trans. Microw. Theory Tech.*, vol. 51, pp. 727–733, Mar. 2003.

[139] J. Krupka, K. Derzakowski, B. Riddle, and J. Baker-Jarvis, "A dielectric resonator for measurements of complex permittivity of low loss dielectric materials as a function of temperature," *Meas. Sci. Technol.*, vol. 9, pp. 1751–1756, Jul. 1999.

[140] D. Slocombe, *The Electrical Properties of Transparent Conducting Oxide Composites*. PhD thesis, Cardiff University, 2012.

[141] K. Rudzka, Á. V. Delgado, and J. L. Viota, "Maghemite functionalization for antitumor drug vehiculization," *Mol. Pharm.*, vol. 9, pp. 2017–2028, Jun. 2012.

[142] K. Rudzka, J. L. Viota, J. A. Muñoz-Gamez, A. Carazo, A. Ruiz-Extremera, and Á. V. Delgado, "Nanoengineering of doxorubicin delivery systems with functionalized maghemite nanoparticles," *Colloids Surfaces B Biointerfaces*, vol. 111, pp. 88–96, May. 2013.

[143] J. H. Du, C. Sun, S. Bai, G. Su, Z. Ying, and H. M. Cheng, "Microwave electromagnetic characteristics of a microcoiled carbon fibers/paraffin wax composite in ku band," *J. Mater. Res.*, vol. 17, pp. 1232–1236, Jan. 2011.

[144] E. Múzquiz-Ramos, V. Guerrero-Chávez, B. Macías-Martínez, C. López-Badillo, and L. García-Cerda, "Synthesis and characterization of maghemite nanoparticles for hyperthermia applications," *Ceram. Int.*, vol. 41, pp. 397–402, Jan. 2015.

[145] K. Spiers, J. Cashion, and K. Gross, "Characterization of magnetite and maghemite for hyperthermia in cancer therapy," *Key Eng. Mater. Bioceram.*, vol. 254-256, pp. 213–216, Dec. 2003.

[146] Z. Li, L. Wei, M. Gao, and H. Lei, "One-pot reaction to synthesize biocompatible magnetite nanoparticles," *Adv. Mater.*, vol. 17, pp. 1001–1005, Apr. 2005.

[147] A. R. Dinesen, C. T. Pedersen, and C. Bender Koch, "The thermal conversion of lepidocrocite (γ-feooh) revisited," *J. Therm. Anal. Calorim.*, vol. 64, pp. 1303–1310, Jun. 2001.

[148] T. S. Gendler, V. P. Shcherbakov, M. J. Dekkers, A. K. Gapeev, S. K. Gribov, and E. McClelland, "The lepidocrocite-maghemite-haematite reaction chain - I. Acquisition of chemical remanent magnetization by maghemite, its magnetic properties and thermal stability," *Geophys. J. Int.*, vol. 160, pp. 815–832, Dec. 2005.

[149] R. Agr and R. September, "Evidence for a simple pathway to maghemite in earth and mars soils," *Geochim. Cosmochim. Acta*, vol. 66, pp. 2801–2806, Feb. 2002.

[150] K. Haneda and A. H. Morrish, "Magnetite to maghemite transformation in ultrafine particles," *J. Phys. Colloq.*, vol. 38, pp. 321 – 323, Apr. 1977.

[151] T. W. Swaddle and P. Oltmann, "Kinetics of the magnetite-maghemite-hematite transformation, with special reference to hydrothermal systems," *Can. J. Chem.*, vol. 58, pp. 1763–1772, Sep. 1980.

[152] M. Fang, V. Ström, R. T. Olsson, L. Belova, and K. V. Rao, "Particle size and magnetic properties dependence on growth temperature for rapid mixed co-precipitated magnetite nanoparticles," *Nanotechnology*, vol. 23, p. 145601, Apr. 2012.

[153] A. Espinosa, A. Serrano, A. Llavona, J. Jimenez de la Morena, M. Abuin, A. Figuerola, T. Pellegrino, J. F. Fernández, M. Garcia-Hernandez, G. R. Castro, and M. A. Garcia, "On the discrimination between magnetite and maghemite by xanes measurements in fluorescence mode," *Meas. Sci. Technol.*, vol. 23, p. 015602, Jan. 2012.

[154] I. Chamritski and G. Burns, "Infrared- and raman-active phonons of magnetite, maghemite, and hematite: a computer simulation and spectroscopic study," *J. Phys. Chem. B*, vol. 109, pp. 4965–8, Mar. 2005.

[155] A. M. Jubb and H. C. Allen, "Vibrational spectroscopic characterization of hematite, maghemite, and magnetite thin films produced by vapor deposition," *ACS Appl. Mater. Interfaces*, vol. 2, pp. 2804–2812, Oct. 2010.

[156] W. Kim, C. Y. Suh, S. W. Cho, K. M. Roh, H. Kwon, K. Song, and I. J. Shon, "A new method for the identification and quantification of magnetite-maghemite mixture using conventional x-ray diffraction technique," *Talanta*, vol. 94, pp. 348–52, May. 2012.

[157] D. L. A. de Faria, S. Venâncio Silva, and M. T. de Oliveira, "Raman microspectroscopy of some iron oxides and oxyhydroxides," *J. Raman Spectrosc.*, vol. 28, pp. 873–878, Jul. 1997.

[158] O. N. Shebanova and P. Lazor, "Raman study of magnetite (Fe_3O_4): Laser-induced thermal effects and oxidation," *J. Raman Spectrosc.*, vol. 34, pp. 845–852, Jun. 2003.

[159] B. Z. Tang, Y. Geng, J. W. Y. Lam, B. Li, X. Jing, X. Wang, F. Wang, A. B. Pakhomov, and X. X. Zhang, "Processible nanostructured materials with electrical conductivity and magnetic susceptibility: Preparation and properties of maghemite polyaniline nanocomposite films," *Chem. Mater.*, vol. 11, pp. 1581–1589, Mar. 1999.

[160] T. Fukuchi, "ESR techniques for the detection of seismic frictional heat," in *Earthq. Res. Anal. - Seismol. Seism. Earthq. Geol.*, ch. 16, pp. 317–340, InTech, 2012.

[161] M. M. Noginov, N. Noginova, O. Amponsah, R. Bah, R. Rakhimov, and V. A. Atsarkin, "Magnetic resonance in iron oxide nanoparticles: Quantum features and effect of size," *J. Magn. Magn. Mater.*, vol. 320, pp. 228–2232, Nov. 2008.

[162] B. P. Weiss, S. Sam Kim, J. L. Kirschvink, R. E. Kopp, M. Sankaran, A. Kobayashi, and A. Komeili, "Ferromagnetic resonance and low-temperature magnetic tests for biogenic magnetite," *Earth Planet. Sci. Lett.*, vol. 224, pp. 73–89, Apr. 2004.

[163] M. Darbandi, F. Stromberg, J. Landers, N. Reckers, B. Sanyal, W. Keune, and H. Wende, "Nanoscale size effect on surface spin canting in iron oxide nanoparticles synthesized by the microemulsion method," *J. Phys. D. Appl. Phys.*, vol. 45, p. 195001, Apr. 2012.

[164] T. Chen, H. Xu, Q. Xie, J. Chen, J. Ji, and H. Lu, "Characteristics and genesis of maghemite in chinese loess and paleosols: Mechanism for magnetic susceptibility enhancement in paleosols," *Earth Planet. Sci. Lett.*, vol. 240, pp. 790–802, Nov. 2005.

[165] C. Ciobanu, S. Iconaru, E. Gyorgy, M. Radu, M. Costache, A. Dinischiotu, P. Le Coustumer, K. Lafdi, and D. Predoi, "Biomedical properties and preparation of iron oxide-dextran nanostructures by maple technique," *Chem. Cent. J.*, vol. 6, p. 17, Mar. 2012.

[166] D. W. Collinson, K. M. Creer, and S. K. Runcorn, "Methods in palaeomagnetism," in *Proc. NATO Adv. Study Inst. Palaeomagnetic Methods*, p. 609, Elsevier Science, 1964.

[167] F. Stacey, *The Physical Principles of Rock Magnetism.* Developments in solid earth geophysics, Elsevier Science, 2012.

[168] C. Suryanarayana and M. Grant Norton, *X-Ray Diffraction: A Practical Approach.* New York: Springer US, 1 ed., 1998.

[169] P. Russo, D. Acierno, M. Palomba, G. Carotenuto, R. Rosa, A. Rizzuti, and C. Leonelli, "Ultrafine magnetite nanopowder: Synthesis, characterization, and preliminary use as filler of polymethylmethacrylate nanocomposites," *J. Nanotechnol.*, vol. 2012, pp. 1–8, Jul. 2012.

[170] H. E. Ghandoor, H. M. Zidan, M. M. H. Khalil, and M. I. M. Ismail, "Synthesis and some physical properties of magnetite (Fe_3O_4) nanoparticles," *Int. J. Electrochem. Sci.*, vol. 7, pp. 5734–5745, Jun. 2012.

[171] J. Sun, S. Zhou, P. Hou, Y. Yang, J. Weng, X. Li, and M. Li, "Synthesis and characterization of biocompatible Fe_3O_4 nanoparticles," *J. Biomed. Mater. Res. Part A*, pp. 333–341, Sep. 2006.

[172] G. C. Allen, M. T. Curtis, A. J. Hooper, and P. M. Tucker, "X-ray photoelectron spectroscopy of iron-oxygen systems," *J. Chem. Soc. Dalt. Trans.*, pp. 1525–1530, Jan. 1974.

[173] A. A. Elsherbini, M. Saber, M. Aggag, A. El-Shahawy, and H. A. Shokier, "Magnetic nanoparticle-induced hyperthermia treatment under magnetic resonance imaging," *Magn. Reson. Imaging*, vol. 29, pp. 272–280, Aug. 2011.

[174] M. A. Gilleo, "Superexchange interaction energy for Fe^{3+}-O^{2-}-Fe^{3+} linkages," *Phys. Rev.*, vol. 109, pp. 777–781, Feb. 1958.

[175] A. Rosencwaig, "Double exchange and electron hopping in magnetite," *Can. J. Phys.*, vol. 47, pp. 2309–2317, Nov. 1969.

[176] T. S. Herng, W. Xiao, S. M. Poh, F. He, R. Sutarto, X. Zhu, R. Li, X. Yin, C. Diao, Y. Yang, X. Huang, X. Yu, Y. P. Feng, A. Rusydi, and J. Ding, "Achieving a high magnetization in sub-nanostructured magnetite films by spin-flipping of tetrahedral Fe^{3+} cations," *Nano Res.*, vol. 8, pp. 2935–2945, Aug. 2015.

[177] A. Bengtson, D. Morgan, and U. Becker, "Spin state of iron in Fe_3O_4 magnetite and h-Fe_3O_4," *Phys. Rev. B*, vol. 87, pp. 1–13, Apr. 2013.

[178] J. F. W. Bowles, R. A. Howie, D. J. Vaughan, and J. Zussman, *Rock-Forming Minerals: Non-Silicates: Oxides, Hydroxides and Sulphides.* London: Geological Society of London, 2011.

[179] J. Nell and B. J. Wood, "High-temperature electrical measurements and thermodynamic properties of Fe_3O_4-$FeCr_2O_4$-$MgCr_2O_4$-$FeAl_2O_4$ spinels," *Am. Mineral.*, vol. 76, pp. 405–426, 1991.

[180] J. Tang, M. Myers, K. A. Bosnick, and L. E. Brus, "Magnetite Fe_3O_4 nanocrystals: Spectroscopic observation of aqueous oxidation kinetics," *J. Phys. Chem. B*, vol. 107, pp. 7501–7506, Sep. 2003.

[181] K. Jordan, A. Cazacu, G. Manai, S. F. Ceballos, S. Murphy, and I. V. Shvets, "Scanning tunneling spectroscopy study of the electronic structure of Fe_3O_4 surfaces," *Phys. Rev. B*, vol. 74, pp. 1–6, Aug. 2006.

[182] S. Emori, C. K. Umachi, D. C. Bono, and G. S. Beach, "Generalized analysis of thermally activated domain-wall motion in Co/Pt multilayers," *J. Magn. Magn. Mater.*, vol. 378, pp. 98–106, Oct. 2015.

[183] M. Z. Ansar, S. Atiq, K. Alamgir, and S. Nadeem, "Frequency and temperature dependent dielectric response of Fe_3O_4," *J. Sci. Res.*, vol. 6, pp. 399–506, Aug. 2014.

[184] Z. Švindrych, A. Youssef, and Z. Janů, "Link between magnetic and dielectric properties in magnetite," in *Acta Phys. Pol. A*, vol. 118, (Košice), pp. 940–941, Jul. 2010.

[185] C. Zhang, C. J. Li, G. Zhang, X. J. Ning, C. X. Li, H. Liao, and C. Coddet, "Ionic conductivity and its temperature dependence of atmospheric plasma-sprayed yttria stabilized zirconia electrolyte," *Mater. Sci. Eng. B Solid-State Mater. Adv. Technol.*, vol. 137, pp. 24–30, Oct. 2007.

[186] N. Tsuda, K. Nasu, A. Yanase, and K. Siratori, *Electronic Conduction in Oxides*. Springer Series in Solid-State Sciences, Springer Berlin Heidelberg, 2013.

[187] D. K. Kim, M. S. Amin, S. Elborai, S.-H. Lee, Y. Koseoglu, M. Zahn, and M. Muhammed, "Energy absorption of superparamagnetic iron oxide nanoparticles by microwave irradiation," *J. Appl. Phys.*, vol. 97, pp. 10J510–10J510–3, May. 2005.

[188] N. Church, J. M. Feinberg, and R. Harrison, "Low-temperature domain wall pinning in titanomagnetite: Quantitative modeling of multidomain first-order reversal curve diagrams and AC susceptibility," *Geochemistry Geophys. Geosystems*, vol. 12, pp. 1–18, Jul. 2011.

[189] Z. Wang, Z. Tian, Y. Dong, L. Li, L. Tian, Y. Li, and B. Yang, "Nanodiamond-conjugated transferrin as chemotherapeutic drug delivery," *Diam. Relat. Mater.*, vol. 58, pp. 84–93, Jun. 2015.

[190] J. A. Cuenca, E. Thomas, S. Mandal, O. Williams, and A. Porch, "Microwave determination of sp^2 carbon fraction in nanodiamond powders," *Carbon J.*, vol. 81, pp. 174–178, Jan. 2015.

[191] J. A. Cuenca, E. Thomas, S. Mandal, O. Williams, and A. Porch, "Investigating the broadband microwave absorption of nanodiamond impurities," *IEEE Trans. Microw. Theory Tech.*, 2015.

[192] I. Pope, L. Payne, G. Zoriniants, E. Thomas, O. Williams, P. Watson, W. Langbein, and P. Borri, "Coherent anti-stokes raman scattering microscopy of single nanodiamonds," *Nat. Nanotechnol.*, vol. 9, pp. 940–946, Oct. 2014.

[193] O. Shenderova and D. Gruen, "Ultrananocrystalline diamond," in *Ultrananocrystalline Diam.* (O. Shenderova and D. Gruen, eds.), ch. 9, pp. 291–326, New York: William Andrew Publishing, 2006.

[194] S. Osswald, G. Yushin, V. Mochalin, S. O. Kucheyev, and Y. Gogotsi, "Control of sp^2/sp^3 carbon ratio and surface chemistry of nanodiamond powders by selective oxidation in air," *J. Am. Chem. Soc.*, vol. 128, pp. 11635–11642, May. 2006.

[195] A. M. Panich, A. I. Shames, N. A. Sergeev, M. Olszewski, J. K. McDonough, V. N. Mochalin, and Y. Gogotsi, "Nanodiamond graphitization: a magnetic resonance study," *J. Phys. Condens. Matter*, vol. 25, p. 245303, Jun. 2013.

[196] F. Y. Xie, W. G. Xie, L. Gong, W. H. Zhang, S. H. Chen, Q. Z. Zhang, and J. Chen, "Surface characterization on graphitization of nanodiamond powder annealed in nitrogen ambient," *Surf. Interface Anal.*, vol. 42, pp. 1514–1518, May. 2010.

[197] O. Shenderova, A. M. Panich, S. Moseenkov, S. C. Hens, V. Kuznetsov, and H.-M. Vieth, "Hydroxylated detonation nanodiamond: FTIR, XANES, and nmr studies," *J. Phys. Chem. C*, vol. 115, pp. 19005–19011, Oct. 2011.

[198] T. Y. Leung, W. F. Man, P. K. Lim, W. C. Chan, F. Gaspari, and S. Zukotynski, "Determination of the sp^3/sp^2 ratio of a-c:h by XANES and XANES," *J. Non. Cryst. Solids*, vol. 254, pp. 156–160, Sep. 1999.

[199] G. Speranza and N. Laidani, "Measurement of the relative abundance of sp^2 and sp^3 hybridised atoms in carbon-based materials by XANES: A critical approach. Part II," *Diam. Relat. Mater.*, vol. 13, pp. 451–458, Nov. 2004.

[200] D. Slocombe, A. Porch, E. Bustarret, and O. Williams, "Microwave properties of nanodiamond particles," *Appl. Phys. Lett.*, vol. 102, p. 244102, Jun. 2013.

[201] A. C. Ferrari and J. Robertson, "Raman spectroscopy of amorphous, nanostructured, diamond-like carbon, and nanodiamond," *Philos. Trans. A. Math. Phys. Eng. Sci.*, vol. 362, pp. 2477–2512, Nov. 2004.

[202] U. Ott, "Nanodiamonds in meteorites: properties and astrophysical context," *J. Achiev. Mater. Manuf. Eng.*, vol. 37, pp. 779–784, Dec. 2009.

[203] S. Osswald, V. N. Mochalin, M. Havel, G. Yushin, and Y. Gogotsi, "Phonon confinement effects in the raman spectrum of nanodiamond," *Phys. Rev. B*, vol. 80, p. 75419, Aug. 2009.

[204] A. C. Ferrari, "Raman spectroscopy of graphene and graphite: Disorder, electron-phonon coupling, doping and nonadiabatic effects," *Solid State Commun.*, vol. 143, pp. 47–57, Apr. 2007.

[205] X. Liu, Z. Zhang, and Y. Wu, "Absorption properties of carbon black/silicon carbide microwave absorbers," *Compos. Part B Eng.*, vol. 42, pp. 326–329, Nov. 2011.

[206] H. Yang, M. Cao, Y. Li, H. Shi, Z. Hou, X. Fang, H. Jin, W. Wang, and J. Yuan, "Enhanced dielectric properties and excellent microwave absorption of sic powders driven with nio nanorings," *Adv. Opt. Mater.*, vol. 2, pp. 214–219, Dec. 2014.

[207] H. Kwon, S.-G. Kim, B.-W. Lee, W.-C. Seo, and M. Leparoux, "Corrigendum to 'mechanical properties of nanodiamond and multi-walled carbon nanotubes dual-reinforced aluminum matrix composite materials' [msa 632 (2015) 72-77]," *Mater. Sci. Eng. A*, vol. 639, p. 335, Apr. 2015.

[208] A. Porch, D. I. Odili, and P. A. Childs, "Microwave characterisation of carbon nanotube powders," *Nanoscale Res. Lett.*, vol. 7, p. 429, Aug. 2012.

[209] T. Zhao, C. Hou, H. Zhang, R. Zhu, S. She, J. Wang, T. Li, Z. Liu, and B. Wei, "Electromagnetic wave absorbing properties of amorphous carbon nanotubes," *Sci. Rep.*, vol. 4, pp. 1–7, Jan. 2014.

[210] A. Porch, D. Slocombe, J. Beutler, P. Edwards, A. Aldawsari, T. Xiao, V. Kuznetsov, H. Almegren, S. Aldrees, and N. Almaqati, "Microwave treatment in oil refining," *Appl. Petrochemical Res.*, vol. 2, pp. 37–44, Aug. 2012.

[211] S. Evans and A. bin Azeman, "Radiofrequency and microwave dielectric properties of aqueous cryoprotectant agents : dimethyl sulphoxide and 2,3-butanediol," *Phys. Med. Biol.*, vol. 43, pp. 2817–2829, Oct. 1998.

[212] C. Gabriel, T. Y. A. Chan, and E. H. Grant, "Admittance models for open ended coaxial probes and their place in dielectric spectroscopy," *Phys. Med. Biol.*, vol. 39, pp. 2183–220, Dec. 1994.

[213] B. M. Bode and M. S. Gordon, "Macmolplt: a graphical user interface for GAMESS," *J. Mol. Graph. Model.*, vol. 16, pp. 133–138, Jun. 1998.

[214] M. S. Gordon and M. W. Schmidt, "Advances in electronic structure theory: GAMESS a decade later," in *Theory Appl. Comput. Chem. first forty years*, ch. 41, pp. 1167–1189, Elsevier, Oct. 2005.

[215] M. D. Hanwell, D. E. Curtis, D. C. Lonie, T. Vandermeersch, E. Zurek, and G. R. Hutchison, "Avogadro: an advanced semantic chemical editor, visualization, and analysis platform," *J. Cheminform.*, vol. 4, p. 17, Jan. 2012.

[216] J. S. Bulmer, J. Martens, L. Kurzepa, T. Gizewski, M. Egilmez, M. G. Blamire, N. Yahya, and K. K. K. Koziol, "Microwave conductivity of sorted cnt asSEMblies," *Sci. Rep.*, vol. 4, pp. 1–8, Jan. 2014.

[217] Y. Wang, M. Jasiswal, M. Lin, S. Saha, B. Ozyilmaz, and K. P. Loh, "Electronic properties and applications of nanodiamond," *ACS Nano*, vol. 6, pp. 1018–1025, Feb. 2012.

[218] C. H. Ao and S. C. Lee, "Indoor air purification by photocatalyst TiO_2 immobilized on an activated carbon filter installed in an air cleaner," *Chem. Eng. Sci.*, vol. 60, pp. 103–109, Jan. 2005.

[219] W. Wang, G. Huang, J. C. Yu, and P. K. Wong, "Advances in photocatalytic disinfection of bacteria: Development of photocatalysts and mechanisms," *J. Environ. Sci.*, vol. 34, pp. 232–247, Jun. 2015.

[220] M. Altomare, M. V. Dozzi, G. L. Chiarello, A. Di Paola, L. Palmisano, and E. Selli, "High activity of brookite TiO_2 nanoparticles in the photocatalytic abatement of ammonia in water," *Catal. Today*, vol. 252, pp. 184–189, Nov. 2014.

[221] J. Zhang, P. Zhou, J. Liu, and J. Yu, "New understanding of the difference of photocatalytic activity among anatase, rutile and brookite TiO_2," *Phys. Chem. Chem. Phys.*, vol. 16, pp. 20382–20386, Aug. 2014.

[222] Y. Ohama and D. V. Gemert, "Principles of TiO_2 photocatalysis," in *Appl. Titan. Dioxide Photocatal. to Constr. Mater.* (Y. Ohama and D. V. Gemert, eds.), pp. 5–10, Springer Netherlands, 2011.

[223] D. Dvoranová, Z. Barbieriková, and V. Brezová, "Radical intermediates in photoinduced reactions on TiO_2 (an epr spin trapping study)," *Molecules*, vol. 19, pp. 17279–17304, Oct. 2014.

[224] R. Konaka, E. Kasahara, W. C. Dunlap, Y. Yamamoto, K. C. Chien, and M. Inoue, "Irradiation of titanium dioxide generates both singlet oxygen and superoxide anion," *Free Radic. Biol. Med.*, vol. 27, pp. 294–300, Aug. 1999.

[225] S. Xu, J. Shen, S. Chen, M. Zhang, and T. Shen, "Active oxygen species ($^1O_2$,$O_2^{\cdot-}$) generation in the system of TiO_2 colloid sensitized by hypocrellin b," *J. Photochem. Photobiol. B Biol.*, vol. 67, pp. 64–70, May. 2002.

[226] J. Chin, S. Scierka, T. Kim, and A. Forster, "A photoconductivity technique for the assessment of pigment photoreactivity," in *Proc. 81st Annu. Meet. FSCT*, (Philadelphia), National Institute of Standards and Technology, Nov. 2003.

[227] G. D. Arndt, W. H. Hartwig, and J. L. Stone, "Photodielectric detector using a superconducting cavity," *J. Appl. Phys.*, vol. 39, pp. 2653–2656, May. 1968.

[228] W. H. Hartwig and J. J. Hinds, "Characteristics of photodielectric optical detectors using superconducting cavities," *J. Appl. Phys.*, vol. 42, p. 137, Jan. 1971.

[229] W. H. Hartwig and J. J. Hinds, "Use of superconducting cavities to resolve carrier trapping effects in cds," *J. Appl. Phys.*, vol. 40, pp. 2020–2027, Apr. 1969.

[230] H. K. Dunn, L. M. Peter, S. J. Bingham, E. Maluta, and A. B. Walker, "In situ detection of free and trapped electrons in dye-sensitized solar cells by photo-induced microwave reflectance measurements," *J. Phys. Chem. C*, vol. 116, pp. 22063–22072, Sep. 2012.

[231] R. Janes, M. Edge, J. Robinson, J. Rigby, and N. Allen, "Microwave photodielectric and photoconductivity studies on titanium dioxide exposed to continuous polychromatic irradiation; Part II:," *J. Photochem. Photobiol. A Chem.*, vol. 127, pp. 111–115, Oct. 1999.

[232] M. Edge, R. Janes, J. Robinson, N. Allen, F. Thompson, and J. Warman, "Microwave photodielectric and photoconductivity studies on titanium dioxide exposed to continuous, polychromatic irradiation Part I: A novel analytical tool to assess the photoactivity of titanium dioxide," *J. Photochem. Photobiol. A Chem.*, vol. 113, pp. 171–180, May. 1998.

[233] N. Allen, Y. Chow, F. Thompson, T. Jewitt, M. Hornby, and L. Simpson, "Electrophotographic and microwave photodielectric studies on titanium dioxide pigments in the solid state," *J. Photochem. Photobiol. A Chem.*, vol. 60, pp. 369–381, Aug. 1991.

[234] S. Grabtchak and M. Cocivera, "Microwave response due to light-induced changes in the complex dielectric constant of semiconductors," *Phys. Rev. B*, vol. 58, pp. 4701–4707, Aug. 1998.

[235] C. C. Mercado, F. J. Knorr, J. L. McHale, S. M. Usmani, A. S. Ichimura, and L. V. Saraf, "Location of hole and electron traps on nanocrystalline anatase TiO_2," *J. Phys. Chem. C*, vol. 116, pp. 10796–10804, May. 2012.

[236] R. Janes, M. Edge, J. Robinson, J. Rigby, and N. Allen, "Microwave photodielectric and photoconductivity studies on titanium dioxide exposed to continuous polychromatic irradiation; Part II:," *J. Photochem. Photobiol. A Chem.*, vol. 127, pp. 111–115, Oct. 1999.

[237] M. R. Hoffmann, S. T. Martin, W. Choi, and D. W. Bahnemannt, "Environmental applications of semiconductor photocatalysis," *Chem. Rev.*, vol. 95, pp. 69–96, Jan. 1995.

[238] S. C. Ke, T. C. Wang, M. S. Wong, and N. O. Gopal, "Low temperature kinetics and energetics of the electron and hole traps in irradiated TiO_2 nanoparticles as revealed by epr spectroscopy," *J. Phys. Chem. B*, vol. 110, pp. 11628–11634, May. 2006.